Doctoral Thesis

Double-Wall System as 3-D Shear Walls in Residential Buildings with Earthquake Loads.

submitted in satisfaction of the requirements for the degree of
Doctor of Science in Civil Engineering
of the Vienna University of Technology, Faculty of Civil Engineering

Dissertation

Doppelwandsystem als 3-D Schubwände in Wohnhäusern bei Belastung durch Erdbeben.

ausgeführt zum Zwecke der Erlangung des akademischen Grades eines
Doktors der technischen Wissenschaft
eingereicht an der Technischen Universität Wien Fakultät für Bauingenieurwesen
von

Dipl.-Ing. Falko Ducia
Matrikelnummer 6816412
Petrusgasse 1A 1030 Wien

Gutachter: Univ. Prof. Dipl.-Ing. Dr.techn. Andreas Kolbitsch
Institut für Hochbau und Technologie Technische Universität
Wien Karlsplatz 13 E206/4, 1040 Wien

Gutachter: Univ. Prof. Baris Binici
Middle East Technical University, Department of Civil
Engineering, Structural and Earthquake Engineering Laboratory
K2-308 06531, Ankara/Turkey.

Vienna, January 2015

Ein großes Danke geht an meine liebe Frau, Dipl.-Ing Nadejda Ducia, sie hatte immer Verständnis für mein Verkriechen in dieser Arbeit und auch für die mentale und organisatorische Unterstützung einfach Danke, auch für Deinen Wahlspruch: „Better late than never“

Dank an

Die vorliegende Arbeit wurde auf Basis einer Idee von Erich Kastner (†2014) verfasst. Herr Kastner war der Erfinder und Promotor der punktförmigen Verbindung von Betonfertigteilen [1], wie die Verbindung der beiden Außenschalen bei Doppelwände oder die beiden Betonschichten bei 3-Schicht Fassadenelementen (Sandwichwänden) [2].

Erst durch diese Erfindung war es möglich die erdbebensichere Konstruktion von Doppelwänden zu entwickeln. Herr Kastner war auch maßgebend bei den Erstellen der Versuchskörper beteiligt, durch sein fachliches Wissen und sein Geschick, jede Situation zu einem guten Ende zu führen, sind wir alle ihm zu großem Dank verpflichtet.

Ein großer Dank auch an Univ. Prof. Dipl.-Ing. Dr.techn. Andreas Kolbitsch, [3] der sich sehr mit der Thematik beschäftigt hat und mir viele wertvolle Hinweise und Anregungen gab.

Danken möchte ich hier auch meinem Zweitbegutachter, Univ. Prof. Baris Binici (METU Middle East Technical University - Ankara Türkei) als Leiter des Department of Civil Engineering, Structural and Earthquake Engineering Laboratory [4] war er mit seinem Team maßgebend am Erfolg der Versuche beteiligt.

Univ. Prof. Baris Binici hat mit mir den Versuchsaufbau und die Art der Versuche erarbeitet und war auch an der Interpretation der Resultate (und Ihrer Auswirkungen auf die Türkischen Normen) mit Rat und Tat zur Seite. Seine Erfahrung gab mir sehr wertvolle Anregungen für diese Arbeit. Vielen Dank für die vielen Stunden kreativer Arbeit.

Die Versuchsaufbauten und die Versuchsdurchführungen wurden von Prof. Dr. Erdem Canbay und seinem Team souverän und präzise durchgeführt, Danke dafür.

Die für die analytischen Berechnungen notwendige Software, ATENA wurde von Červenka Consulting s.r.o, Prag zur Verfügung gestellt. Dabei war Herr Ing. Radomír Pukl CSc als Specialist in Bruchmechanik eine wertvolle Stütze bei der Bändigung des Programms. Den Herren Evan Bentz und Michael P. Collins, University Toronto möchte ich für die freie Verwendung des Programms „Response-2000" danken.

Bedanken möchte ich auch bei der Firma Franz Oberndorfer GmbH & Co KG in 4263 Gunskirchen / Österreich, [5], Herrn H. Oberndorfer und Herrn DI W. Pröll die die finanziellen Mittel zur Durchführung der Versuche zur Verfügung gestellt haben.

Acknowledgements

This thesis was written on the basis of an idea by Erich Kastner (d. 2014). Mr. Kastner was the inventor and promoter [1] of a point-like connection of precast concrete elements like double walls and 3-Layer- façade elements (sandwich panels) [2].

Only through this invention did it become possible to construct earthquake-resistant design for double walls. Mr. Kastner was also critically involved in the creation of the specimens at the Earthquake Laboratory at the Middle East Technical University in Ankara. We owe him a great debt of gratitude for his professional knowledge and flair for bringing every situation to a favorable conclusion.

I am grateful to my advisor, Univ. Prof. Dipl.-Ing. Dr.techn. Andreas Kolbitsch, who engaged himself wholeheartedly in the subject matter and gave me many valuable comments and suggestions.

I would like also to thank my second supervisor, Univ. Prof. Dr. Baris Binici, the head of the Department of Civil Engineering, Structural and Earthquake Engineering Laboratory [4] at the METU (Middle East Technical University, Ankara), for his help during and after the experimental course (where he and his team was instrumental in the success of the testing), and also for his advice and assistance in the interpretation of the results (and their impact on the Turkish Standards). His experience gave me some much appreciated suggestions for this thesis. Thank you for the numerous hours of creative work.

The experimental setups and the experimental procedures were carried out authoritatively and accurately by Prof. Dr. Erdem Canbay and his team. Thank you for the excellent work.

ATENA, the necessary software for the analytical calculations, was provided by Červenka Consulting SRO, Prague. Of great support here was Ing. Radomír Pukl CSc, a specialist in fracture mechanics and expert on the "inner workings" of ATENA. I would also like to thank Evan Bentz and Michael P. Collins, both professors of Toronto University, for the free use of the "Response-2000" program.

I am grateful also to the company Franz Oberndorfer GmbH Co KG, 4263 Gunskirchen / Austria [5], and in particular Mr. H. Oberndorfer and Mr. DI W. Pröll, who provided the financial means for the tests in Ankara.

Kurzfassung

Die vorliegende Arbeit leistet einen Beitrag zur Verwendung von Doppel-Wänden im Einsatz bei Hochbauten mit Erdbebenbelastungen. Doppelwände, auch als Dreifachwand, Gitterträgerwand, Dreikammerwand, Elementwand oder Hohlwand bezeichnet, werden in Mitteleuropa heute schon sehr oft und gerne als "Halbfertigteile" im Hochbau eingesetzt [6]. Die Doppelwand ermöglicht eine schnelle, präzise und weitgehend wetterunabhängige Fertigung von Geschoßbauten. Für den Einsatz dieser Bauweise sind (außer einem Hebezeug beim Versetzten der Elemente) keine, dauernd auf der Baustelle vorhandenen, Großgeräte notwendig. Ein Nachteil war bis heute, verursacht durch die Verbindung der beiden Beton-Außen-Schalen mittels Gitterträger, die Unmöglichkeit die Ortbetonkerne bei Wandelemente, bei T-Stücken und in Ecken konstruktiv, gemäß den verschiedenen Erdbebennormen, zu verbinden. Durch den Einsatz von punktförmigen Verbindungen (Kappema-Welle) [7] ergibt sich die Möglichkeit horizontale Bewehrungselemente (Körbe, einzelne Bewehrungsstäbe) zu verschieben um kraftschlüssige Verbindungen zu erhalten.
In dieser Arbeit wurden Versuche von 6 Doppelwandbauteile, im Maßstab 1:1 an der METU (Middle East Technical University) in Ankara durchgeführt. Durch die Begrenzung der maximal möglichen aufzubringenden Kraft von 1.000.- kN und der Notwendigkeit die Versuchskörper im Maßstab 1:1 zu prüfen ergaben sich die mögliche Versuchskörper Größe. Die Versuche zeigten eine ausgezeichnete Duktilität, der Duktilitätsfaktor beträgt rund 6, somit sind diese Bauteile hoch duktil. Ein Vergleich der Probekörper schließt den ersten Teil der Arbeit ab.
Im zweiten Teil der Arbeit wurde die Versuch mittels des 3-D Simulationsprogramms ATENA [8] berechnet und mit den Versuchsergebnissen verglichen.
Durch die Größenbegrenzung der Versuchskörper werden die originalen Versuchskörper maßlich und belastungsmäßig variiert und abgeändert.
Abschließend werden Empfehlungen für die Nutzung dieser Doppelwandelemente und die ergänzenden Berechnungen mit einem nichtlinearen Berechnungsprogramm, für Hochbauten im Belastungsfall Erdbeben zusammengestellt.

Schlagwörter: Stahlbeton Fertigteile, 3D-Wandscheiben, seismisch, erdbebensicher, Doppelwand, zyklische Last, Hysteresis Verhalten, Reaktionswand Test,

Abstract

This thesis addresses the possibility of double walls to be used as earthquake-shear walls for building constructions.

Double walls (also called hollow and cavity walls) are already very often used in Central Europe as "semi-finished parts" in building construction [9]. The double wall system enables fast and accurate construction of multi-storey buildings, regardless of weather conditions. Except for lifting equipment for the offset of the elements, the use of this design requires no major equipment to be constantly present on the site. Until today, the connection of the two-concrete shells using lattice girders was a disadvantage. As a result it was impossible to constructively connect the wall elements, T-pieces and corners with an “in situ concrete core”, in compliance with earthquake standards. The use of point-like compounds (KAPPEMA-wave) [7] provides the possibility to move horizontal reinforcement elements (baskets, individual reinforcing bars) in order to gain frictional connections.

The first part of this study documents and describes the seismic testing of a strong wall, which was carried out on six double wall components (in scale 1:1) at the METU (Middle East Technical University) in Ankara, Turkey. The possible size of the test specimens arose as a result of limiting the maximum applied force to 1000 kN, and also from considering the need for the test specimens to be tested in scale 1:1. It was proved that the ductility of the double wall elements has a ductility ratio of about 6, which is higher than expected. A comparison of the test specimens concludes this first part of the study.

The second part consists of analytical studies, conducted parallel to the tests using the 3-D simulation program ATENA [8]. Both results are compared, leading finally to the compiling of recommendations for the use of these double-wall elements in buildings under seismic load. Because of the restricted size of the specimens, the maximal force applied was limited to 1000 kN; the analytic investigations with larger specimens showed the possibility of using double-wall as earthquake-proof building elements.

In the appendix a calculation of a 5-storey building [10] and of the two main elements (T and U-connection) is carried out.

Key words: RC-Prefabrication, Earthquake, Double-Walls, Strong Wall Test, Flange Shear Wall, hysteresis behavior, reinforced concrete shear walls, cyclic loading

Table of Contents

List of Figures

List of Tables

1 Introduction

1.1 General

Conventional precast construction has many drawbacks due to the difficulties associated with connections between structural elements for seismic resistance. Since the beginning of the use of precast RC-parts, solutions were sought to connect these precast parts in a way to make them earthquake-resistant. One of these attempts was published by Fischinger et al. in 1987 [11].

Prefabricated concrete can only be connected by external links, so that they can transmit torques and forces in several axes from one component to another component.

A semi precast system capable of overcoming such difficulties is the double wall system. This system distinguishes itself through the use of both precast and cast-in-place components. In the double wall system, precast concrete shells serve mainly as formwork and allow the reinforcement to be constructed at the factory. In addition it is possible to put all the necessary electrical installations into these concrete precast-shells.

The regions between the interconnected shells are then filled with cast-in-situ concrete on the construction site. In this way, monolithic building elements finally show the same effectiveness as cast-in-situ concrete walls and slabs. This will be confirmed with the results of this study, performed with 6 Reaction-wall tests at the METU in Ankara [4]. Further details about the system are presented in the next chapter. The key advantages of double wall systems can be summarized as follows:

- Faster construction due to ease of assembly.
- A minimum of construction workers needed for installation on site.
- Architectural flexibility as walls and columns can be placed arbitrarily.
- Accurate steel detailing, removing the need for quality control on site.
- Good and secured concrete quality.
- Robust earthquake performance due to the presence of many structural walls which are connected.
- Less inspection on the construction site.
- Cost reductions due to installation of equipment ducts, electro inserts in the factory, which removes the need for drilling and plastering.
- Energy efficiency due to integrated insulation (thermos-walls) and pipes for heating and cooling.
- Lower costs due to mass factory production.

The double wall system has been one of the most efficient construction technologies available since the early seventies **[9].** It was applied very successfully in countries such as Germany, Austria, Italy, Greece, the United Arab Emirates, Australia, and Japan. It should be especially stressed that the system is composed of a well-proven set of products that have been used for years all over the world. The single parts for the use of the double wall system have all the necessary European approvals. For example, in Germany and Austria filigree slabs have a market share of almost 90% and double wall elements of around 30%.

The needs of the European construction sector – from the perspective of seismic safety, energy efficiency, guaranteed quality of the final product and speed of construction – call for new approaches in the construction and design of buildings.

Since double wall constructions are only produced today in a single precast plant in eastern Turkey, this technology of production and processing, and also the static and dynamic calculation of buildings with double walls, is not "standard" in residential and office construction.

One of the most important prerequisites for entering a new market with a new technology is to qualify the product for seismic safety, and especially in Turkey, normal double-walls made with lattice girder cannot be used easily as earthquake-proof components. In order to demonstrate the seismic performance of one special type of double walls, a research project was initiated with the Middle East Technical University, Department of Civil Engineering, and structural Mechanics Laboratory.

The objective of this study is to demonstrate and prove that selected double-wall products show the same effectiveness as cast-in-situ concrete elements, and that they can be designed and constructed in earthquake-prone areas by following the design and construction guidelines of cast-in-place structural walls. The results of the research findings are presented in **Chapter 6** (Summary and Conclusion, **p.171**) of this thesis.

1.2 Double Wall System

1.2.1 The Walls

A double wall is a semi-finished product and consists of two thin precast concrete slabs, between 5cm and 7cm thick and produced in the production plant, which are connected through reinforcement elements, namely the lattice girder or the wave (***Figure 1***). After the erection on the construction site, the empty space between the shells is filled with cast-in-situ concrete. The inner surfaces of the shells are roughened in the production plant in order to transfer the forces together with the connecting reinforcement.

Consequently, the total cross section made of precast slabs and cast-in-situ concrete has a joint structural effect in the bond and is ideally suited to carry vertical and horizontal loads. Through the use of double wall elements, extensive casting works and a major part of the reinforcement works are done in the factory, which significantly reduces the construction time.

The attractive feature of this system is the complete independence from grid dimensions, whereby almost every architectural requirement can be realized. There is also the possibility to produce double walls with inside thermal insulation (***Figure 2***). The insulation thickness is usually around 5 to 20 cm depending on the respective structural-physical requirements of the thermal protection calculation. Inside the shell, the insulation is well-protected against environmental effects and fire. The insulation is also prepared in the factory, thereby removing the need for any insulation needs on site. This property enables the double wall system to be a complete structural system, with only the need for window/door installation and minor finishing.

The two alternatives to constructing a double wall are the use of lattice girder and a point-like connection like the wave. The lattice girder has been the classical method of constructing double walls in Europe for the last five decades. The lattice girder system has a continuous reinforcement placed about 35 to 40 cm away from the wall edge to bear pressure during concrete casting.

This lattice girder placement does not allow the use of connection reinforcement with sufficient development length between adjacent walls. Without sufficient horizontal connection cages, adjacent walls will behave as independent walls and do not benefit from the advantages of increased stiffness and strength. Furthermore, the continuous reinforcement obstructs the reinforcement (important for seismic detailing) that needs to be placed between the two shells. In fact these are the main reasons for the previous disuse of double walls in earthquake zones.

From the beginning of the 21st century, the use of waves (***Figure 3***) to connect the two shells became possible. With a German approval [7], they can be also used for earthquake-proof constructions. The waves are composed of stainless steel sticks connected to a thin shell steel wave in the central portion. The sticks penetrate into the concrete shells and are flush to the shell surfaces. This became possible through the use of stainless steel for the sticks. Waves are discrete connection elements and exhibit important advantages such as:

1- Allowing to connect adjacent double walls due to the available space (lattice girder does not allow for such a space).
2- Thinner shell thickness, down to 5 cm.
3- Excellent pullout strength, thereby reducing the amount of reinforcement.
4- Allowing the use of any vertical and horizontal reinforcement between the two shells.
5- Allowing the use of insulation material adjacent to one shell from the inside.
6- Reduction in the amount of steel necessary for the connection of two shells.

With the invention of waves, it became possible to safely design and construct double wall systems for seismic resistance.

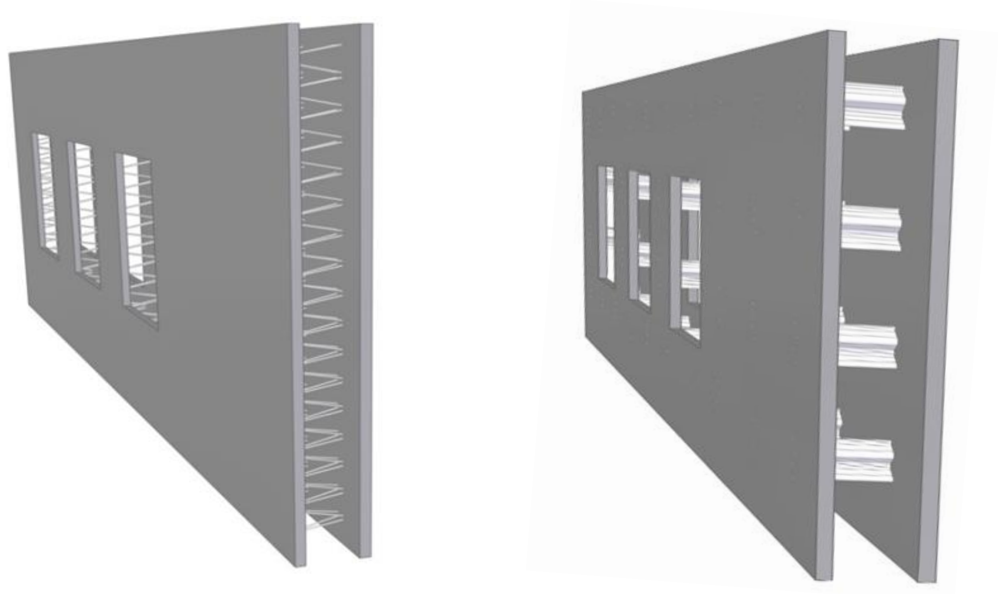

a) Lattice girder connection

b) Wave connection

Figure 1 Double Walls [7].

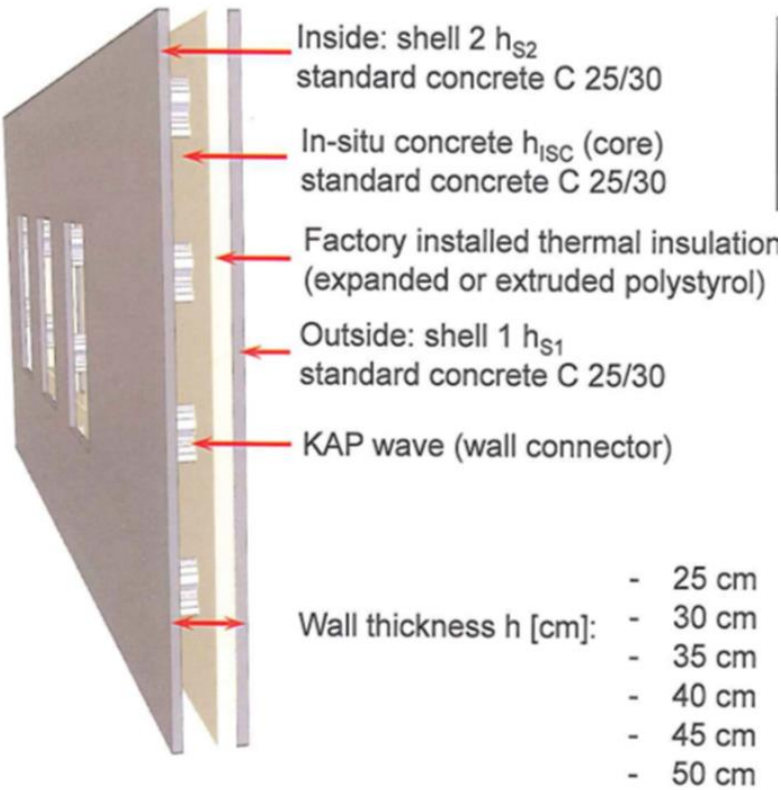

Figure 2 Insulated double wall [7],

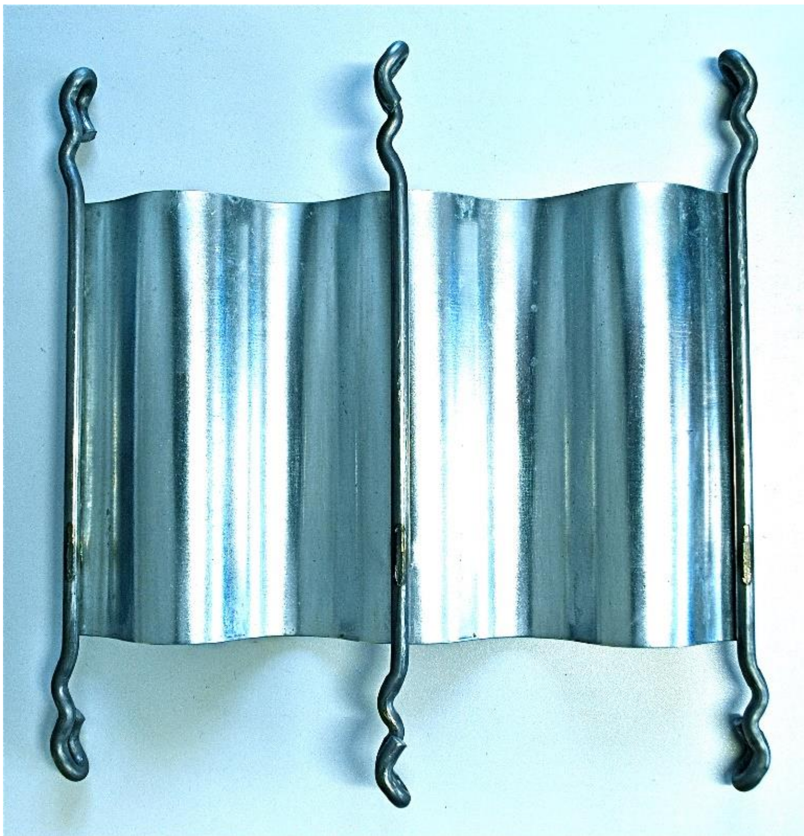

Figure 3 *KAPPEMA wave with integrated sticks.*

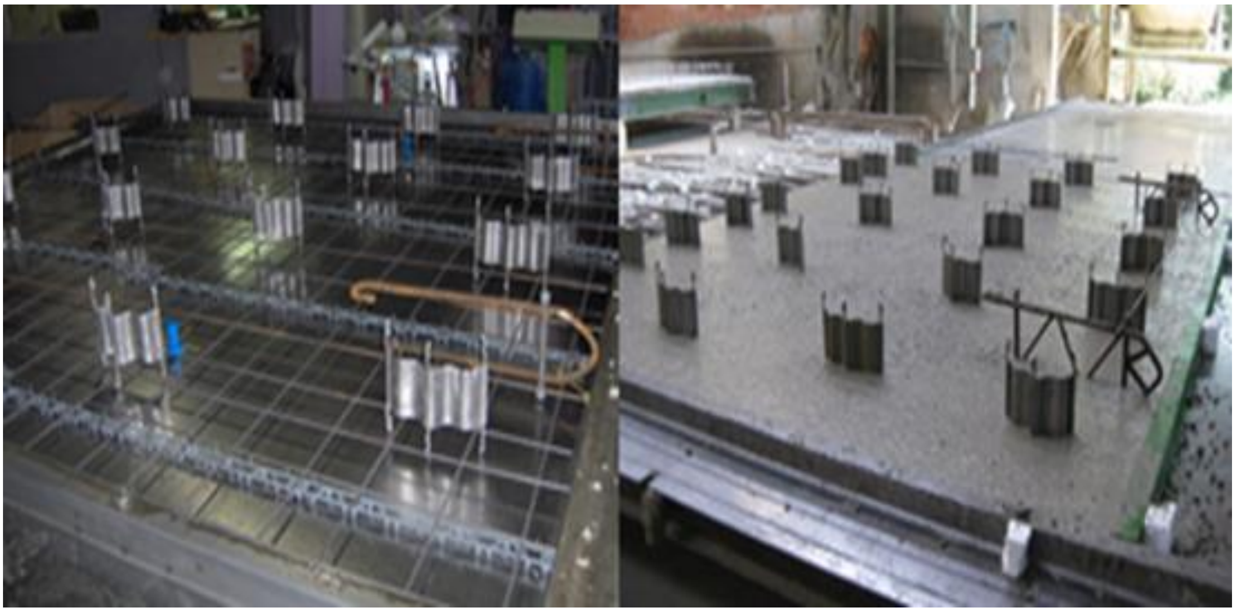

Figure 4 *Production of the double wall, first shell with waves [7].*

Figure 5 Lifting after casting second shell –I [12].

Figure 6 Lifting of a finished double wall element II [7].

Figure 7 *Transportation* [12].]

In fact, due to the limited space for connecting reinforcement steel bars the double wall system with lattice girder needs in situ casting for connections and corners.
With the system of point-type connection there is enough space between the waves for reinforcement bars to connect. (*Figure 8*).

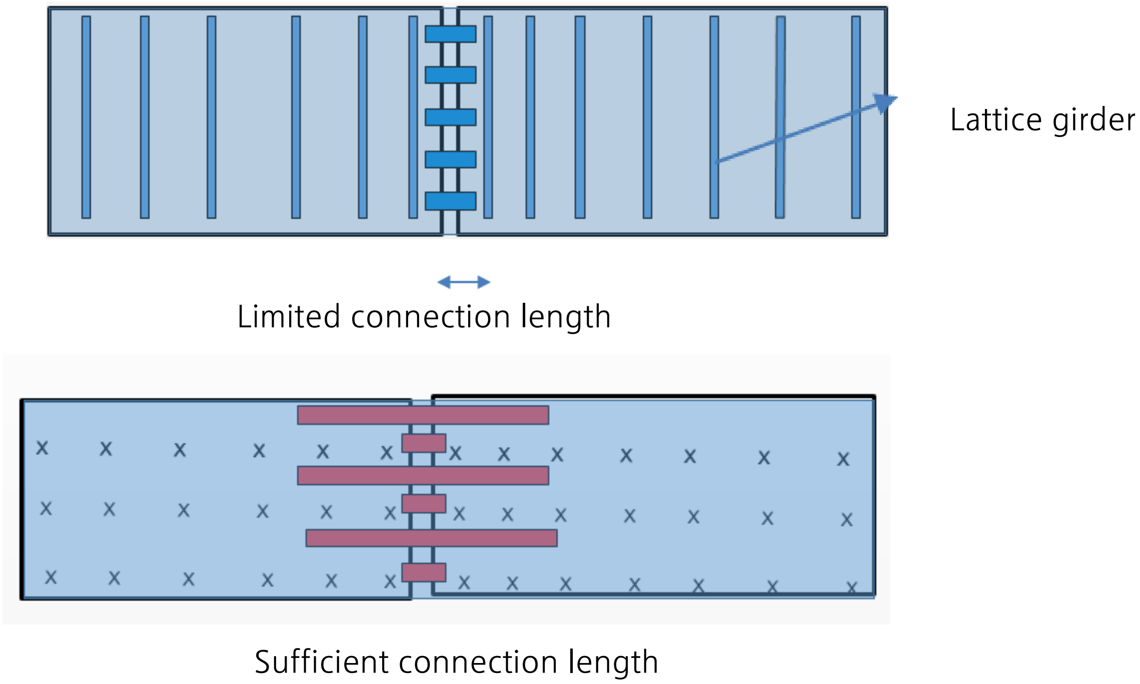

Figure 8 *Lattice girder versus wave.*

In fact, it is also possible to connect two double walls with a lattice girder. A Chinese admission shows (***Figure 9*** *and* ***Figure 10***) the complicated way to do this.

This means a very large amount of additional formwork and additional reinforcement work on site.

Formwork

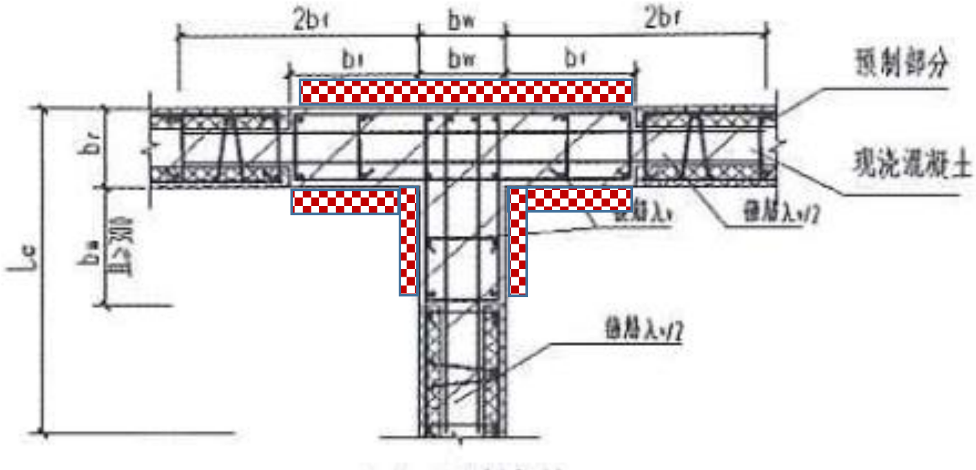

Figure 9 *Chinese admission double-wall lattice girder wall intersection* ***[128]***.

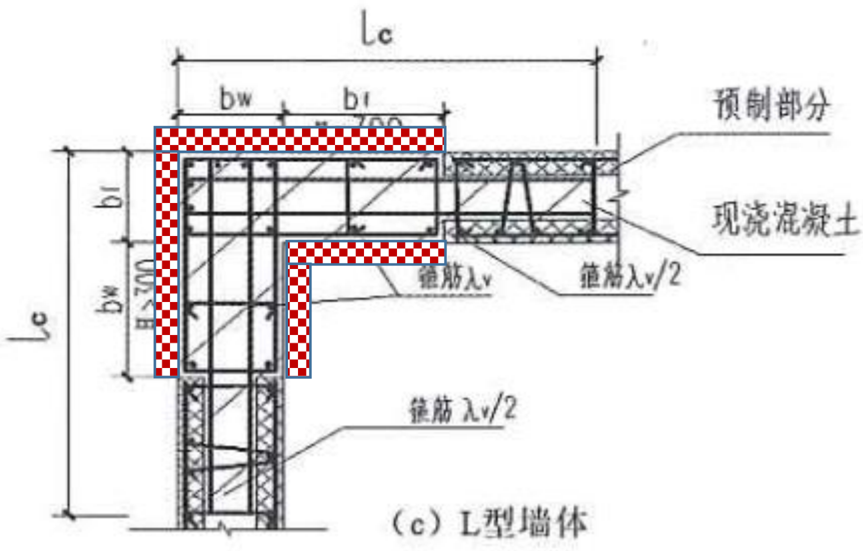

Figure 10 *Chinese admission double-wall lattice girder corner* ***[128]***.

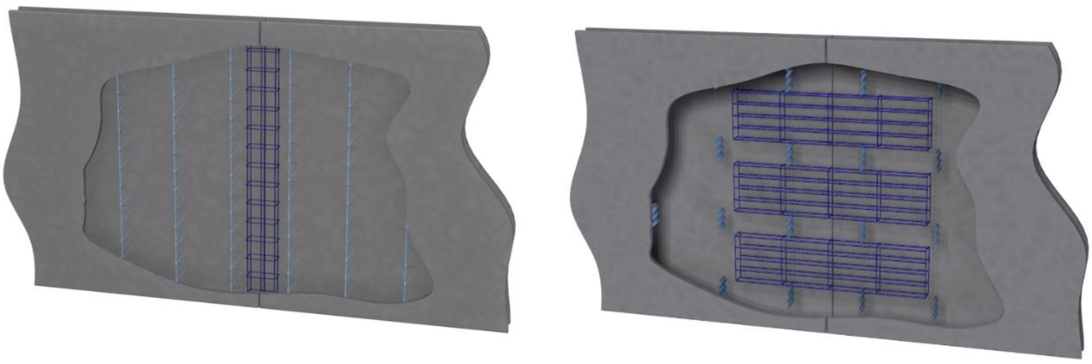

a) Lattice girder b) Wave, after connection of reinforcement

Figure 11 *Advantages of waves: connection of two walls.*

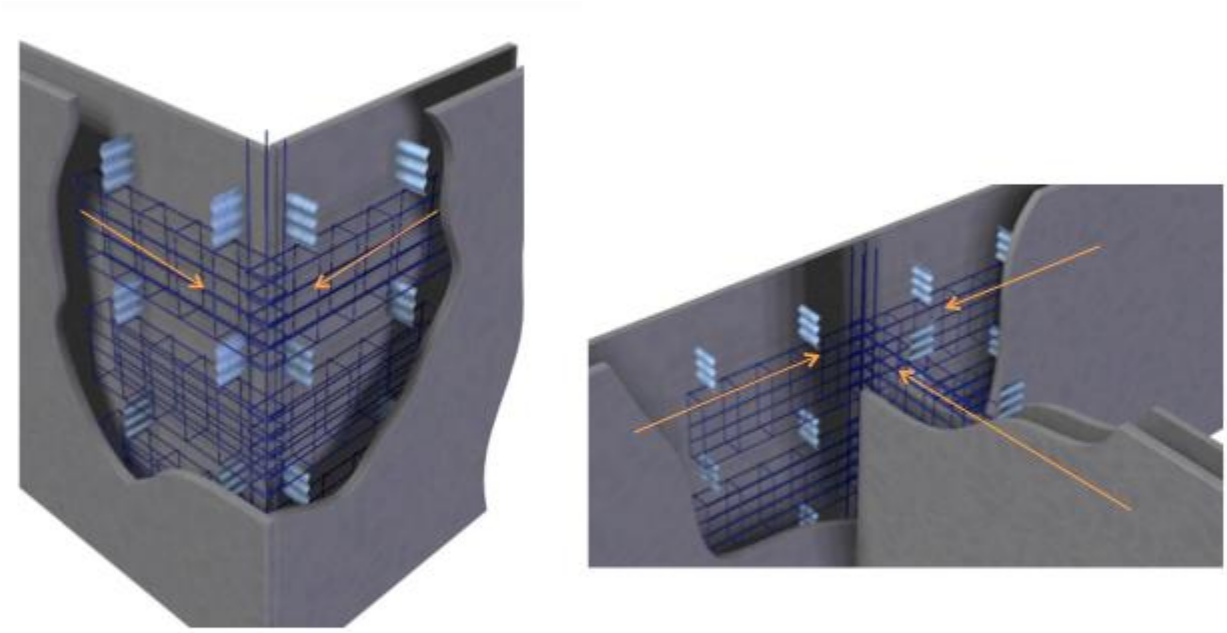

a) Wave connection of a corner b) Wave connection on a wall junction-

Figure 12 *Possible wave connections.*

1.2.2 Slabs

Filigree slabs are also constructed with lattice girders. A bottom shell is cast with the lattice girder and shipped to site for concrete casting (*Figure 13 and Figure 14*). The bottom shell can be reinforced concrete or prestressed concrete depending in the desired span. The untensioned filigree slabs, which are also often referred to as large-scale slabs, are produced as "semi-finished floor slabs". The 5 cm thick concrete slabs (which can be thicker if desired) are produced up to 3m width. The structurally required bottom reinforcement and the lattice girder which guarantees the assembly stiffness as well as the bond to the upper concrete are already integrated in the precast plant.

The individual elements are connected to floor slabs by means of cast-in-situ concrete with the necessary connection reinforcement (*Figure 15*). These floor slabs guarantee the rigid diaphragm action. Furthermore, the semi-finished construction also enables the execution of continuous beams, flat slabs, and the development of joists as T-beams. With the use of filigree slabs, complex casting work and extensive reinforcement, work on the construction site can be spared.

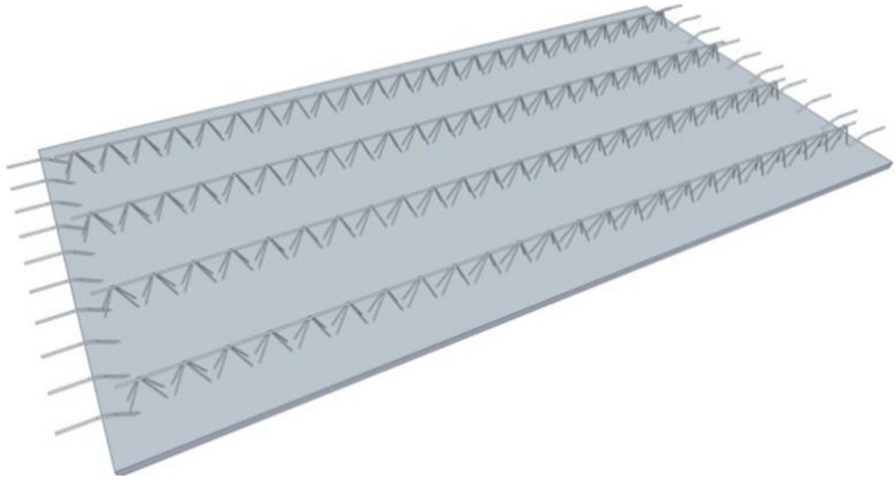

a) Filigree slab [12].

b) Stacking

c) Lifting in position

Figure 13 Filigree slab construction I [12].

a) Reinforcement Placement

b) Concrete Casting

Figure 14 Filigree slab construction on the construction site II. [12]

1.2.3 Construction System

A building system consists of structural elements such as walls, floors and roof elements as well as columns, beams and stairs. In the double wall system, the precast concrete components are manufactured in a production facility and then transported to the building site. On the building site, the structural elements are assembled and fixed by the help of in situ concrete casting. As explained in the previous sections, double wall systems consist of precast concrete shells, connected by lattice girders with a central gap. The floor system is made up of filigree slabs composed of a concrete shell with a lattice girder. After the assembly of the precast concrete elements, proper reinforcement is placed on site to ensure monolithic moment resisting connections. Later, the walls, slabs and wall-slab connections are completed with in situ concrete (*Figure 16*) This step is the main difference with standard precast construction, where it is very difficult to obtain monolithic connections without concrete works (i.e. usually done by welding steel pieces). After the hardening of concrete, they can serve as a monolithic wall-floor system. The assembly steps on site are summarized in Figure 17 and *Figure 19*. Wall installation and concrete casting in the field are also shown there.

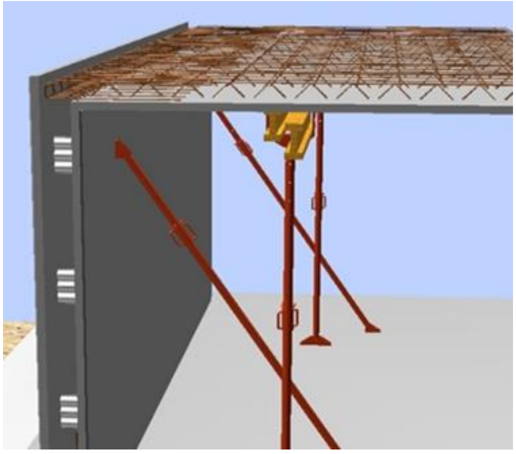

a) Connection wall-slab

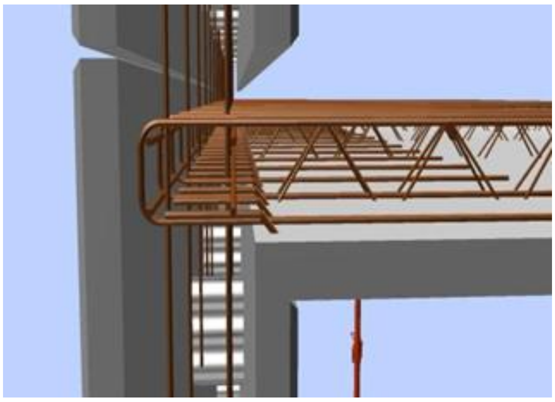

b) Detail

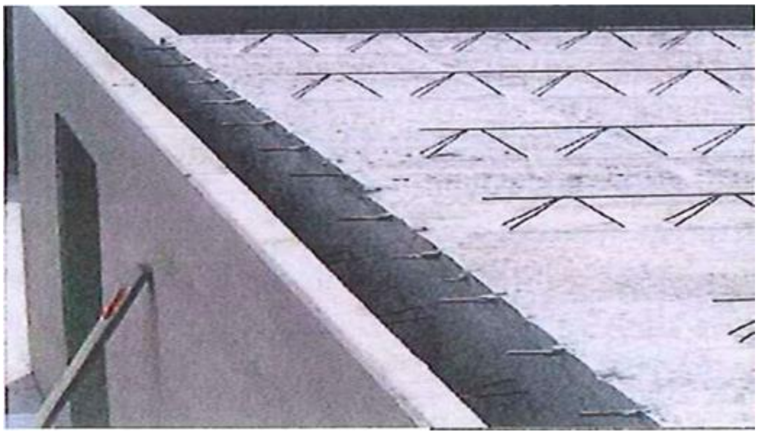

b) Simple connection wall-slab

Figure 15 Wall-slab connection [12].

c) Wall-slab in situ connection

Figure 16 Construction of wall-slab connections [12].

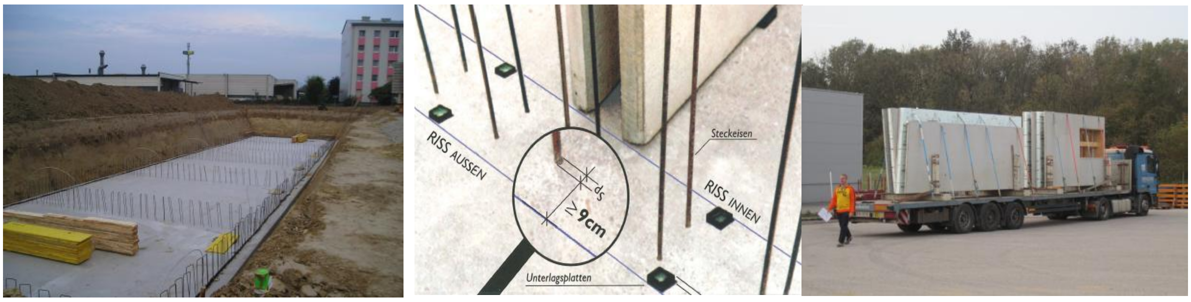

a) Foundation b) Layout of walls c) Delivery of double wall elements.

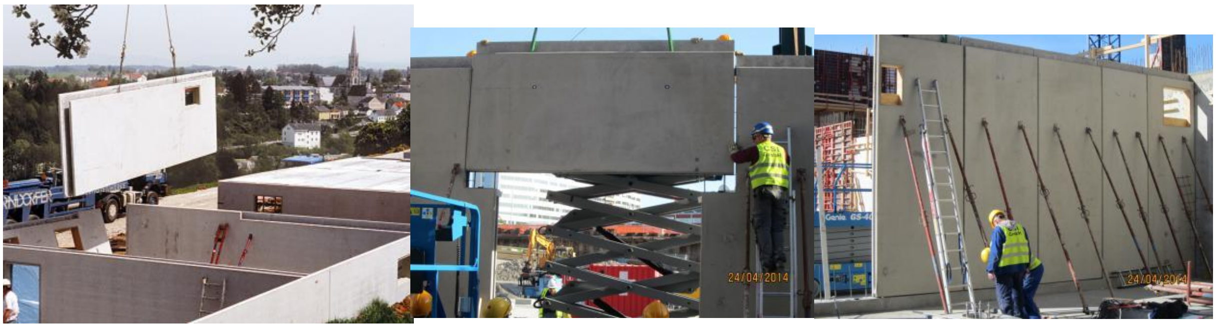

d) Assembly of double walls e) Assembly of double walls f) Placing of props

g) Assembly of wall h) Preparation of slabs i) Filling in concrete

Figure 17 Steps for constructing a double wall system I [12].

k) Connection Wall-Slab

l) Finishing

m) 'Nearly finished' finishing

Figure 18 Steps for constructing a double wall system II [12].

a) Erection of double walls.

b) Concrete casting.

Figure 19 Construction with double wall system III [12].

1.2.4 Relevance for Building Constructions

The most popular type of building construction material in most countries is the cast in place reinforced concrete. Tunnel form building technology became popular in the last two decades for mid-rise construction. *Figure 20* presents a typical floor plan of a mid to high-rise building from Turkey, while *Figure 21* shows a typical office building plan. It can be seen that walls, used almost in every bay, are the main lateral load bearing members to provide resistance against lateral loads due to wind and earthquake forces. Despite its robust construction methodology, the tunnel form building construction has the following main drawbacks:

- Formwork installation and removal locations limits the architectural building plans, thereby resulting in similar buildings all over the country,
- Reinforcement placement is done on site requiring extensive site quality control, which is an area where Turkish regulations are weak,
- Formwork removal time may limit construction speed,
- Buildings with long span (longer than about 10m) can be economically handled only with post tensioning, a technology which is usually not economical for mid-rise construction due to a lack of know-how.

One can easily state that double wall systems are actually perfect candidates for such buildings. On the other hand, in mid to high rise office buildings walls are usually used in the central region (and sometimes at the ends) of the floor plan and columns are used at other locations to provide clear space and architectural flexibility. An example of office building layout is shown in Figure 20. Such floor plans can also be easily constructed with the double wall system by employing double wall columns (described later as one of the test specimens).

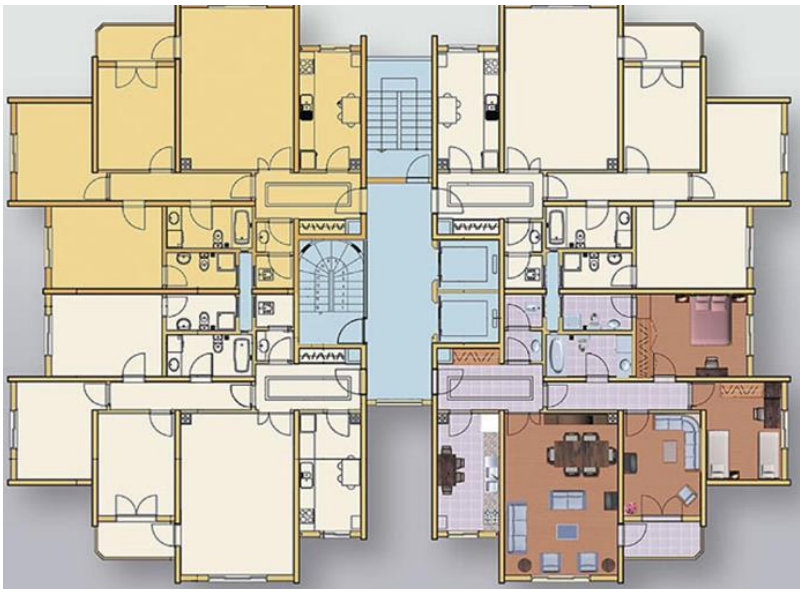

Figure 20 Residential building plan Turkey [129].

Figure 21 Office-Building Plan [4].

This architectural plan for a residential building, classic with columns and beams has been transformed to a double-wall-building

Figure 24 shows the 3-D layout of a Chinese residential building:

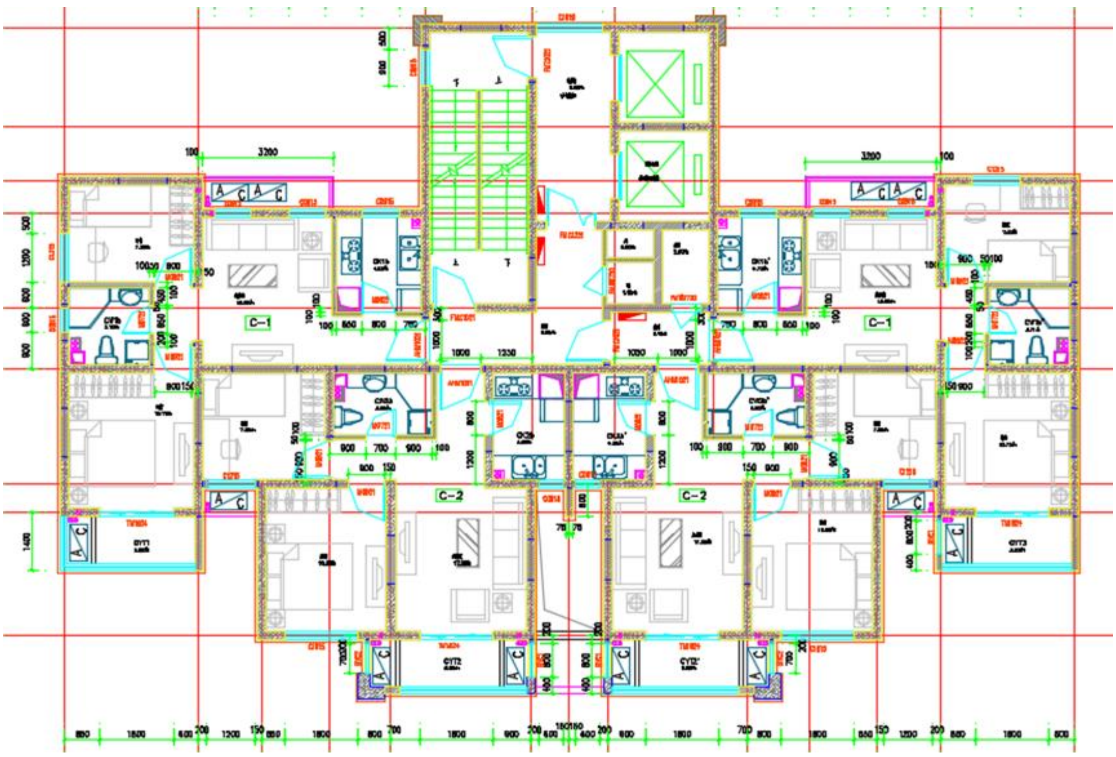

Figure 22 Residential building plan Taiyuan PR China [Plan:"The Institute of Shan Xi Architectural Design and Research"].

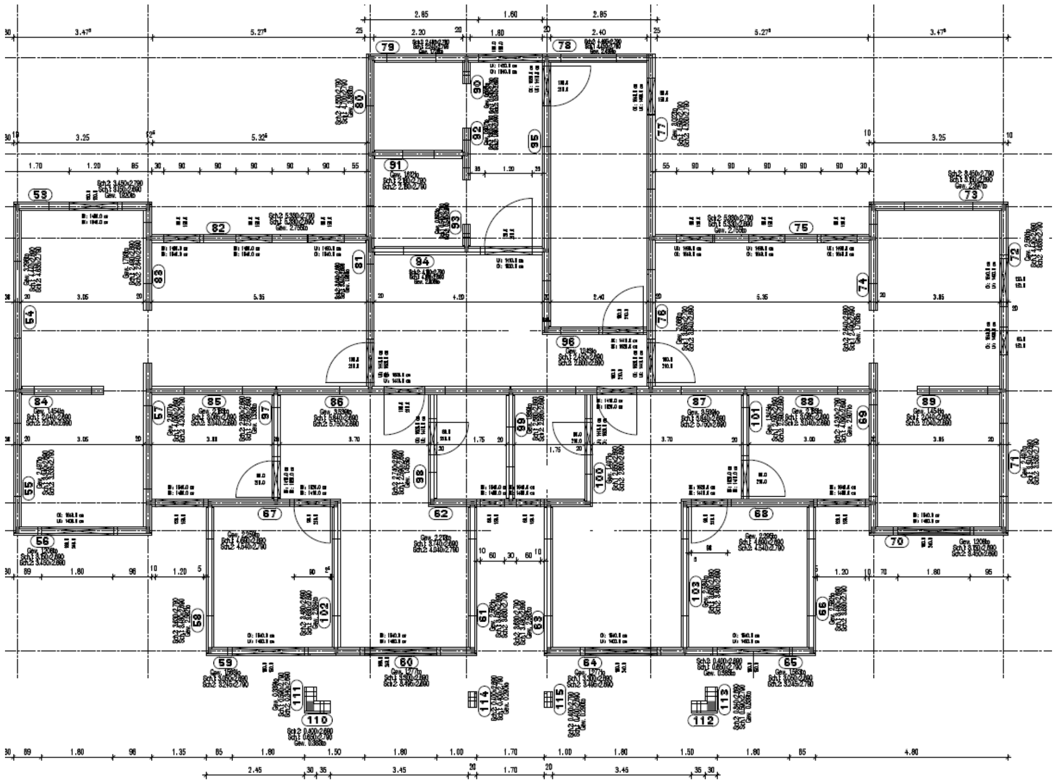

Figure 23 Residential building double-wall plan Taiyuan PR China [12].

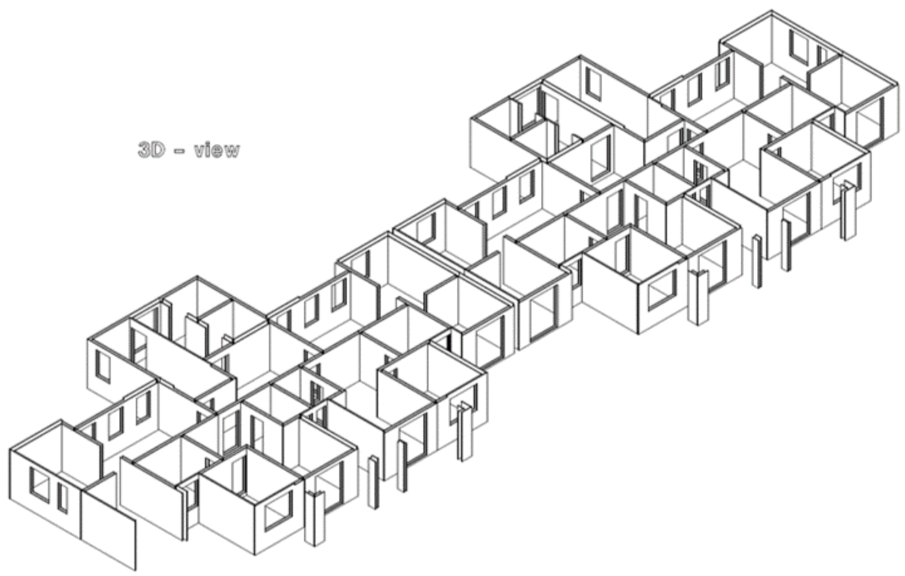

Figure 24 3-D view of residential building Taiyuan PR China [12].

Figure 22 shows this plan as an architectural plan, with a static column-binder system as designed by the Construction Bureau Shan Xi, Tai Yuan, Shan Xi. (*Figure 23)* shows the same plan as the "Institute of Shan Xi Architectural Design and Research", transformed into a pure seismic-double-wall-system, as drawn by Oberndorfer.

1.3 Objectives and Scope

With the invention of the point to point connection of two outer shells of a double wall, it is now possible to make "quasi in situ" compounds for single walls and to generate T-walls and corners for better seismic behavior.

In order to address the issue of seismic resistance for the double wall system a research project was initiated. The objectives of the study can be summarized as follows:

1) To show experimentally and analytically the efficiency of the connection between adjacent rectangular double walls and demonstrate that a number of adjacent walls can behave as monolithic walls.
2) To show experimentally the efficiency of the connection between the components of T and U section double walls. The U-type was necessary, because for symmetrical reasons is it not possible to test a single corner.
3) To prove that seismic detailing rules of major Earthquake Codes can be constructed with the double wall system.
4) To prove that seismic performance of the double walls detailed according to the major Earthquake Codes is sufficient.
5) To demonstrate that columns produced with the double wall idea exhibit sufficient ductility under earthquake-simulated loadings.
6) To demonstrate that double wall-filigree slab connection exhibit sufficient deformability.
7) To show that tested double walls comply with the performance limit states of the major Earthquake Codes. This can be shown by the "Ductility Ratio" as
    i. *"The ratio of the total deflection to the deflection at elastic limit. The deflection at elastic limit is the deflection at which strength behavior can be assumed to change from elastic to plastic"* (IADC-2006, [13]).
8) To demonstrate that experimental member capacities and ductility can be estimated by using standard sectional analysis.

In order to achieve these objectives, an experimental program was conducted.

For the objectives listed in item #1), two specimens (one monolithic and one composed of two adjacent double walls) were tested. For the purpose of investigation of objectives #2, #3 and #4, double walls with a section of U and T were tested.

There are numerous tests and papers about flanged walls with earthquake loads and with cyclic loads. [14]

Specimen #5, which is a column specimen, was tested to fulfil the objective set forth with item #5. Specimen #6 was tested to examine the performance of the double wall-filigree slab connection performance. The details of the test specimens and results of the cyclic tests are presented in Chapter 6.

3. The analytical studies to address the items #7 and #8 above are presented in Chapter 4. Important findings, conclusions from the complete research program along with the recommendations on the use of double wall system are given in Chapter 6.2.

1.4 Literature review

1.4.1 Introduction

This chapter serves as a summary of relevant research that has been conducted until to date. In the past, the majority of research focused on monotonic and in situ casted concrete shear walls. More recently, research has been focused on the performance of flanged shear walls under cyclic and dynamic loading.

1.4.2 Background

Over the past forty years, some researchers used the finite element method to study the effects of different design parameters on the response of reinforced concrete members. In 1972, Yuzugullu [12] used the finite element method to study the monotonic behavior of a shear wall-frame system which was tested at the University of Tokyo.

Shear walls transfer lateral loads from a horizontal diaphragm above to a diaphragm or wall below, or to the foundation. Shear walls resist loads being induced in the walls from the horizontal diaphragms. It is well known that squat shear walls, as used in industrial and nuclear facilities [15], [14] commonly have an aspect ratio smaller than 0.5 and have a very high stiffness and strength. These shear walls are not part of this study.

In building construction the typical failure behaviors of reinforced concrete walls fall predominantly under the following types:

1. Diagonal Tension Failure

   Diagonal tension failure is generally observed in shear walls with light horizontal web reinforcement. This failure is characterized by one or more wide inclined cracks in respect to each loading direction. Cracking is not widespread over the wall web as the damage is concentrated in the inclined cracks. Yielding of horizontal web reinforcement is observed as the cracks widen with increasing displacement demands on the wall.

   The orientation of the failure plane (typically assumed to form at an angle of approximately 45 degrees) is influenced strongly by the presence of a large beam (if any) at the top of the wall, and the aspect ratio of the wall. A stiff top beam and foundation contribute to the formation of a corner-to-corner crack.

Figure 25 presents the final condition of a squat wall which failed by diagonal tension.

Figure 25 Diagonal tension failure, tested by Hidago et al, (2001) [16].

2. Diagonal Compression Failure
   A diagonal compression failure may be triggered if a diagonal tension failure is prevented by providing adequate horizontal web reinforcement. Resistance of the concrete compression struts in the web of the wall deteriorates as the inclined cracks in two opposite directions open and close successively under cyclic loading. The crushing of the concrete struts in the web of the wall triggers a diagonal compression failure.

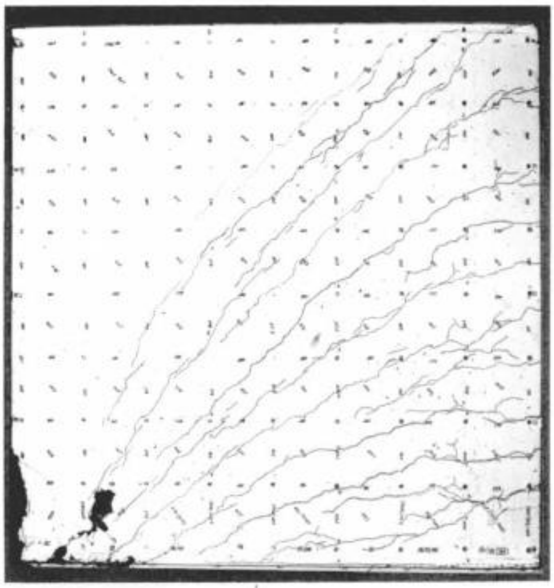

Figure 26 Diagonal compression failure of wall S4 tested by Maier and Thürlimann [121].

3. Sliding Shear

   Heavily reinforced walls subjected to a large number of displacement cycles may be susceptible to sliding shear failure. This failure is similar to a diagonal compression failure in the sense that it is also a result of concrete crushing. Shear walls that fail in sliding shear initially experience inclined shear cracking. Inclined shear cracks that form in each direction intersect each other due to cyclic loading and the strength of the concrete between these cracks deteriorates as a result of subsequent displacement cycles at higher amplitude.

4. Mixed Failure Mode

   A mixed failure mode is shear failure at a displacement that is greater than the displacement corresponding to the peak flexural strength. Wall behavior is governed initially by flexure (i.e., flexural cracking and yielding of vertical boundary element reinforcement), which is similar to the initiation of flexural failure. For a wall that exhibits a mixed failure mode, wall shear strength is initially equal to or greater than the shear force corresponding to wall flexural strength. However, the shear resistance of the wall degrades with displacement cycles of increasing amplitude.

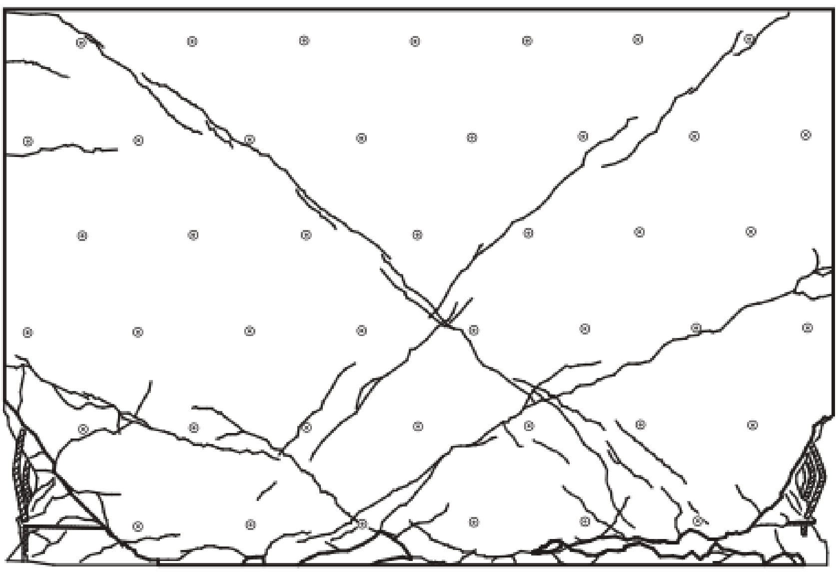

Specimen M3 (n=0.10, $\rho_v = \rho_h = 0.003$)

Figure 27 Specimen M3, Greifenhagen [95].

For the past forty years, some researchers have used the finite element method to study the effects of different design parameters on the response of reinforced concrete members.

In most pictures of earthquake damage, ends of single shear walls are shown. This particular diagonal-compression behavior can be avoided by consistent application of double walls with earthquake-proof connections.

Figure 28 *Chile 2010 Earthquake* *[Photo Prof. R.T. Leon Georgia Institute of Technology].*

1.4.3 Flanged Shear Walls

Most shear walls are used in Colum-beam-RC construction for better earthquake-security. These type of shear wall are singe walls, with the known problem of the wall-edges.

In 1973, Heidebrecht *et al*. [17] studied the interaction of shear walls and frames and derived a closed form solution for lateral displacements.

In Europe in 1994, Lind, P. *et al.*, ETH-Zürich published a first numerical model on concrete walls [18].

At the University of Toronto in 1998 F. Vecchio wrote about 3-D shear walls [19], and since 2002 D. Palermo and F.J. Vecchio have published some very important theoretical and experimental papers about shear walls as "Behaviour of Cyclically Loaded Shear Walls" [20], demonstrating in 2004 [21] that the critical wall-end can be strengthened by a transverse wall. Since every residential or office building consists of walls, every wall can be a part of the earthquake-safe construction.

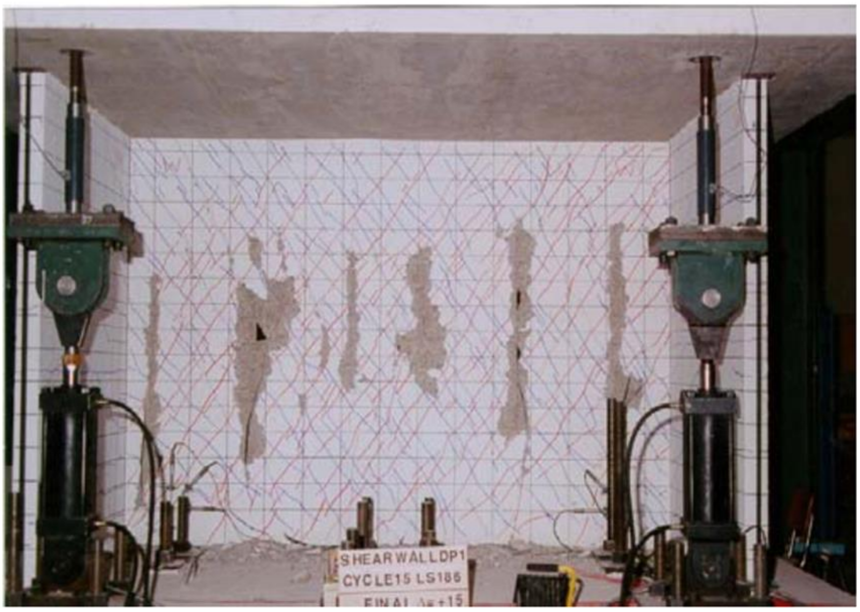

Figure 29 DP1 at failure, Palermo [98].

In nearly every residential and office building there is the possibility to use all walls as shear walls. If they are connected, the benefit is:

- Less reinforcement with more earthquake security.
- Flexible design of the floor plan.
- High degree of prefabrication.
- Quality control already takes place in the precast plant.

1.4.4 Cyclic Loading and Analytic Modeling

In the analysis of reinforced concrete behavior within structures, realistic loading conditions and realistic models and analysis procedures are required to produce accurate and reasonable results for the simulation of behavior within the building. Cyclic loading is an adequate way to get verifiable results. If a shaking table test can give you an overview of a construction, the test with the strong wall is internationally accepted for the purposes of comparing earthquake-proof systems.

One of the steps was a May 1971 paper written by E. Anderheggen (*Starr-plastische Traglastberechnung mittels der Methode der Finiten Elemente-ETH-Zürich)* [22] and [23].

Since Lee *et al*. [24] proposed to use special models to describe plastic working capacity of a reinforced concrete structure.

Two major obstacles that most researchers experienced in the development of cyclic models for reinforced concrete are the lack of understanding in the cyclic response of reinforced concrete and the numerical problems associated with complex rules for load reversals and stress-strain relationships in material models. In order to obtain a detailed understanding of the cyclic behavior of reinforced concrete elements and to gather essential experimental data needed for the formulation of such behavior, Stevens *et al*. [25] conducted cyclic tests on three reinforced concrete panels at Toronto University. In these tests, two panels with different amounts of reinforcement were subjected to load reversals in pure shear, while one other panel was subjected to reversed cyclic shear combined with biaxial compression. The average stress- strain relationship for these panels was then used as a basis for the development of a material model for concrete. Two other researchers also used the results from these panel tests to verify their concrete models. Stevens *et al*. also proposed a concrete model based on the modified compression field theory. Xu [26] proposed the model using a smeared non-orthogonal cracking approach, and Izumo *et al*, [27] developed the hysteresis constitutive law for reinforced concrete by combining several existing constitutive laws developed in Japan. The analytical results at the element level (a finite element model consist of one element) of these three models agreed well with the results of the panel tests, which are quasi affine to our tests.

For the analytic solutions, the smeared crack approach is the most favored in the context of fixed cracks. In fixed crack formulations, separate models are required to model the normal stress and shear stress hysteretic behavior. This, however, is at odds with test observations. When equal amounts of reinforcement are provided in the longitudinal and transverse directions, cracks experience minimal rotation, and a fixed crack procedure will provide an accurate simulation. However, under the more general case of varying amounts of reinforcement, which is common in practice, the fixed crack assumption may not realistically represent behavior. The approach used here for the reversed cyclic loading is based on a smeared rotating crack approach, which more accurately models the response of cracked reinforced concrete under general loading conditions.

For using a realistic scenario, the constitutive models for cyclic loading of concrete should simulate the actual behavior. The shape of the unloading and reloading curves of concrete should accurately predict the energy dissipation of the structure and the damage of the material due to load cycling. Partial unloading/reloading rules must be considered. The models must not be limited to the compressive behavior alone and should include the tensile loadings – this plays a key role in the overall behavior of reinforced concrete structures.

Structural response of concrete elements under cyclically loads can be simulated by nonlinear finite element analysis. This is a general approach based on principles of mechanics and should provide an objective tool for all types of geometry, material properties and loading. Such simulation is now used to supplement experimental investigations, where it significantly increases the value of experimental data. The goal of this approach is to provide a tool more general than simple design formulas, which are usually valid for very limited ranges of parameters. The scope of application for complex nonlinear analysis is aimed at the development of new technical solutions of anchors, special loading types and investigation of failure cases. It is not meant for normal design, which can be accomplished by simple design formulas.

An algorithm for nonlinear analysis is based on three basic parts:

- Finite element technique, constitutive model and nonlinear solution methods, which should compose a balanced approximation. Nevertheless, the constitutive models decide the material behavior, and therefore they are treated more extensively here, while the finite elements and nonlinear solution are mentioned only briefly.
- With reference to research authorities in the field of concrete mechanics and materials, such as RILEM, FIB, FRAMCOS, it is recognized that the most important effects to be included in the constitutive model of concrete are
- Tensile fracturing and compressive confinement.

Several constitutive models covering these effects are implemented in the computer code ATENA, [8], [28] and [29] which is a finite element package designed for computer simulation of concrete structures.

In the design of buildings, reinforced concrete shear walls act as major earthquake-resisting members. These structural walls provide an efficient bracing system and offer great potential for lateral load resistance. The properties of these seismic shear walls dominate the seismic response of the buildings and it is therefore important to evaluate the response of the walls appropriately. The evaluation is important in assessing the seismic performance. The use of realistic concrete models will therefore improve the evaluation of the lateral load resisting components.

1.4.5 Ductility and Overstrength

In 1988 Duarte et al. [30] wrote about the "Local Ductility Coefficient" which is now known as overstrength. The definition of overstrength provided by Osteraas and Krawinkler in 1990 [31] reads as follows:

"Overstrength, which is defined here as member or structural capacity greater than that assumed in design, may be beneficial or, under certain circumstances, detrimental to seismic behavior. When the yield level under lateral loading of a structure is increased by overstrength, the inelastic seismic demands on the structure are decreased. If relative member overstrengths are not well balanced or tuned, inelastic structural capacity will be reduced...Inelastic demand and structural capacity can be partially characterized by ductility. Local ductility is the basic measure of member performance and relates to detailing considerations, low cycle fatigue, and a large body of laboratory test data. Global ductility is the basic measure of structural response and offers a convenient design parameter. Overstrength models are implemented to relate local and global ductility."

1.4.6 Low-Cycle-Fatigue Behavior of Concrete Members

The effect of Low-Cycle Fatigue Behavior of Reinforcing Steel was first published by Mander *et al*. in 1994 [32], who proposed an energy-based fatigue model.

Sucuoglu et al. [33] worked out that:

"*...Seismic performance of degrading systems reduce remarkably in the short and medium period ranges under long duration strong excitations which produce a number of significant response cycles. This reduction is mainly caused by the fatigue component of damage function and it has to be considered realistically in seismic performance evaluation of existing structures.* "

2 Experimental Program

2.1 General

In order to have no interpretation problems with scaling materials, we decided to perform the tests in the 1:1 scale. In this case we had the problem of respecting the load limits. When we looked for an earthquake laboratory with the necessary equipment and manpower, our choice was the Middle East Technical University at Ankara, Department of Civil Engineering and the Structural Mechanics Laboratory Earthquake Engineering Research Center.

Figure 30 *Strong wall Middle East Technical University, Ankara* [4].

2.2 Test Specimen

2.2.1 Overview

As described in the previous section, double wall systems are constructed by placing concrete double shells side by side, placing connecting reinforcement cages, and casting concrete monolithically at the central hollow regions. Therefore, it is important to examine whether such walls act as single walls or not. For this purpose, the first two specimens of the experimental program were tested to compare the seismic response of two double walls, one cast monolithically (Specimen #1), the other one composed of two walls constructed side by side and having monolithically cast concrete at the central region (Specimen #2). Steel cages were place at the intersection of the two walls in order to ensure proper shear transfer for Specimen two. Specimens three and four were tested in order to examine the seismic response of U and T section double walls, respectively. These specimens were designed and detailed according to the Turkish Earthquake Code (TEC 2007, [34]). In other words, boundary regions and the web sections were reinforced by following the requirements of TEC. Such walls may be encountered in buildings around elevator shafts and at the intersection of two perpendicular bays. Furthermore, the experimental data examining the seismic response of walls with U and T sections is extremely scarce. Hence, the aim was to observe the possible failure mechanisms and the cyclic performance for such walls.

Table 1 is the summary of the vertical load bearing specimens tested in the course of this study. The reinforcement drawings of all the walls are presented in ***Figure 34***, ***Figure 49***, ***Figure 50***, ***Figure 63***, ***Figure 76***, ***Figure 88*** and ***Figure 103***. The sizes of the test specimens were selected to reflect as closely as possible the full scale dimensions of typical double walls (and columns) used in actual buildings. All of the specimens were tested with fixed boundary at the specimen base and axial/lateral forces applied at the top.

Table 1 Summary of test specimen

Properties	Specimen #1	Specimen #2	Specimen #3	Specimen #4	Specimen #5	Speciumen #6
Type	Wall	Wall	Wall	Wall	Column	Wall-Slab
Section	Rectangular	Rectangular	U-Type	T-Type	Square	Rectangular
No. of double walls composimg the specimen	1	2	3	2	1	2 + slab
Height [mm]	2.500	2.500	2.600	2.600	2.650	3.600
Depht [mm]	3.000	3.000	1.400	1.700	350	2.200
Thickness [mm]	350 (250 *)	350 (250 *)	200	200	350	200
	*) concrete					
Conrete Surface [cm²]	7.500	7.500	6.800	5.000	1.225	-
Axial Load [kN]	602	610	-	-	602	-
Concrete shell f_c [Mpa]	45	43	45	45	45	45
Concrete core f_c [Mpa]	28	27	25	25	22	25
Φ 6, f_y , f_u[Mpa]	340,470	340,470	340,470	340,470	340,470	340,470
Φ 8, f_y , f_u [Mpa]	380,540	380,540	380,540	380,540	380,540	380,540
Φ 12, f_y f_u [Mpa]	490,610	490,610	490,610	490,610	490,610	490,610
Φ 14, f_y f_u [Mpa]	325,455	325,455	325,455	325,455	325,455	325,455

2.2.2 Concrete Modeling

Usually the precast outer shells are produced in an eight hour cycle, which means, that the concrete needs a good early strength quality. Normally a concrete with a minimum quality of C25/30 (according to EN 206-1 and ÖN 3303) is used; for our specimen it was a C30/37 with a maximum aggregate size of 16 mm.

For the "in situ" concrete a C25/30, with a maximum aggregate size of 16 mm, was used for all samples.

Foundations and heading where also produced with C30/37-16mm aggregate size.

2.2.3 Formworks, casting and curing

The preparation stages of all specimens are described in detail in the relevant sections. In general, the construction of the test specimens was conducted in several stages. First, the formwork for the concrete shells and the steel reinforcement cages were prepared.

Afterwards, concrete casting was completed for the first shell, which was left for curing for about 24 hours. Ensuring that the concrete compressive strength was at least 10 MPa, the first shell was lifted with the crane, rotated with the in-house built rotating device, and placed on top of the second shell.

The double wall system was then left for curing for at least 7 days. In the final stage of the specimen preparation, the double wall was lifted to the vertical position and placed on its foundation.

Then, concrete was cast at the central hollow region of the double walls. Concrete casting was conducted slowly in order to avoid high pressure and any cracking of the shells. Ready mixed concrete was used for all specimens, the only exception being the first shells of the first two specimens. Concrete was cured for 28 days in an indoor environment and then the specimen was carried to its position in front of the reaction wall to prepare the instrumentation and conduct testing.

Figure 31 Formwork for the foundation specimen #3 [4].

2.2.4 Instrumentation

Several measurements were taken in order to record the response of specimens during tests. Load cells were used to measure the applied lateral and axial loads. Linear variable differential transducers (LVDTs) were employed to measure the lateral displacement of the specimens and the relative displacements of the walls between two points. The instrumentation employed for each test specimen and the recorded channel numbers for the instruments are shown in detail in the relevant section.

All instrument readings and all of the measured values were saved in an Excel file and analyzed.

2.2.5 Test Setup

All of the test specimens were tested under lateral cyclic displacement excursions to simulate seismically-induced displacement demands. Before applying the lateral load, axial load was applied and held approximately constant throughout loading. In specimens #3, #4 and# 6 no axial load was applied.

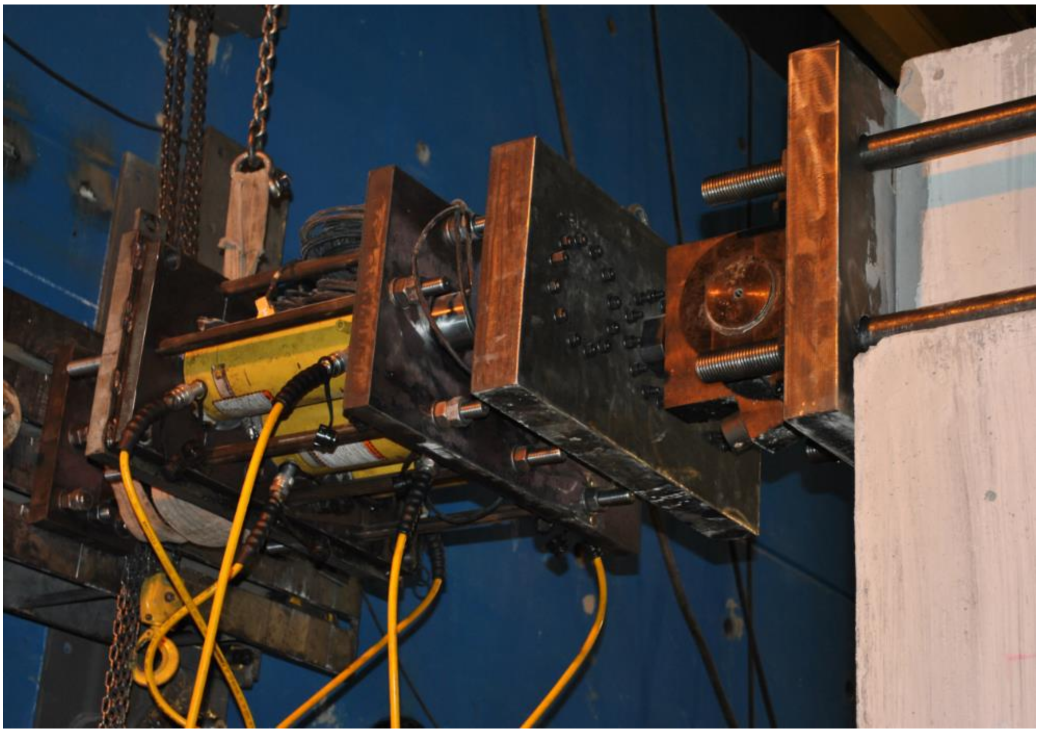

Figure 32 *Hydraulic cylinders.*

It is well-known that the presence of axial force tends to increase the moment capacity of an RC section. In the case of columns the presence of axial load is very influential on the seismic response. However for walls, the level of axial loads in actual buildings are very small. Furthermore, walls close to the ends of the buildings in the plan may even undergo tension during seismic load reversals, which reduces the shear capacity and deformability. Hence we opted to apply no axial force for the testing of specimens #3 and #4.

Interstorey drift ratio (or simply drift ratio), defined as the lateral displacement of the point of application of the lateral load divided by the height of the lateral loading point, was the controlling lateral displacement quantity.

At each increment the load was maintained constant for at least two minutes to measure the load and deformation response of the walls, mark the cracks, and take photographs on the wall crack pattern. Pressure transducers in the hydraulic supply line of the rams provided accurate measurement of the applied load. Each displacement excursion was repeated twice prior to moving to the next cycle. Displacement loading histories of the specimens are shown in the appropriate section.

2.2.6 Test Results

Measured response of the test specimens along with the observed damage patterns are presented in the appropriate chapters. The results are provided for each specimen in the upcoming sections. A summary of the test results for the vertical loadbearing elements is provided in ***Table 2***. In this table, measured response parameters important for the seismic performance are summarized. First cracking load and deformation values are obtained from the visual observations. The yield and ultimate displacement were found from an idealized elastic perfectly plastic response as shown on each graph (red lines).

The first yield point is defined by connecting the origin with a line passing through 70% of the ultimate load on the initial loading curve.

The extension of this line to 85% of the ultimate load gave the yield displacement. The ultimate deformation at 15% capacity drop is taken as the ultimate displacement level.

Displacement ductility was found by dividing the ultimate displacement with the yield displacement.

Table 2 Summary of test results for vertical bearing Elements.

Response Parameters	Specimen #1	Specimen #2	Specimen #3	Specimen #4	Specimen #5
First Cracking Load (kN)	450,00	495,00	233,00	109,00	13,00
First Cracking DR. (%)	0,06	0,05	0,05	0,03	0,04
DR. at First Yielding (%)	0,13 (0,12)*	0,1(0,11)	0,26(0,17)	0,27(0,25)	0,5(0,8)
Ultimate Load (kN)	1057 (895)	1052 (1011)	731(570)	635 (395)	57(53)
DR. at Ultimate Load (%)	0,20	0,20	1,25	0,60	1,70
DR at Ultimate Disp. (%)	0,85(0,8)	0,75(0,5)	1,26(1,0)	1,1(1,0)	3,2(3,5)
Displacement Ductility	6,5(6,7)	7,5(4,5)	4,9(5,9)	4,1(4,0)	6,4(4,4)
Failure Mode	Flexure-Shear	Flexure-Shear	Flexure-Shear	Flexure-Shear	Flexure

2.3 Specimen # 1

2.3.1 Perform Construction

The first specimen was used to test the system. The maximal load was limited to about 1.000.-.kN. Considering the fact that the specimen has no decrease scale, it had to be taken into account that the dimensions of the wall should be about the same size as a single wall used in a residential building.

For the first two specimens there was a second consideration to bear in mind: the "inside-insolation".

It is possible to build a thermal insulation inside of a double wall. This isolation can be made of polystyrene or inorganic cement foam. With the same test-set-up it can be tested whether the insulation has a negative influence on the all-over behavior of the specimen.

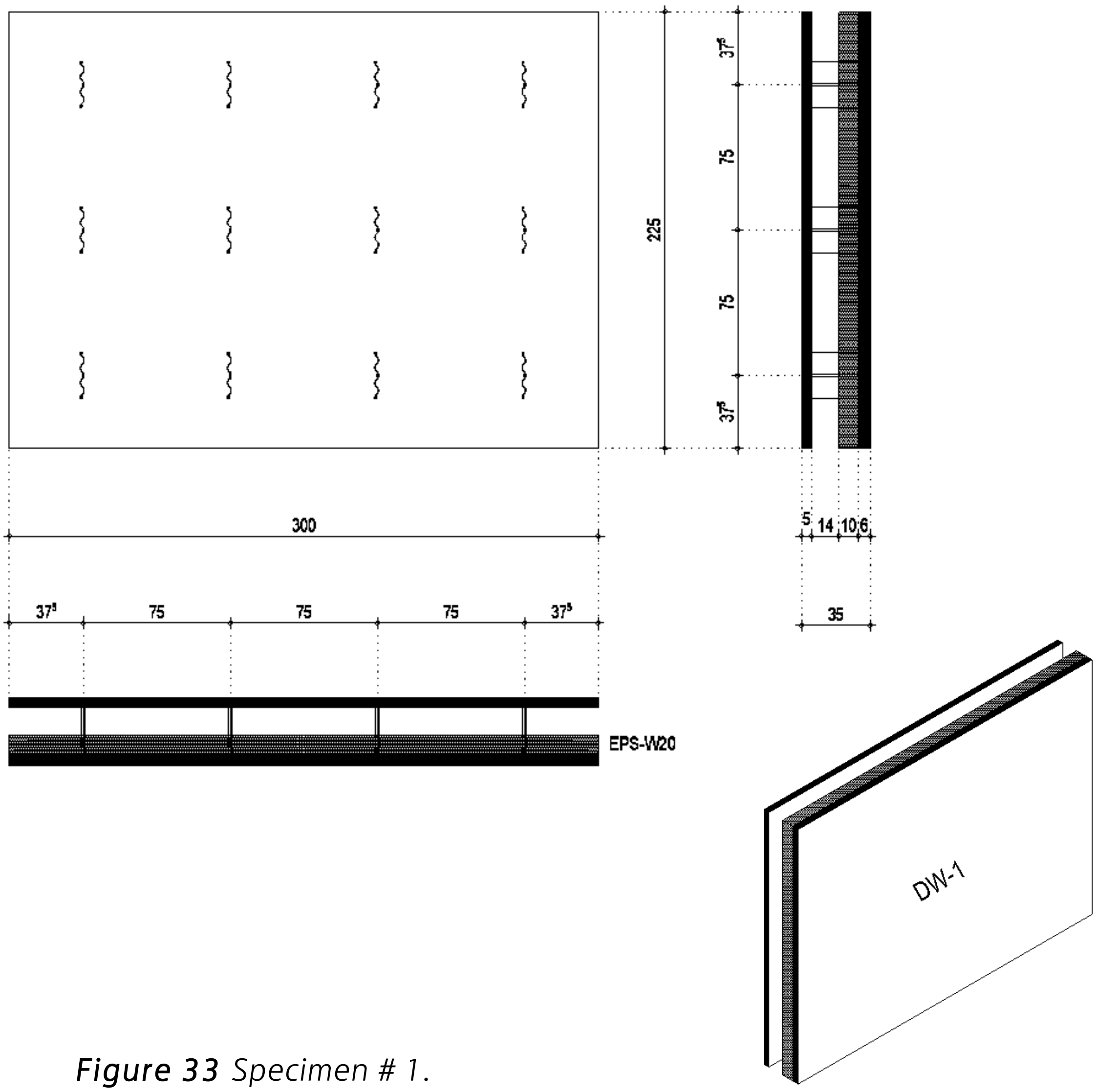

Figure 33 Specimen # 1.

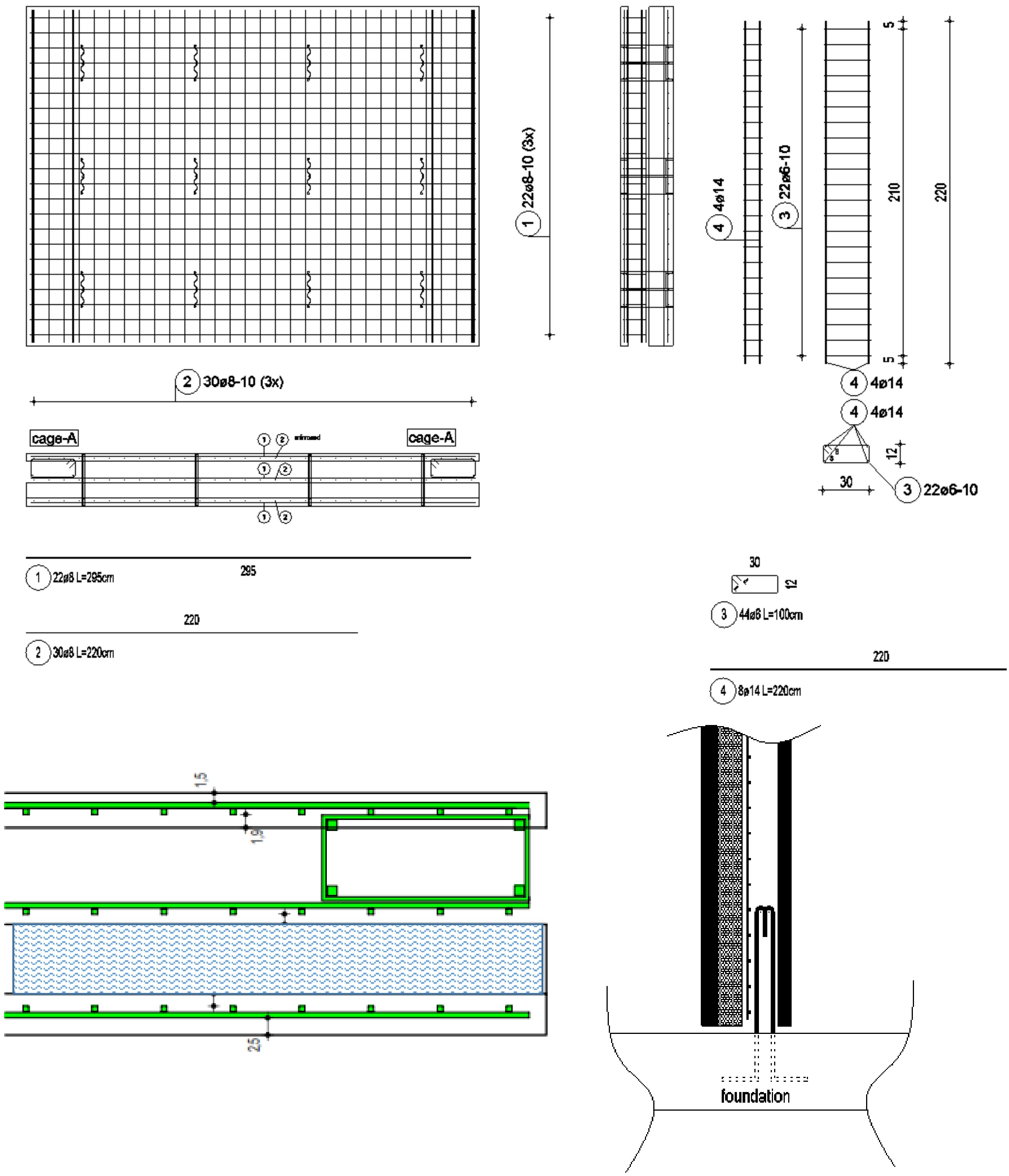

Figure 34 Reinforcement for specimen #1.

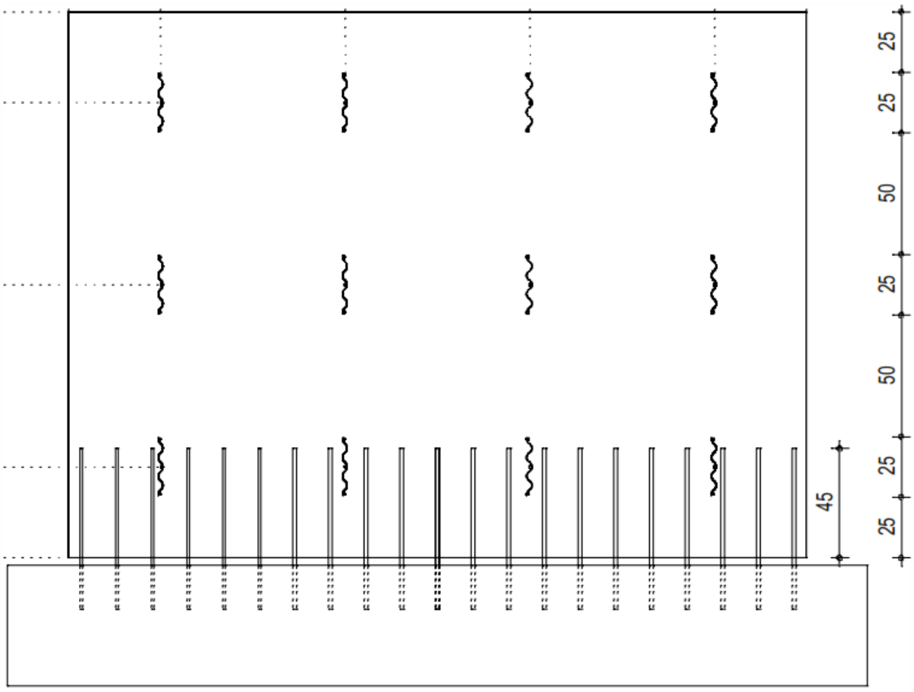

Figure 35 *Distribution of the waves.*

Figure 36 *Preparation of shell 1 for specimen #1 [7].*

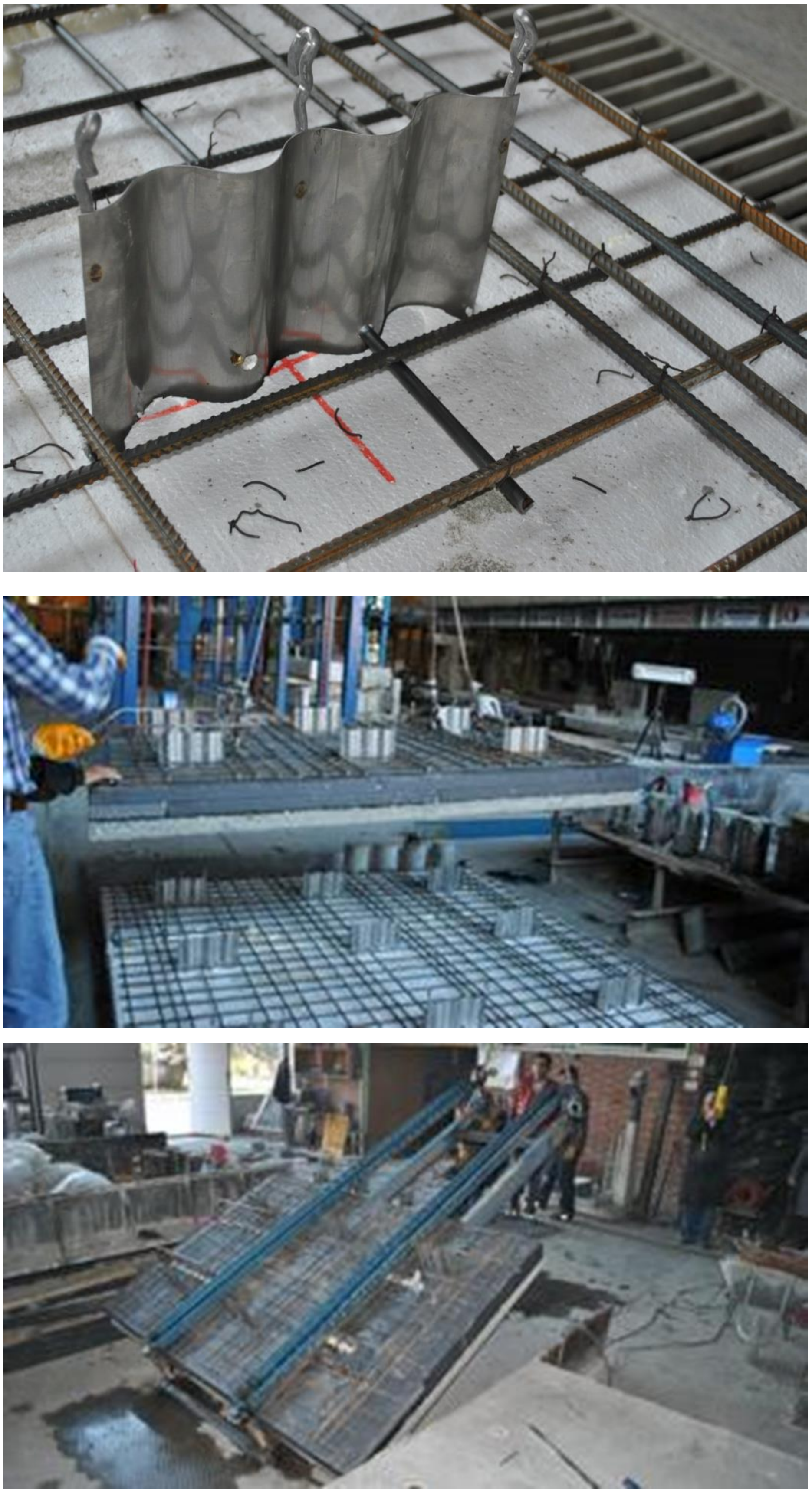

Figure 37 *Preparing of Specimen #1 [7].*

Figure 38 *Preparation of specimen #1 (continued).*

2.3.2 Loading

During the testing of specimens #1 (and #2), in order to avoid failure at the foundation, axial load was released at a drift ratio of 0.2%. Beyond this lateral drift ratio, no axial load was applied.

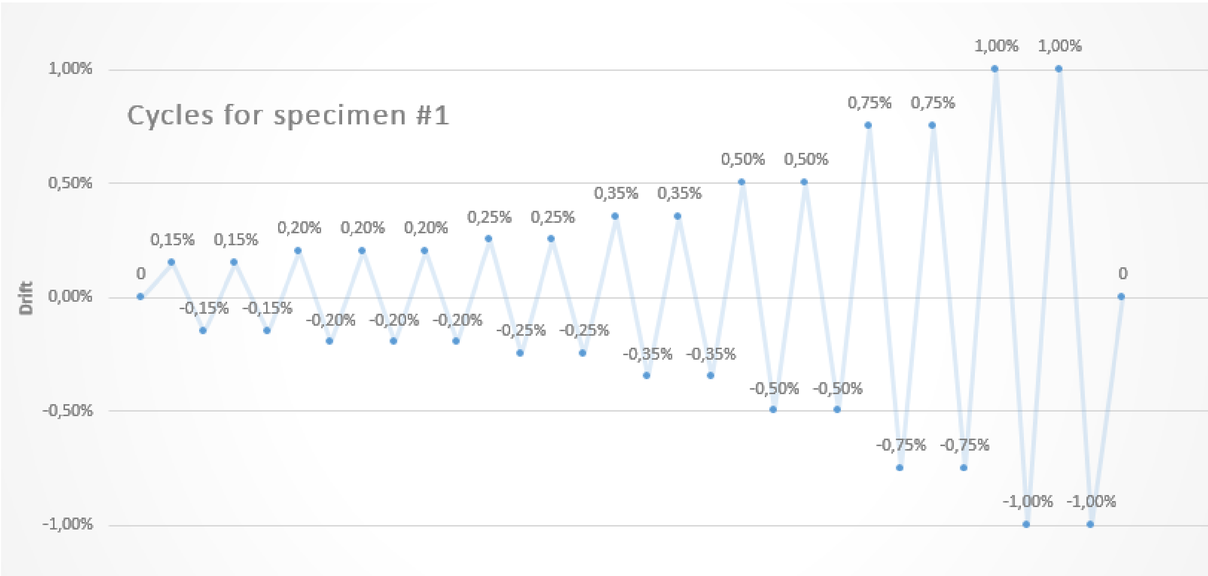

Figure 39 *Cyclic loading of specimen #1.*

Specimen-#1		Numbers	cyclus	way	analytic: full steps/cyclus
					step: 0,10 mm
H = 2,45 m					
		first crack	0,06%	1,47 mm	14,70
			0,15%	3,68 mm	36,75
			0,20%	4,90 mm	49,00
			0,25%	6,13 mm	61,25
			0,35%	8,58 mm	85,75
			0,50%	12,25 mm	122,50
			0,75%	18,38 mm	183,75
			1,00%	24,50 mm	245,00

Figure 40 *Cyclic loading numeric numbers for specimen #1.*

2.3.3 Instrumentation and Setup

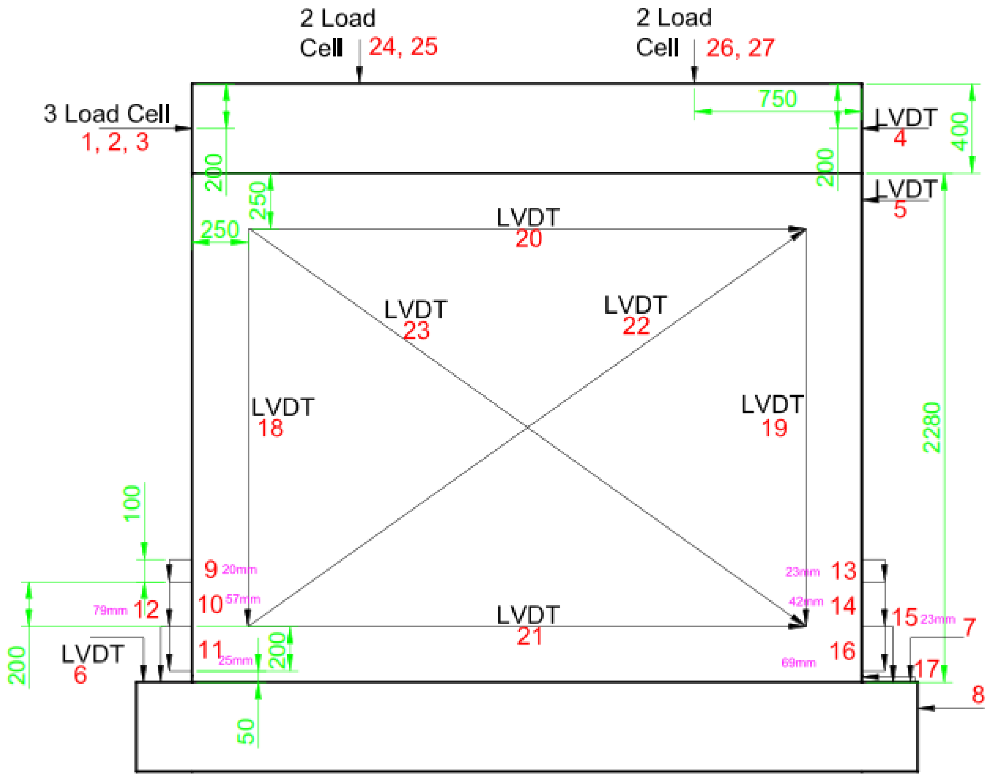

Figure 41 Instrumentation of specimen #1 [4].

Figure 42 Test setup for specimen #1.

2.3.4 Displacement and Strain Measurement and Damage Pictures

The lateral load deformation response of this specimen is presented in ***Figure 40.*** Measured moment-curvature response measured at the wall base (gauges 12 and 15, shown in ***Figure 41,*** were used) are presented in ***Figure 44.*** The damage pictures of the specimen are presented from ***Figure 46*** to ***Figure 48.***

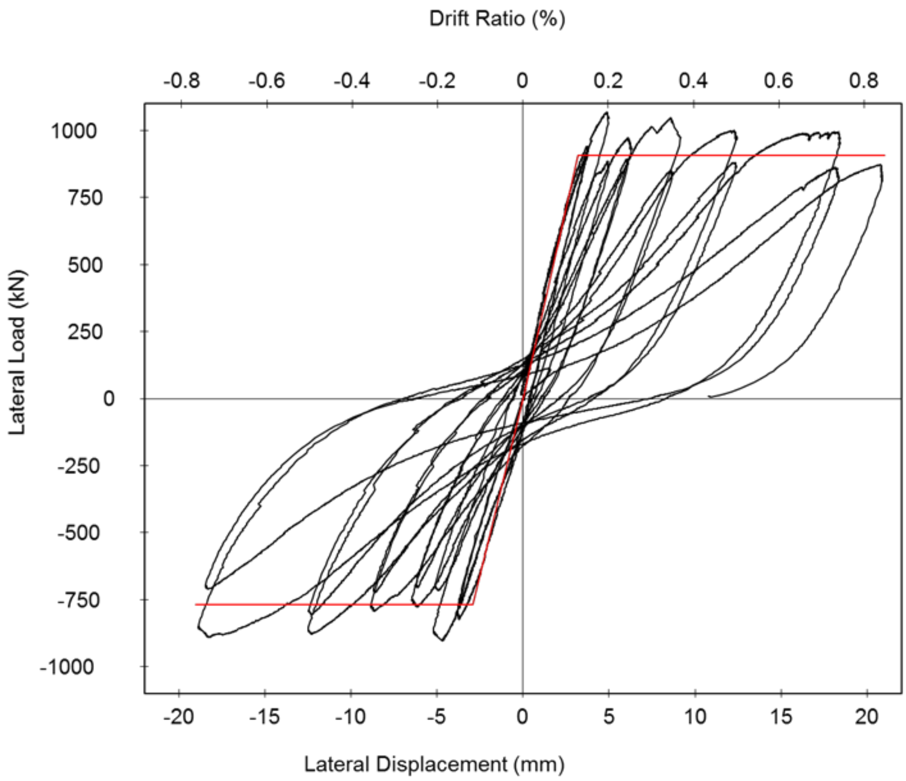

Figure 43 *Lateral load deformation responses of specimen #1* ***[4]***.

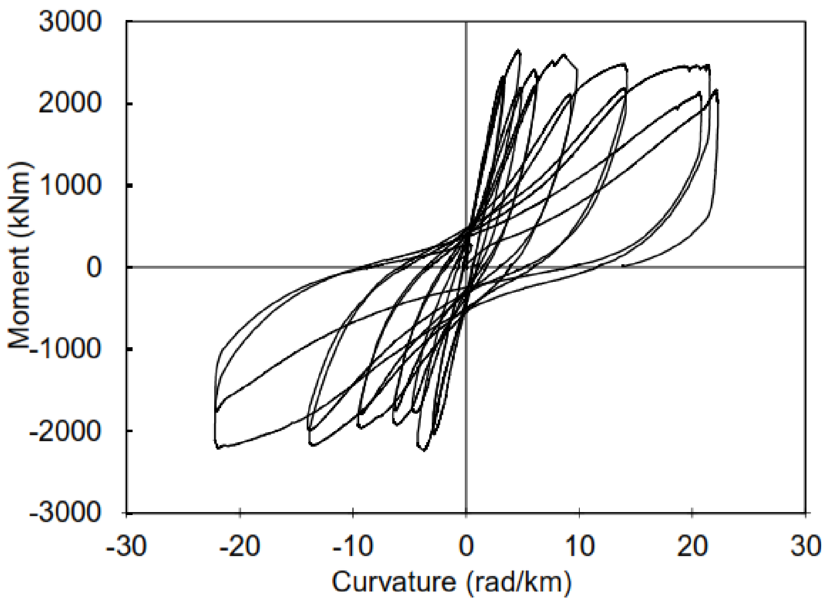

Figure 44 *Moment-curvature response of specimen #1 at wall base* ***[4]***.

Specimen #1 experienced base cracking at a drift ratio of about 0.06 %.

Beyond this drift ratio level, a number of flexure cracks occurred starting from the base level towards the upper portions of the wall. Cracks occurred on the tension side of the wall depending on the direction of the wall that was subjected to tension.

At about 0.2% drift ratio, wall base shear capacity was reached. Inclined cracking was observed to occur starting at about 0.25% drift ratio. The longest shear cracking spanning from both sides of the wall was observed at about 0.35% drift ratio.

Lateral load carrying capacity of the wall slightly decreased while displacing the wall from 0.2% to 0.25% drift ratio, however it picked up beyond 0.25% without evidencing any significant failure event.

Beyond 0.35% drift ratio, the width of the base cracks significantly increased (up to a few millimeters).

At a drift ratio of about 0.75%, the lateral capacity of the wall did not drop significantly. This showed that the wall behaved in a ductile manner in both directions of loading.

The lateral load carrying capacity of the wall was about 1050 kN in the positive direction, whereas it was about 900 kN in the negative direction of loading.

An elastic perfectly plastic envelope was drawn on the lateral load-displacement figure as shown in ***Figure 43***. The linear portion of this idealization was plotted by passing a line from the origin towards the 70% of the ultimate capacity in the loading direction.

The yield plateau was designated at 85% of the ultimate strength of the wall. Based on this idealized response, it can be stated that the wall had a displacement ductility of at least 6.5 in both directions.

Despite relatively squat dimensions of the (H/L=0.85), the double wall system was able to behave in a very ductile manner.

This proves the success of the designed reinforcement in shear and flexure. It should be noted that the concrete shell with insulation material did not sustain any deformations or damage. The central part and the adjacent concrete shell carried all of the lateral forces. The final crack map of the wall is shown in ***Figure 48***.

Figure 45 *Picture and damages at 0.1% drift ratio (DR).*

0.2% (DR)

0.25% (DR)

Figure 46 Pictures of damage at drift ratio (DR) 0.2% for specimen #1.

0.35% (DR)

0.5% (DR)

Figure 47 Pictures of damage at different drift ratios (DR) for specimen #1.

0.75% (DR)

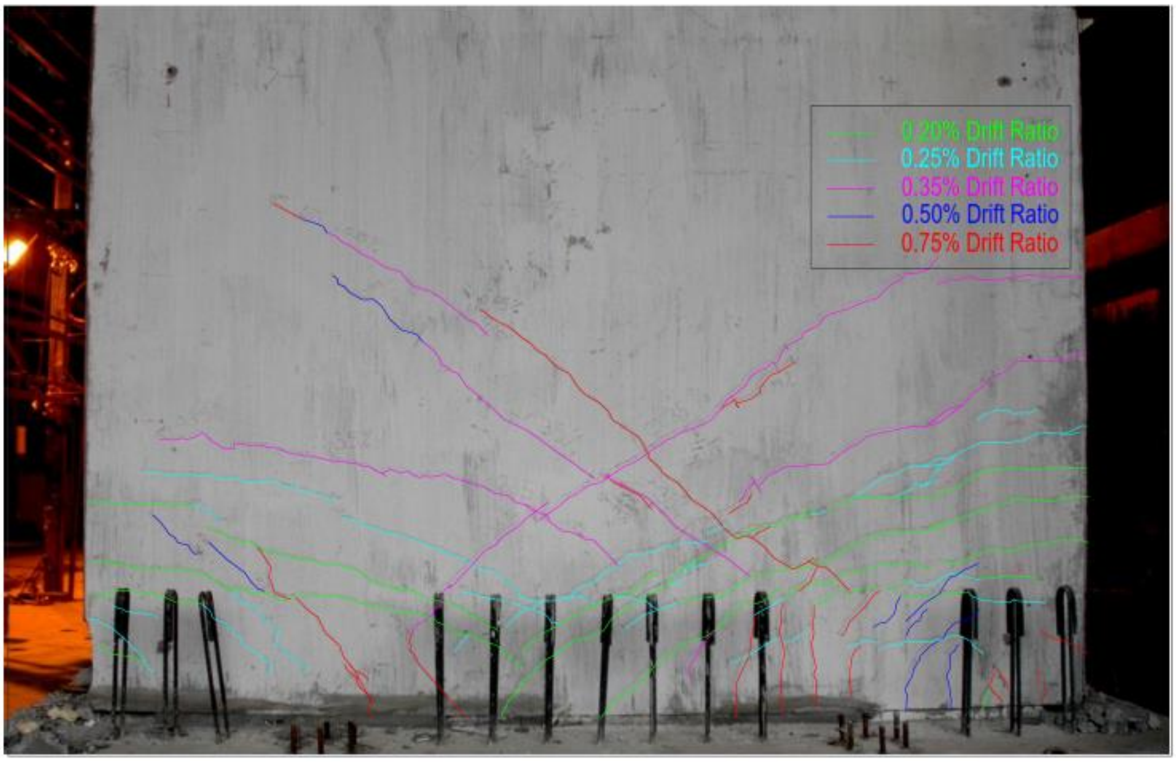

Figure 48 Final crack map specimen #1 [4].

2.4 Specimen #2

2.4.1 Perform Construction

The test of specimen #2 corresponds to the test of specimen #1, with the difference that the two outer double wall cups were not concreted continuously to 3m, but were composed of two 1.5 m long elements. The experiment was carried out to show that the compound with reinforcing steel in the core-in-situ concrete alone, brings the same results as specimen #1, in which the outer shells were of one piece.
Furthermore, the evidence should be provided that the rods of the wave-connection can replace the various standards-prescribed hooks.

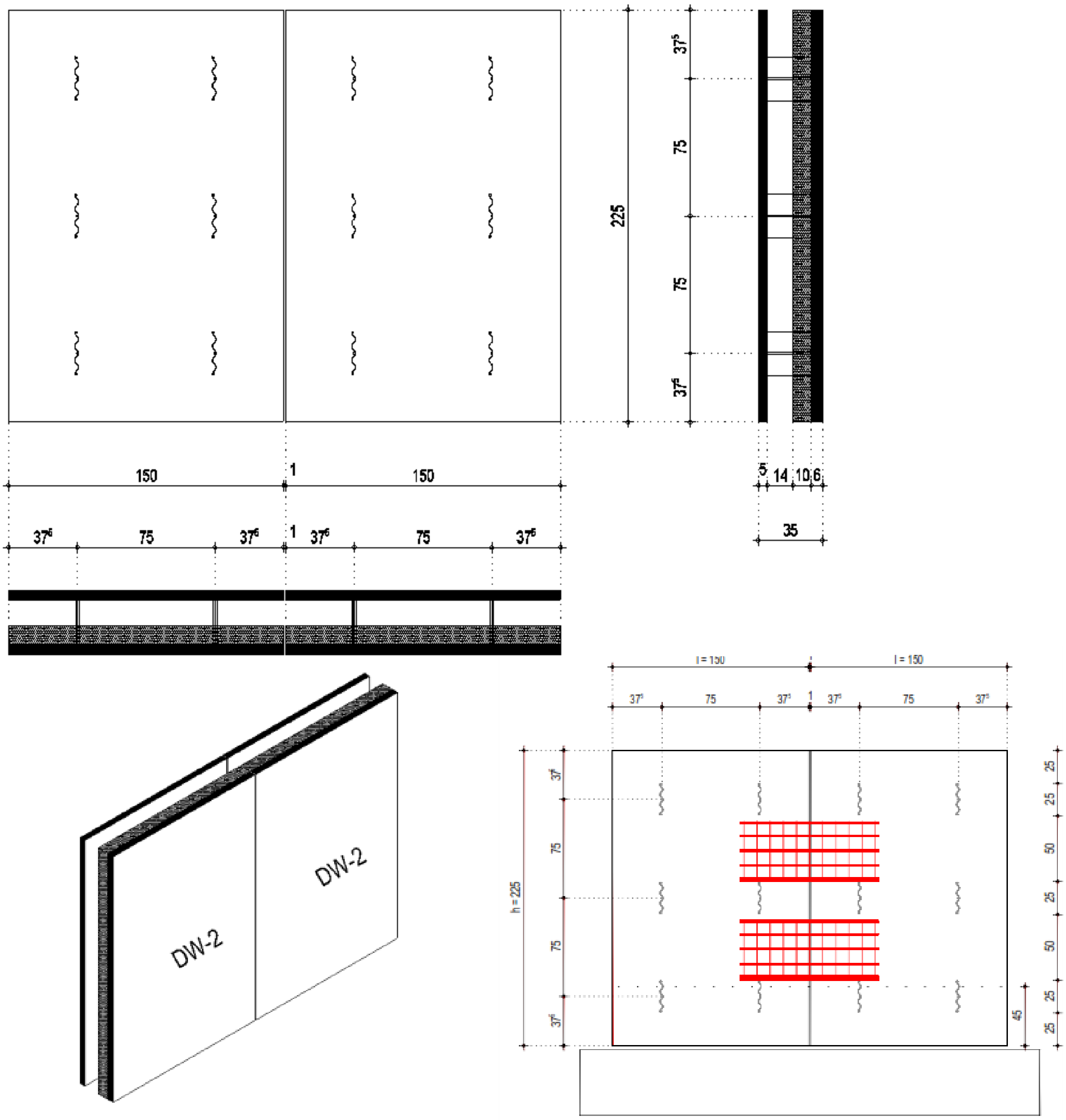

Figure 49 Section and reinforcement for specimen #2 1st part.

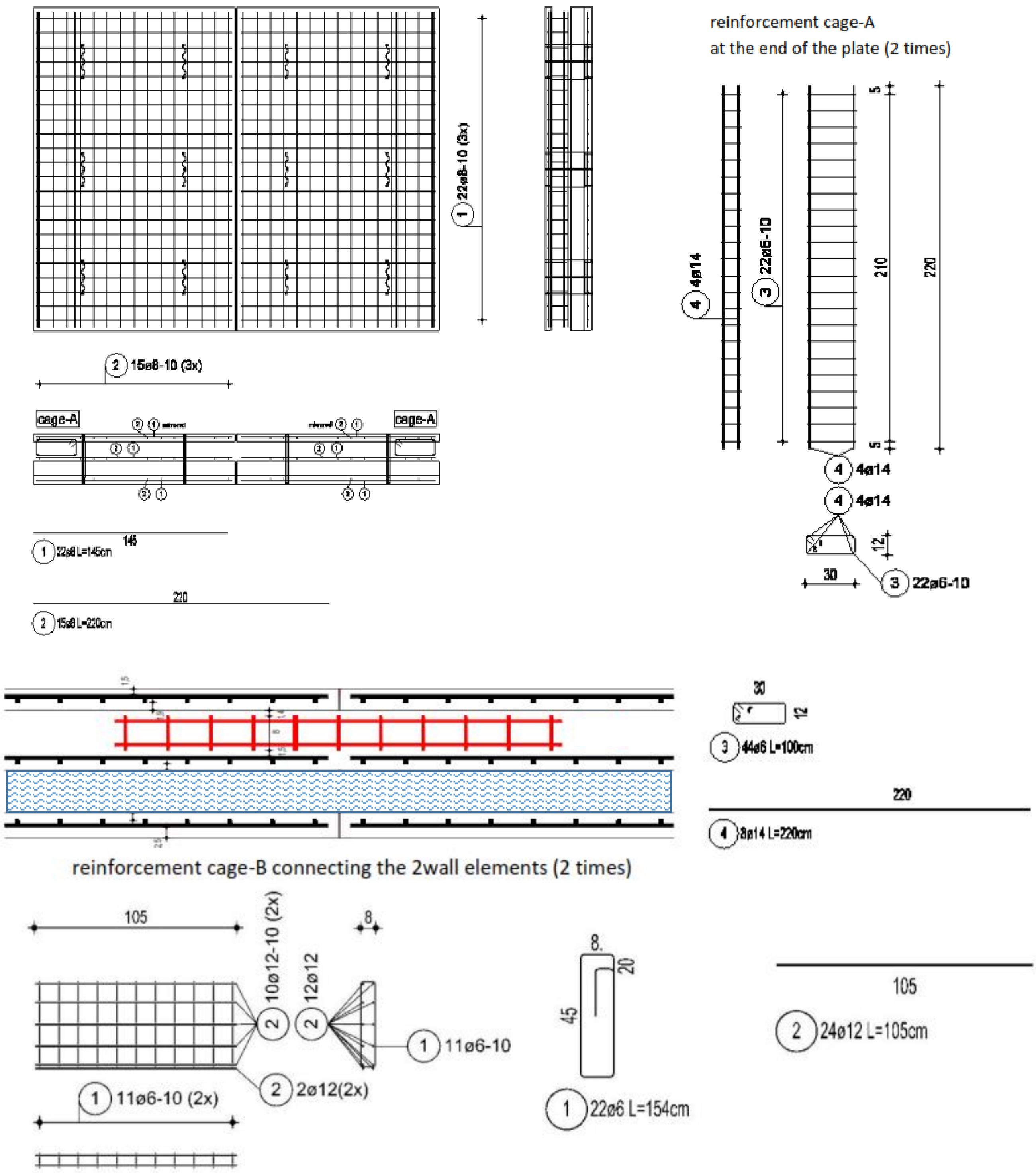

Figure 50 Section and reinforcement for specimen #2 2nd part.

2.4.2 Loading

During the testing of specimens #2 (and #1), in order to avoid failure at the foundation, axial load was released at a drift ratio of 0.2%. Beyond this lateral drift ratio, no axial load was applied.

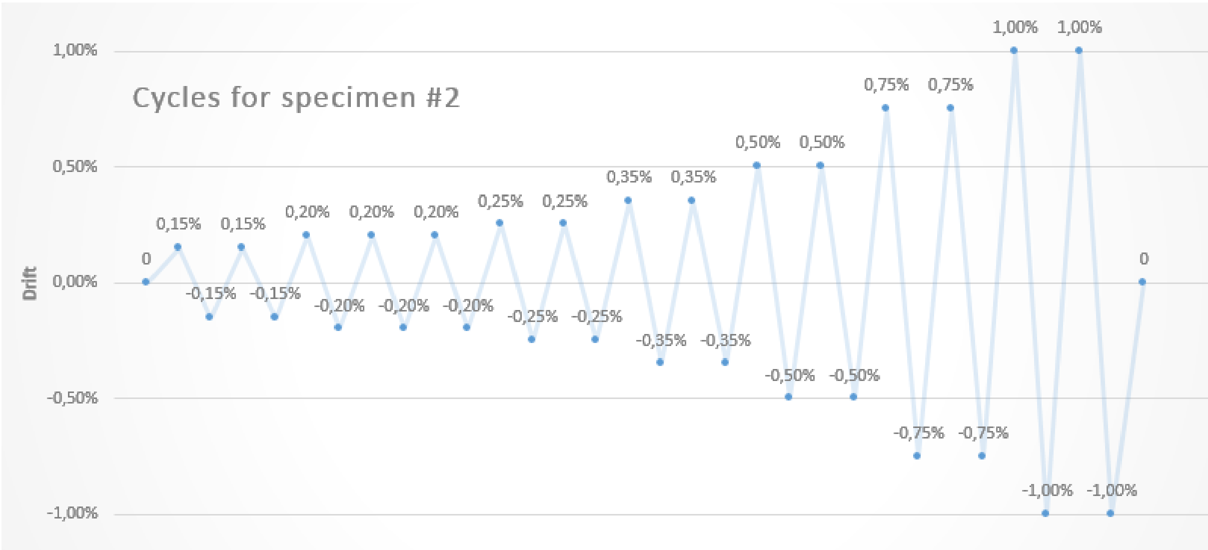

Figure 52 *Cyclic loading of specimen #2.*

Specimen-#2		Numbers	cyclus	way	analytic: full steps/cyclus
					step: 0,10 mm
H = 2,45 m					
		first crack	0,06%	1,47 mm	14,70
			0,15%	3,68 mm	36,75
			0,20%	4,90 mm	49,00
			0,25%	6,13 mm	61,25
			0,35%	8,58 mm	85,75
			0,50%	12,25 mm	122,50
			0,75%	18,38 mm	183,75
			1,00%	24,50 mm	245,00

Figure 53 *Cyclic loading numeric numbers for specimen #2.*

2.4.3 Instrumentation and Setup

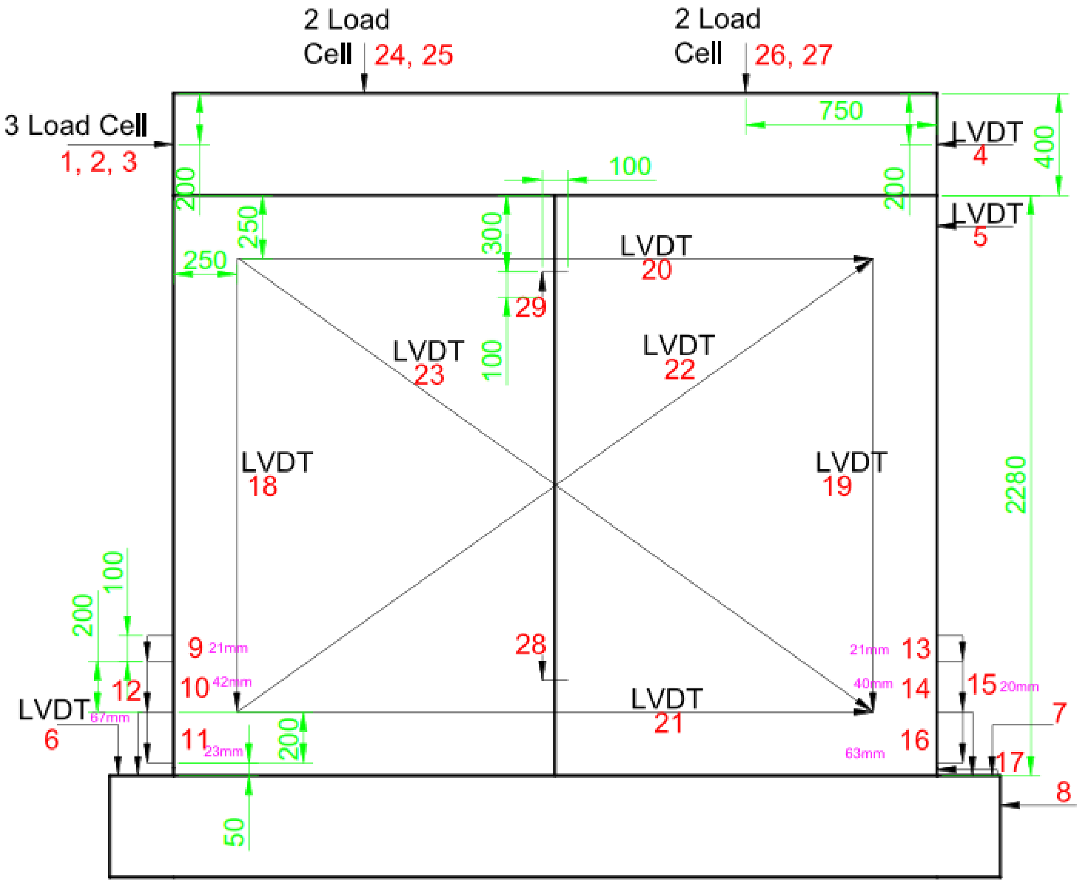

Figure 54 Instrumentation of specimen #2 [4].

Figure 55 Setup of specimen #2.

2.4.4 Displacement and Strain Measurement and Damage Pictures

The lateral load deformation response of specimen #2 is presented in ***Figure 56***. Measured moment-curvature response measured at the wall base (gauges 12 and 15, shown in ***Figure 54***, were used) is presented in ***Figure 56***. The damage pictures of the specimen are presented in ***Figure 58*** et seq.

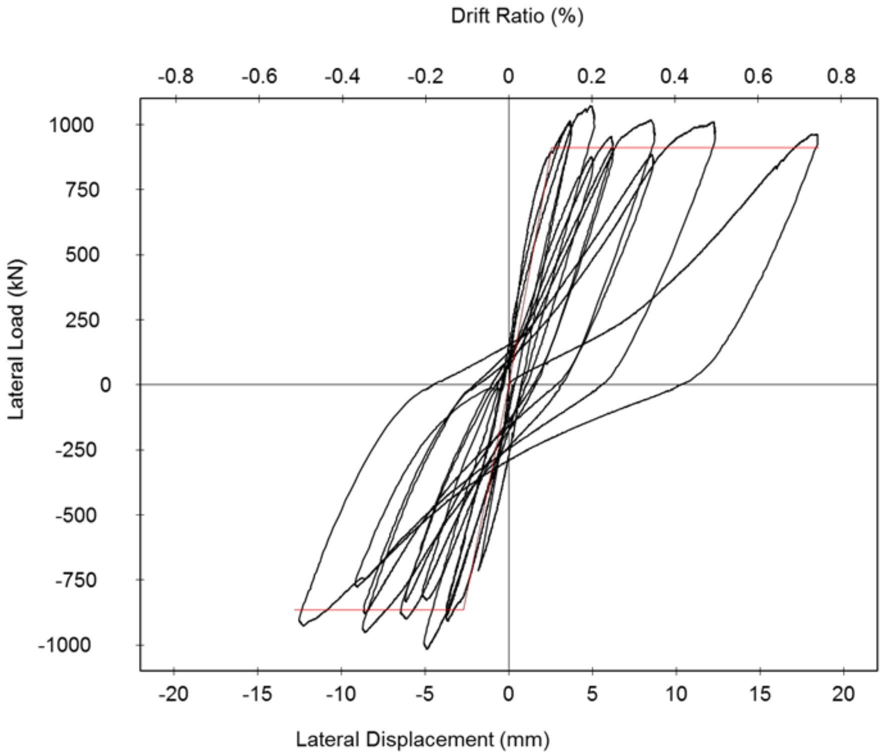

Figure 56 *Lateral load deformation response of specimen #2* ***[4]*** .

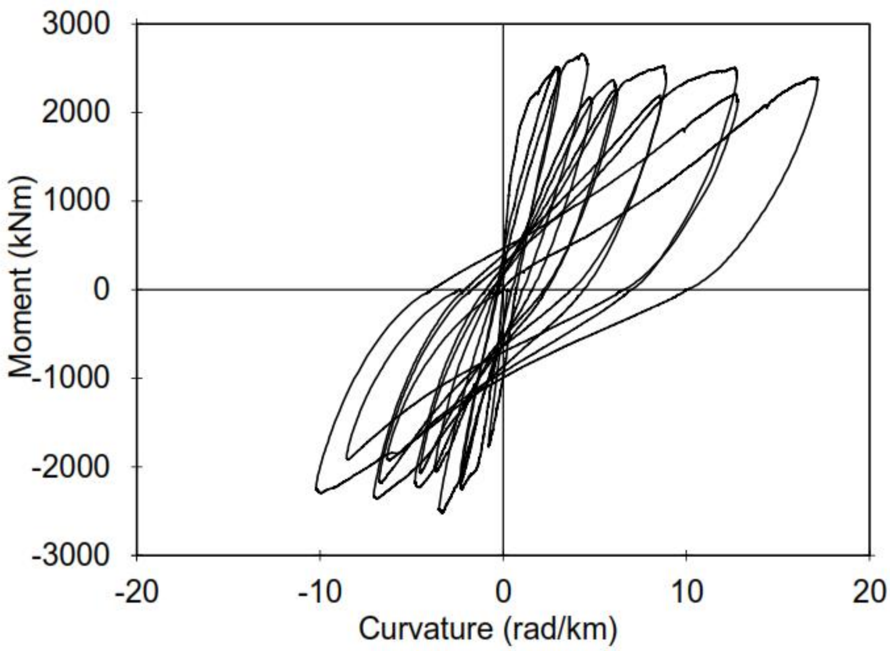

Figure 57 *Moment curvature response of specimen #2 at wall base* ***[4]***.

Figure 58 *Pictures of damage at drift ratio (DR) 0.2% for specimen #2.*

Figure 59 *Pictures of damage at drift ratio (DR) 0.35% for specimen #2.*

Figure 60 Pictures of damage at drift ratio (DR) 0.5% for specimen #2.

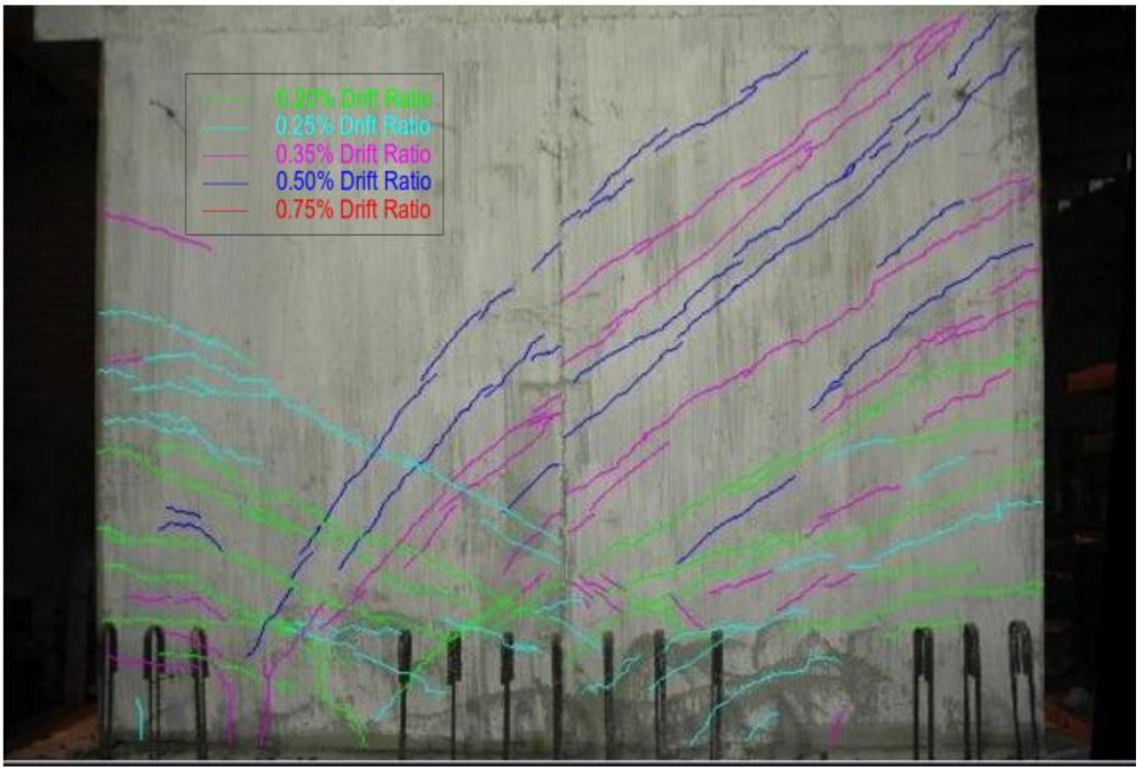

Figure 61 Final crack map specimen #2 [4].

2.5 Specimen # 3

In order to receive a load in a wall axis of a corner configuration must be U-formed. The result is now two identical wall corners. The dimensions were chosen so as to get a roughly similar concrete cross-section:

2.5.1 Perform Construction

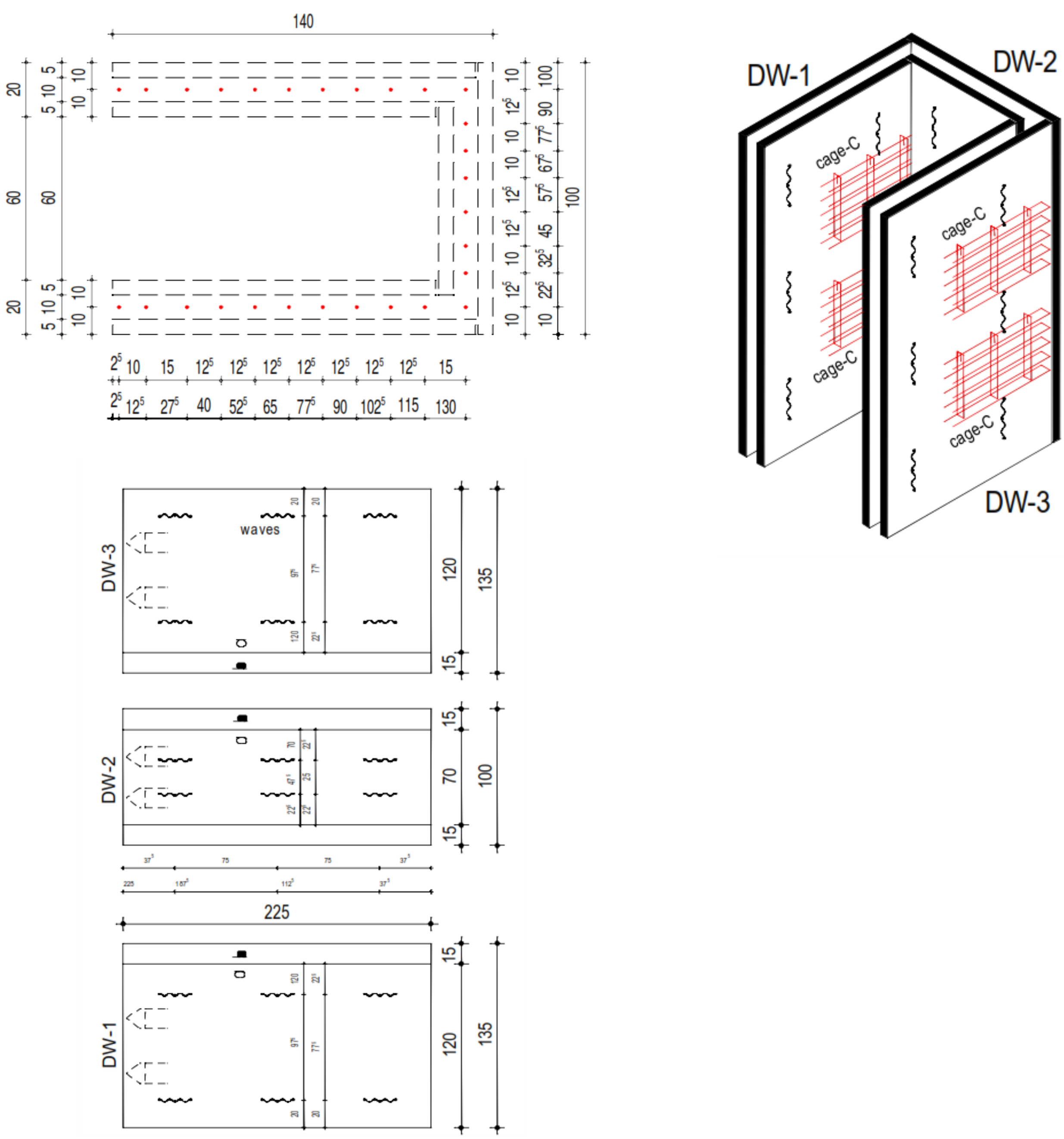

Figure 62 Sections and reinforcement drawings for specimen #3 I.

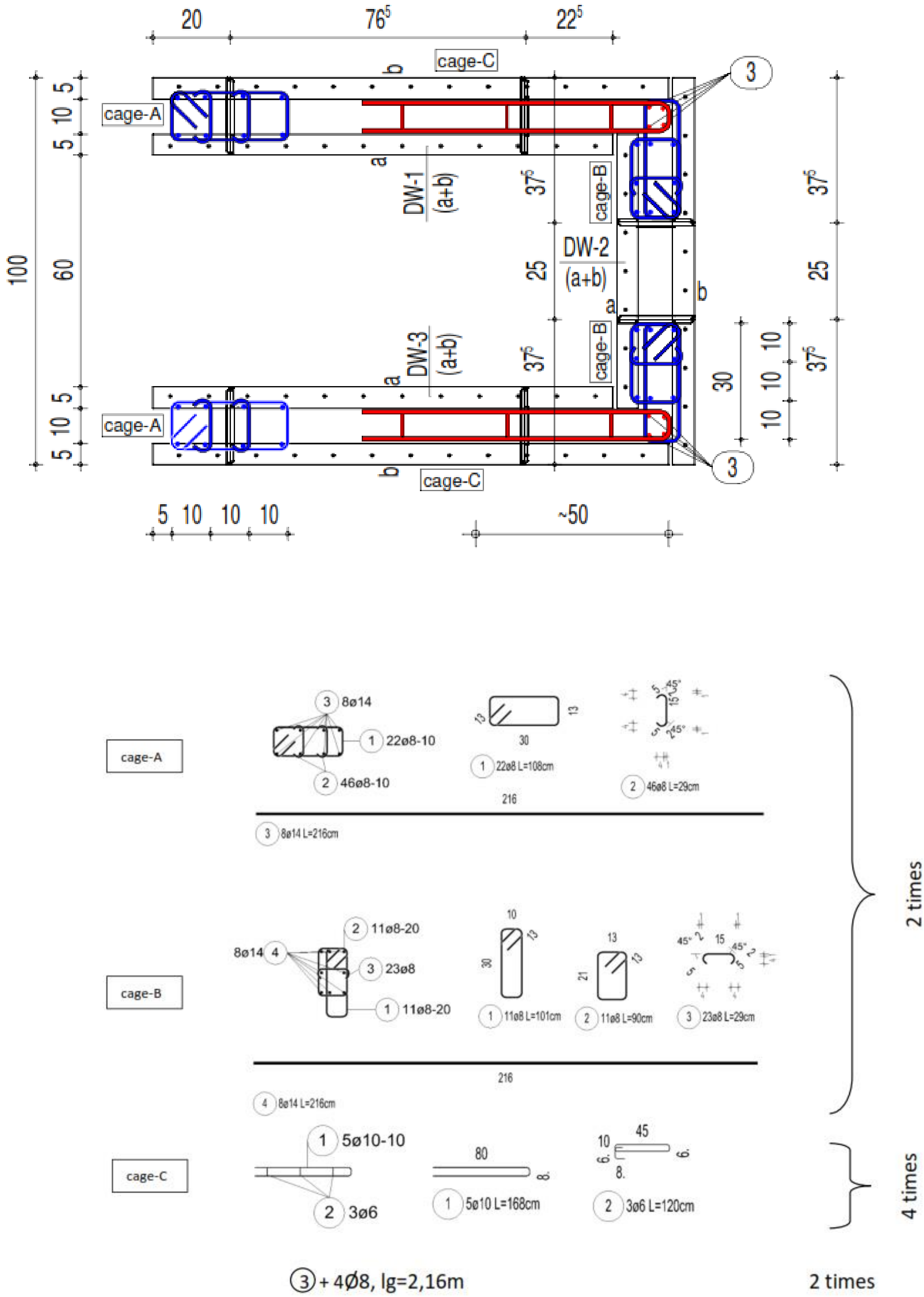

Figure 63 Sections and reinforcement drawings for specimen #3 II.

Figure 64 Preparation of specimen # 3 [7].

2.5.2 Loading

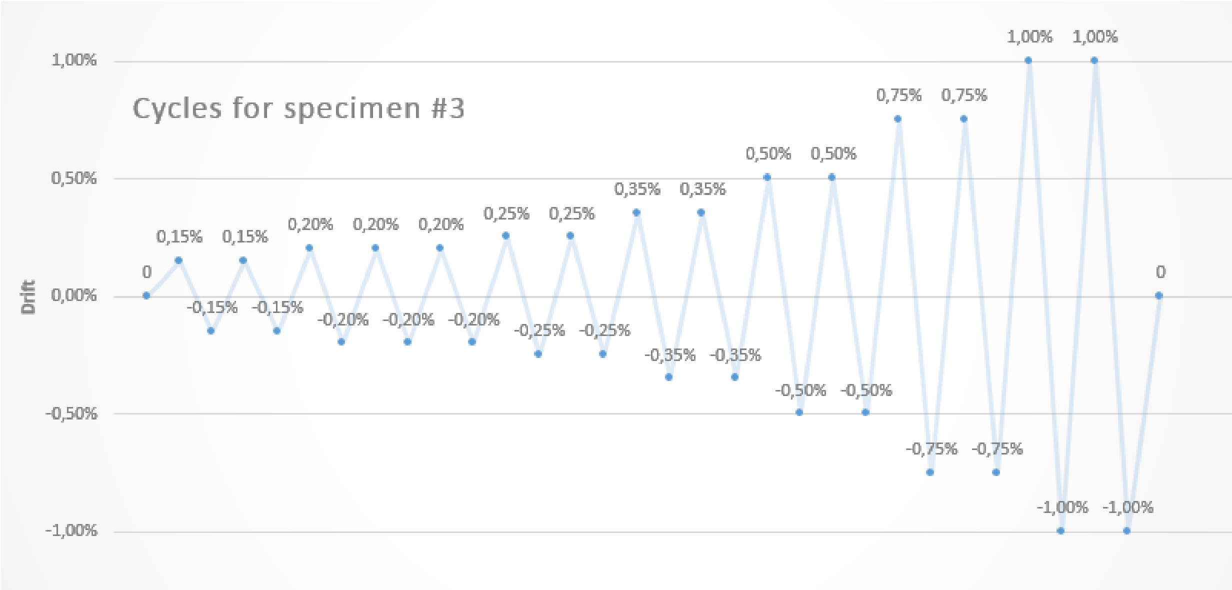

Specimen-#3	Numbers	cyclus	way	analytic: full steps/cyclus
				step: 0,10 mm
H = 2,45 m				
	first crack	0,05%	1,23 mm	12,25
		0,15%	3,68 mm	36,75
		0,20%	4,90 mm	49,00
		0,25%	6,13 mm	61,25
		0,35%	8,58 mm	85,75
		0,50%	12,25 mm	122,50
		0,75%	18,38 mm	183,75
		1,00%	24,50 mm	245,00

Figure 65 Cyclic loading numeric numbers for specimen #3.

2.5.3 Instrumentation and Setup

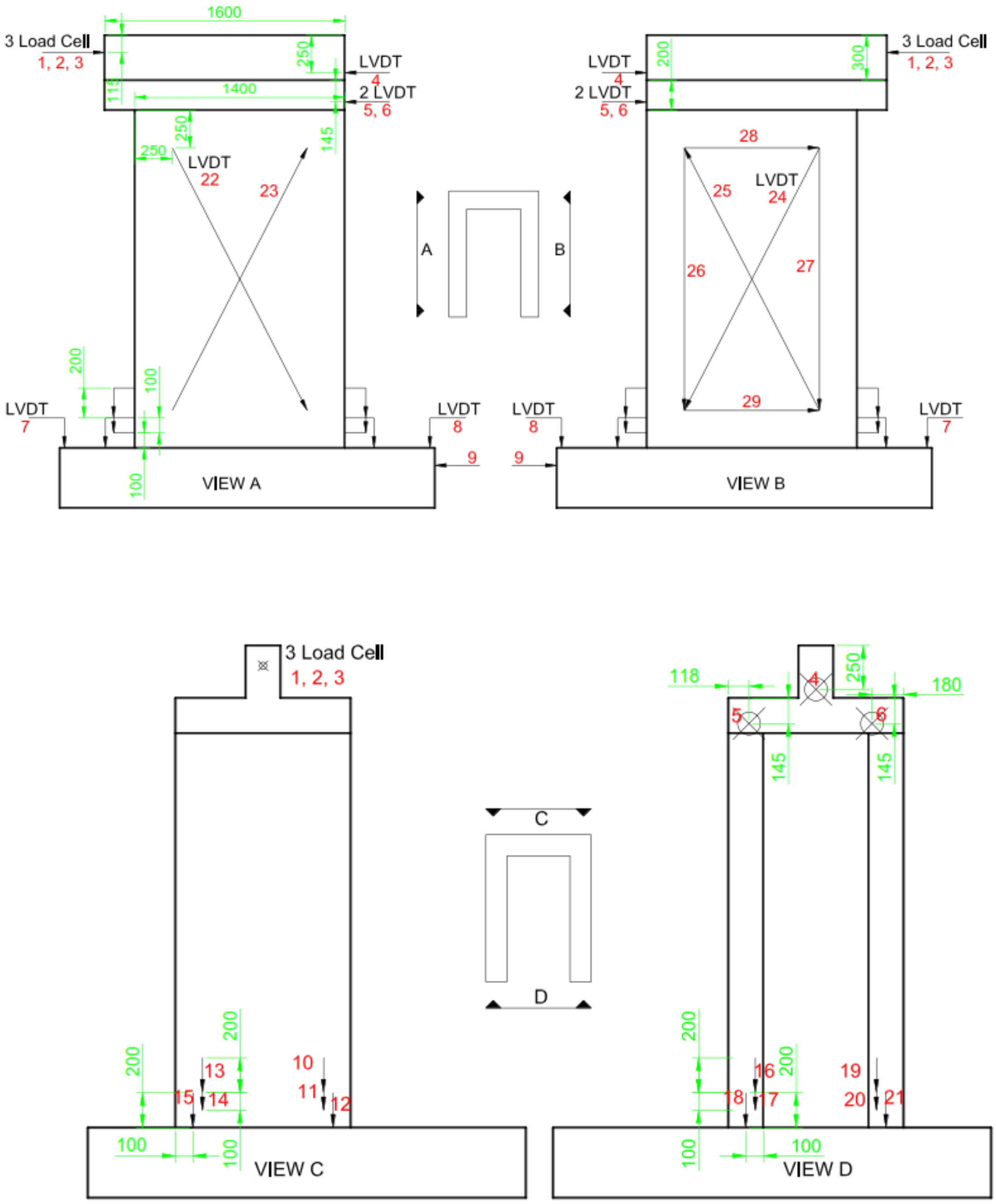

Figure 66 Instrumentation specimen #3 [4].

Figure 67 *Test setup for specimen #3 left (#4 at the right).*

2.5.4 Displacement and Strain Measurement and Damage Pictures

The lateral load deformation response of specimen #3 is presented in ***Figure 65***. Measured moment-curvature response measured at the wall base (gauges shown in ***Figure 66*** were used) is presented in ***Figure 68***. The damage pictures of the specimen are presented in ***Figure 70*** et seq.

First cracks were observed at a drift ratio beyond 0.05%. After wall base cracking, inclined cracks were seen on the two webs of the wall section. Inclined cracks, which were concentrated at the bottom half of the wall, spread towards the top region beyond a drift ratio of 0.5%. First yielding of the wall occurred at about a lateral force of 600 and 500 kN in positive and negative directions, respectively. In the positive direction of loading, hardening of the load deformation response was observed. This was mainly due to the presence of significant web reinforcement distributed on two legs of the U section. On the other hand, hardening response was not observed for the negative direction of loading due to the presence of the reinforcement concentrated in the flange. Lateral load carrying capacity of the wall was about 700 kN in the positive direction of loading, whereas it was about 600 kN in the negative direction of loading. In the negative direction of loading some strength degradation was observed, whereas no strength drop was seen in the positive direction of loading. The main reason of the strength drop was the concrete crushing at the toe of the wall. The most significant damage on the wall occurred at the base and at the slab-wall interface.

The test was stopped due to the severe damage occurred at the loading beam slab interface. A bilinear envelope was drawn on the lateral load-displacement figure as shown in ***Figure 68***. Based on this idealized response, it can be stated that the wall had a displacement ductility (or ductility ratio) of about 4.9 and 5.9 in the positive and negative directions, respectively. Although the wall was much slender (H/L ≈1.7) compared to specimens #1 and #2, inclined shear cracking was observed. Despite shear cracking, the double wall was able to behave in a very ductile manner.

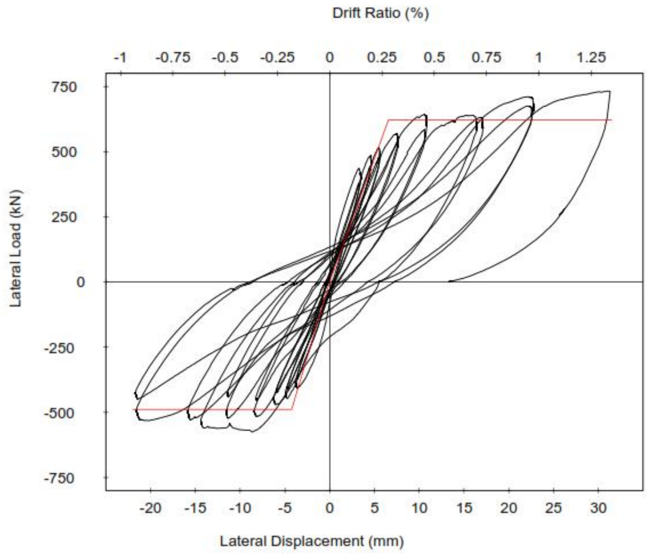

Figure 68 *Lateral load deformation response of specimen #3 [4].*

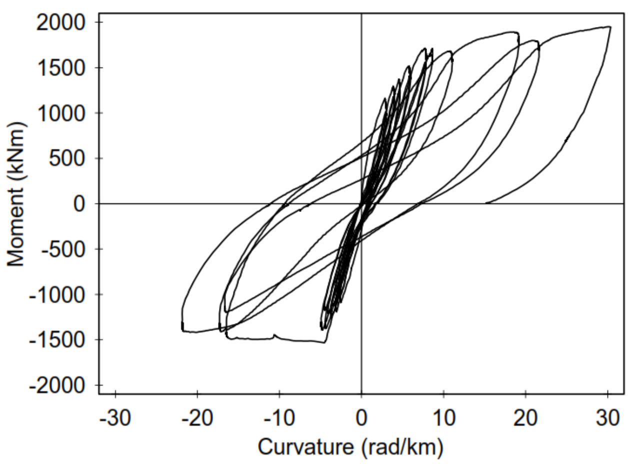

Figure 69 *Moment curvature response of specimen #3 at wall base [4].*

Figure 70 *Picture of damage at 0.15% drift ratio (DR) for specimen #3.*

a) -0.35% DR

b) + 0.50% DR

Figure 71 *Pictures of damage at different drift ratio (DR) for specimen #3.*

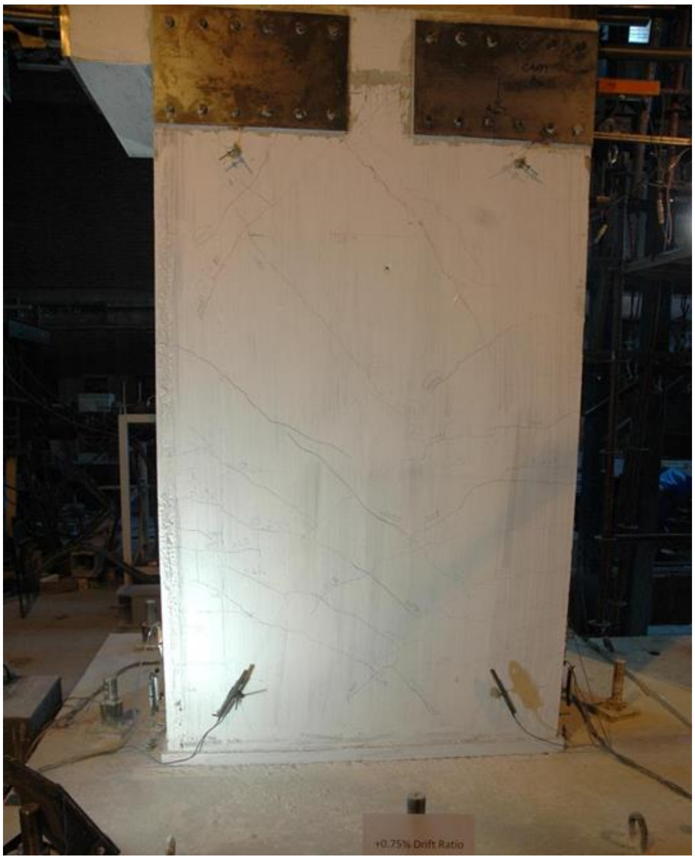

Figure 72 *Picture of damage at 0.75% drift ratio (DR) for specimen #3.*

Figure 73 *Pictures of damage at 1,0% drift ratio (DR) for specimen #3.*

Figure 74 Picture of damage at 1.0% drift ratio (DR) for specimen #3 [4].

2.6 Specimen # 4

The lateral load deformation response of Specimen #4 is presented in ***Figure 81***. Measured moment-curvature response measured at the wall base by using the measurements at the wall base is presented in ***Figure 82***. The damage pictures of the specimen are presented in ***Figure 83*** et seq.

2.6.1 Perform Construction

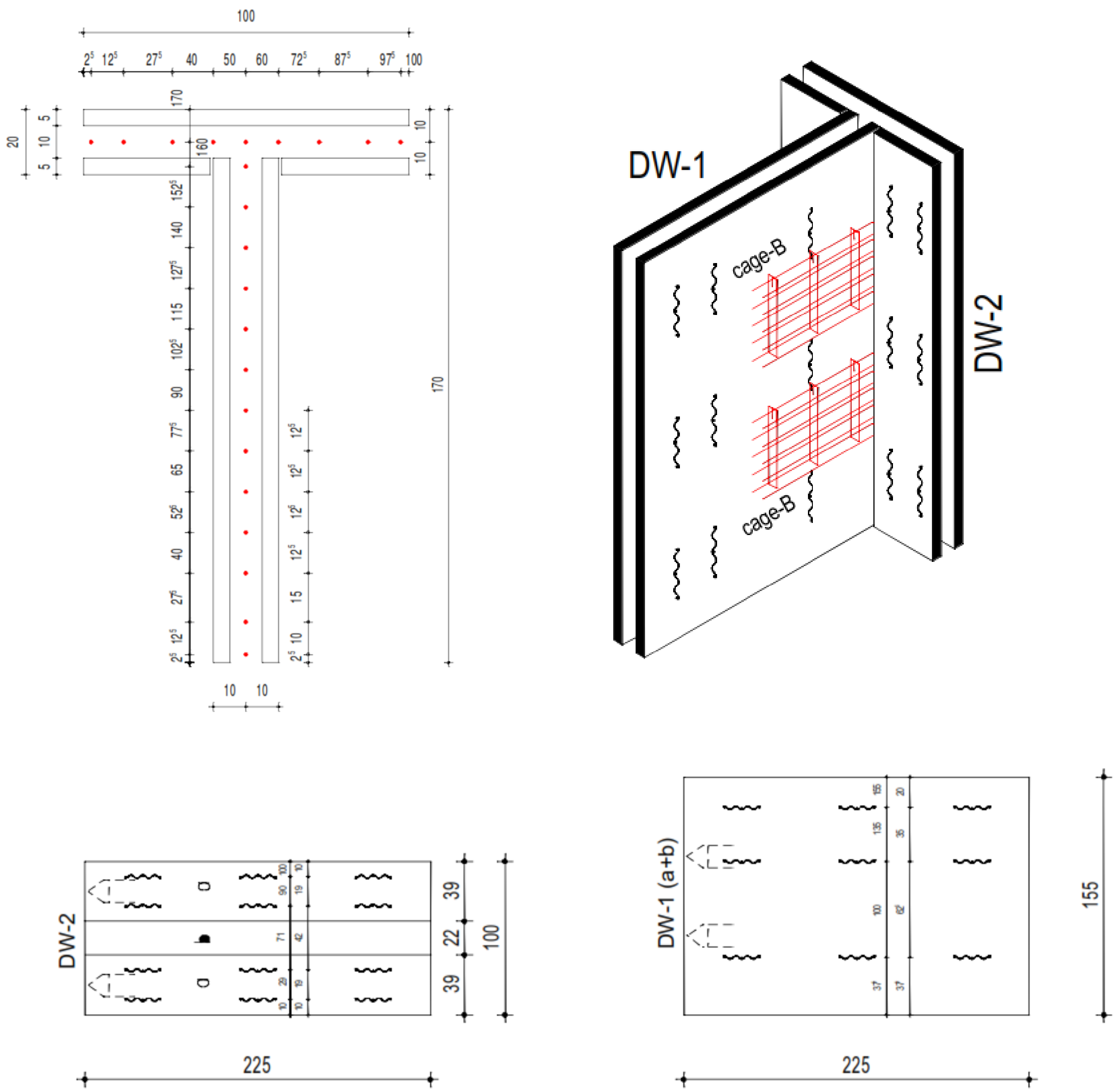

Figure 75 *Sections and reinforcement drawings for specimen #4 I.*

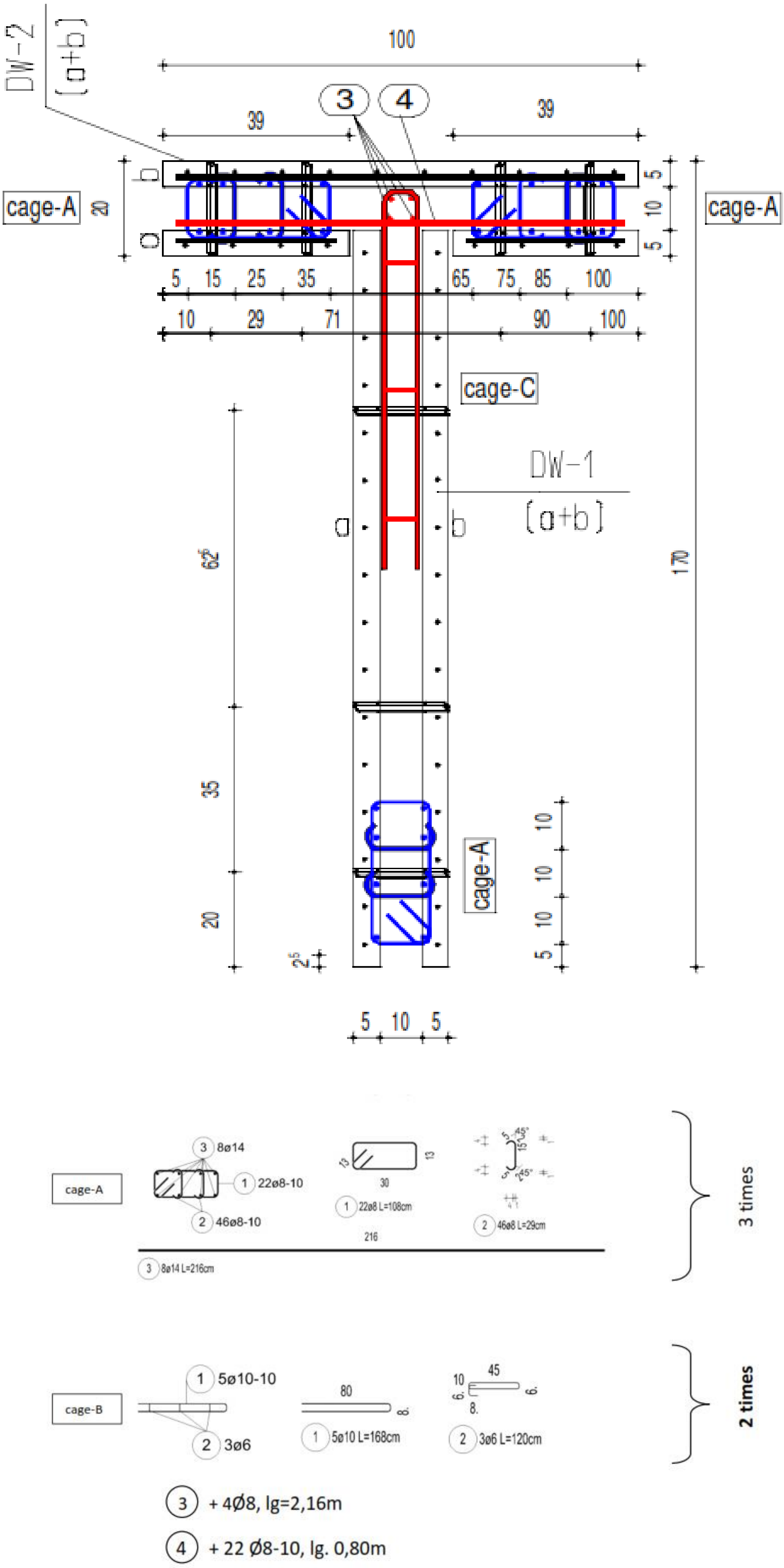

Figure 76 Sections and reinforcement drawings for specimen #4 II.

Figure 77 Casting specimen # 3 with cage [7].

2.6.2 Loading

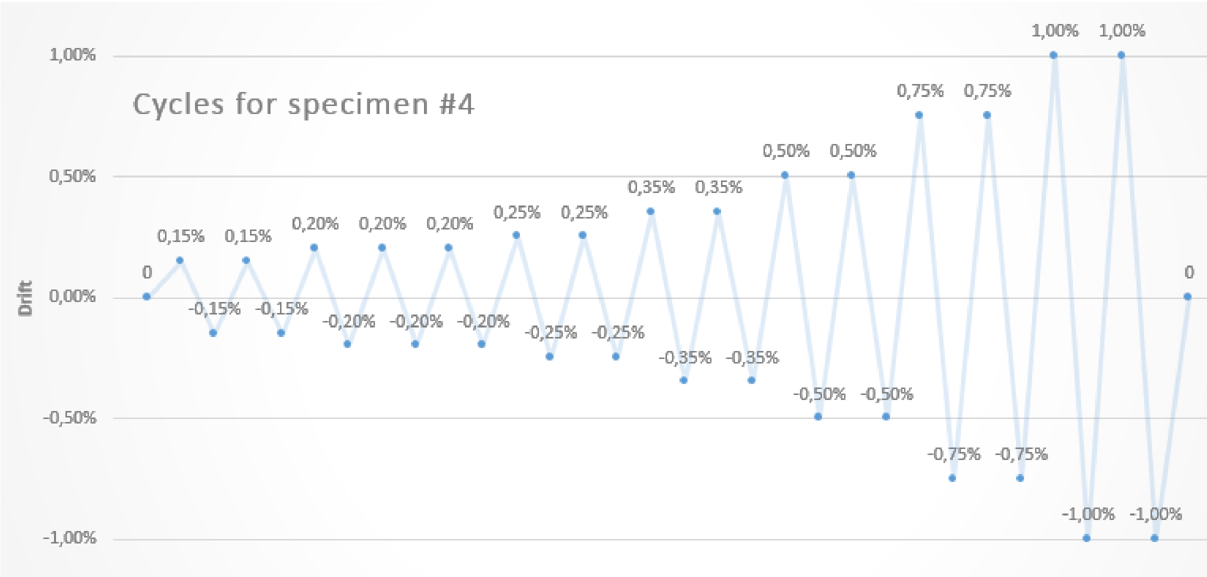

Specimen-#4		Numbers	cyclus	way	analytic: full steps/cyclus
					step: 0,10 mm
H = 2,45 m					
		first crack	0,03%	0,74 mm	7,35
			0,15%	3,68 mm	36,75
			0,20%	4,90 mm	49,00
			0,25%	6,13 mm	61,25
			0,35%	8,58 mm	85,75
			0,50%	12,25 mm	122,50
			0,75%	18,38 mm	183,75
			1,00%	24,50 mm	245,00

Figure 78 Cyclic loading numeric numbers for specimen #4.

2.6.3 Instrumentation and Setup

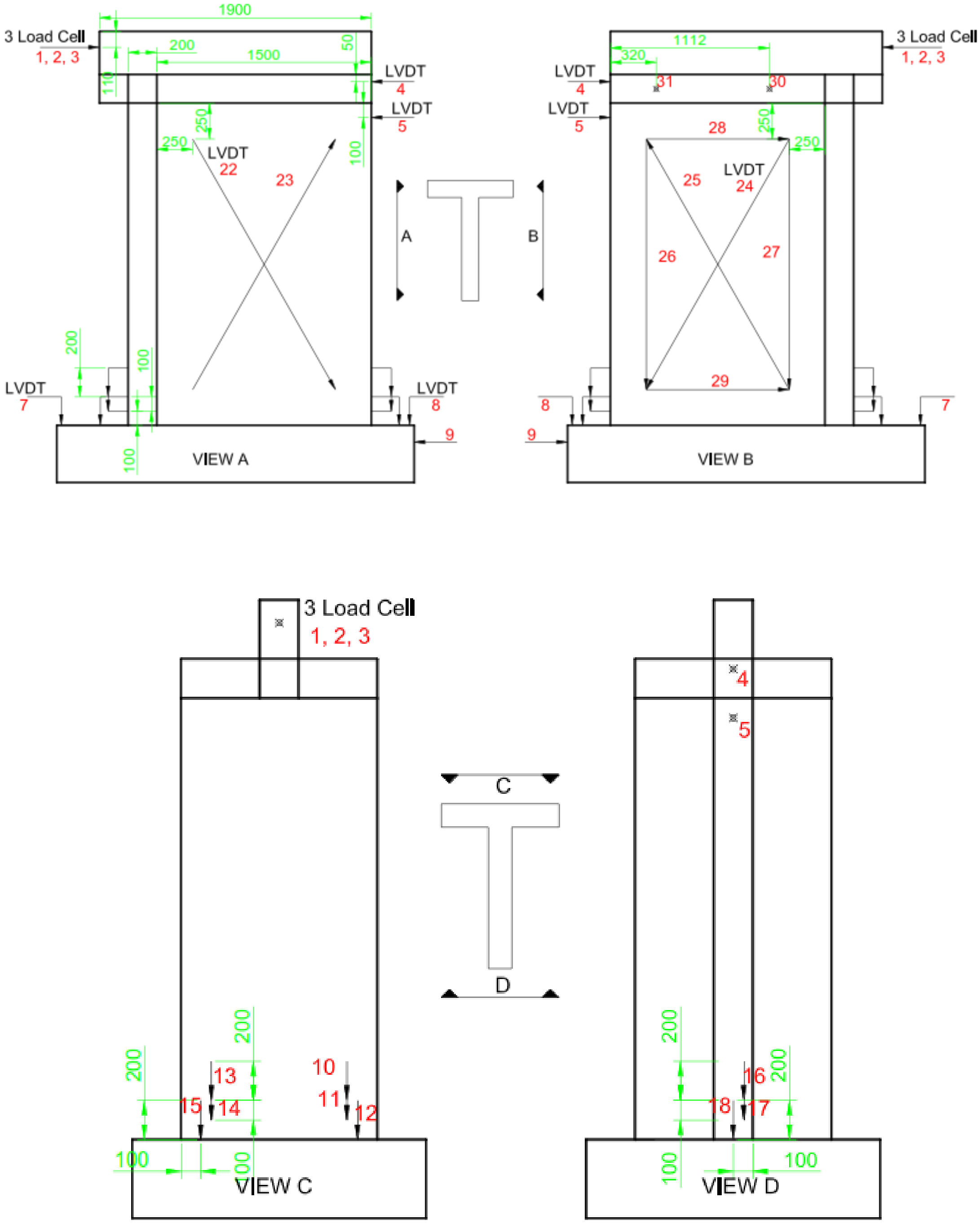

Figure 79 Instrumentation of specimen #4 [4].

Figure 80 Test setup specimen #4.

2.6.4 Displacement and Strain Measurement and Damage Pictures

Similar to specimen #3, first cracks were observed at a drift ratio beyond 0.03%.

After wall base cracking, flexural cracks on the flange and inclined cracks on the web were seen beyond a drift ratio of 0.3%.

The flexural cracks occurred up to a height of about 1 m, and their spacing was about the size of transverse reinforcement spacing. Crushing of the wall initiated at a drift ratio of about 0.75%, beyond which strength degradation started. The wall base shear capacity was about 600 kN and 400 kN, in the positive and negative directions of loading, respectively.

This asymmetry can be attributed to the difference of longitudinal reinforcement placement between the flange and the web of the wall. The width of the inclined cracking from loaded corner of the specimen enlarged as 1% drift ratio was attained. Crushing of the wall toe and diagonal cracking marked the onset of wall deformation capacity. Beyond a drift ratio of 1% the wall was not able to sustain its lateral strength. The bilinear capacity diagrams shown in ***Figure 81*** indicate that the displacement ductility of the wall was about 4.

Measured moment-curvature response measured at the wall base by using the measurements at the wall base shown in ***Figure 79*** is presented in ***Figure 82***. The damage pictures of the specimen are presented in ***Figure 83*** et seq.

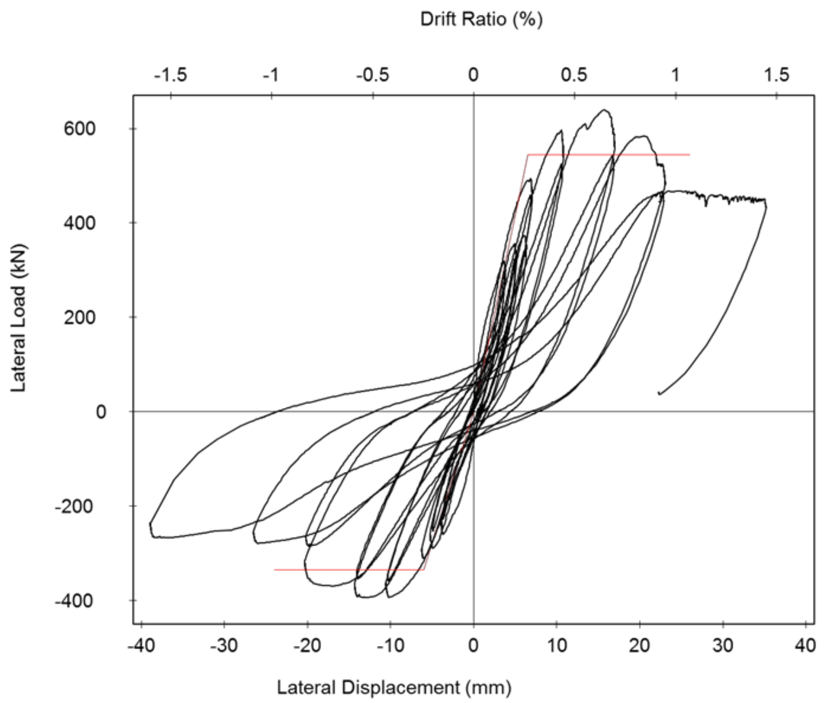

Figure 81 Lateral load deformation response of specimen #4 [4].

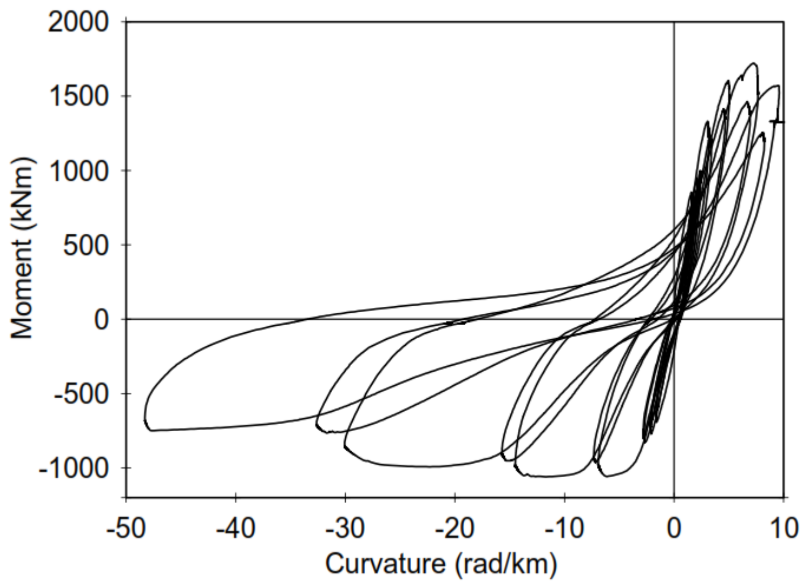

Figure 82 Moment curvature response of specimen #4 at wall base [4].

0.15 % DR (drift ratio).

0.35 % DR (drift ratio)

Figure 83 Pictures of damages at different drift ratios (DR) for specimen #4.

0.5 % DR (drift ratio).

0.75 % DR (drift ratio).

Figure 84 Pictures of damages at different drift ratios (DR) for specimen #4 [4].

Figure 85 Pictures of damages at drift ratio (DR) 1.0% for specimen #4 I [4].

Figure 86 *Pictures of damages at drift ratio (DR) 1.0% for specimen #4 II* [4].

2.7 Specimen # 5

2.7.1 Perform Construction

The fifth test specimen was a column constructed similar to the idea of a double wall. The objective of this test was to examine whether the double wall-column specimen could exhibit seismic performance similar to that which can be observed in typical reinforced concrete columns.

In addition to the 2 precast -5 cm-shells, on both sides of the column a perforated steel-sheet was used as integrated formwork. A paper from 2012 by Pirringer et al. [35] shown, that this can also be used for bearing purposes.

We used a **"Lochblech Rv 5.0-8.0"** [36] steel 1.4301, [37] with the aperture percentage of:

$$P_o = \frac{90.69R^2}{T^2} = 36.4\% \qquad (1)$$

Where R = radius of holes [mm] and T = division in[mm]

For the used Rv 5.0-8.0 $P_0 = 36.4\%$.

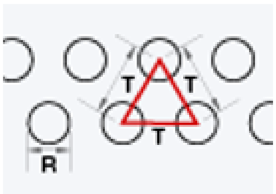

Figure 87 Perforated sheet formula explanation.

Specimen #5 experienced flexural cracking starting from about 0.3% drift ratio. Cracks spaced at about 15 cm spread from the column base up to about 1 m from the base. The width of the cracks enlarged as the lateral deformation demands increased. The column reached to its lateral load carrying capacity at about 1% drift ratio. Beyond this drift ratio, plastic deformations took place, which were reflected as cracking and crushing of concrete. Most of the observed damage took place at the bottom 50 mm region. This region underneath the shells is actually filled by the concrete while casting the central portion of the column. Once the lower strength concrete at the bottom was damaged, the deformations and damage were concentrated in this zone, while no significant damage was seen on the shells. This phenomenon is evident from Figure 30. It can be observed that most of the plastic deformations took place within the bottom 50 mm upon examining the moment-curvature results. The failure of the column, which was taken as the point with a 15 % capacity drop in the lateral strength, was mainly due to the crushing of concrete. Based on the envelope curve drawn on the load- deformation response on **Figure 96**, it can be stated that the displacement ductility of the column was about 6.5 and 4.5 in the positive and negative directions, respectively.

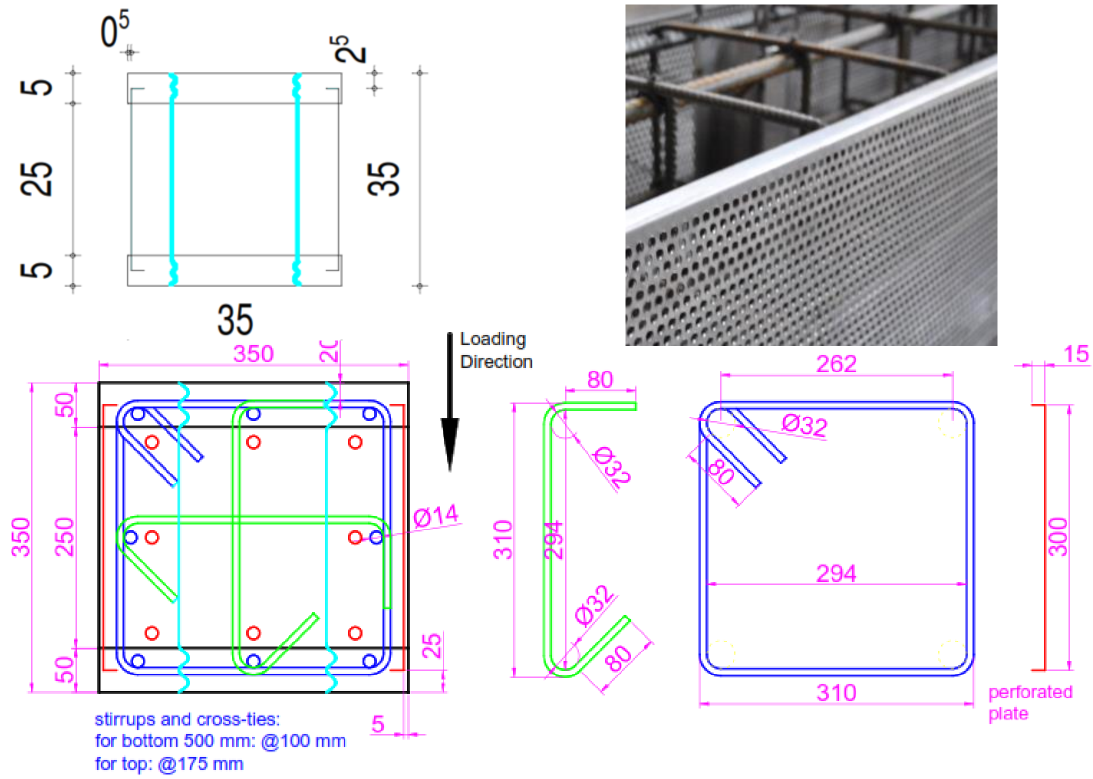

Figure 88 *Sections and reinforcement drawings for specimen #5.*

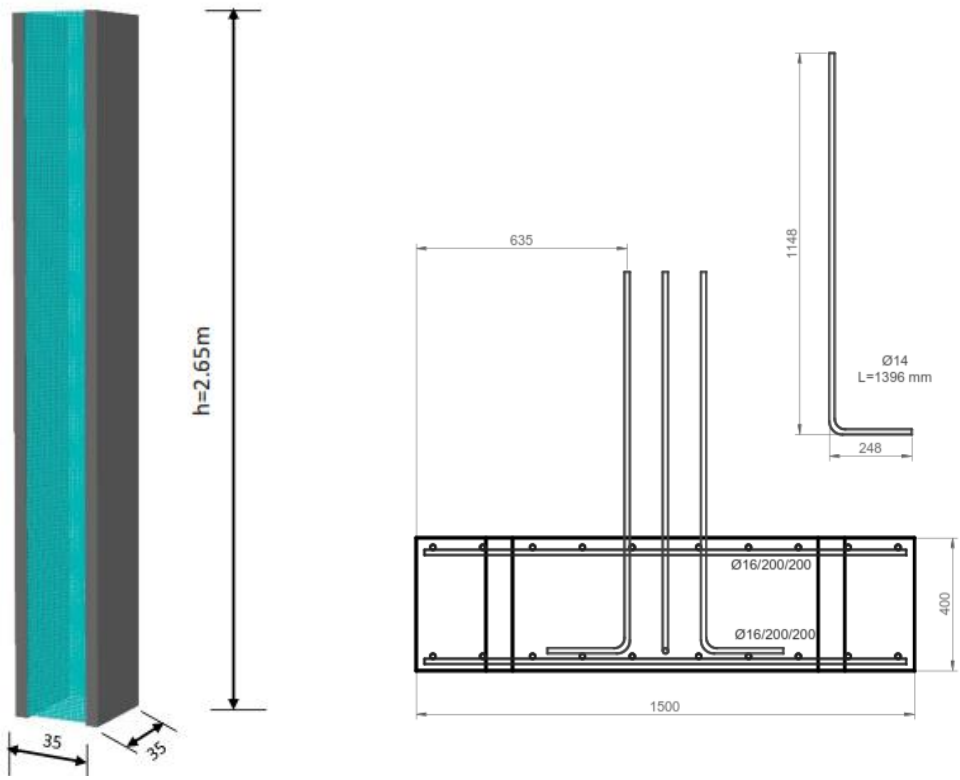

Figure 89 *Section of specimen base and 3-D view of specimen #5.*

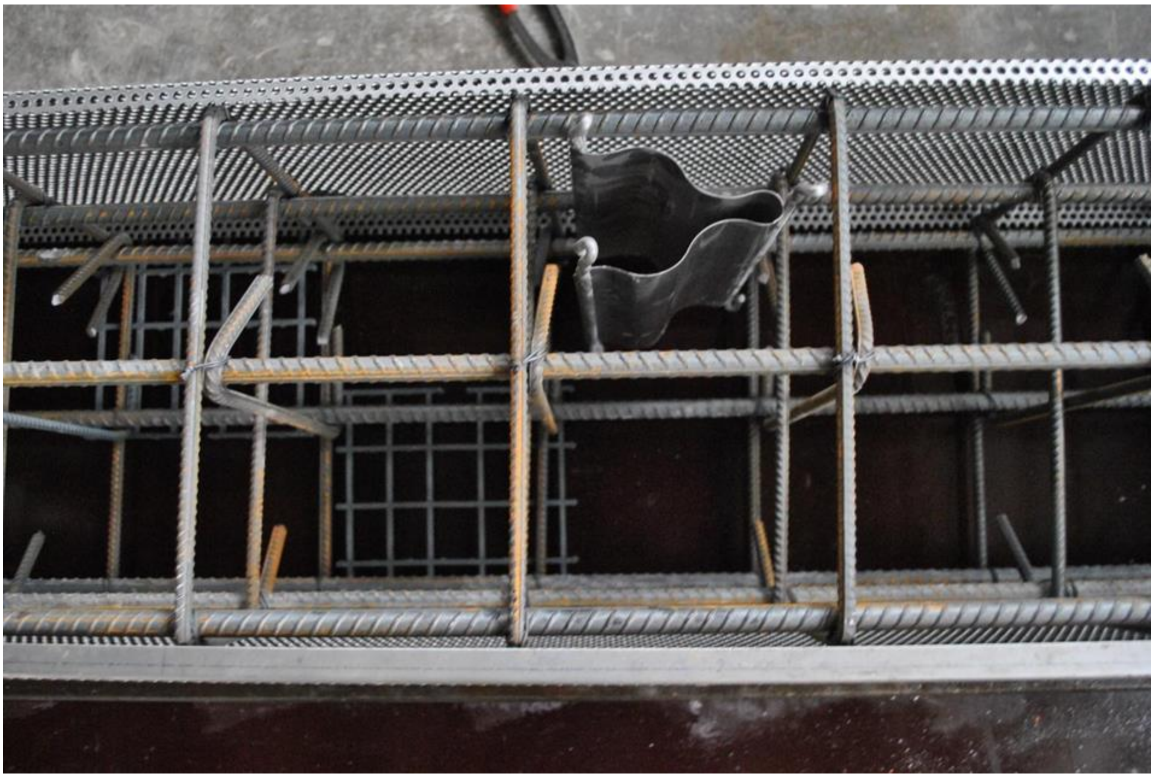

Figure 90 Preparation of specimen #5 I [7].

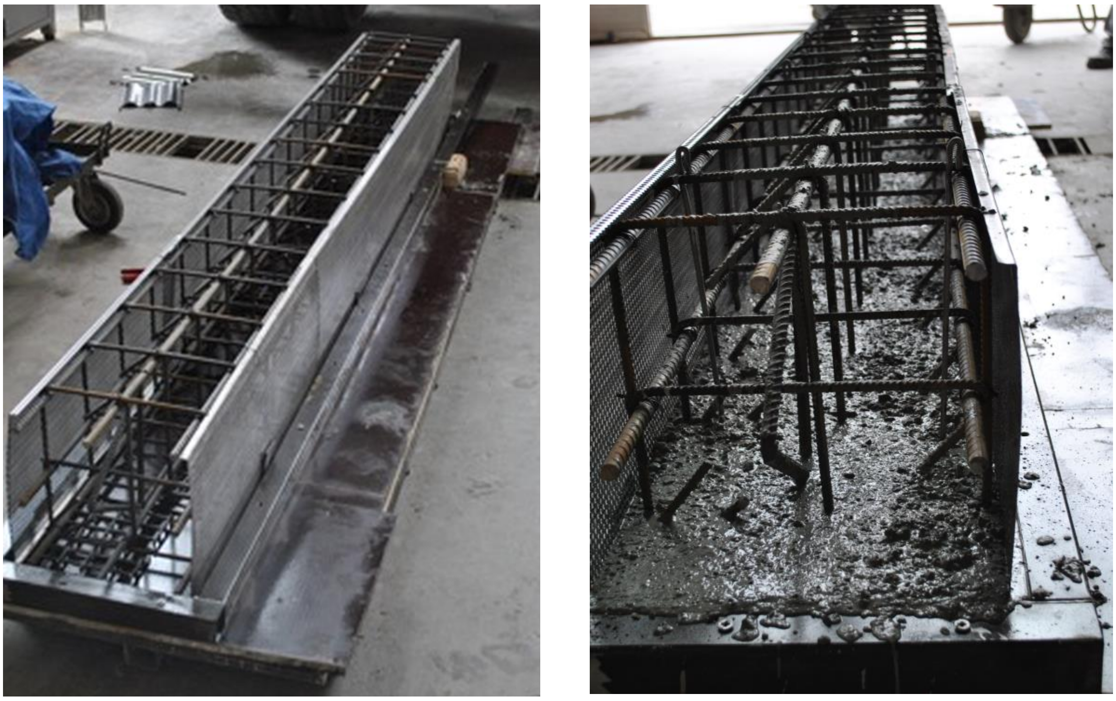

Figure 91 Preparation of specimen #5 II [7].

Stick, as part of the wave

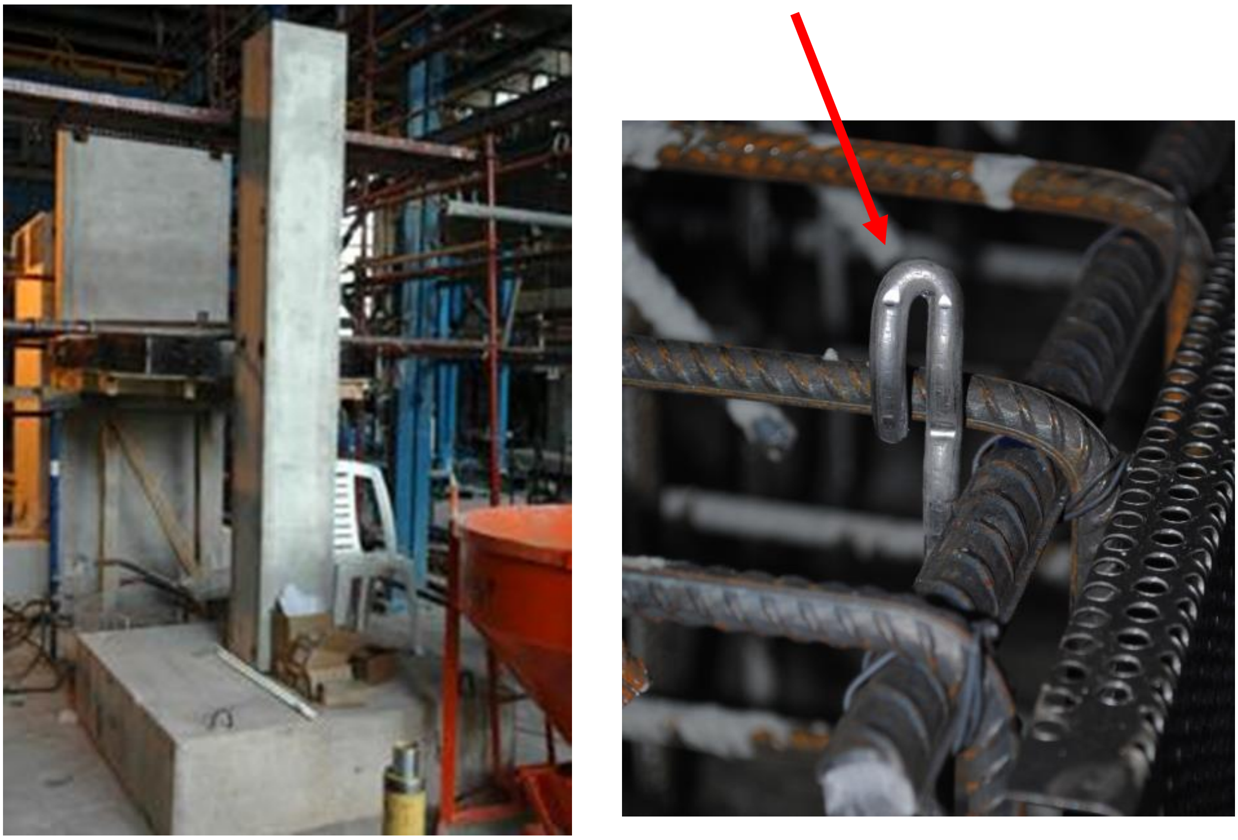

Figure 92 *Preparation of specimen #5 III.*

2.7.2 Loading

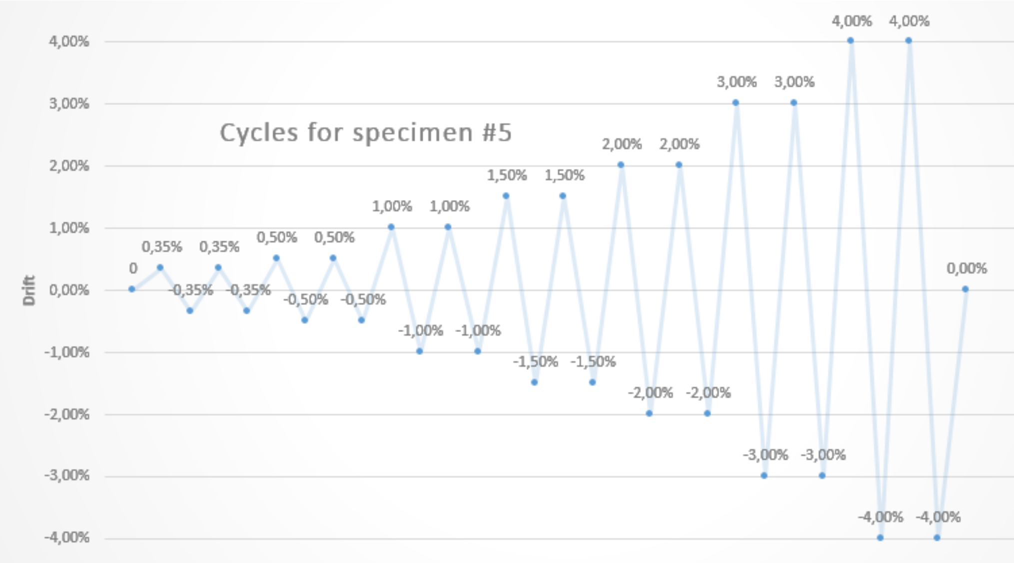

Specimen-#5		Numbers	cyclus	way	analytic: full steps/cyclus
					step: 0,10 mm
H = 2,61 m					
		first crack	0,35%	9,14 mm	91,35
			0,50%	13,05 mm	130,50
			1,00%	26,10 mm	261,00
			1,50%	39,15 mm	391,50
			2,00%	52,20 mm	522,00
			2,50%	65,25 mm	652,50
			3,00%	78,30 mm	783,00
			4,00%	104,40 mm	1044,00

Figure 93 Cyclic loading numeric numbers for specimen #5.

2.7.3 Instrumentation and Setup

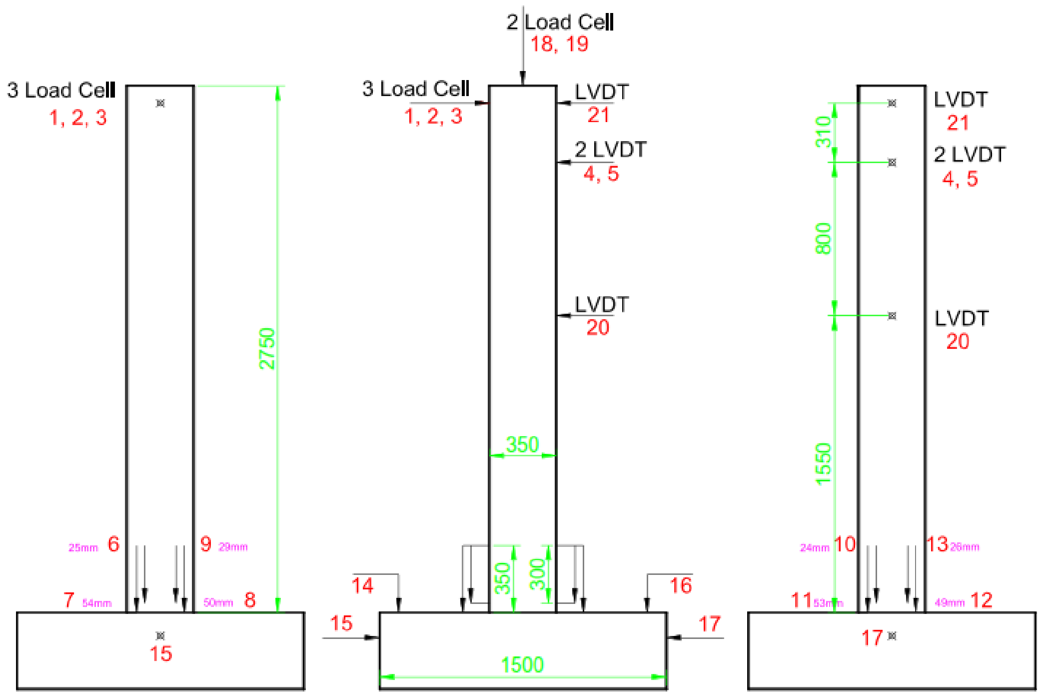

Figure 94 Instrumentation of specimen #5 [4].

Figure 95 Test setup of specimen #5 [4].

2.7.4 Displacement and Strain Measurement and Damage Pictures

The lateral load deformation response of specimen #5 is presented in ***Figure 96***. Measured moment-curvature response measured at the wall base (gauges shown in **Figure 94** were used) is presented in ***Figure 97***. The damage pictures of the specimen are presented in ***Figure 99*** et seq.

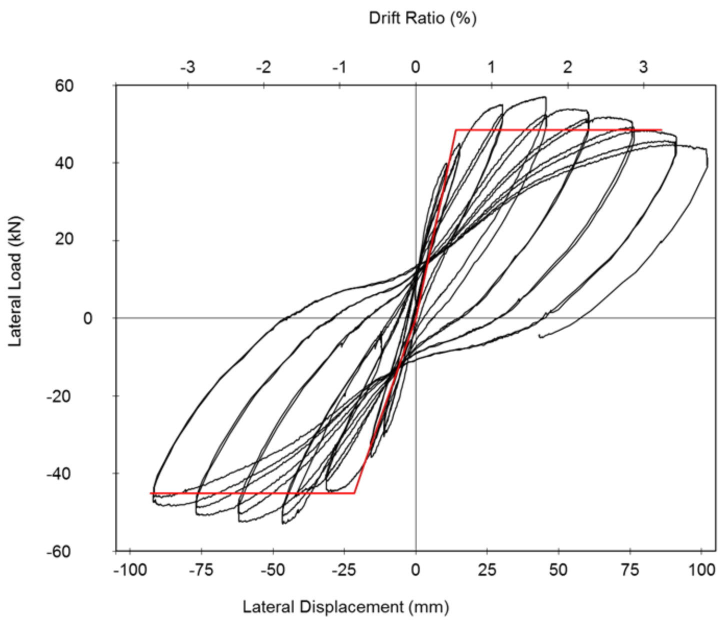

Figure 96 *Lateral load deformation response of specimen #5* ***[4]***.

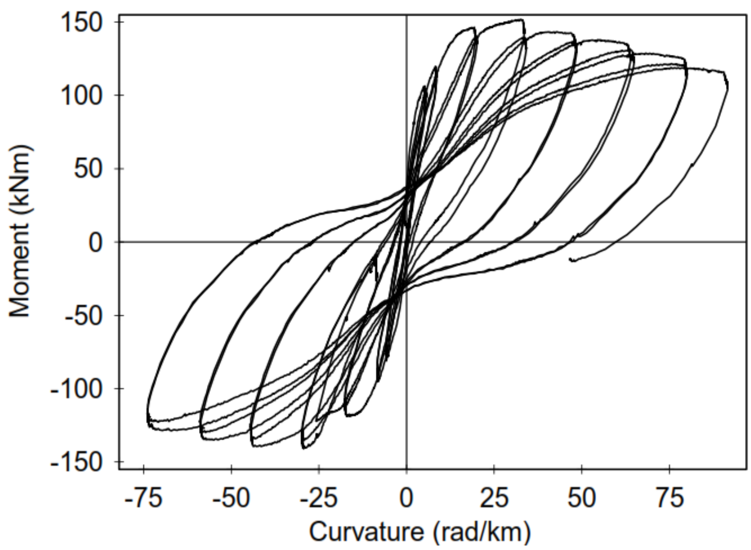

Figure 97 *Moment curvature response of specimen #5 within bottom 350 mm* ***[4]***.

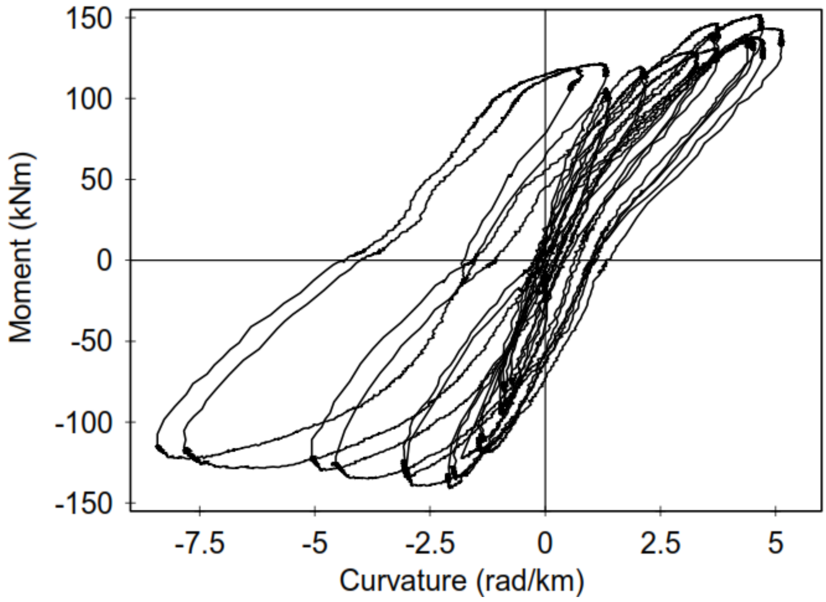

Figure 98 Moment curvature response of specimen #5 at column base within 300mm excluding bottom 50 mm [4].

Specimen #5 experienced flexural cracking starting from about 0.3% drift ratio. Cracks spaced at about 15 cm spread from the column base up to about 1 m from the base. The width of the cracks enlarged as the lateral deformation demands increased. The column reached to its lateral load carrying capacity at about 1% drift ratio. Beyond this drift ratio, plastic deformations took place, which were reflected as cracking and crushing of concrete. Most of the observed damage took place at the bottom 50 mm region. This region underneath the shells is actually filled by the concrete while casting the central portion of the column. Once the lower strength concrete at the bottom was damaged, the deformations and damage were concentrated in this zone, while no significant damage was seen on the shells. This phenomenon is evident from Figure 30. It can be observed that most of the plastic deformations took place within the bottom 50 mm upon examining the moment-curvature results. The failure of the column, which was taken as the point with a 15 % capacity drop in the lateral strength, was mainly due to the crushing of concrete. Based on the envelope curve drawn on the load- deformation response on ***Figure 96***, it can be stated that the displacement ductility of the column was about 6.5 and 4.5 in the positive and negative directions, respectively.

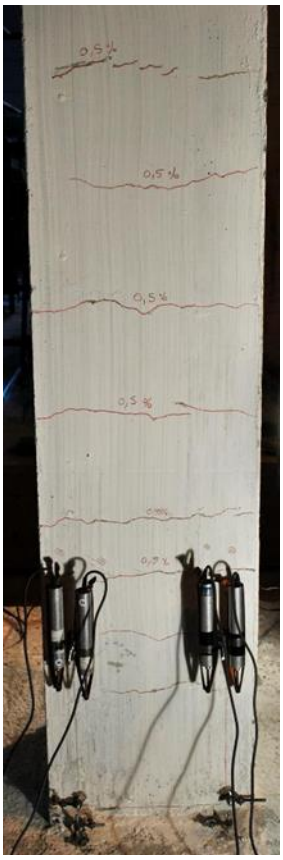

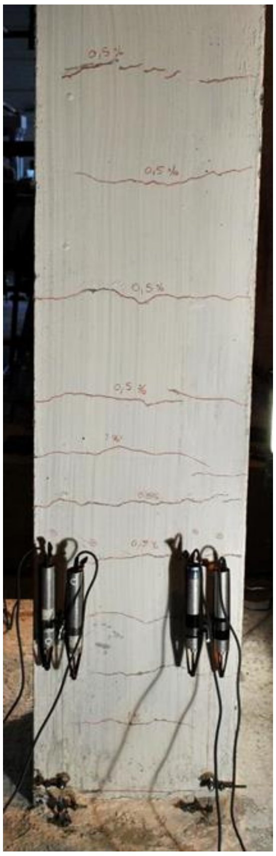

0.5 % (DR) 1.0 % (DR) 1.5 % (DR) 2.5 % (DR)

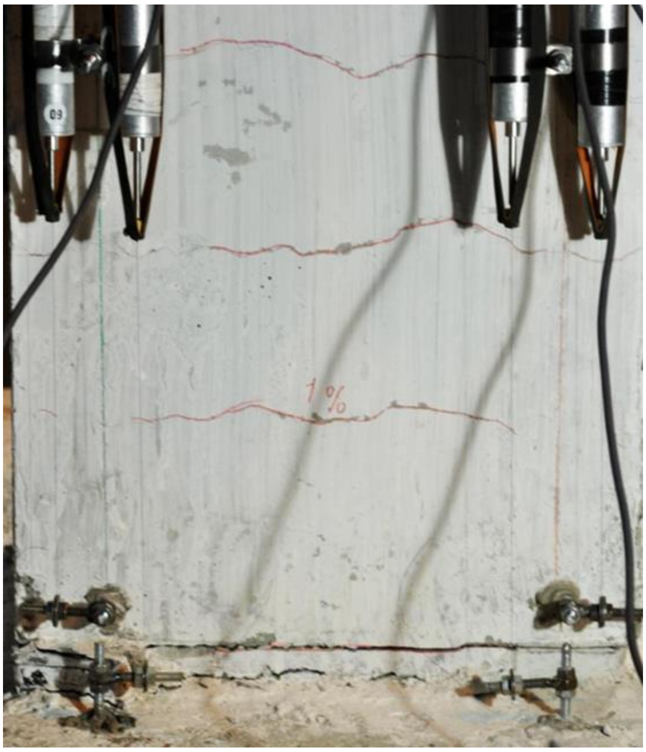

2.0 % (DR) 2.5 % (DR).

Figure 99 *Pictures of damages at different drift ratios (DR) for specimen #5* ***[4]***.

3.0 % (DR).

4.0 % (DR)

4.0 % (DR).

4.0 % (DR).

Figure 100 Pictures of damages at different drift ratios (DR) for specimen #5 [4].

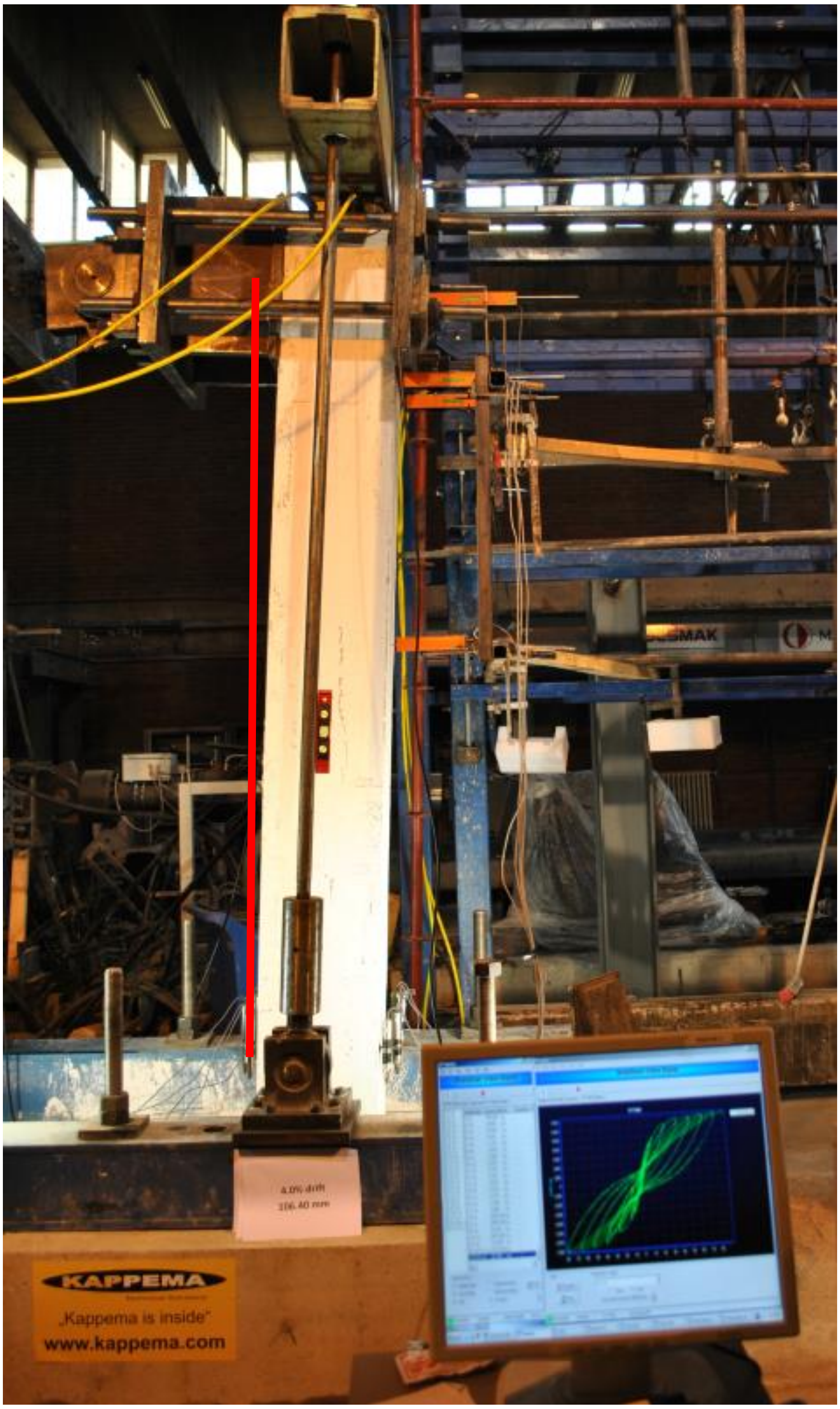

Figure 101 *Picture with final (4.0%) DR and specimen #5.*

2.8 Specimen # 6

2.8.1 Perform Construction

The seismic performance of the connections are extremely important for the overall performance of the double wall system. The sixth specimen was a filigree slab-double wall connection test. The objective of the test was to observe the deformation capacity of the connection.

Specimen #6, the filigree slab-double wall specimen, was constructed by first casting the first storey wall and the slab with a monolithic connection. The shells of the wall and filigree was produced in a similar manner as described above. Reinforcement for the target moment capacity was place at the connection region.

Concrete for the second storey double wall was cast afterwards.

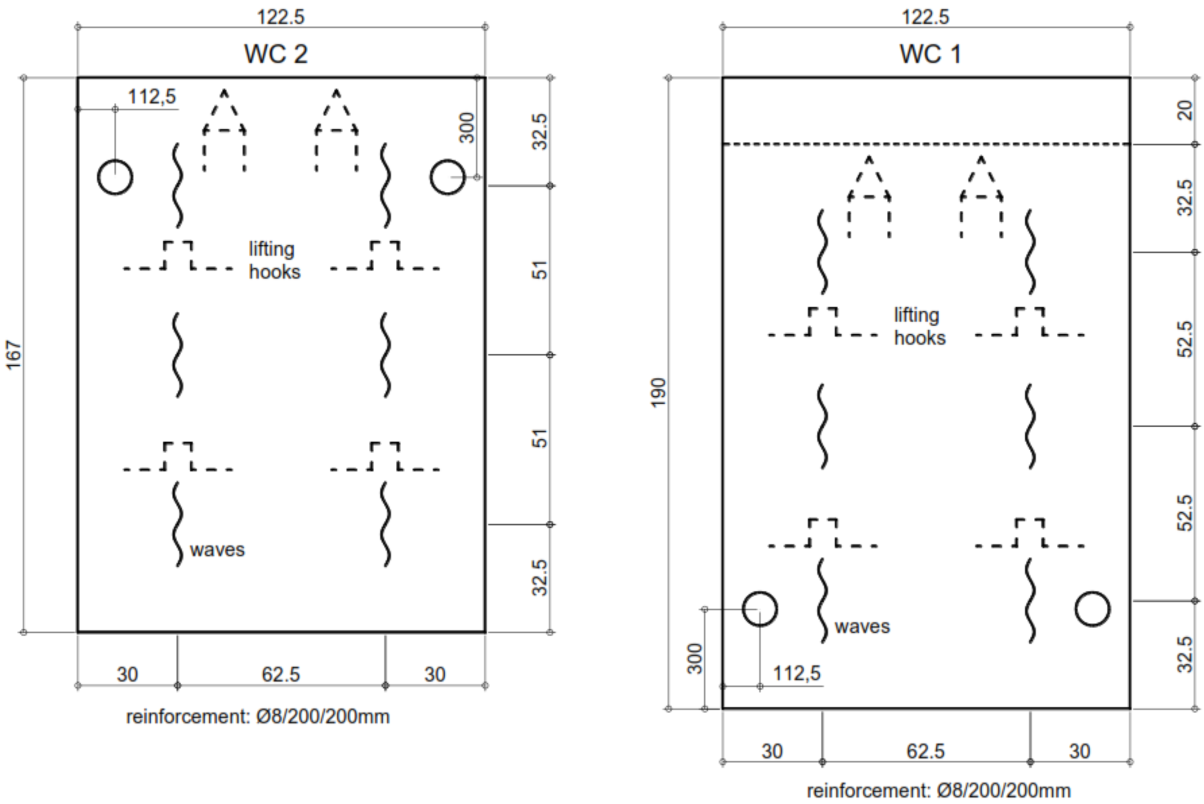

Figure 102 *Detail of the filigree slab-double-wall connection specimen #6 I.*

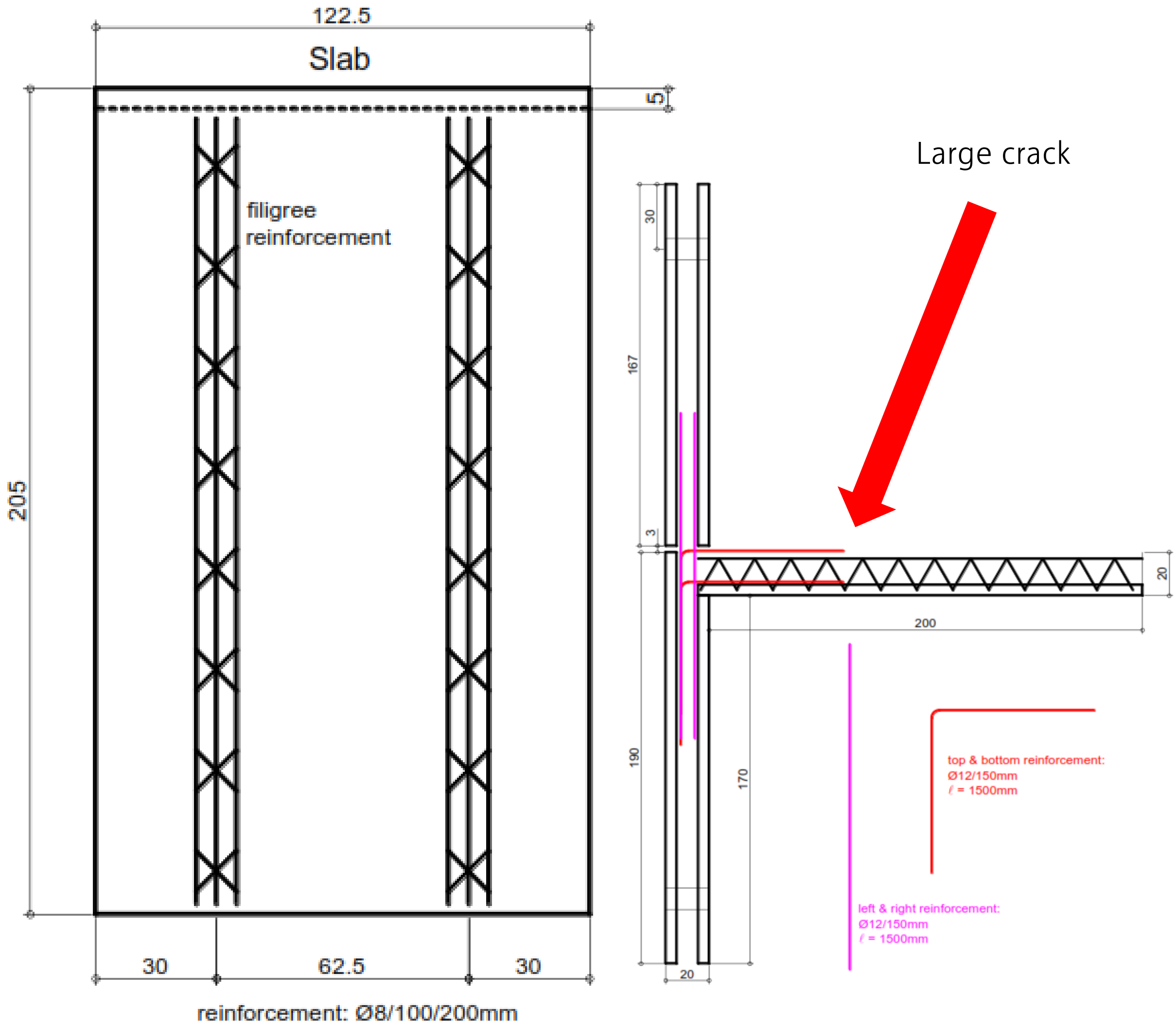

Figure 103 *Details of the filigree slab-double-wall connection specimen #6 II.*

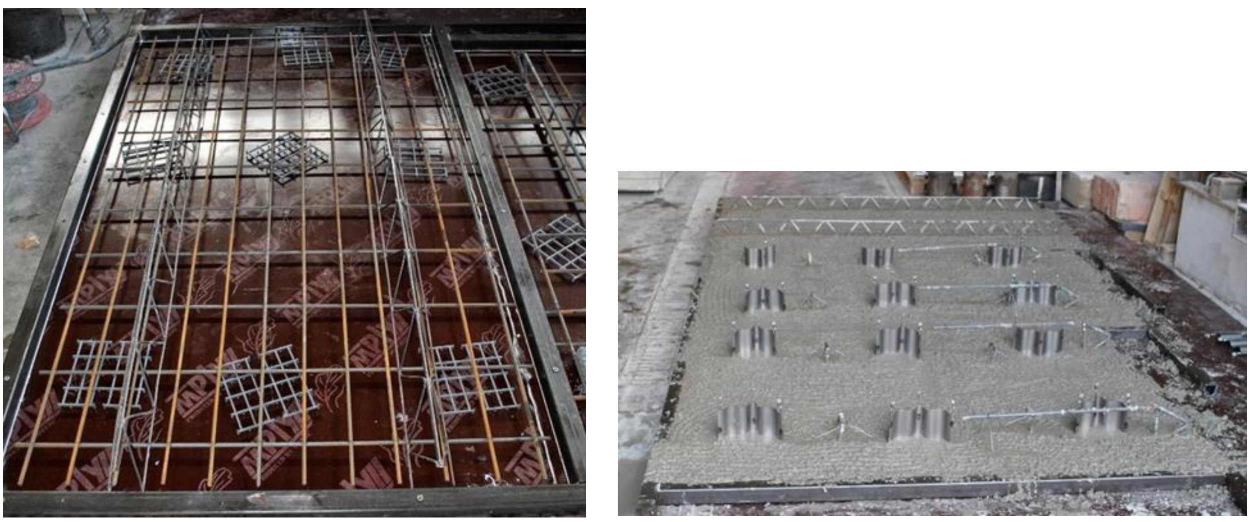

Figure 104 *Preparation of specimen #6 I [7].*

Figure 105 *Preparation of Specimen #6 II [7].*

2.8.2 Loading

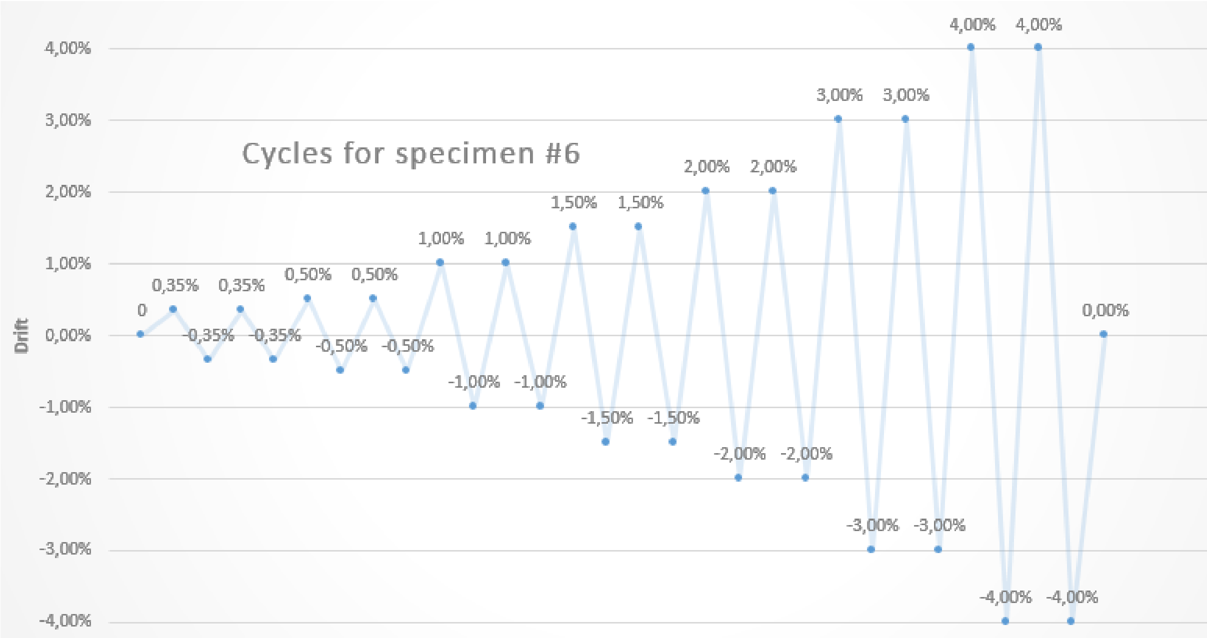

Specimen-#6		Numbers	cyclus	way	analytic: full steps/cyclus
					step: 0,10 mm
H = 1,97 m					
		first crack	0,30%	5,91 mm	59,10
			0,35%	6,90 mm	68,95
			0,50%	9,85 mm	98,50
			1,00%	19,70 mm	197,00
			1,50%	29,55 mm	295,50
			2,00%	39,40 mm	394,00
			3,00%	59,10 mm	591,00
			4,00%	78,80 mm	788,00

Figure 106 Cyclic loading numeric numbers for specimen #6.

2.8.3 Instrumentation and Setup

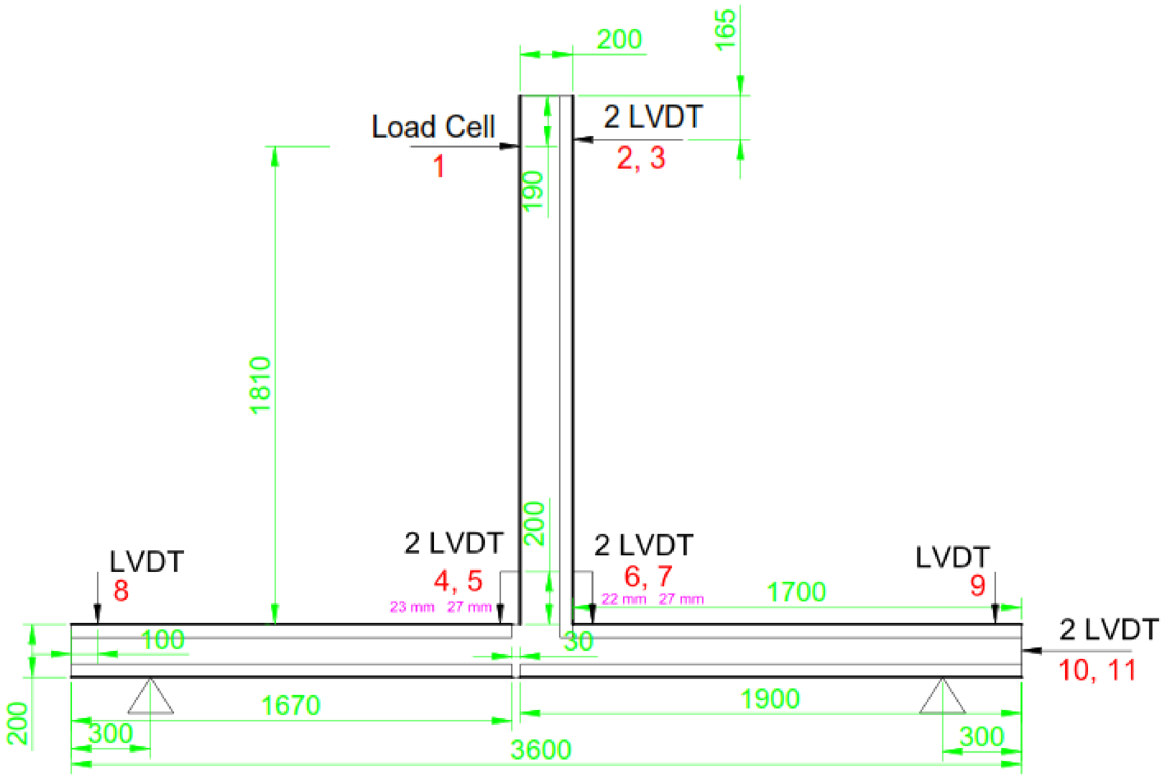

Figure 107 Instrumentation of specimen #6 [4].

Figure 108 Test setup for specimen #6.

2.8.4 Displacement and Strain Measurement and Damage Pictures

The lateral load deformation response of specimen #6 is presented in ***Figure 110***. Measured moment-curvature response measured at the wall base (gauges shown in **Figure 107** were used) is presented in **Figure 111**. The damage pictures of the specimen are presented in **Figure 112** to **Figure 114**.

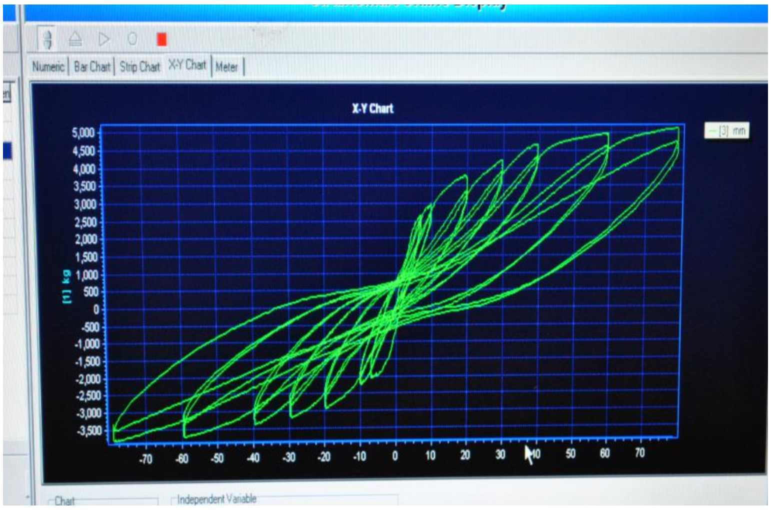

Figure 109 *Lateral load deformation (no corrections) during test of specimen #6.*

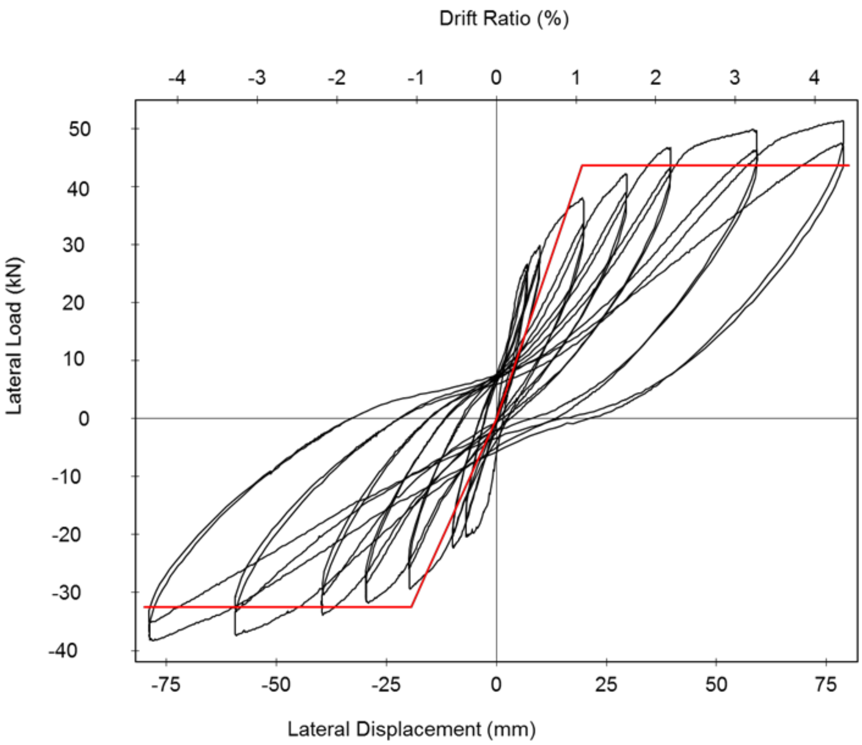

Figure 110 *Lateral load deflection response of specimen #6* ***[4]***.

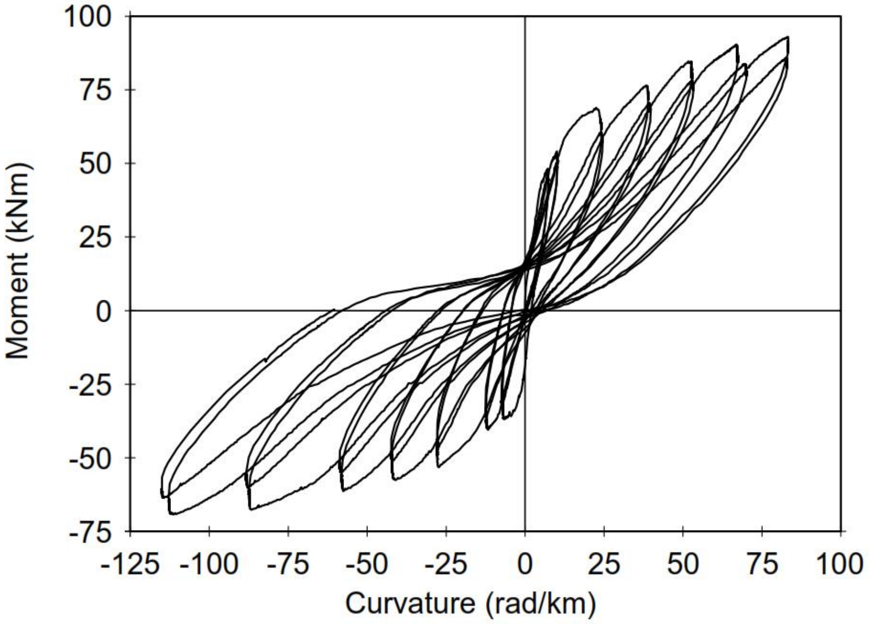

Figure 111 Moment curvature response of specimen #6 [4].

Specimen #6 cracked at about 15 cm spread from the wall base up to about 1 m from the base. The width of the cracks enlarged as the lateral deformation demands increased.

The slab-wall connection exhibited a very ductile response with a hardening response. Beyond about 0.5% drift ratio, plastic deformations took place, which were reflected as extensive crack openings in the slab-wall joint region. The major damage observed during the testing of this specimen was the inclined cracking of the wall-slab connection (Figure 114).

Despite significant cracking, no strength degradation was observed either in the positive or negative direction of loading. The displacement ductility deduced from the idealized elastic perfectly plastic response curve shown in *Figure 110* was 4.1. However due to the fact that no strength degradation was observed, a higher ductility capacity is available for the specimen. The results of this test showed that the slab-column connection was able to sustain cyclically induced deformation demands without any sudden loss of strength or instability in the slab-wall connection region.

0.35 % (DR)

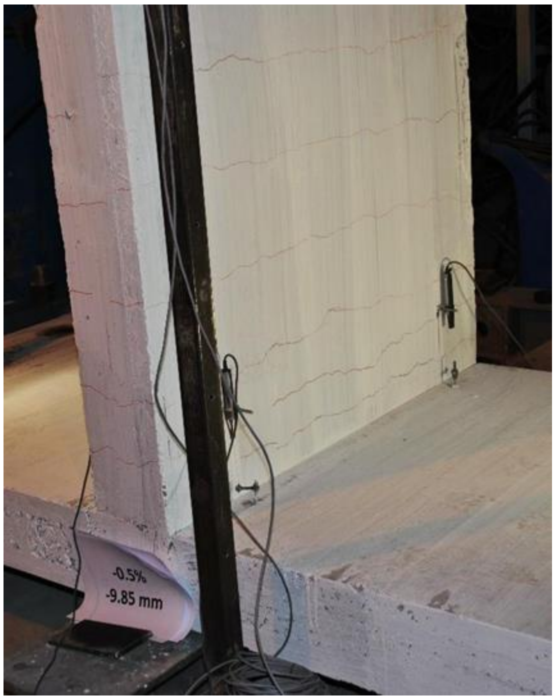

-0.5 % (DR).

1.5 % (DR)

-2.0 % (DR).

Figure 112 Pictures of damages at different drift ratios (DR) for specimen #6 I.

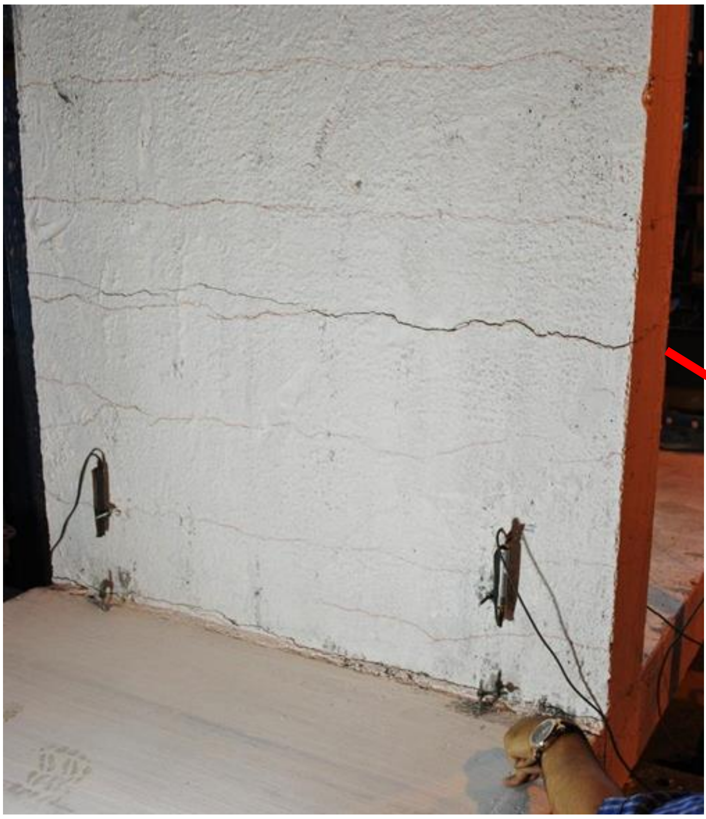

3.0 %)DR)

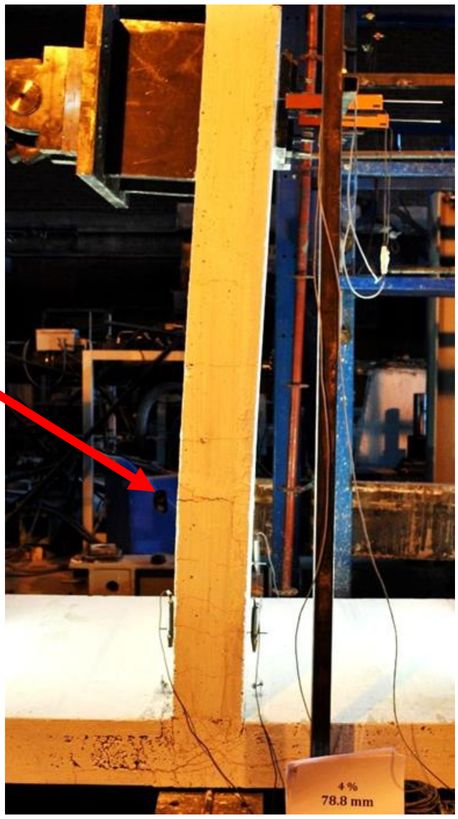

4.0 % (DR).

4.0 % (DR)

Figure 113 Pictures of damages at different drift ratios (DR) for specimen # 6 II.

Figure 114 Pictures of damage at 4,0 % drift ratio (DR) for specimen #6.

3 Test Results

3.1 Specimen #1 versus Specimen #2

The objective of testing specimens #1 and #2 was to observe the difference of behavior when the same wall length is constructed monolithically and with an interface between shells.

The comparisons of the load-deformation responses of specimens #1 and #2 are shown in **Figure 115**, where it can be observed that the two measured curves perfectly follow each other. This proves that casting monolithic central region and providing reinforcement cages connecting the two shells (as in Specimen #2) ensures monolithic response of the doubles built with adjacent panels.

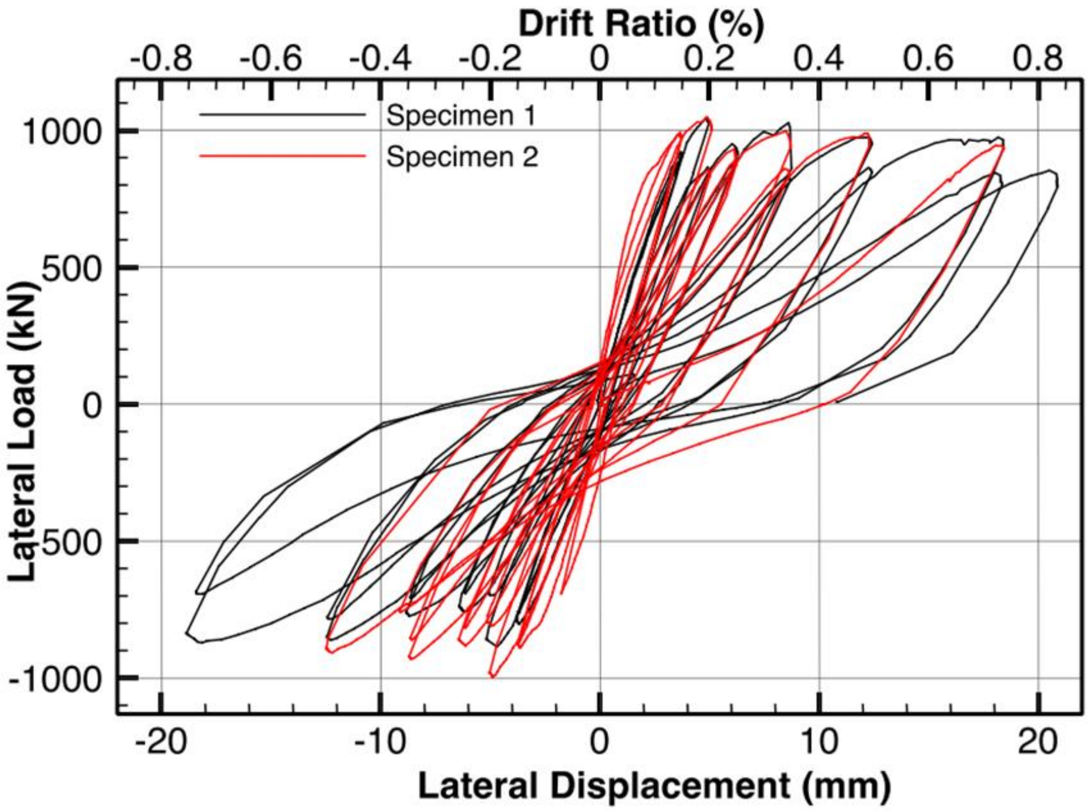

Figure 115 Comparison of load-deformation responses of specimen #1 and #2 [4].

3.2 Specimen #3 and #4

The average displacement ductility value observed in specimen #3 was 5 whereas this value was 4 for specimen #4. This result reveals that the specimen with the U-section behaved in a more ductile manner compared to the T section. The difference between the deformation capacities of the two specimens can be attributed to the presence of two webs in the U-section specimen (T-section had only one web). In the positive direction of loading, which put the flange under tension, the behavior was very similar with up to 0.6 % drift ratio for both specimens. Beyond this deformation level, specimen with the T-section experienced strength degradation, whereas specimen with the U-section experienced hardening. The reason for this difference is again the presence of a higher compression zone in the U-section delaying the concrete crushing. Furthermore, the two webs connected to the flange helped in achieving a more stable load carrying capacity. In short, the superior performance of the specimen was expected and had no relation to the use of the double wall system.

- The behavior of specimen #3 with the U section was very ductile and it did not experience any strength drop up to 1.25% drift ratio. The ductility of this specimen was as high as 7.5. This result shows that U section double walls can exhibit good seismic performance when detailed according to seismic design principles.
- The behavior of specimen #4 with the T section was ductile and it was able to sustain its lateral load carrying capacity up to 0.8% drift ratio. The ductility of this specimen was about 4. This result shows that T section double walls can exhibit acceptable ductility levels when detailed according to seismic design principles.
- The response of specimen #3 was better compared to specimen #4 due to the presence of two web sections. This fact was reflected both in the load-carrying capacity and ductility.
- The precast double wall column behaved in a very ductile manner. The significant damage zone was limited with the bottom 50 mm, which was left as a gap under the concrete shells (cast in place concrete filled this gap). This specimen was able to reach up to 3% drift ratio without losing its lateral strength.
- Comparisons with previous test results revealed that the behavior of precast column was as good as a similar column prepared with cast in place concrete.
- Moment curvature results for the test specimens show that the strength and section response of the double walls can be conducted with standard section analysis procedures of reinforced concrete. This fact enables the use of existing analysis tools for structural design when double wall systems are employed.
- The test results show that double wall precast vertical load bearing members can be designed as ductile elements. They can be used safely for earthquake-

resistant design of buildings upon correct design and detailing. As the double walls can be designed with any desired reinforcement detailing, one can easily follow the rules of earthquake codes during their production.

- The displacement ductility levels of all the tested walls ranged between about 4 and 7.5. It should be recognized that tested walls were squatter than that would be constructed in multi-storey buildings. One easily realizes that the seismic behavior of building walls will even be more ductile than those observed in the tests. It is known that the overstrength factor assumed by the Turkish Earthquake Code is 1.5.

3.3 Specimen #5 Column Direct Comparison with Other Test

In order to evaluate the seismic performance of the precast double wall column specimen, the response of this column is compared to the performance of a similar cast-in-place column tested at Middle East Technical University. The details of the column and the test setup are shown in ***Figure 116***. The column tested by Acun [38] in 2010 had a compressive strength of 25MPa and was subjected to an axial load ratio of 20% of f_c A_g similar to specimen #5. The results of load-deformation response for the test of Acun [38] and specimen #5 are shown in ***Figure 116***. It can be observed that the two results are very similar to each other in terms of deformation capacity. Although the column tested by Acun (2010) had a slightly higher lateral force carrying capacity, the shape of the hysteretic curves, the strength degradation rate and displacement ductility of the two columns are similar. Both specimens were able to sustain drift demands of up to 3% without losing significant lateral strength. The damage picture of the column tested by Acun (2010) shown in ***Figure 117*** shows that the visible damage in the plastic hinge zone is much more severe for the cast in place concrete column compared to the precast double wall column. These results clearly show that the behavior of the precast double wall columns are as good as, if not better, than those built with cast-in-place concrete.

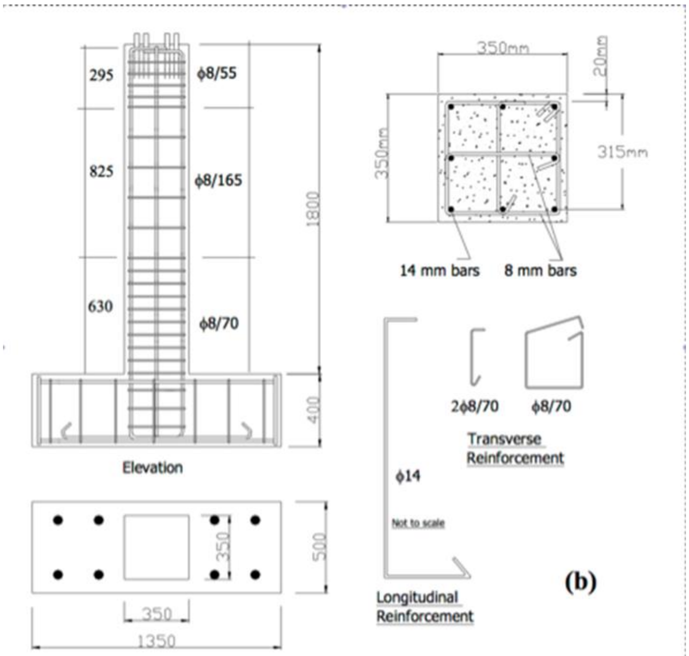

Figure 116 Test column by Acun (2010) I [38].

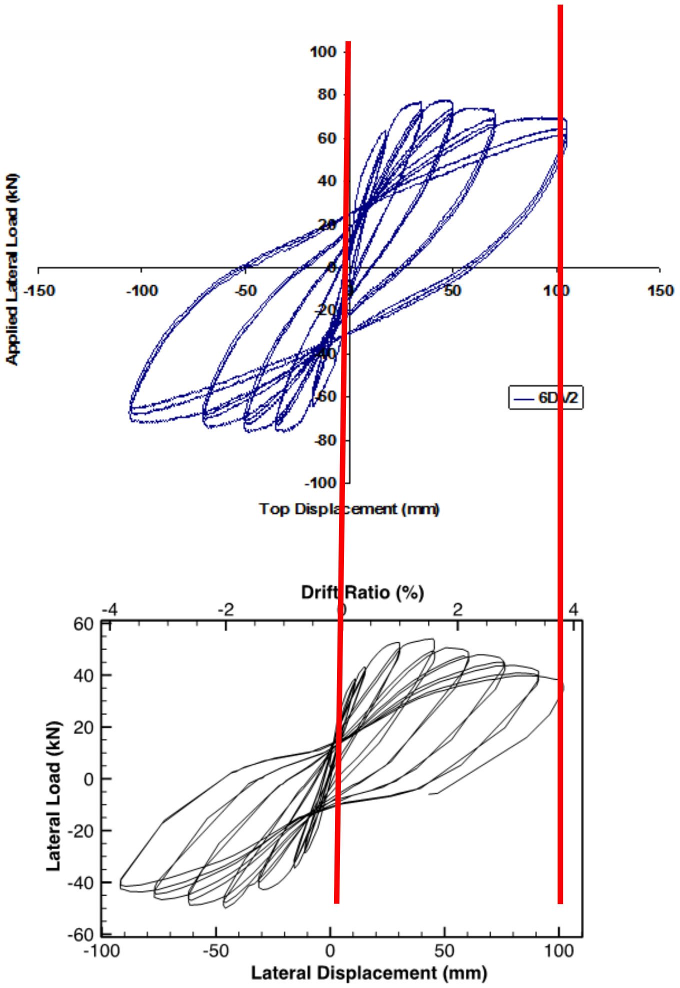

Figure 117 Response diagram Acun- specimen #5.

3.4 Specimen #6

Specimen #6 experienced flexural cracking starting from about 0.3% drift ratio. Cracks spaced at about 15 cm spread from the wall base up to about 1 m from the base. The width of the cracks got larger as the lateral deformation demands increased. The slab-wall connection exhibited a very ductile response with a hardening response. Beyond about 0.5% drift ratio, plastic deformations took place, which were reflected as extensive crack opening in the slab-wall joint region. The major damage observed during the testing of this specimen was the inclined cracking of the wall-slab connection (***Figure 114***). Despite significant cracking, no strength degradation was observed either in the positive or negative direction of loading. The displacement ductility deduced from the idealized elastic perfectly plastic response curve shown in ***Figure 111*** was 4.1. However, due to the fact that no strength degradation was observed a higher ductility capacity is available for the specimen. The results of this test showed that the slab-column connection is able to sustain cyclically-induced deformation demands without any sudden loss of strength or instability in the slab-wall connection region.

Through a clever arrangement of reinforcement (different lengths of the connecting reinforcement), the arising singe large cracks can be split.

3.5 Further Test Observations

The average displacement ductility value observed in specimen #3 was 5, whereas this value was 4 for specimen #4. This result reveals that the specimen with the U-section behaved in a more ductile manner compared to the T section. The difference between the deformation capacities of the two specimens can be attributed to the presence of two webs in the U-section specimen (T-section had only one web). In the positive direction of loading, which put the flange under tension, the behavior was very similar with up to 0.6 % drift ratio for both specimens. Beyond this deformation level, specimen with the T-section experienced strength degradation, whereas specimen with the U-section experienced hardening. The reason for this difference is again the presence of a higher compression zone in the U-section delaying the concrete crushing. Furthermore the two webs connected to the flange helped in achieving a more stable load-carrying capacity. In short, the superior performance of the specimen was expected and had no relation to the use of the double wall system.

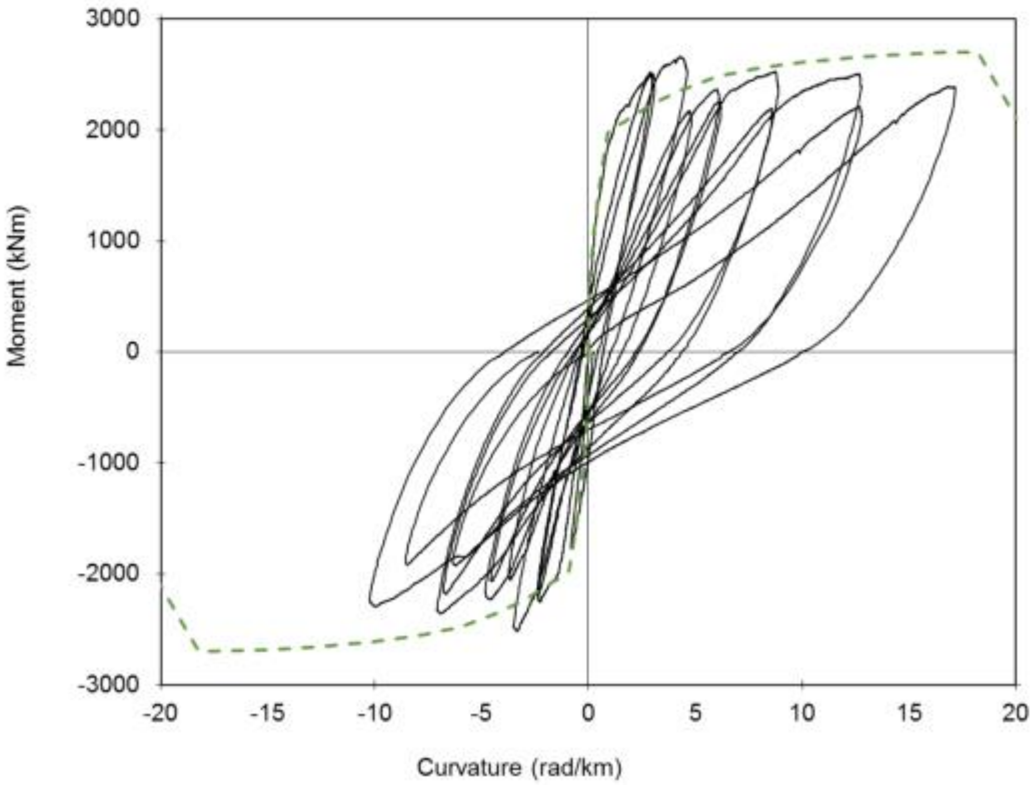

Figure 118 Computed (with Response-2000, [123] green dashed line) vs. measured moment -curvature response for Specimen #2 [4].

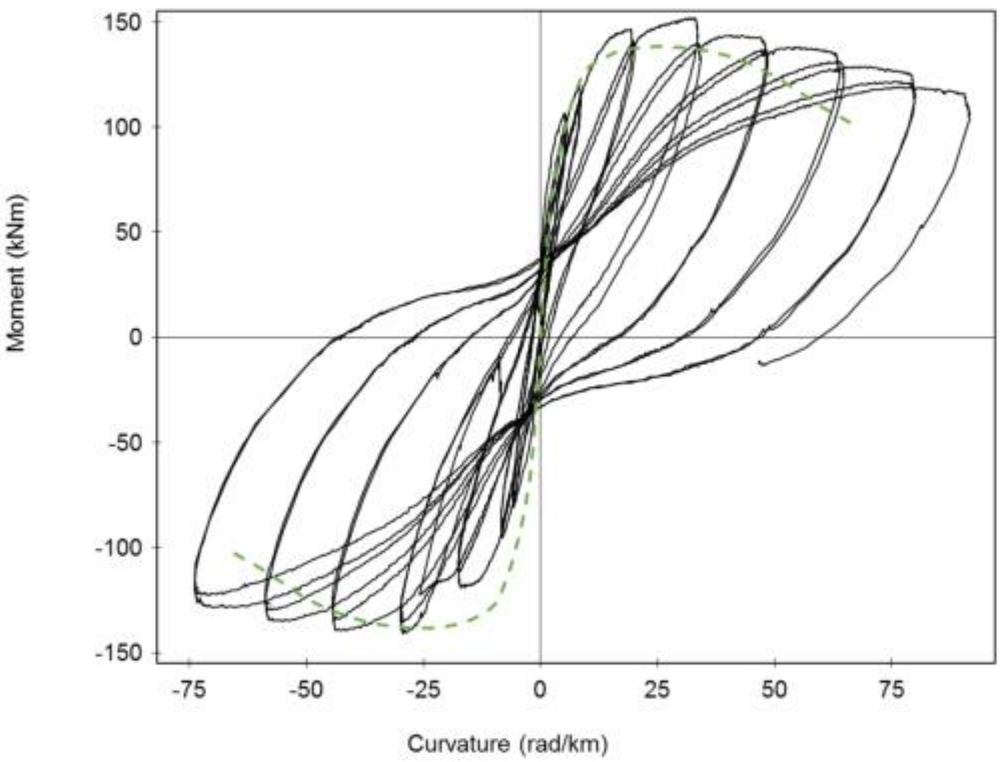

Figure 119 Computed (Response 2000- [39] green dashed line) vs. measured moment-curvature response for Spec.#5 [4].

The moment-curvature responses of all test specimens were computed during the preparation of the test setup in order to estimate the lateral strength. The computed moment curvature response [39], [40], [41] versus measured moment curvature response for Specimen #2 (i.e. specimen with the highest lateral load carrying capacity) and Specimen #5 (column specimen) are presented in *Figure 118* and *Figure 119* as examples. Standard section analysis procedures were used along with parabolic stress-strain model for concrete and elasto-plastic hardening model for steel reinforcement. It can be observed that the lateral strength and ultimate curvature estimations are in reasonable agreement with the measured quantities. Further refinement can be made by using more detailed stress-strain models for confined concrete. Similar results were also found for the other specimens. Such estimations enable us to comfortably say that standard reinforced concrete section calculations can be performed to compute the capacity of structural elements built with double walls for design and performance estimation objectives. More detailed numeric calculations will be discussed in Chapter 5.

4 Analytic Program

4.1 Analytic Model

The program system ATENA [8] offers a variety of material models for different materials and purposes. For the purposes required here, the reinforcement multilinear uniaxial model with cycling was selected. In some cases the use of isotropic elastic material law is used for the 10cm insolation within specimen #1 and specimen #2.

ATENA uses updated Lagrangian formulation, and supports the 3rd level of non-linear behavior (i.e. the highest). In this case we are interested in the behavior of infinitesimal particles of volume dV. Their volume will vary dependent on the loading level applied and, consequently, on the amount of current deformations. This method is usually used to calculate civil engineering structures.

4.1.1 Material Model Concrete General Introduction

Choosing a model for concrete from within the possibilities of the ATENA program led to the selection of the three-dimensional "Fracture-plastic-model" as a constitutive material model for concrete.

This model combines plasticity with fracture.

Fracture-plastic model combines constitutive models for tensile (fracturing) and compressive (plastic) behavior. The fracture model is based on the classical orthotropic smeared crack formulation and crack band model. It employs Rankine failure criterion, exponential softening, and it can be used as a rotated or fixed crack model. The hardening/softening plasticity model is based on Menétrey-Willam failure surface. The model uses a return mapping algorithm for the integration of constitutive equations. Special attention is given to the development of an algorithm for the combination of the two models. The combined algorithm is based on a recursive substitution, and it allows for the two models to be developed and formulated separately. The algorithm can handle cases when failure surfaces of both models are active, but also when physical changes such as crack closure occur. The model can be used to simulate concrete cracking, crushing under high confinement, and crack closure due to crushing in other material directions.

For more detailed description of the model see Cervenka *et al*. (2014) [29]. The fracture is modelled by an orthotropic smeared crack model based on Rankineensile criterion. Hardening-softening plasticity model based on the Menétrey-William three-parameter failure surface is used to model concrete crushing [42]. The model used here differs from the other published formulations in its ability to handle physical changes like crack closure, and it is not restricted to any particular shape of hardening/softening laws. Also within the proposed approach it is possible to formulate entirely separately, and their combination can be provided for in a different algorithm or model. The method of strain decomposition as introduced by de Borst (1986) [29] is used to combine fracture and plasticity models together. Both models are developed within the framework of the return mapping algorithm. This approach guarantees the solution for all magnitudes of strain increment. From an algorithmic point of view the problem is then transformed into finding an optimal return point on the failure surface. The combined algorithm must determine the separation of strains into plastic and fracturing components, while it must preserve the stress equivalence in both models. The algorithm is based on a recursive iterative scheme. It can be shown that such a recursive algorithm cannot reach convergence in certain cases such as, for instance, softening and dilating materials. For this reason the recursive algorithm is extended by a variation of the relaxation method to stabilize convergence.

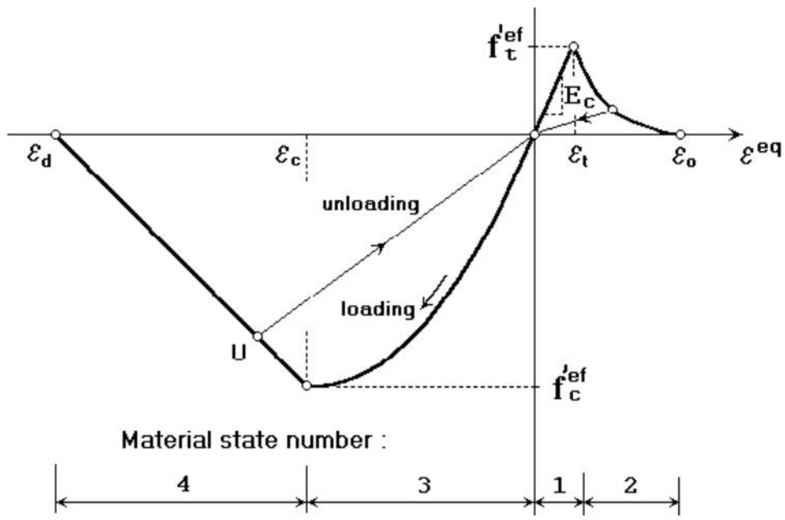

Figure 120 *Uniaxial stress-strain law for concrete (ATENA Theory, [29].)*

Tension before Cracking:

The behavior of concrete in tension without cracks is assumed linear elastic. E_c is the initial elastic modulus of concrete, $f_t^{'ef}$ is the effective tensile strength derived from the biaxial failure function,

$$\sigma_c^{ef} = E_c \varepsilon^{eq}, 0 \leq \sigma_c \leq f_t^{'ef} \qquad (1)$$

Tension after Cracking:

Two types of formulations are used for the crack opening:

- A fictitious crack model based on a crack-opening law and fracture energy. This formulation is suitable for modeling of crack propagation in concrete. It is used in combination with the crack band,

- A stress-strain relation in a material point. This formulation is not suitable for normal cases of crack propagation in concrete and should be used only in some special cases.

In following subsections five softening models are described:

1. Exponential Crack Opening Law

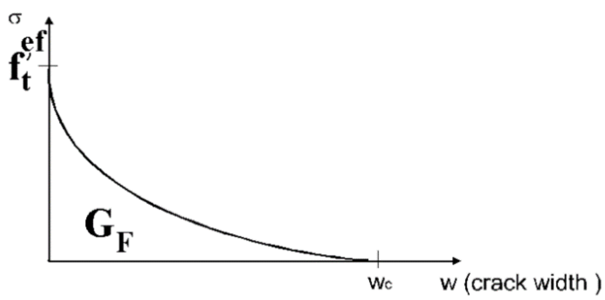

Figure 121 Exponential crack opening law ***[29]***.

This function of crack opening was derived experimentally by Hordij (1991) [**29**].

$$\frac{\sigma}{f_t^{\prime ef}} = \left\{1 + \left(c_1 \frac{w}{w_c}\right)^3\right\} exp\left(-c_2 \frac{w}{w_c}\right) - \frac{w}{w_c}(-c_1^3) exp(-c_2) \qquad (2)$$

$$w_c = 5{,}14 \frac{G_f}{f_t^{\prime ef}} \qquad (3)$$

where w is the crack opening, w_c is the crack opening at the complete release of stress, σ is the normal stress in the crack (crack cohesion). Values of the constants are, c_1 =3, c_2 =6.93. $\boldsymbol{G_f}$ is the fracture energy needed to create a unit area of stress-free crack, $f_t^{\prime ef}$ is the effective tensile strength derived from a failure function, Eq.*(11)*. The crack opening displacement w is derived from strains according to the crack band theory in Eq.*(7)*

2. Linear Crack Opening Law

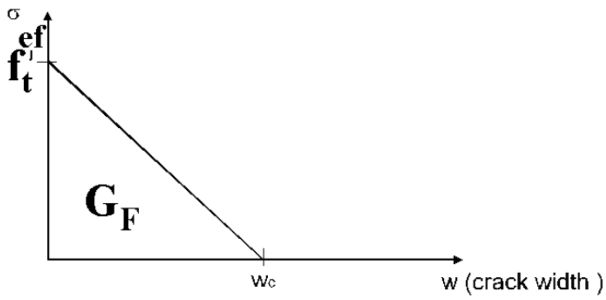

Figure 122 Linear crack opening law [29].

$$\frac{\sigma_c^{ef}}{f_t^{\prime ef}} = \frac{f_t'}{w_c}(w_c - w), w_c = \frac{2G_f}{f_t'} \qquad (4)$$

3. Linear Softening Based on Local Strain

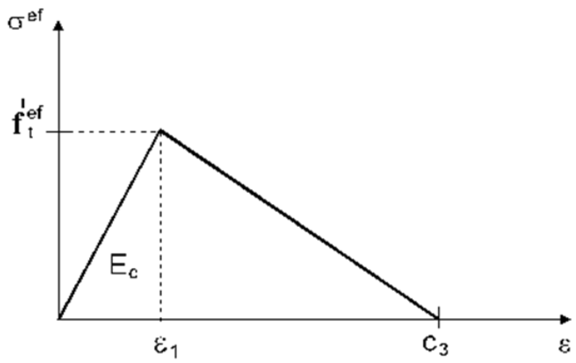

Figure 123 Linear softening based on strain [29].

The descending branch of the stress-strain diagram is defined by the strain c_3 corresponding to zero stress (complete release of stress).

4. SFRC Based on Fracture Energy

(SFRC = Steel Fiber Reinforced Concrete)

Here not used

5. SFRC Based on Strain

(SFRC = Steel Fiber Reinforced Concrete)

Here not used

Compression before Peak Stress:

The formula recommended by CEB-FIP Model Code 90 [43] has been adopted for the ascending branch of the concrete stress-strain law in compression *Figure 124*. This formula enables wide range of curve forms, from linear to curved, and is appropriate for normal as well as high strength concrete.

$$\sigma_c^{ef} = f_c'^{ef} \frac{kx-x^2}{1+(k-2)x}, x = \frac{\varepsilon}{\varepsilon_c}, \text{k}= \frac{E_0}{E_c} \quad (5)$$

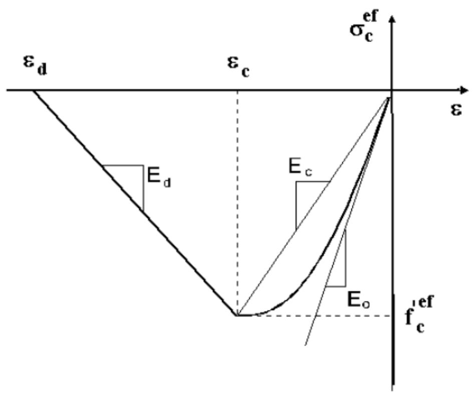

Figure 124 Compressive stress-strain diagram [29].

Key to the symbols in the above formula:

σ_c^{ef} – concrete compressive stress,

$f_c'^{ef}$ - concrete effective compressive strength,

x - normalized strain,

ε - strain,

ε_c - strain at the peak stress $f_c^{\prime ef}$

k - shape parameter,

E_o - initial elastic modulus,

E_c - secant elastic modulus at the peak stress, $E_c = \frac{f_c^{\prime ef}}{\varepsilon_c}$

Parameter k may have any positive value greater than or equal 1.

Examples: k=1. linear, k=2. - parabola.

As a consequence of the above assumption, distributed damage is considered before the peak stress is reached, contrary to the localized damage, which is considered after the peak.

Compression after Peak Stress:

The softening law in compression is linearly descending. There are two models of strain softening in compression, one based on dissipated energy, and other based on local strain softening.

1. Fictitious Compression Plane Model

This compression plane model is based on the assumption that compression failure is localized in a plane normal to the direction of compressive principal stress. All post-peak compressive displacements and energy dissipation are localized in this plane. It is assumed that this displacement is independent of the size of the structure. This hypothesis is supported by experiments conducted by Van Mier (1986).

This assumption is analogous to the Fictitious Crack Theory for tension, where the shape of the crack-opening law and the fracture energy are defined, and considered as material properties.

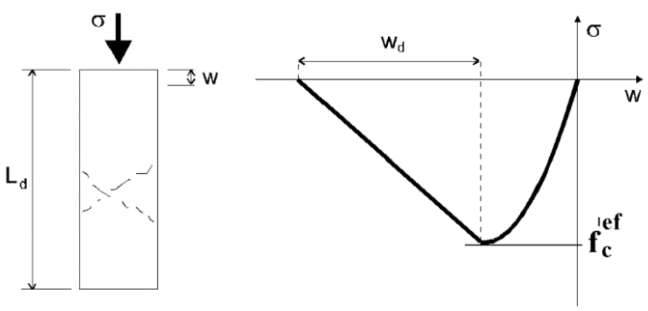

Figure 125 Softening displacement law in compression [29].

In the event of compression, the end point of the softening curve is defined by means of the plastic displacement w_d. In this way, the energy needed for generation of a unit area of the failure plane is indirectly defined. From the experiments of Van MIER (1986), the value of w_d =0.5mm for normal concrete. This value is used as default for the definition of the softening in compression.

The softening law is transformed from a fictitious failure plane, *(**Figure 125**)*, to the stress-strain relation valid for the corresponding volume of continuous material *(**Figure 124**)*. The slope of the softening part of the stress-strain diagram is defined by two points: a peak of the diagram at the maximal stress and a limit compressive strain ε_d at the zero stress. This strain is calculated from a plastic displacement w_d and a band size L'_d according to the following equation:

$$\varepsilon_d = \varepsilon_d + \frac{w_d}{L'_d} \qquad (6)$$

The advantage of this formulation is reduced dependency on finite element mesh.

2. Compression Strain Softening Law Based on Strain.

A slope of the softening law is defined by means of the softening modulus E_d. This formulation is dependent on the size of the finite element mesh.

Localization Limiters

A so-called localization limiter controls localization of deformations in the failure state. It is a region (band) of material, which represents a discrete failure plane in the finite element analysis. In tension it is a crack, in compression it is a plane of crushing. In reality these failure regions have some dimension. However, since according to the experiments, the dimensions of the failure regions are independent of the structural size, they are assumed to be identical planes.

In the case of tensile cracks, this approach is known as the "crack band theory", Bazant, Oh (1983). Here the same concept is also used for the compression failure. The purpose of the failure band is to eliminate two deficiencies which occur in connection with the application of the finite element model: element size effect and element orientation effect.

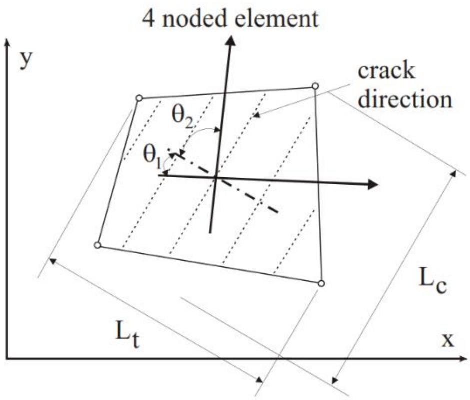

Figure 127 Definition of localization bands [29].

1. Element Size Effect.

The direction of the failure planes is assumed to be normal to the principal stresses in tension and compression, respectively. The failure bands (for tension L_t and for compression L_d) are defined as projections of the finite element dimensions on the failure planes as shown in *Figure 127*.

2. Element Orientation Effect.

The element orientation effect is reduced, through further increasing of the failure band for skew meshes, by the following formula (proposed by Cervenka et al., 1995). An angle θ is the minimal angle (min (θ_1, θ_2)) between the direction of the normal to the failure plane and element sides. In case of a general quadrilateral element the element sides directions are calculated as average side directions for the two opposite edges. The above formula is a linear interpolation between the factor γ =1.0 for the direction parallel with element sides, and $\gamma = \gamma^{max}$, for the direction inclined at 45°. The recommended (and default) value of γ^{max} = 1.5.

Fracture Process, Crack Width

The process of crack formation can be divided into three stages, *Figure 128*. The uncracked stage is before a tensile strength is reached. The crack formation takes place in the process zone of a potential crack with decreasing tensile stress on a crack face due to a bridging effect. Finally, after complete release of the stress, the crack opening continues without the stress.

The crack width w is calculated as a total crack opening displacement within the crack band.

$$w = \epsilon_{er} L'_t \tag{7}$$

where ϵ_{er} is the crack opening strain, which is equal to the strain normal to the crack direction in the cracked state after the complete stress release.

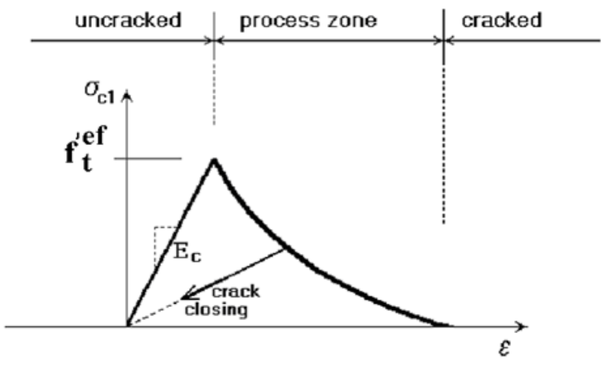

Figure 128 Stages of crack opening [29].

It has been shown, that the smeared model based on the refined crack band theory can successfully describe the discrete crack propagation in plain as well as reinforced concrete (Cervenka et al. 1991, 1992, and 1995 [29]).

It is also possible that the second stress, parallel to the crack direction, exceeds the tensile strength. Then the second crack, in the direction orthogonal to the first one, is formed using the same softening model as the first crack. (Note: The second crack may not be shown in a graphical post-processing. It can be identified by the concrete state number in the second direction at the numerical output.)

Biaxial Stress Failure Criterion of Concrete

Compressive Failure

A biaxial stress failure criterion according to Kupfer et al. (1969) is used as shown in ***Figure 129***. In the compression-compression stress state the failure function is

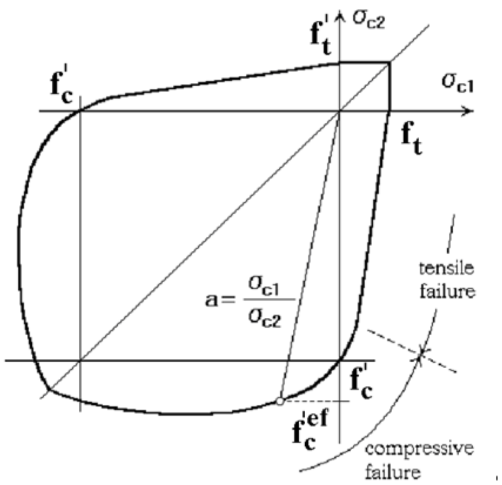

Figure 129 *Biaxial failure function for concrete* ***[29]***.

$$f_c^{\prime ef} = \frac{1 + 3.65a}{(1+a)^2} f_c' \, , a = \frac{\sigma_{c1}}{\sigma_{c2}} \qquad (8)$$

where σ_{c1} , σ_{c2} are the principal stresses in concrete and f'_c is the uniaxial cylinder strength. In the biaxial stress state, the strength of concrete is predicted under the assumption of a proportional stress path.

In the tension-compression state, the failure function continues linearly from the point σ_{c1} =0, σ_{c1} = f'_c into the tension-compression region with the linearly decreasing strength:

$$f_c^{\prime ef}{=}f_c' r_{ec}, \, r_{ec}{=}\left(1 + 5.3278 \frac{\sigma_{c1}}{f_c'}\right), 1.0 \geq r_{ec} \geq 0.9 \qquad (9)$$

where r_{ec} is the reduction factor of the compressive strength in the principal direction 2 due to the tensile stress in the principal direction 1

Tensile Failure

In the tension-tension state, the tensile strength is constant and equal to the uniaxial tensile strength f'_t. In the tension-compression state, the tensile strength is reduced by the relation:

$$f_t'^{ef} = f_t' \, r_{et} \tag{10}$$

where r_{et} is the reduction factor of the compressive strength in the principal direction 2 due to the tensile stress in the principal direction 1 due to the compressive stress in the direction 2. The reduction function has one of the following ***Figure 130 .***

$$r_{et} = 1 - 0.95 \frac{\sigma_{c2}}{f_c'} \tag{11}$$

$$r_{et} = \frac{A + (A-1)B}{AB}, B = Kx + A, x = \frac{\sigma_{c2}}{f_c'} \tag{12}$$

The relation in Eq. *(11)* is the linear decrease of the tensile strength and *(12)* is the hyperbolic decrease

$$f_c'^{ef} = \frac{1 + 3.65a}{(1+a)^2} f_c', a = \frac{\sigma_{c1}}{\sigma_{c2}} \tag{13}$$

Two predefined shapes of the hyperbola are given by the position of an intermediate point r, x. Constants K and A define the shape of the hyperbola. The values of the constants for the two positions of the intermediate point are given in the following table.

Table 3 Points for tension-compression failure function concrete.

type	point		parameters	
	r	x	A	K
a	0,5	0,4	0,7	1,125
b	0,5	0,2	1,0625	6,0208

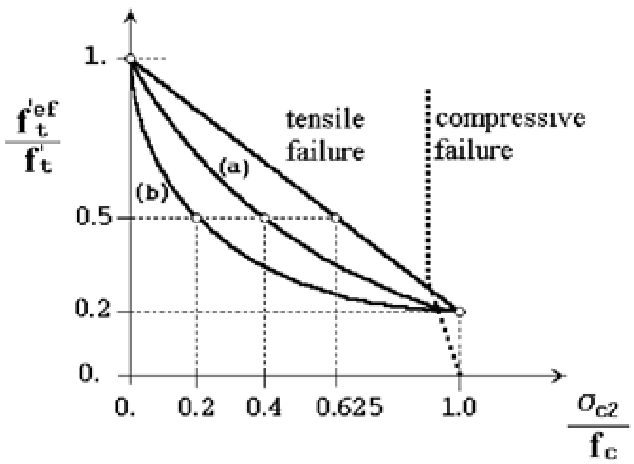

Figure 130 *Tension-compression failure function for concrete* ***[29]***.

Two Models of Smeared Cracks

The smeared crack approach for modeling of the cracks is adopted in the first ATENA model "SBETA". Within the smeared concept two options are available for crack models: the fixed crack model and the rotated crack model. In both models the crack is formed when the principal stress exceeds the tensile strength. It is assumed that the cracks are uniformly distributed within the material volume. This is reflected in the constitutive model by an introduction of orthotropic.

Fixed Crack Model

In the fixed crack model (Cervenka 1985 **[44]**, Darwin 1974 [**45**]) the crack direction is given by the principal stress direction at the moment of the crack initiation. During further loading this direction is fixed and represents the material axis of the orthotropic

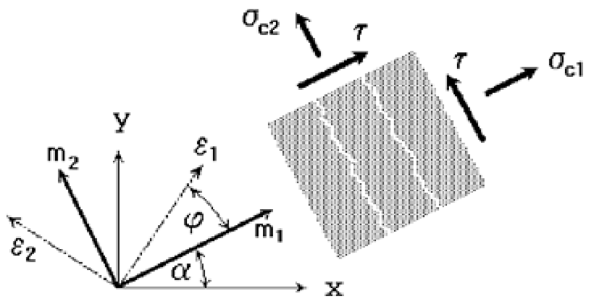

Figure 131 Fixed crack model. Stress and strain state [29].

The principal stress and strain directions coincide in the uncracked concrete, because of the assumption of isotropy in the concrete component. After cracking the orthotropic is introduced. The weak material axis m1 is normal to the crack direction, the strong axis m2 is parallel with the cracks.

In a general case the principal strain axes ε_λ and ε_2 rotate and need not to coincide with the axes of the orthotropic m_1 and m_2. This produces a shear stress on the crack face as shown in ***Figure 131***. The stress components $\propto_{c1}$ and $\propto_{c2}$ denote, respectively, the stresses normal and parallel to the crack plane and, due to shear stress, they are not the principal stresses.

Rotated Crack Model

In the rotated crack model (Veccho1986 [46], Crisfield1989 [47]), the direction of the principal stress coincides with the direction of the principal strain. Thus, no shear strain occurs on the crack plane and only two normal stress components must be defined, as shown in ***Figure 132***

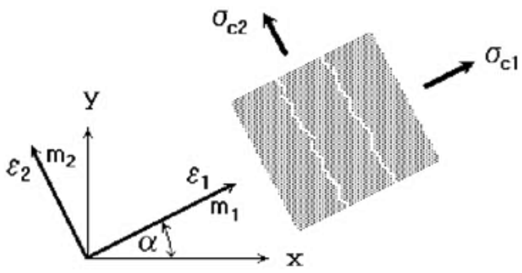

Figure 132 Rotated crack model. Stress and strain state [29].

If the principal strain axes rotate during the loading the direction of the cracks rotate, too. In order to ensure the co-axiality of the principal strain axes with the material axes the tangent shear modulus Gt is calculated according to Criesfield (1989) as

$$G_t = \frac{\sigma_{c1} - \sigma_{c2}}{2(\varepsilon_1 - \varepsilon_2)} \qquad (14)$$

Shear Stress and Stiffness in Cracked Concrete

In the case of the fixed crack model, the shear modulus is reduced according to the law derived by Kolmar (1986) after cracking. The shear modulus is reduced with growing strain normal to the crack (Figure 133) and this represents a reduction of the shear stiffness due to the crack opening

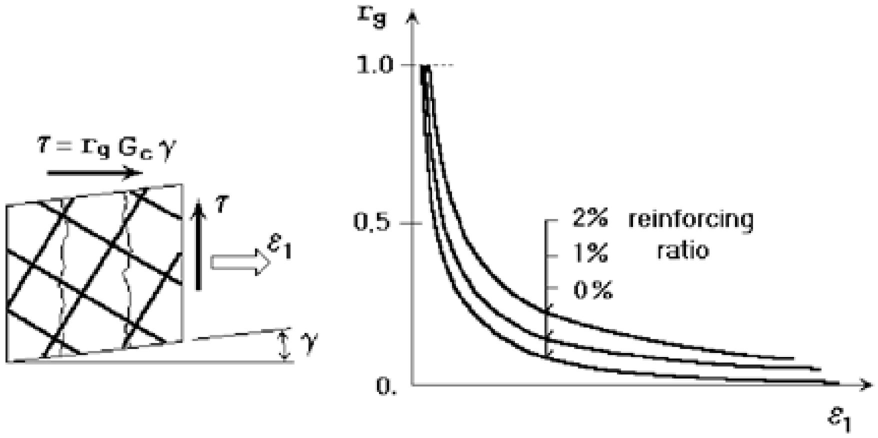

Figure 133 Shear relation factor [29].

$$G = r_g\, G_c, r_g = c_3\, \frac{-ln\{1000\varepsilon_u | c_1\}}{c_2} \qquad (15)$$

$$c_1 = 7 + 333(p - 0{,}005), c_2 = 10 - 167(p - 0{,}005) \qquad (16)$$

$$0 \leq p \leq 0.02 \tag{17}$$

Where r_g is the shear retention factor, G is the reduced shear modulus and G_c is the initial concrete shear modulus

$$G_c = \frac{E_c}{2(1+\nu)} \tag{18}$$

where E_c is the initial elastic modulus and ν is the Poisson's ratio. The strain ε_u is normal to the crack direction (the crack opening strain), c_1 and c_2 are parameters depending on the reinforcing crossing the crack direction, p is the transformed reinforcing ratio (all reinforcement is transformed on the crack plane) and c_3 is the user's scaling factor. By default c3=1. In ATENA the effect of reinforcement ratio is not considered, and p is assumed to be 0.0.

There is an additional constraint imposed on the shear modulus. The shear stress on the crack plane $\tau_{uv} = G\gamma$ is limited by the tensile strength f'_t. The secant and tangent shear moduli of cracked concrete are equal.

Compressive Strength of Cracked Concrete

A reduction of the compressive strength after cracking in the direction parallel to the cracks is done by a similar way as found from experiments of Vecchio and Collins (1982) and formulated in the Compression Field Theory. However, a different function is used for the reduction of concrete strength here, in order to allow for users' adjustment of this effect. This function has the form of the Gauss's function (***Figure 134)***. The parameters of the function were derived from the experimental data published by Kollegger et al. (1988) [**48**], which included also data of Collins and Vecchio (Vecchio *et al.*1982)

For the zero normal strain, ε_u there is no strength reduction, and for the large strains, the strength is asymptotically approaching the minimum value.

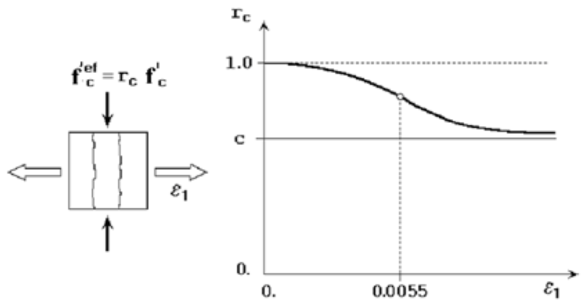

Figure 134 Compressive strength reduction of cracked concrete [29].

The constant c represents the maximal strength reduction under the large transverse strain. From the experiments by Kollegger et al. 1988, the value c= 0.45 was derived for the concrete reinforced with the fine mesh. Other researchers (Dyngeland 1989) found the reductions not less than c=0.8. The value of c can be adjusted by input data according to the actual type of reinforcing.

However, the reduction of compressive strength of the cracked concrete does not have to be affected only by the reinforcing. In the plain concrete, when the strain localizes in one main crack, the compressive concrete struts can cross this crack, causing so-called "bridging effect". The compressive strength reduction of these bridges is also captured by the above model.

Tension Stiffening in Cracked Concrete

The tension stiffening effect can be described as a contribution of cracked concrete to the tensile stiffness of reinforcing bars. This stiffness is provided by the uncracked concrete or not fully opened cracks and is generated by the strain localization process. It was verified by simulation experiments of Hartl (1977) [29] and published in the paper by Margoldova et.al. (1998) [29].

Including an explicit tension stiffening factor would result in an overestimation of this effect. Therefore, in the older ATENA versions (up to1.2.0) no explicit tension stiffening factor is possible in the input. For these analyses ATENA Version has been used.

These are the material parameters for the default formulas:

Table 4 Default Material used for ATENA [28].

Parameter:	*Formula:*
Cylinder strength	$f_c' = -0.85 f_{cu}'$
Tensile strength	$f_t' = 0.24 f_{cu}'^{\frac{2}{3}}$
Initial elastic modulus	$E_c = (6000 - 15.5 f_{cu}')\sqrt{f_{cu}'}$
Poisson's ratio	$\nu = 0.2$
Softening compression	$w_d = -0.0005mm$
Type of tension softening	1 – exponential, based on G_F
Compressive strength in cracked concrete	$c = 0.8$
Tension stiffening stress	$\sigma_{st} = 0.$
Shear retention factor	variable
Tension-compression function type	linear
Fracture energy G_f according to VOS 1983	$G_F = 0.000025 f_t'^{ef}$ *[MN/m]*
Orientation factor for strain localization	$\gamma_{max} = 1.5$ (Sect

4.1.2 Material Advanced Concrete Fracture-Plastic Model used for Analysis

Fracture-plastic model combines constitutive models for tensile (fracturing) and compressive (plastic) behavior. The fracture model is based on the classical orthotropic smeared crack formulation and the crack band model. It employs Rankine failure criterion, exponential softening, and it can be used as rotated or fixed crack model. The hardening/softening plasticity model is based on Menétrey-Willam failure surface. The model uses return mapping algorithm for the integration of constitutive equations. Special attention is given to the development of an algorithm for the combination of the two models. The combined algorithm is based on a recursive substitution, and it allows for the two models to be developed and formulated separately. The algorithm can handle cases when failure surfaces of both models are active, and also when physical changes such as crack closure occur. The model can be used to simulate concrete cracking, crushing under high confinement, and crack closure due to crushing in other material directions.

Material Model Formulation

The material model formulation is based on the strain decomposition into elastic ε_{ij}^{e} , plastic $\varepsilon_{ij}^{p}$and fracturing ε_{ij}^{f}components. (de Borst 1986).

$$\varepsilon_{ij} = \varepsilon_{ij}^{e} + \varepsilon_{ij}^{p} + \varepsilon_{ij}^{f} \qquad (19)$$

The new stress state is then computed by the formula:

$$\sigma_{ij}^{n} = \sigma_{ij}^{n-1} + E_{ijkl}\left(\Delta\varepsilon_{kl} - \Delta\varepsilon_{kl}^{p} - \Delta\varepsilon_{kl}^{f}\right) \qquad (20)$$

where the increments of plastic $\Delta\varepsilon_{kl}^{p}$ and fracturing strain $\Delta\varepsilon_{kl}^{f}$ must be evaluated based om the used material models.

Rankine-Fracturing Model for Concrete Cracking

Rankine criterion is used for concrete cracking

$$F_{i}^{f} = \sigma_{ij}^{\prime t} - f_{ti}^{\prime} \leq 0 \qquad (21)$$

It is assumed that strains and stresses are converted into the material directions, which in the case of the rotated crack model correspond to the principal directions, and in the case of the fixed crack model are given by the principal directions at the onset of cracking. Therefore, $\sigma_{ij}^{\prime t}$ identifies the trial stress and $f_{ti}^{\prime}$ tensile strength in the material direction i. Prime symbol denotes quantities in the material directions. The trial stress state is computed by the elastic predictor.

After some calculating steps a formula for the increment of the fracturing multiplier λ is recovered:

$$\Delta\lambda = \frac{\sigma_{kk}^{\prime t} - f_{tk}^{\prime}}{E_{kkkk}} = \frac{\sigma_{kk}^{\prime t} - f_{t}^{\prime}(w_{k}^{max})}{E_{kkkk}} \text{ and} \qquad (22)$$

$$w_k^{max} = L_t\left(\hat{\varepsilon}_{kk}^{\prime f} + \Delta\lambda\right) \tag{23}$$

This equation must be solved by iterations since for softening materials the value of current tensile strength $f_t'(w_k^{max})$ is a function of the crack opening w, and is based on Hordijk's formula.

The crack opening w is computed from the total value of fracturing strain $\hat{\varepsilon}_{kk}^{\prime f}$ in direction k, plus the current increment of fracturing strain $\Delta\lambda$, and this sum is multiplied by the characteristic length L_t. The characteristic length as a crack band size was introduced by Bazant and Oh [49].

Various methods were proposed for the crack band size calculation in the framework of finite element method. Feenestra (1993) [50] suggested a method based on integration point volume, which is not well suited for distorted elements. In the presented ATENA version the crack band size L_t. is calculated as a size of the element projected into the crack direction,. Cervenka V. et al. (1995) [51] showed that this approach is satisfactory for low order linear elements, which are used throughout this study. They also proposed a modification, which accounts for cracks that are not aligned with element edges.

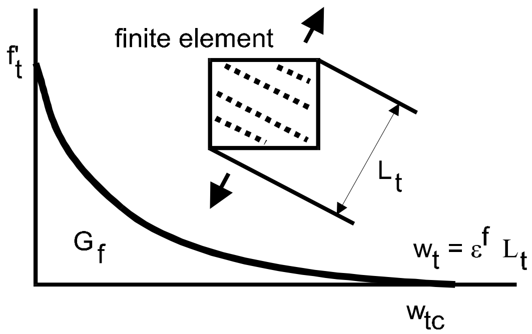

Figure 135 Tensile softening and characteristic length [29].

Shear strength of a cracked concrete is calculated using the Modified Compression Field Theory of Vecchio and Collins (1986) [41], [52].

$$\sigma_{ij} \leq \frac{8{,}18\sqrt{f_c'}}{0{,}31 + \dfrac{24w}{a_g + 16}}\ , i \neq j \tag{24}$$

Where f_c' is the compressive strength in MPa, a_g is the maximum aggregate size in mm, and w is the maximum crack width in mm at the given location. This model is activated by specifying the maximum aggregate size a_g, otherwise the default behavior is used where the shear stress on a crack surface cannot exceed the tensile strength.

Unloading Direction

Crack closure stiffness is controlled by the unloading factor (material parameter) $0 \leq f_U \leq 1$ .The value of 0 corresponds to unloading to origin (default value for backward compatibility),

f_U =1 means unloading direction parallel to the initial elastic stiffness.

Plasticity Model for Concrete Crushing

In the above two formulas the expression $f_c'(\varepsilon_{eq}^p)$ indicates the hardening/softening law, which is based on the uniaxial compressive test. The law is shown in , where the softening curve is linear and the elliptical ascending part is given by the following formula:

$$\sigma = f_{co} + (f_c - f_{co})\sqrt{1 - \left(\frac{\varepsilon_c - \varepsilon_{eq}^p}{\varepsilon_c}\right)^2} \qquad (25)$$

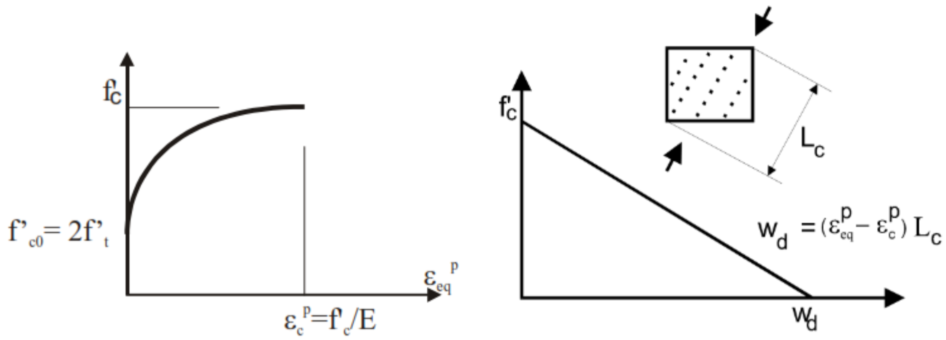

***Figure 136** Compressive hardening/softening and compressive characteristic length. Based on experimental observations by Van Mier **[29]**.*

The return mapping algorithm for the plastic model is based on predictor-corrector approach as is shown in ***Figure 137 .*** During the corrector phase of the algorithm the failure surface moves along the hydrostatic axis to simulate hardening and softening. The final failure surface has the apex located at the origin of the Haigh-Vestergaard coordinate system. Secant method based Algorithm 1 is used to determine the stress on the surface, which satisfies the yield condition and also the hardening/softening law

Algorithm 1: Input is ${}^{(n-1)}\sigma_{ij}, {}^{(n-1)}\varepsilon_{ij}^{p}, \Delta^{(n)}\epsilon_{ij}$

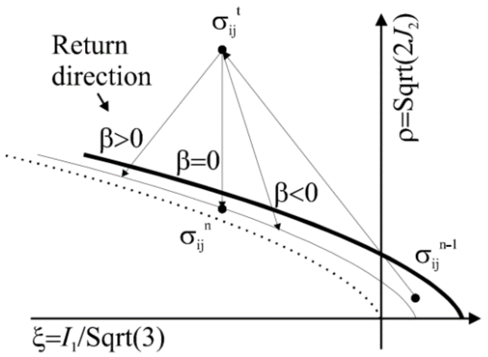

Figure 137 Plastic predictor-corrector algorithm [29].

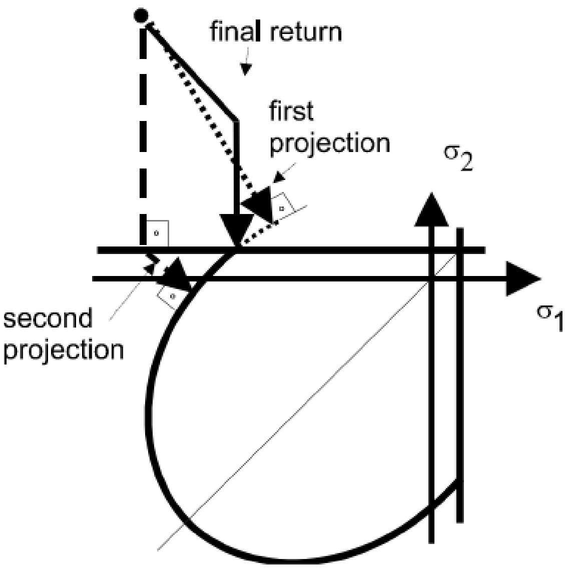

Figure 138 Schematic description of the iterative process. Shown in two dimensions [29].

Combination of Plasticity and Fracture model

The proposed algorithm for the combination of plastic and fracture models is graphically shown in ***Figure 138***. When both surfaces are activated, the behavior is quite similar to the multi-surface plasticity (Simo *et al.* 1988). Contrary to the multi-surface plasticity algorithm the proposed method is more general in the sense that it covers all loading regimes including physical changes such as for instance crack closure. Currently, it is developed only for two interacting models, and its extension to multiple models is not straightforward.

There are additional interactions between the two models that need to be considered in order to properly describe the behavior of a concrete material:

(a) After concrete crushing the tensile strength should decrease as well

(b) According to the research work of Collins (Vecchio and Collins 1986) and coworkers it was also established that the compressive strength should decrease when cracking occurs in the perpendicular direction. This theory is called compression field theory and it is used to explain the shear failure of concrete beams and walls.

The interaction (a) is resolved by adding the equivalent plastic strain to the maximal fracturing strain in the fracture model to automatically increase the tensile damage based on the compressive damage such that the fracturing strains satisfies the following condition:

$$\hat{\varepsilon}_{kk}^{\prime f} \geq \frac{f_t'}{f_c'} \varepsilon_{eq}^{p} \qquad (26)$$

The compressive strength reduction (b) is based on the following formula proposed by Collins:

$$\sigma_c = r_c f_c' \qquad (27)$$

$$r_c = \frac{1}{0{,}8 + 170\varepsilon_1}\ , r_c^{lim} \leq r_c \leq 1{,}0 \qquad (28)$$

Where ε_1 is the tensile strain in the crack. In ATENA the largest maximal fracturing strain is used for ε_1 and the compressive strength reduction is limited by r_c^{lim}. If r_c^{lim} is not specified, then no compression reduction is considered.

Variants of the Fracture Plastic Model

The concrete model *CC3DNonLinCementitious2User* used here includes the following differences:

CC3DCementitious assumes linear response up to the point when the failure envelope is reached both in tension and compression. This means that there is no hardening regime in *Figure 132*. The material CC3DNonLinCementitious on the contrary assumes a hardening regime before the compressive strength is reached.

Suggested Model Parameters

Table 5 *Model parameter used with ATENA.*

f_c (MPa)	20	30	40	50	60	70
E_c (MPa)	24377	27530	30011	32089	33893	35497
N	0.2	0.2	0.2	0.2	0.2	0.2
f_t (MPa)	1.917	2.446	2.906	3.323	3.707	4.066
λ_t	1.043	1.227	1.376	1.505	1.619	1.722
e	0.5281	0.5232	0.5198	0.5172	0.5151	0.5133
f_{co} (MPa)	-4.32	-9.16	-15.62	-23.63	-33.14	-44.11
ε^n	$4.92 \cdot 10^{-4}$	$6.54 \cdot 10^{-4}$	$8.00 \cdot 10^{-4}$	$9.35 \cdot 10^{-4}$	$1.06 \cdot 10^{-3}$	$1.18 \cdot 10^{-3}$
t	$1.33 \cdot 10^{-3}$	$2.00 \cdot 10^{-3}$	$2.67 \cdot 10^{-3}$	$3.33 \cdot 10^{-3}$	$4.00 \cdot 10^{-3}$	$4.67 \cdot 10^{-3}$
A	7.342177	5.436344	4.371435	3.971437	3.674375	3.43856
B	-8.032485	-6.563421	-5.73549	-5.430334	-5.202794	-5.021407
C	-3.726514	-3.25626	-3.055953	-2.903173	-2.797059	-2.719067
n	3	3	3	3	3	3
G_f (MN/m)	$4.87 \cdot 10^{-5}$	$6.47 \cdot 10^{-5}$	$7.92 \cdot 10^{-5}$	$9.26 \cdot 10^{-5}$	$1.05 \cdot 10^{-4}$	$1.17 \cdot 10^{-4}$

4.1.3 Material Model Reinforcement

Reinforcement can be modeled in two distinct forms:

Discrete and smeared.

Discrete reinforcement is in form of reinforcing bars and is modeled by truss elements. The smeared reinforcement is a component of composite material and can be considered either as a single (only one-constituent) material in the element under consideration or as one of the more such constituents. The former case can be a special mesh element (layer), while the later can be an element with concrete containing one or more reinforcements. In both cases the state of uniaxial stress is assumed and the same formulation of stress-strain law is used in all types of reinforcement.

Bilinear Law

The bilinear law, elastic-perfectly plastic, is represented in **Figure 139**.

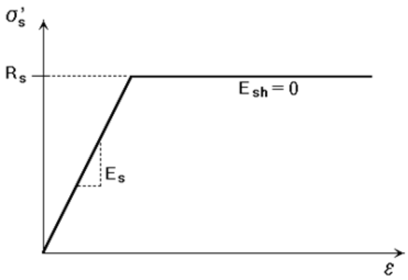

__Figure 139__ The bilinear stress strain law for reinforcement __[29]__.

The initial elastic part has the elastic modulus of steel $\boldsymbol{E_s}$. The second line represents the plasticity of the steel with hardening and its slope is the hardening modulus $\boldsymbol{E_{sh}}$. In case of perfect plasticity $\boldsymbol{E_{sh}}$ =O. Limit strain □L represents limited ductility of steel.

Smeared reinforcement

The spacing s of the smeared reinforcement is assumed infinitely small. The stress in the smeared reinforcement is evaluated in the cracks, therefore it should include also a part of stress due to tension stiffening, which acts in concrete between the cracks

$$\sigma'_{sct} = \sigma'_s + \sigma_{ts} \qquad (29)$$

where $\boldsymbol{\sigma'_s}$ is the steel stress between the cracks (the steel stress in smeared reinforcement), and $\boldsymbol{\sigma'_{sct}}$ is the steel stress in a crack. If no tension stiffening is specified $\boldsymbol{\sigma_{ts}}$=0 and $\boldsymbol{\sigma'_{sct}}$ the discrete reinforcement the steel stress is always $\boldsymbol{\sigma'_s}$

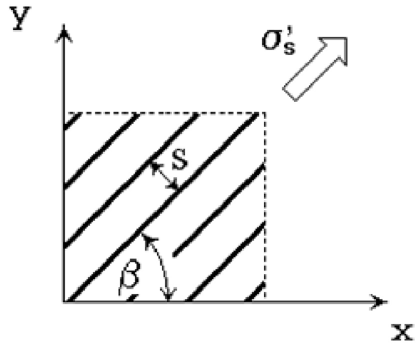

Figure 140 Smeared reinforcement [29].

Cyclic Reinforcement Model

The reinforcing steel stress-strain behavior can be described by the nonlinear model of Mengetto and Pinto (1973) [53] and new Albanesi [54]. In ATENA this model is extended to take account of the isotropic hardening due to an arbitrary hardening law that can be specified for reinforcement.

The stress in the cyclic model is calculated according to the following equation

$$\sigma = (\sigma_0 - \sigma_r)\sigma^* + \sigma_r \tag{30}$$

$$\sigma^* = b\varepsilon^* + \frac{(1-b)\varepsilon^*}{(1+\varepsilon^{*R})^{1/R}}, \varepsilon^* = \frac{\varepsilon - \varepsilon_r}{\epsilon_0 - \epsilon_r}, R = R_0 - \frac{c_1\xi}{c_2 + \xi} \tag{31}$$

Where R_0, c_1 and c_2 are experimentally determined parameters. *Figure 138* shows the meaning of strain values ε_r , ϵ_0 , ξ and stress values σ_r and σ_0 . These values changes for each cycle. The values with the subscript r indicate the point where the cycle started, and the subscript O indicates the theoretical yield point that would be reached during the unloading if the response would not have been modified by the hysteretic behavior. During the calculation of this point the material stress-strain law is considered.

$$\sigma^* = f_R(\varepsilon_{eq}), \epsilon_{eq} = \sum_{i=1}^{N_{inc.}} |\Delta\epsilon_{eq}^i| \tag{32}$$

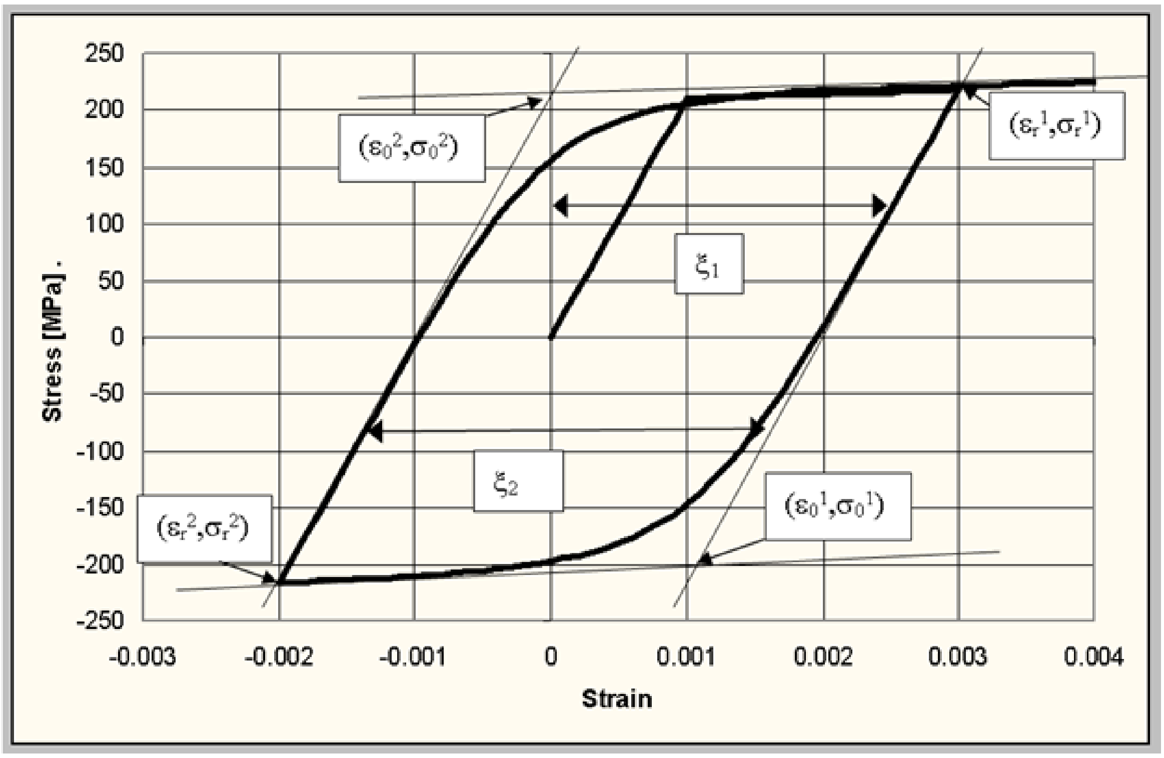

Figure 141 Cyclic reinforcement model based on Mengotto and Pinto (1973) [53].

4.2 ATENA Modeling

4.2.1 ATENA Modeling General

The ATENA geometric models consist of

- Macroelements, where the mesh for the finite elements can be chosen.
- Material Properties
- Loadings (supports are treated as loadings too).
- Nonlinear Solutions

The Macroelements are described in the respective specimen-calculations.
For the Material the following characteristics are used in the numeric simulation.

4.2.2 ATENA Macroelements

ATENA has some possibilities for generating 3D-Models:

- CCIso Tetra-Elements
- CCIso-Bricks and
- CCIso Wedge Elements

For these calculations only the CCIso type was chosen:

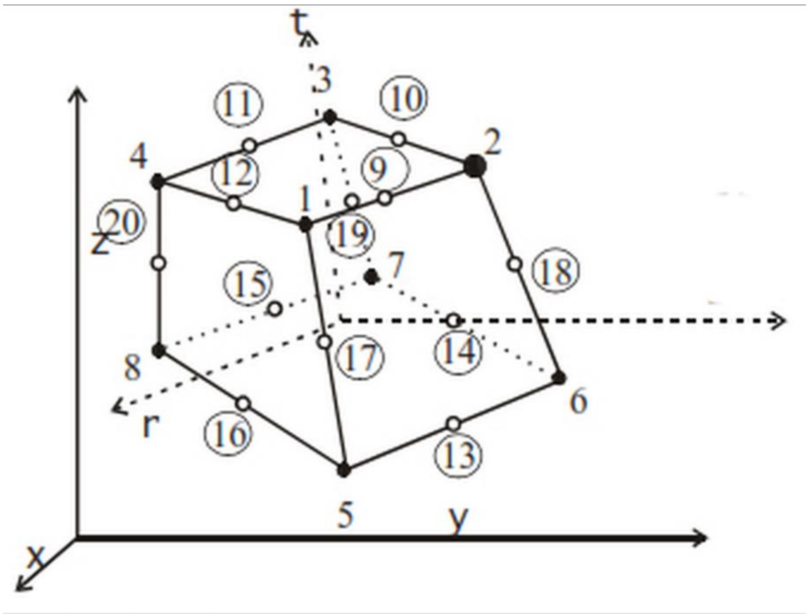

Figure 142 ATENA CCIso Brick 3-D Element [29].

Further information is available in the ATENA Theory [29].

4.2.3 ATENA Material Modeling

<u>Concrete:</u>

Concrete shell and head and footer is **C45** according EC2 [55]

Concrete core with, as tested at METU, fck,zyl = 29.02MPa was these calculated EC-affine Key figures.

Therefore a special configuration of concrete, representing the used concrete quality in the test was composed and called C25+.

Table 6 Concrete figures.

		Wall-core	Wall-shell
	C25	**C25+**	**C45**
$f_{ck,zyl}$	25	28.02	45
$f_{ck,cube}$	30	34.22	55
f_{cm}	33	36.02	53
f_{ctm}	2.6	2.77	3.8
$f_{ctk,0.05}$	1.8	1.94	2.7
$f_{ctk,0.95}$	3.3	3.60	4.9
E_{cm}(MN/1000m²)	31	32.31	36
$-\varepsilon_{cl}$ (o/oo)	2.1	2.13	2.4
$-\varepsilon_{clu}$ (o/oo)	3.5	3.5	3.5
$-\varepsilon_{c2}$ (o/oo)	2.0	2.0	2.0
$-\varepsilon_{c2u}$ (o/oo)	3.5	3.5	3.5
Exponent n	2.0	2.0	2.0
$-\varepsilon_{c3}$ (o/oo)	1.75	1.75	1.75
$-\varepsilon_{c3u}$ (o/oo)	3.5	3.5	3.5

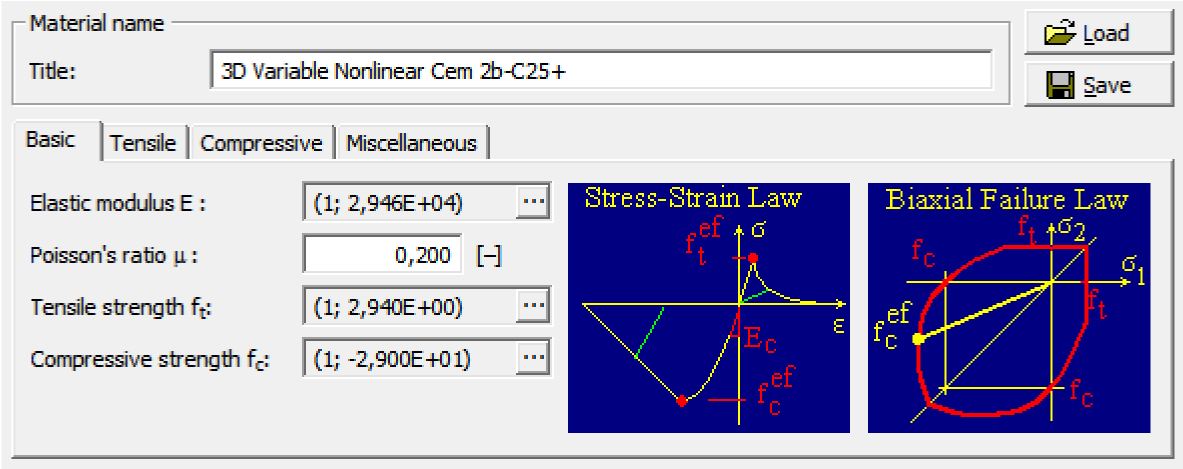

a) C 25+ basic

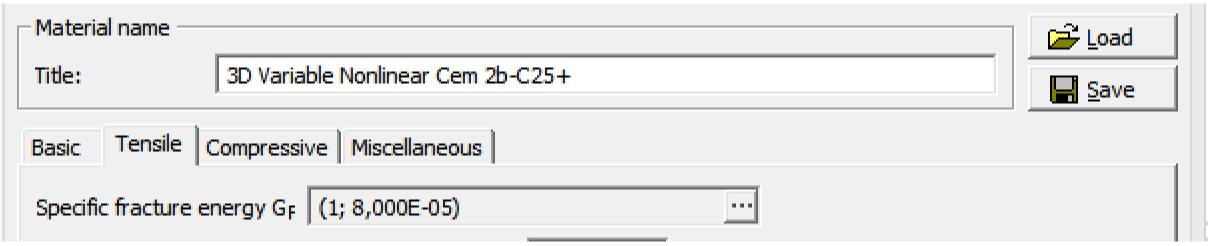

b) C 25+ tensile

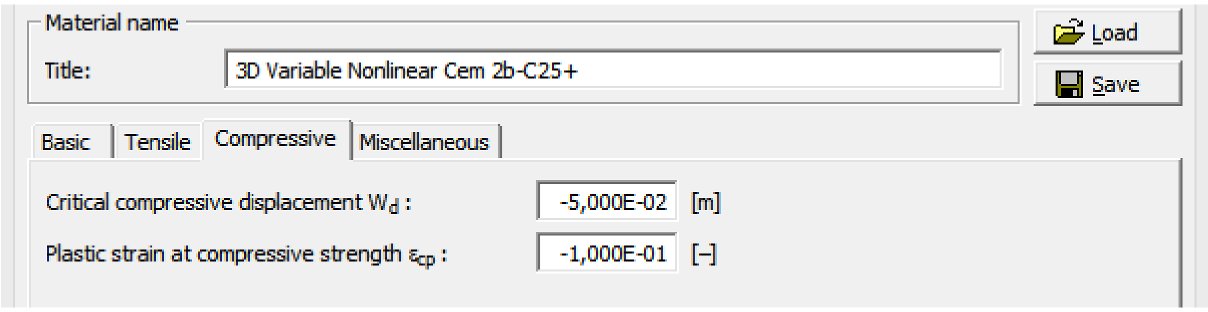

c) C 25+ compressive I

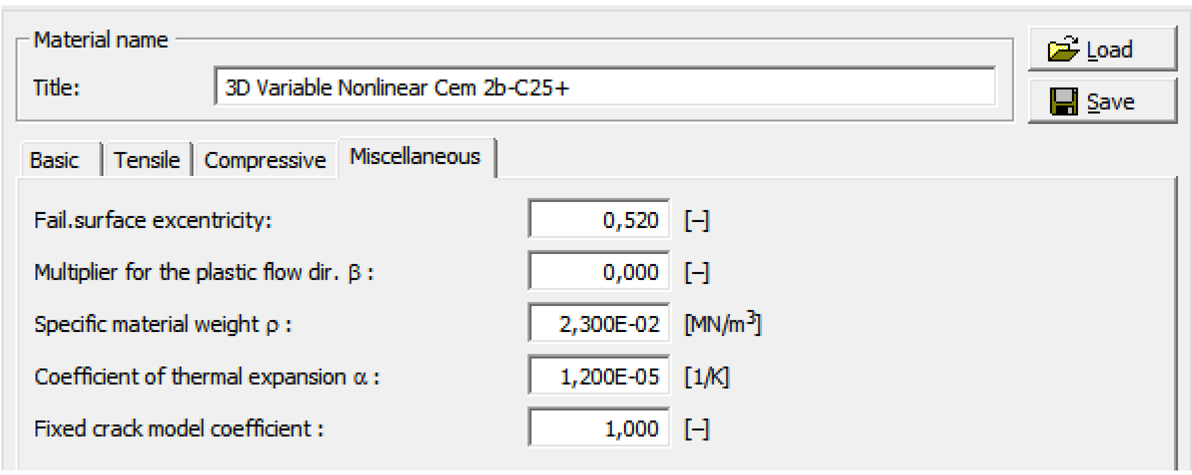

d) C 25+ Miscellaneous

Figure 143 ATENA, Material 3D variable nonlinear C25+.

In recent years there have been many research investigations and proposals in this specific field of concrete fracture mechanics in order to determine the adequate Fracture Energy of concrete. But all of them examine only a small portion of the very complex system.

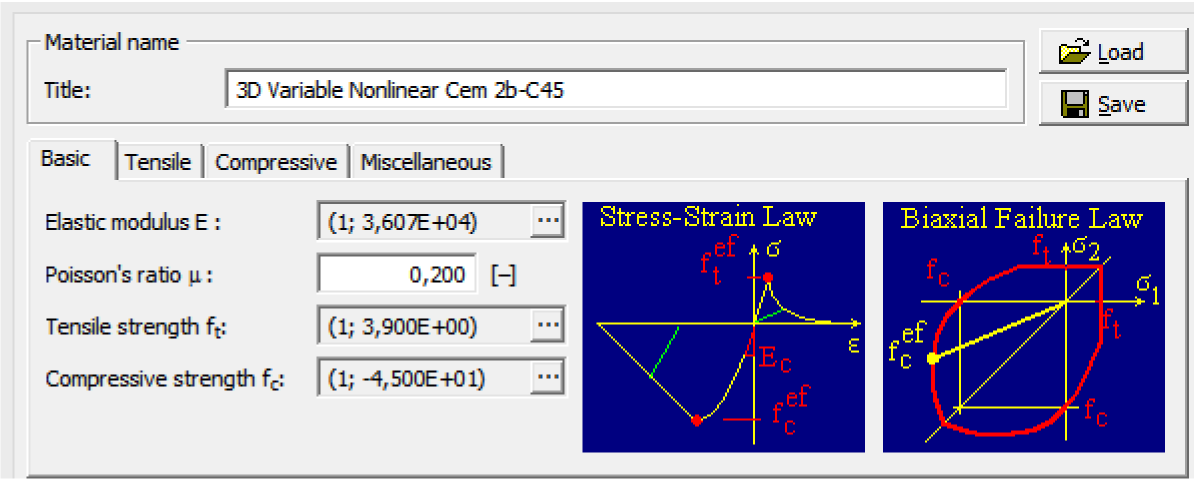

a) C 45 Basic material properties

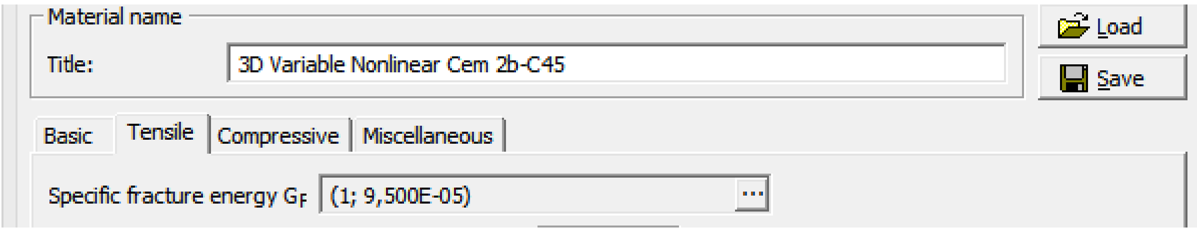

b) C 45 Tensile

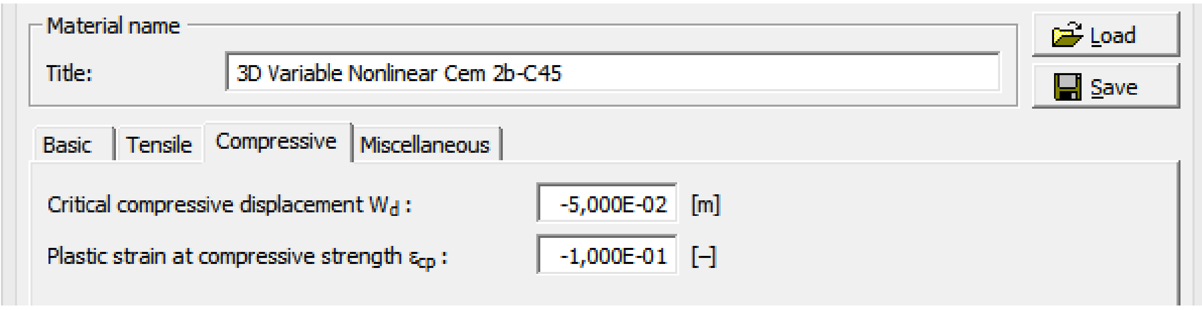

c) C 45 Compressive

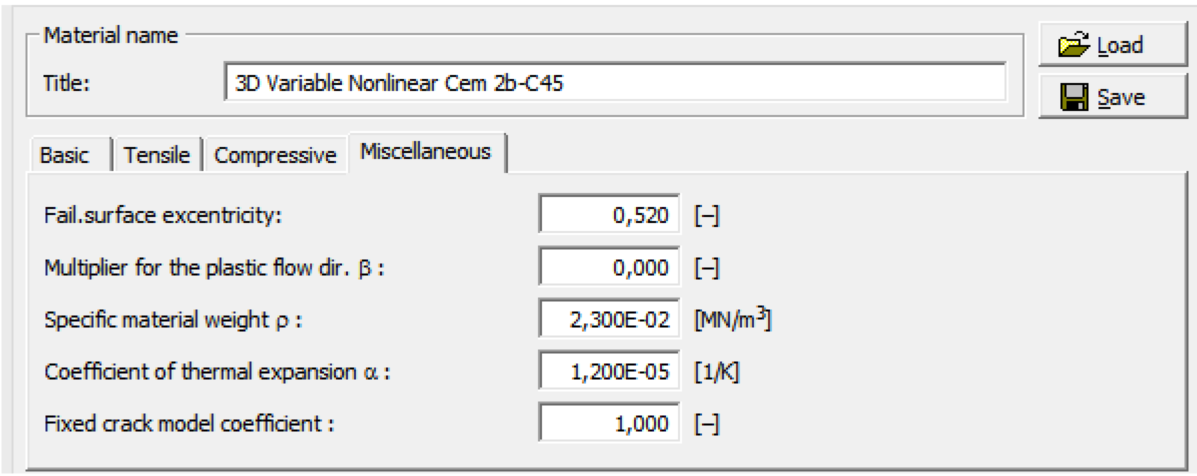

...... d) C 45 miscellaneous

Figure 144 Material 3D variable nonlinear C45

Reinforcement:

As showed in *Figure 141*, the element-model for reinforcement is “cyclic reinforcement” steel.
The test of the different diameters used showed small differences in f_{yk} and f_t:

Table 7 Characteristics reinforcement steel

Steel	f_{yk}		Weight	f_t
Ø 8	380 MPa		0.5	540 MPa
Ø 8	490 MPa		0.5	640 MPa
Ø 6	340 MPa		1	471 MPa
Ø 12	491 MPa		3	610 MPa
Ø 14	325 MPa		1	455 MPa
Weighted arithmetic average				468 MPa
ATENA	**468 MPa**			

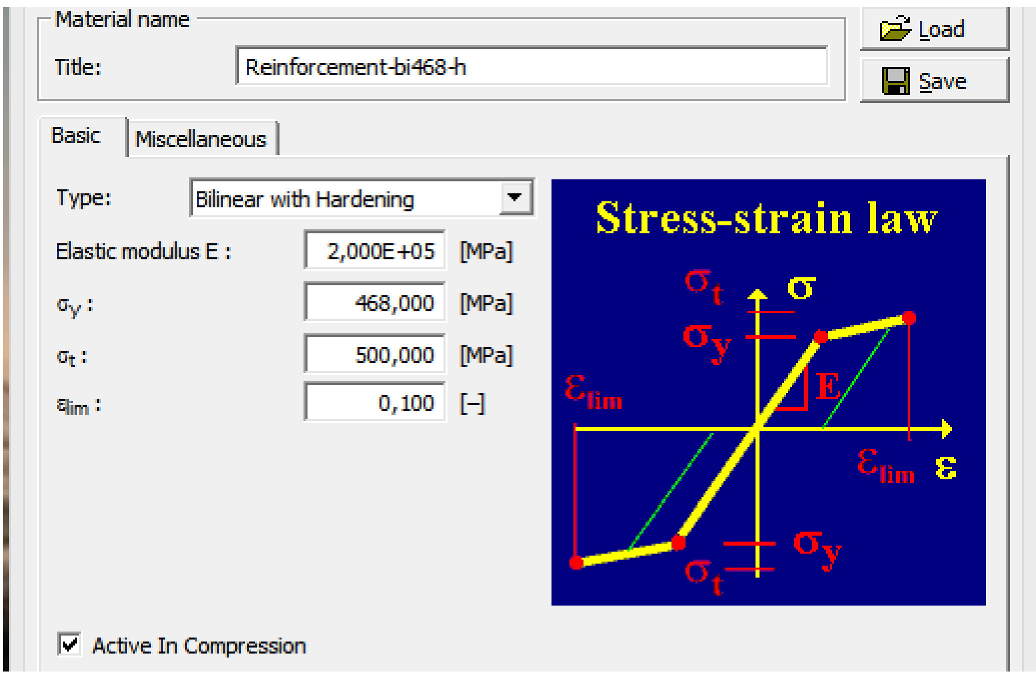

Figure 145 Reinforcement stress-strain law.

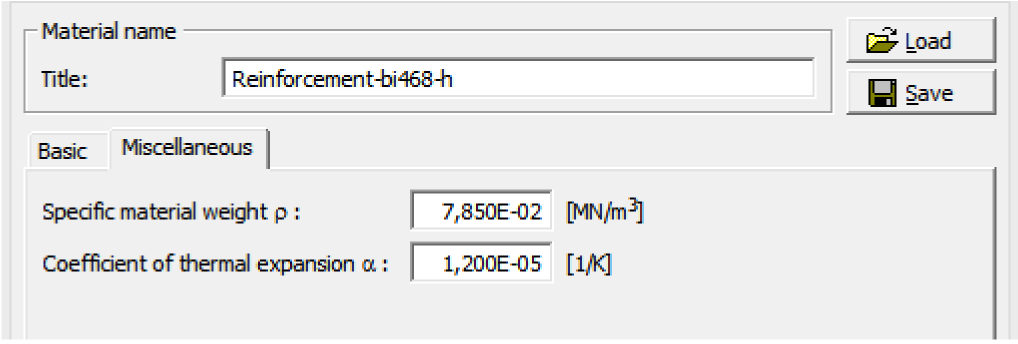

Figure 146 Reinforcement miscellaneous.

Steel plate:

Steel plate for supports and application of forces and deformations

This material is used in concrete for the introduction of force, deformation and support. For the footing and the introduction of force simple steel-elements are used, to avoid singular pressures in the concrete.

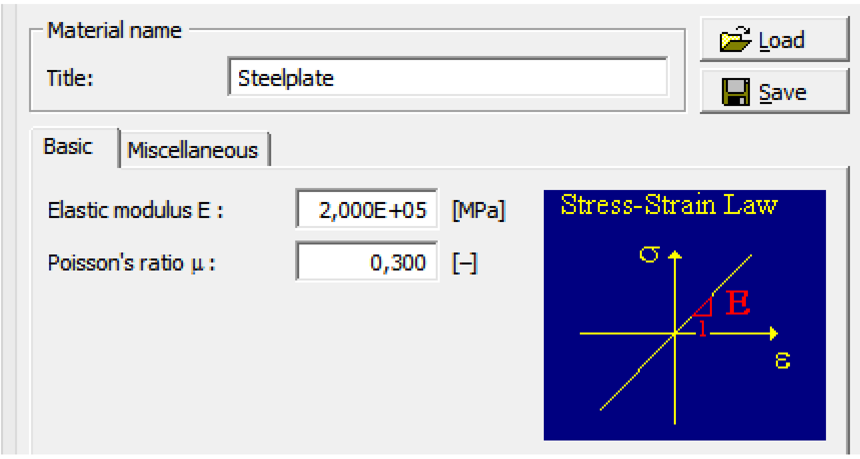

a) Steel plate basic

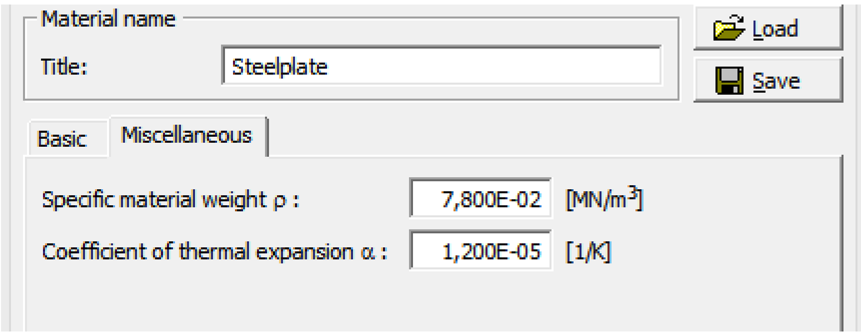

b) Steel plate miscellaneous

Figure 147 Steel plate characteristics.

In specimen #1 and #2, double-wall inbuilt insulation of 10cm polystyrene was used. The following characteristic values were used for the insulation.

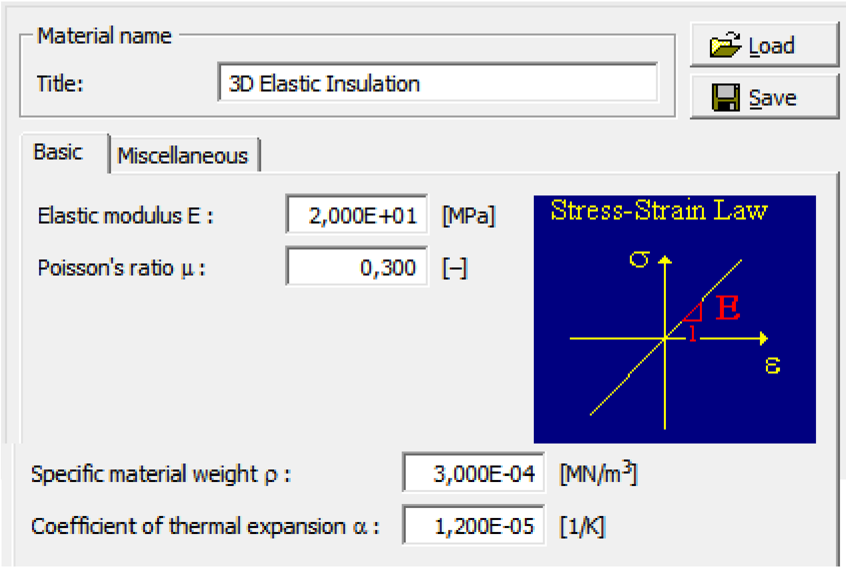

Figure 148 3D Elastic insulation.

Open Contact:

ATENA uses "full contact" between all macroelements. To simulate the open gap between the outer shells of the double wall, a special contact element was used.

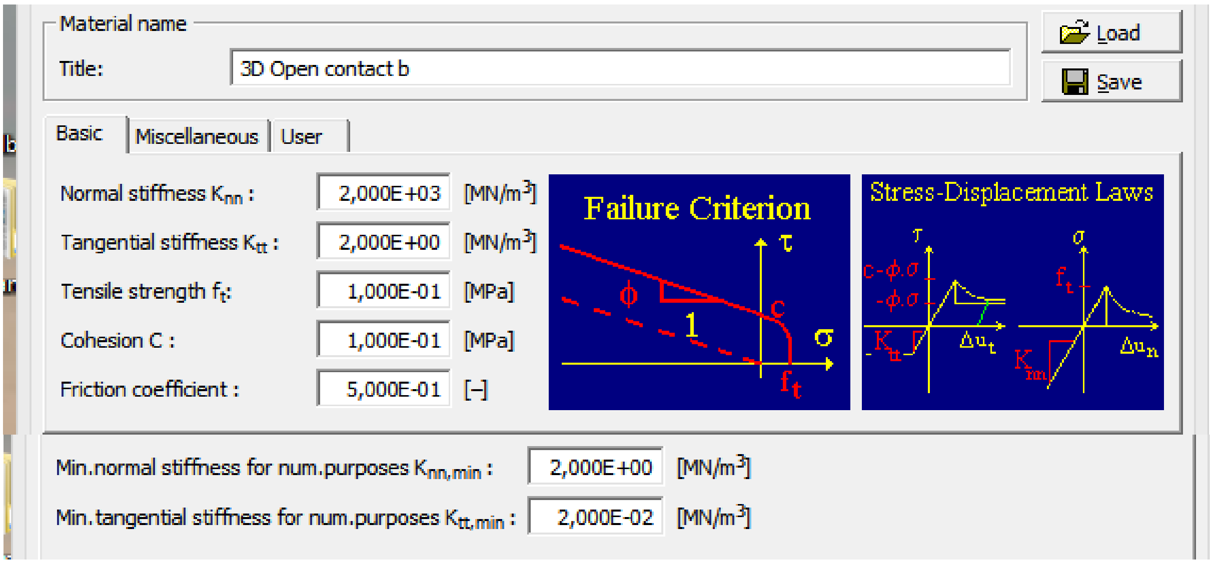

Figure 149 Open contact for 5cm outer elements.

Steel for the Kappema wave:

The material of which the Kappema wave is made is the Steel “1.4003 (X2CrNi12) [37]. For the ATENA calculation these characteristics were taken:

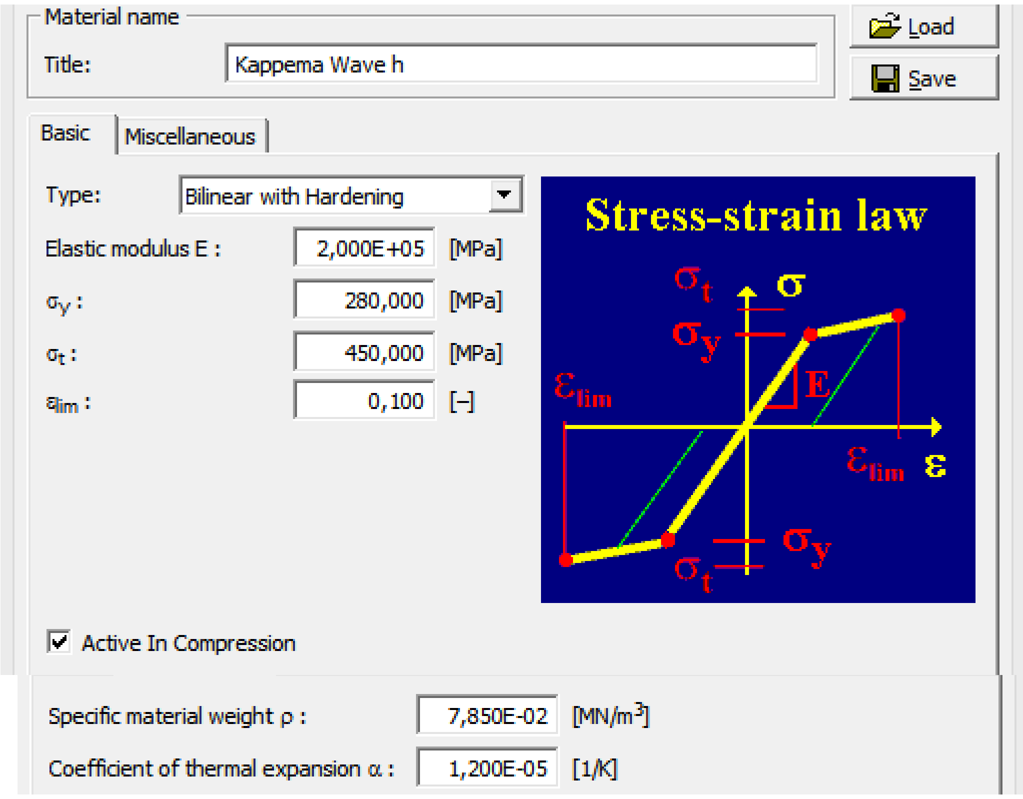

Figure 150 Kappema wave characteristics.

4.2.4 ATENA Loadings

The supports are introduced as loading.

At any macroelement point, lines or surfaces can be fixed or be freed in any direction.

To simulate the cyclic loadings there was an increment of displacement of 0.1 mm in the x-direction (or “Componente 1” in the ATENA nomenclature).

Vertical forces are applied as punctual force (for specimen #1 and #2) and as surface loads for all other specimen.

Horizontal forces are applied, as in the case of the tests, by a gradual shift. As standard for one step is used the a step of 0.1 mm. If difficulties occur with the iteration of calculation, steps were reduced to half or a tenth of standard-steps.

4.2.5 ATENA Solutions for Nonlinear Equations

Newton-Raphson:

For the load case "force" it is suggested that we use the Newton-Raphson method.

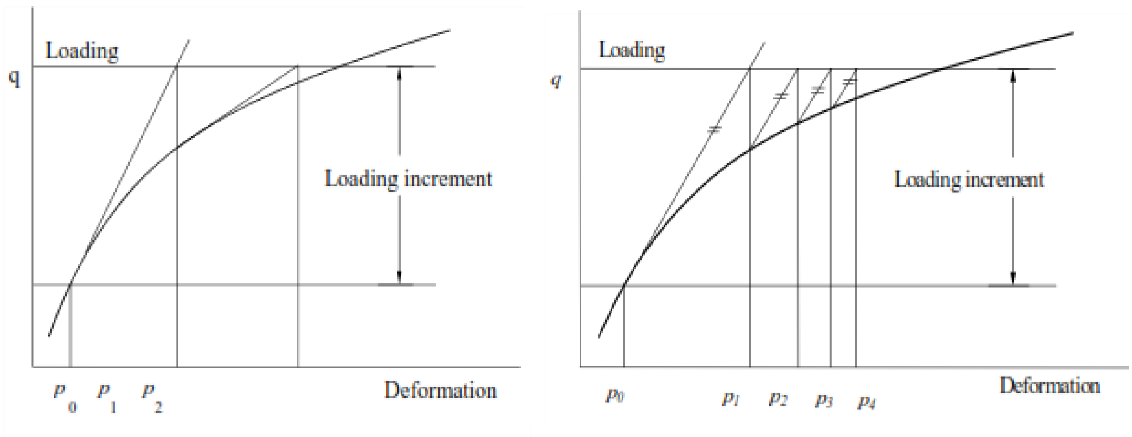

a) full   b) modified Newton-Raphson.

Figure 151 ATENA Full and modified Newton-Raphson method [29].

The most time-consuming part of the solution is the re-calculation of the stiffness matrix

$$\boldsymbol{K}\left(\underline{p_{i-1}}\right)\Delta\underline{p_i} = \underline{q - f\left(\underline{p_{i-1}}\right)} \tag{33}$$

at each iteration. In many cases this is not necessary and we can use matrix $\boldsymbol{K}(p_0)$ from the first iteration of the step. This is the basic idea of the so-called Modified Newton-Raphson method. It produces very significant time savings, but on the other hand it exhibits worse convergence of the solution procedure.

The simplification adopted in the Modified Newton-Raphson method can be mathematically expressed by:

$$\boldsymbol{K}\left(\underline{p_{i-1}}\right) \cong \underline{\boldsymbol{K}\left(\underline{p_o}\right)} \tag{34}$$

Arc-length method:

Next to the Modified Newton-Raphson method, the most widely used method is the Arc-length method.

For the load case "Forced Deflection" (the load case we use for the cyclic "load"), the Arc-length method is the one preferred by the ATENA program.

This method was first employed about fifteen years ago to solve geometrically non-linear structures. Because of its excellent performance it is now quite well-established for geometric non-linearity and material non-linearity alike.

The main reason for the popularity of this method is its robustness and computational efficiency which assures good results even in cases where traditional Newton-Raphson methods fail. Using an Arc-length method, stability problems such as snap back and snap through phenomena can be studied, as well as materially non-linear problems with non-smooth or discontinuous stress-strain diagrams. This is possible due to the changing load conditions during iterations within an increment.

The main idea of this method is well-explained by its name, arc-length. The primary task is to observe the complete load-displacement relationship rather than applying a constant loading increment as in the Newton-Raphson method. Hence this method fixes not only the loading but also the displacement conditions at the end of a step. There are many ways of fixing these, but one of the most common is to establish the length of the loading vector and displacement changes within the step.

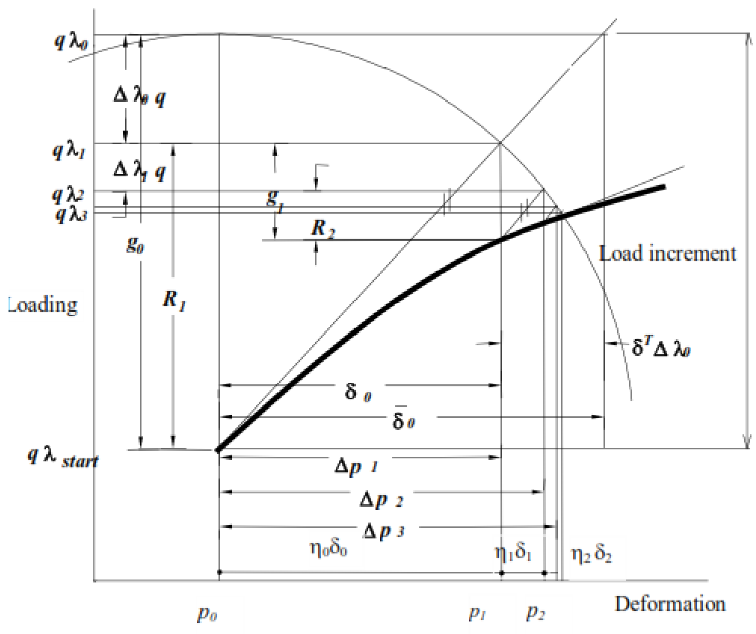

Figure 152 The Arc-length method [29].

From a mathematical point of view it means that we must introduce an additional degree of freedom associated with the loading level (i.e. a problem has n displacement degrees of freedom and one for loading) and in addition a constraint for the new unknown variable must be introduced. The new degree of freedom is usually named λ. There are many possibilities for defining constraints on λ and those implemented in ATENA, as reviewed in the ATENA theory manual [29].

4.2.6 Pre-calculation considerations

As seen in the test, there is the fixing of the specimen on the ground and the application of normal-force and alternating force, introduced by movement in the x-direction.

For the fixing on the ground the surface-contact was the most effective solution.

For the top of the specimen a steel construction brought better results than a quasi-realistic model in concrete.

First the influence of the footing reinforcement was tested by a comparison of different reinforcement layouts:

Due to the surface-fixing, the reinforcement bars fixed on this surface should produce realistic results.

4.3 Analytic Results

4.3.1 General

Shown here is just a sample of calculations carried out last year. It was shown in the calculations that changes must be made, compared with the experiments.

These changes affect the force transmission and the supports. If these parts are modelled analogously to the tests out of reinforced concrete, the results are unrealistic deformations which effectively stop the calculation because of strong local deformations. That was the reason for using a linear-elastic steel for support and force application.

The force was added, just as in the experiments, by gradual shifting. The "standard shift" step was 0.1mm, but multiplied in the first steps by a factor of 5 and later in the plastic range back to 1.0, 0.5 and even 0.1 (corresponding to 0.01 mm). The smallest steps were mainly used to determine exact breaking time and point.

The study of variants was performed on a uniform cross-section with concrete quality C45 and used the earthquake-grade rebar with f_y = 468 [MPa].

4.3.2 Analysis Specimen #1

First a maximum drift in the direction of +x with displacement added on top was calculated 46.62 mm, which is a DR of 1.86%, with a super-elevation of the deformations 8x and visible cracks >0.1 mm:

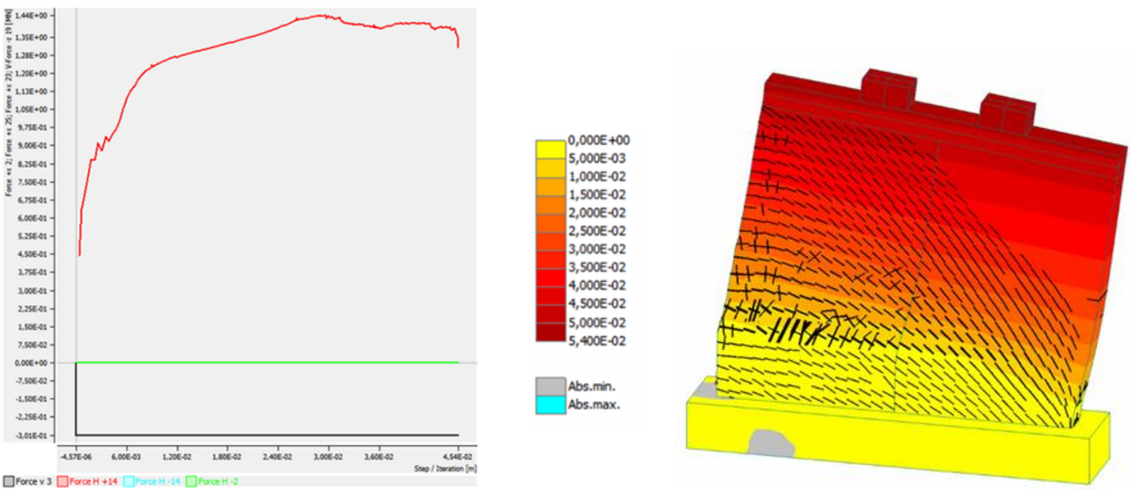

Figure 153 Specimen #1 max drift right.

Strain as ε_{zz} with the maximum of +3.04% and the minimum of -9.09% is shown as example in **Figure 154.**

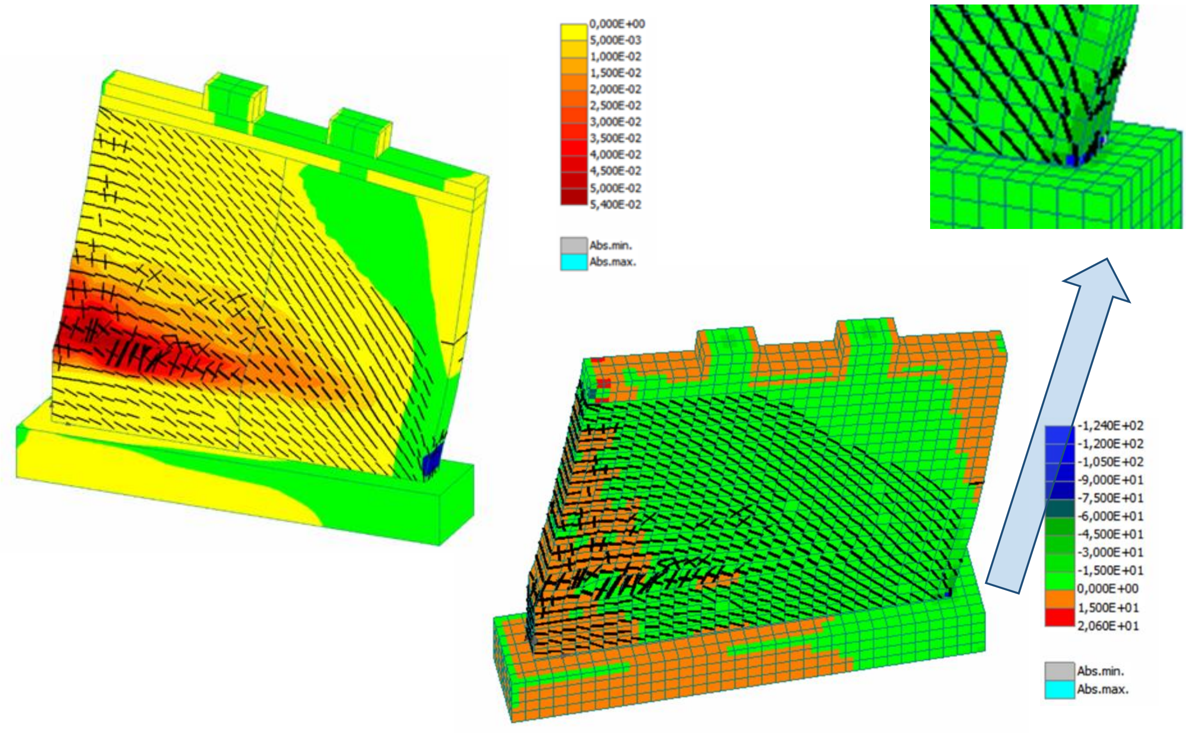

Figure 154 *Strain $\boldsymbol{\varepsilon_{zz}}$ and Stress $\boldsymbol{\sigma_{zz}}$ for Specimen #1.*

The maximum deflection to the left (-x1) was calculated to 27.2 mm, about 1.1% (DR)

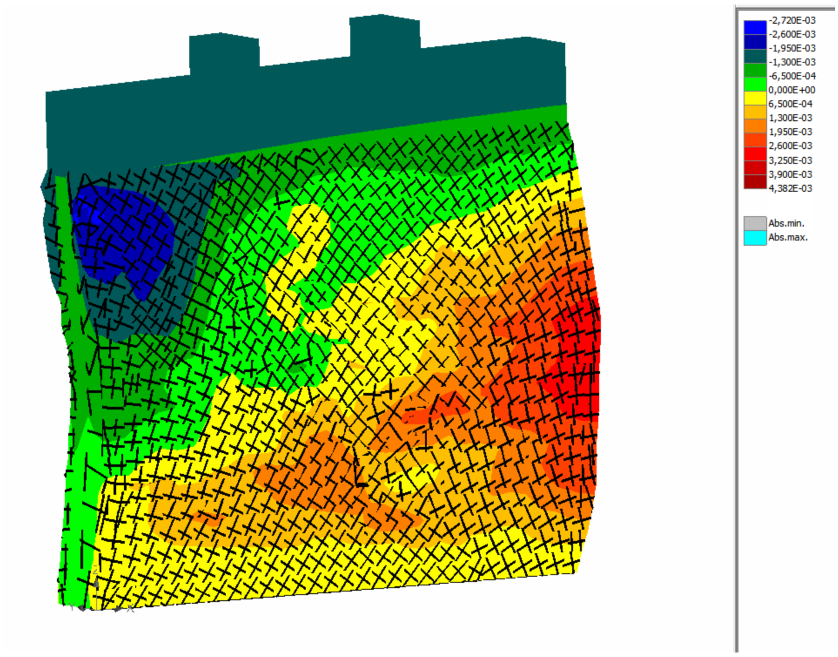

Figure 155 *Deflection to the left specimen #1.*

4.4 Analysis Specimen #2

The difference between specimen #1 and specimen #2 is the use of w rebar cages within the core concrete to replace the non-continuing reinforcement bars from the left to the right outer shells. The crack development is the same as seen with specimen #1

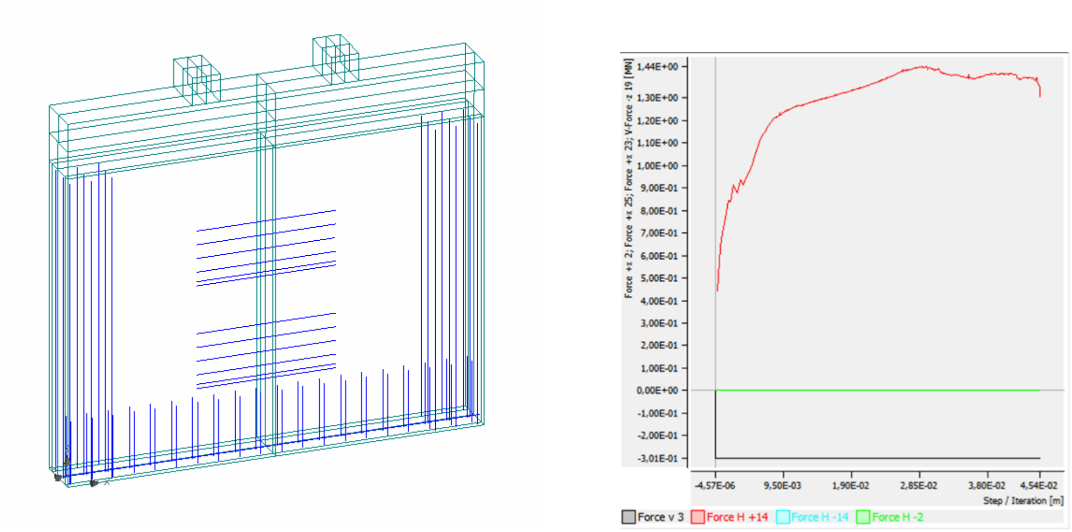

Figure 156 Reinforcement bars and force-displacement diagram for specimen #2.

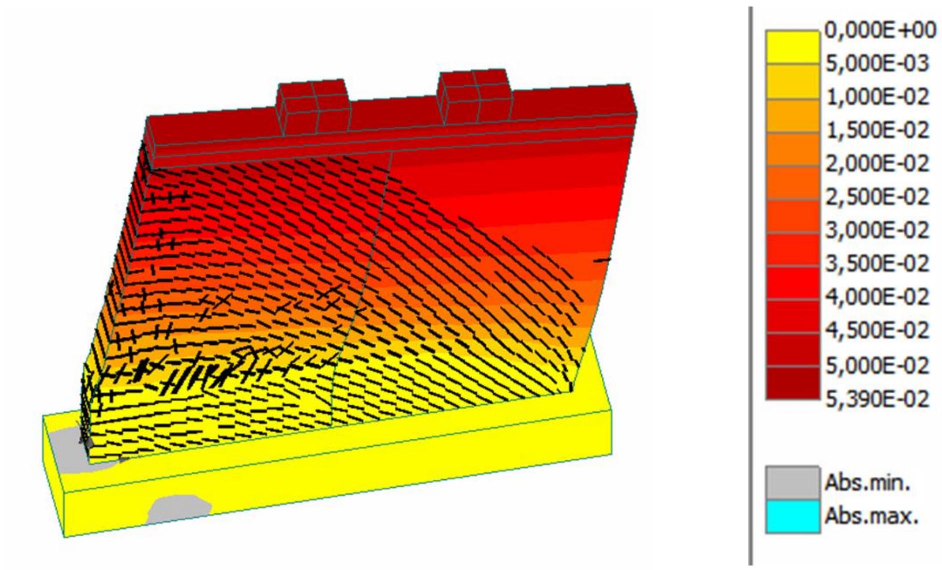

Figure 157 Deflection to the right for specimen # 2.

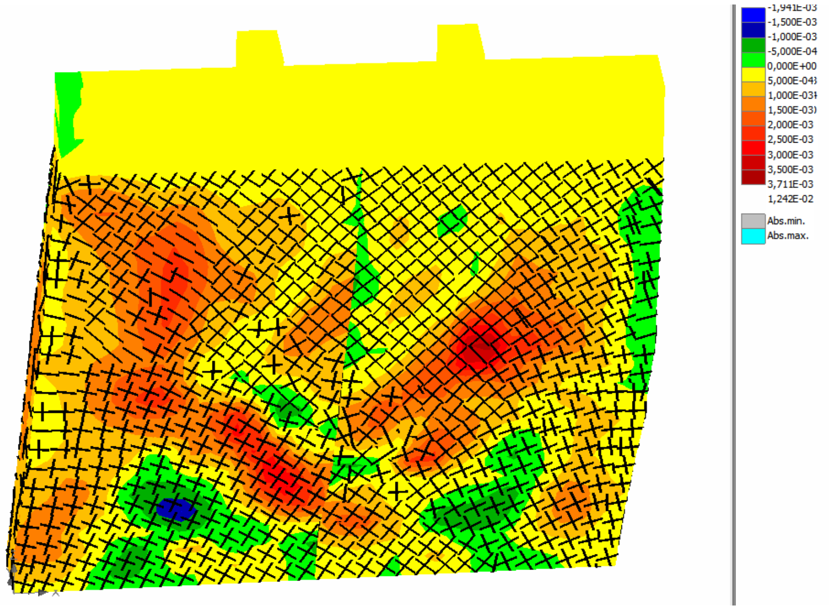

Figure 159 Strain ε_{xx} for specimen #2.

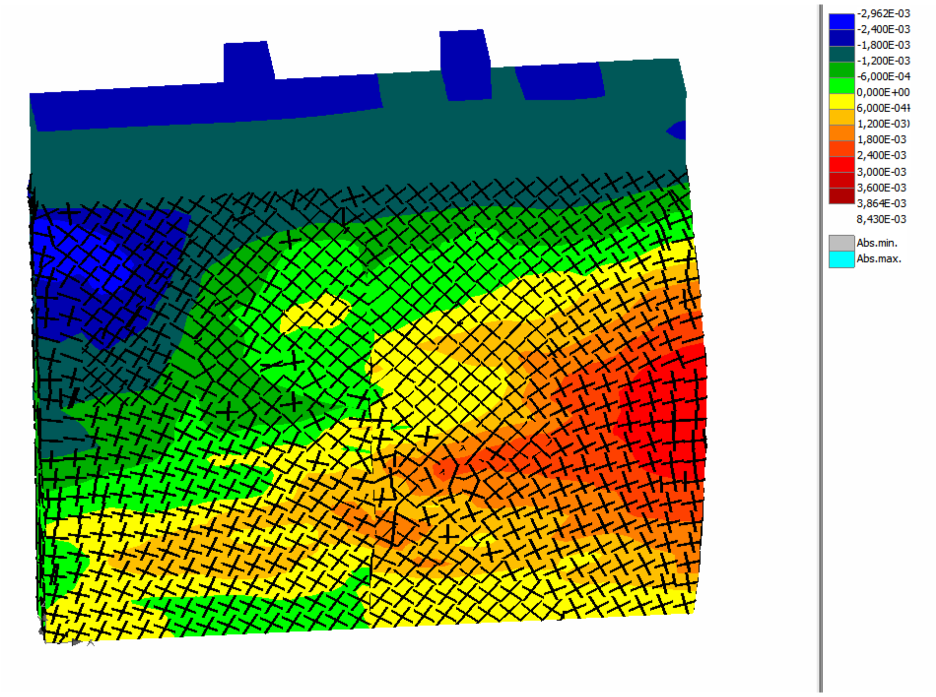

Figure 160 Displacement to the left (-x) for specimen #2

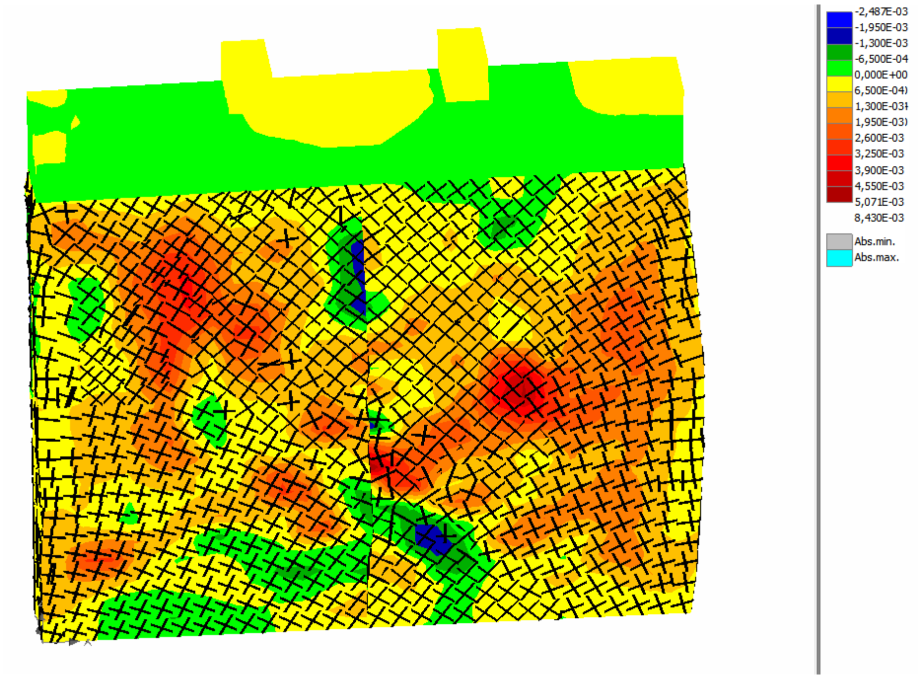

Figure 161 Strain $\boldsymbol{\varepsilon_{xx}}$ for specimen #2.

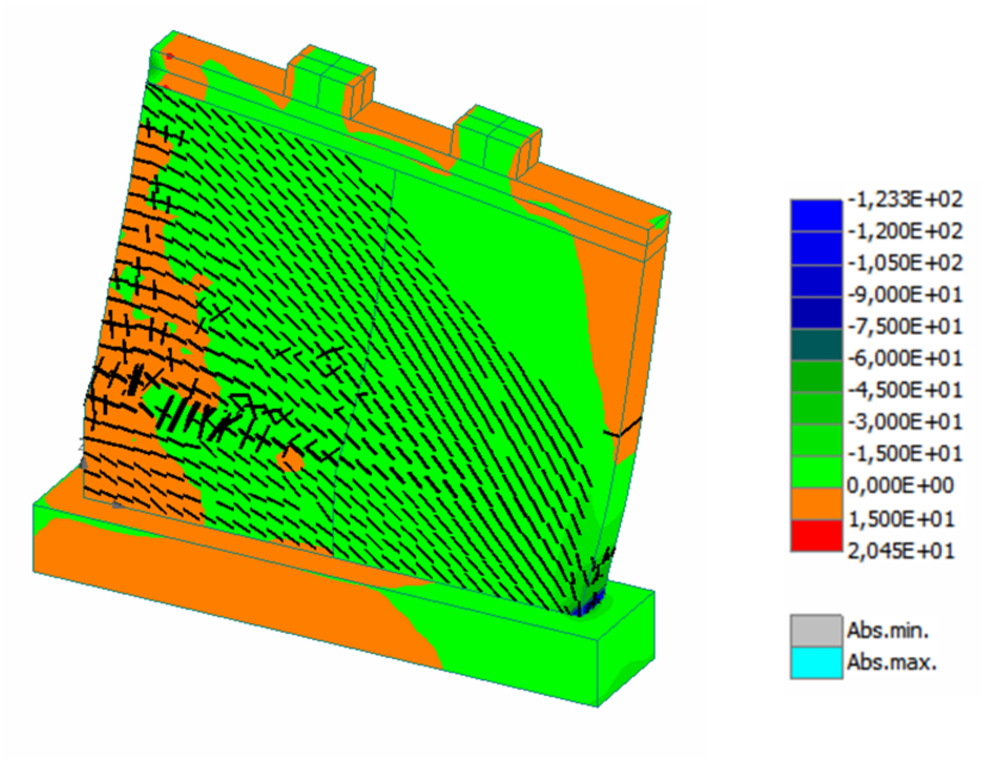

Figure 162 Stress $\boldsymbol{\sigma_{zz}}$ for specimen #2. Superelevation 8x

It is interesting to see that the influence of the inner connection of the two separated outer-double-wall shells can be seen in the deflection and also in the crack-pictures. For the stress-distribution in the z-direction there is no influence to be seen.

4.5 Analysis Specimen #3

This analysis shows a similar crack development to that produced with the tests.

With the possibility to enlarge the straight leg of the specimen from 1.5m to 3.0m it can be seen that the ductile behavior rises up.

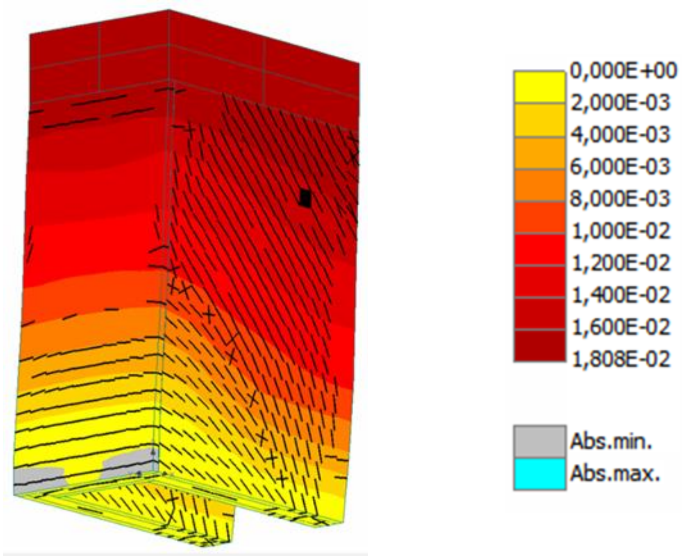

Figure 163 *Deformation right specimen #3 superelevation 2x.*

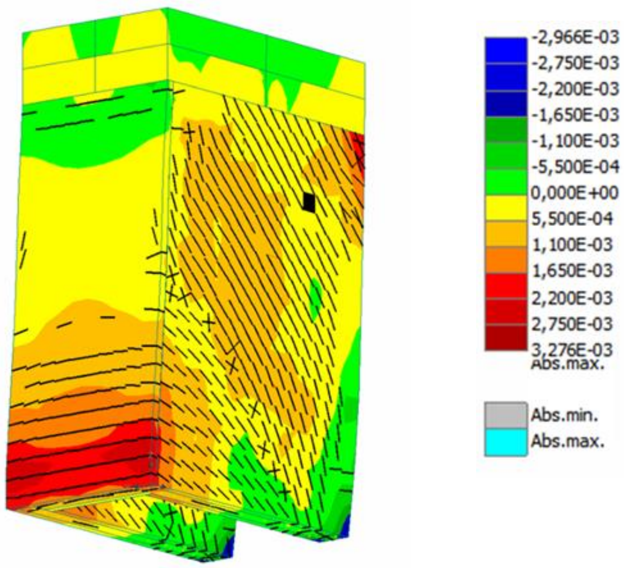

Figure 164 *Strain* ε_{xx} *for specimen #3 superelevation 2x.*

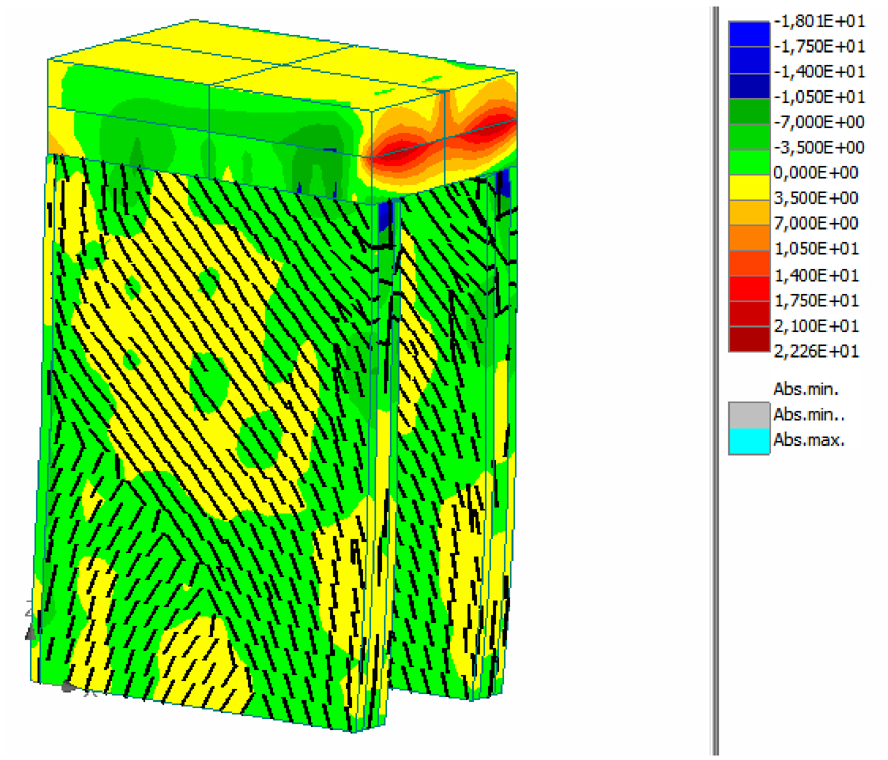

Figure 165 Deformation to right stress $\boldsymbol{\sigma_{zz}}$ for specimen #3 superelevation 2x.

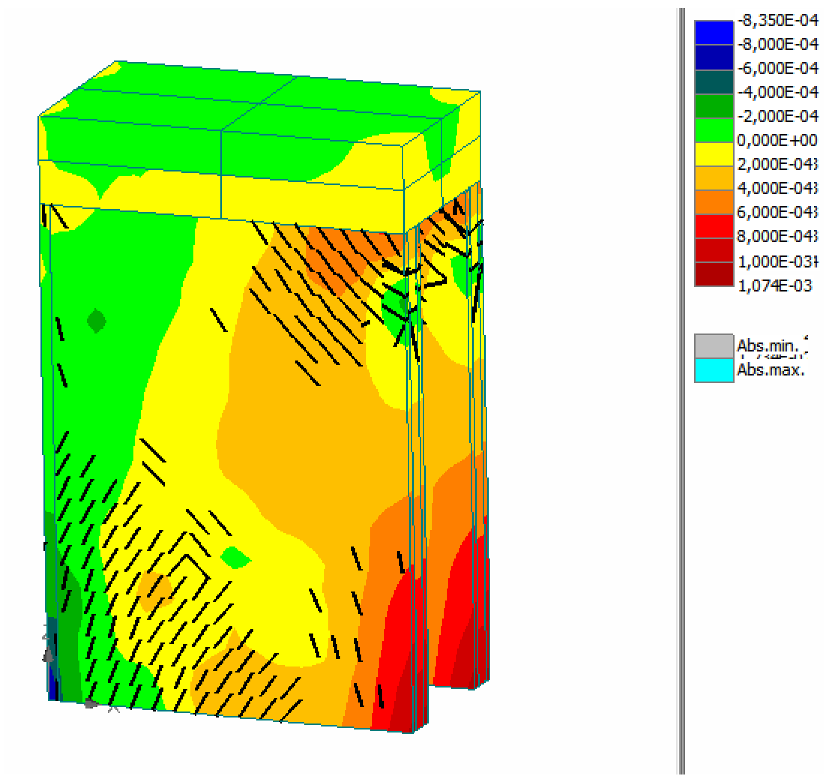

Figure 166 Strain $\boldsymbol{\varepsilon_{zz}}$ for specimen #3 superelevation 2x.

4.6 Analysis Specimen #4

Displacement for specimen #4 in –x-direction, the most interesting load for the connection of the two double walls.

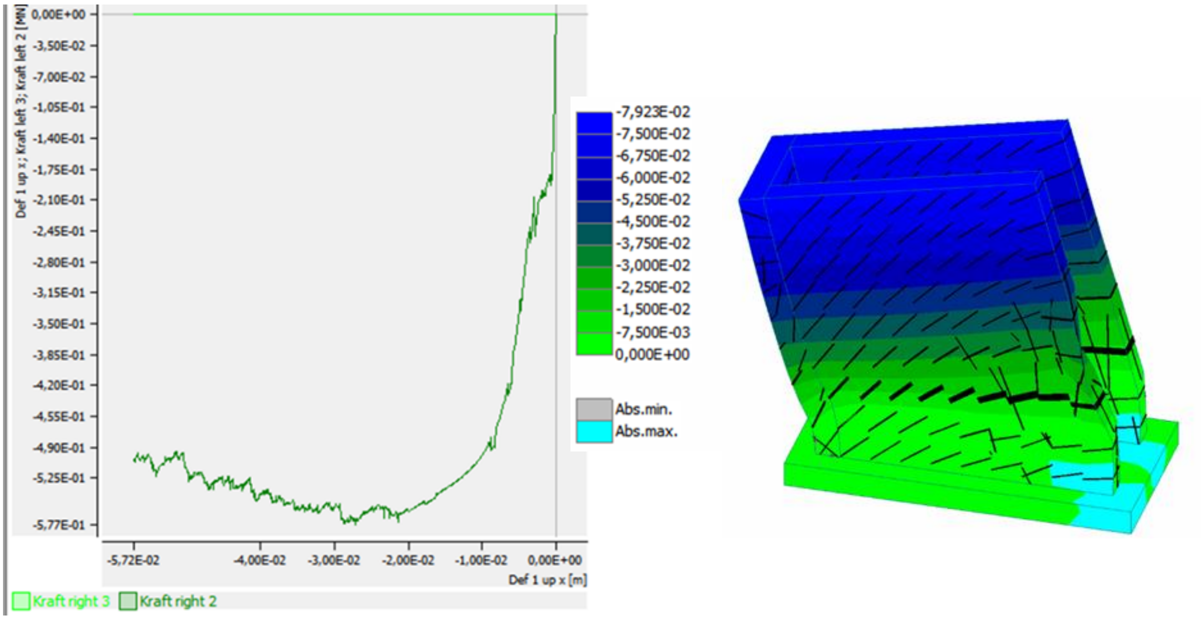

Figure 167 *Stress* $\boldsymbol{\sigma_{zz}}$ *for specimen #4 left superelevation 8x.*

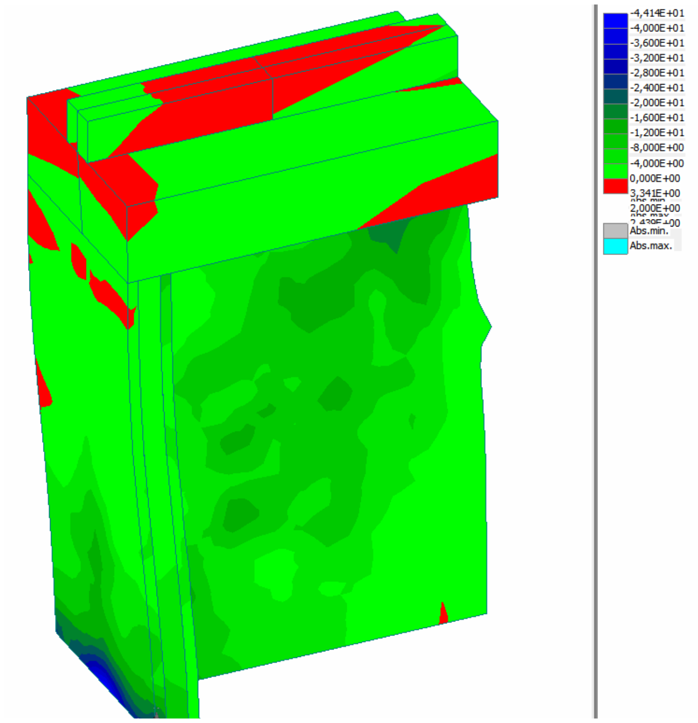

Figure 168 *Stress* $\boldsymbol{\sigma_{zz}}$ *for specimen #4 right superelevation 2x.*

Strain as ε_{zz} for specimen #4. Interesting here is the buckling on the right side, which cannot be explained by higher stress at this point.

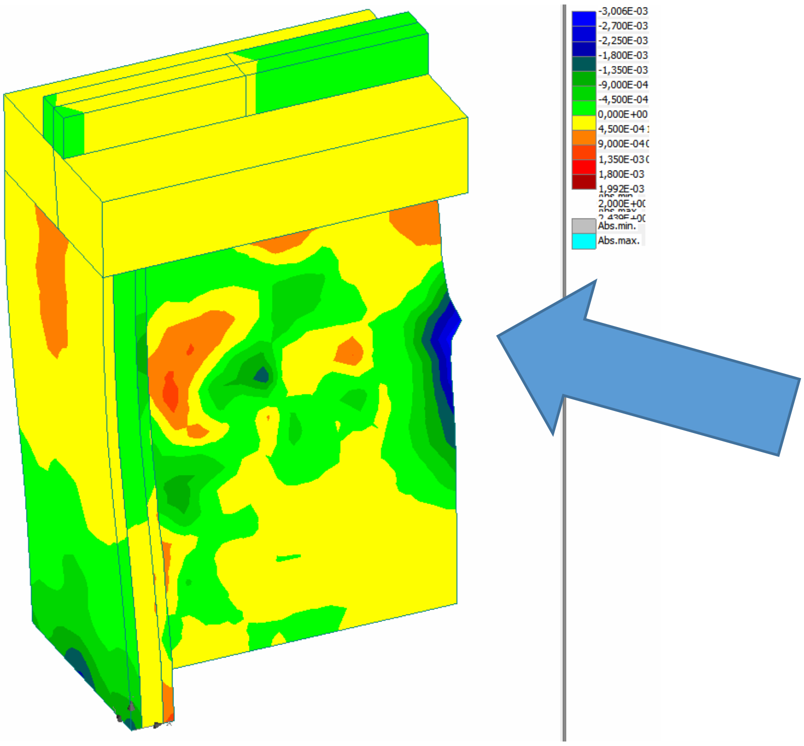

Figure 169 Strain ε_{zz} for max. force left specimen #4 superelevation 2x.

The same specimen #4 with cracks at the third element (integration points) shows that the forces are redirected and concentrated on the T-bar of the specimen.

4.7 Analysis Specimen #5

The column as specimen #5 has a very ductile behavior, the cracks and the distribution of strain and stress within the specimen correspond to the practical tests.

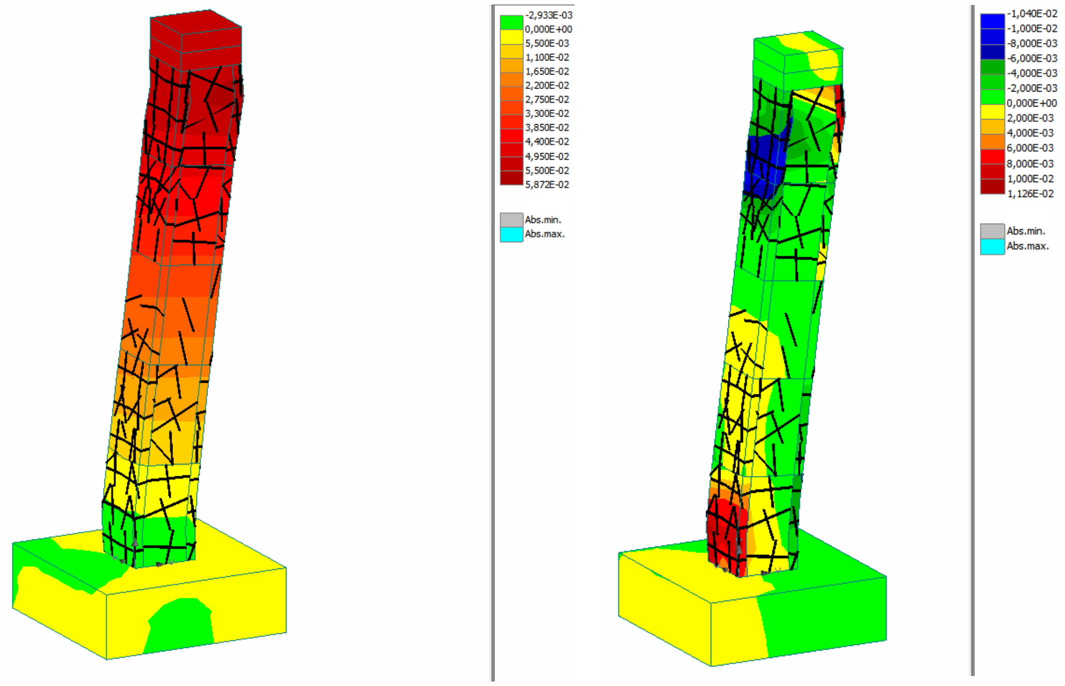

Figure 171 Deflection and strain $\boldsymbol{\varepsilon_{zz}}$ *for specimen #5 superelevation 2x.*

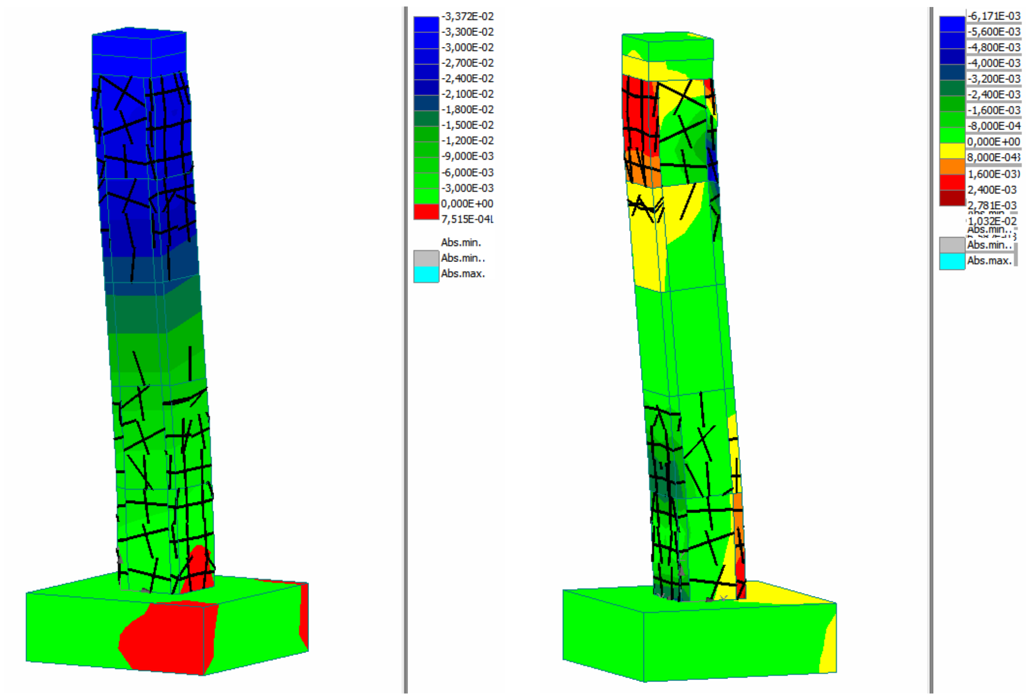

Figure 172 Deflection and strain $\boldsymbol{\varepsilon_{zz}}$ *in direction left for specimen #5 superelevation 2x.*

4.8 Analysis Specimen #6

For the connecting wall-ceiling no additional variants were calculated. The calculation shows the same crack patterns (***Figure 114*** *and* ***Figure 176***), which were also seen in the experiment.

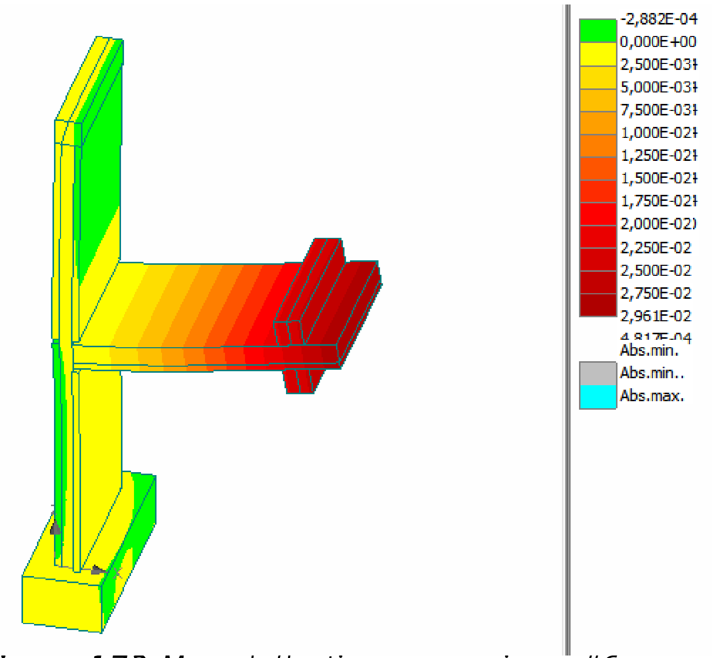

Figure 173 *Max. deflection up specimen #6 superelevation 2x.*

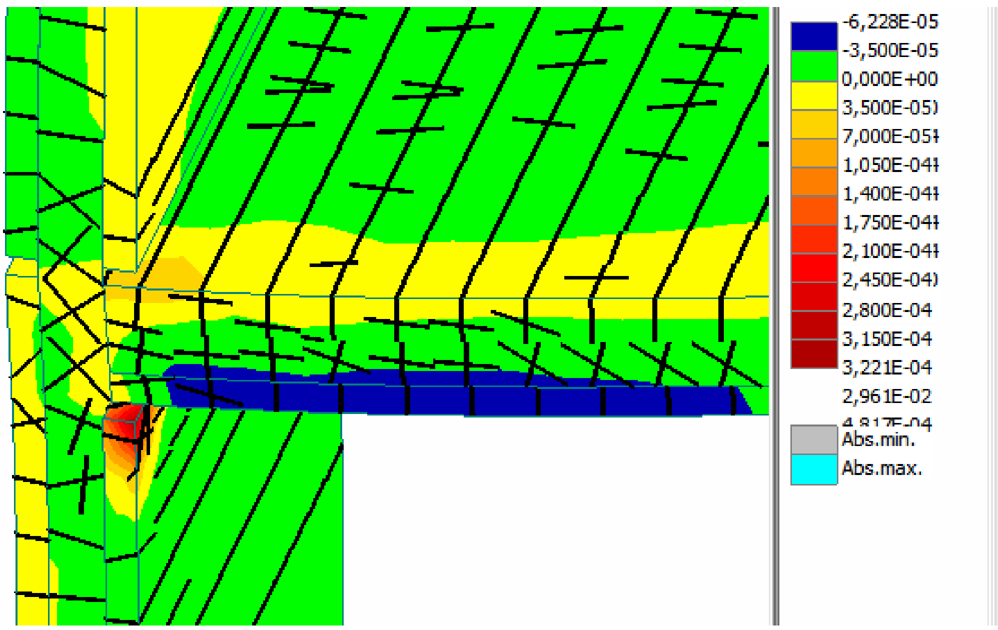

Figure 174 *Detail and max. strain* ε_{zz} *for up specimen#6 superelevation 2x.*

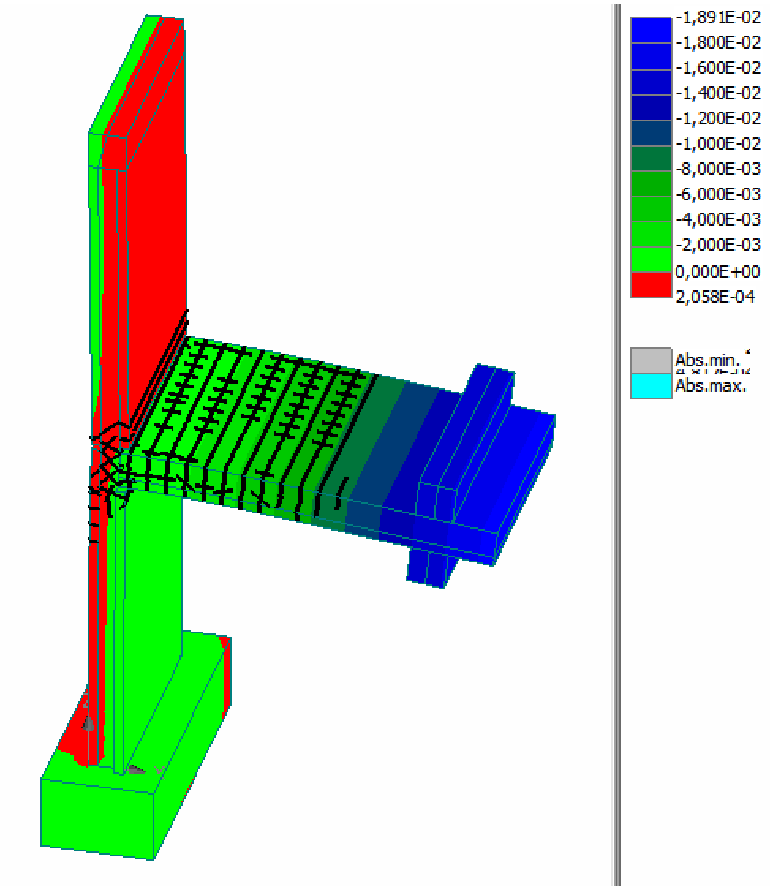

Figure 175 *Max. deflection down specimen #6 superelevation 2x.*

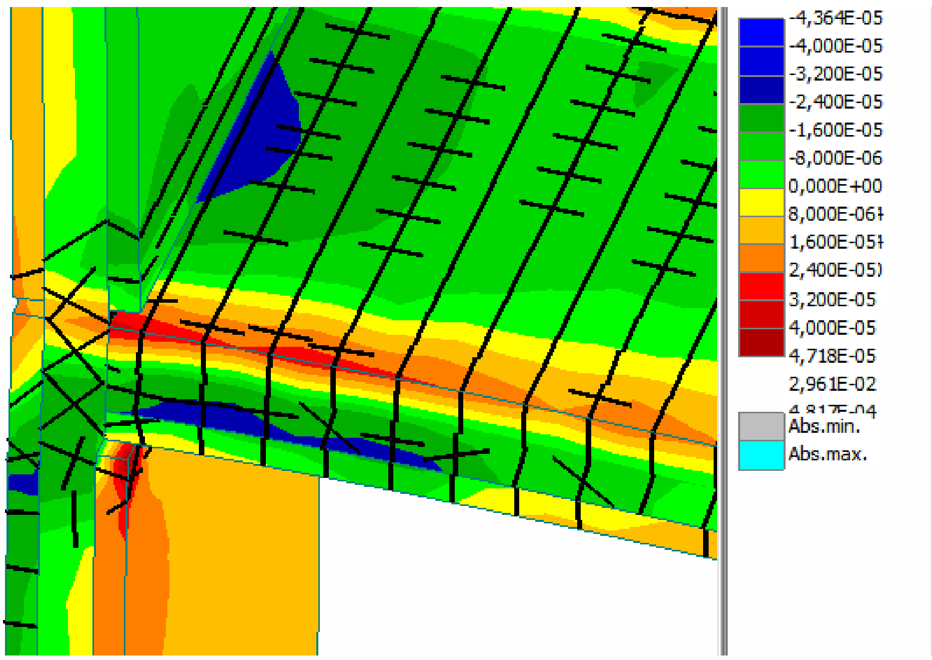

Figure 176 *Detail and max. strain* ε_{zz} *for down specimen#6 superelevation 2x.*

5 Comparison of Experimental and Analytic Results, Discussion

5.1 General

In this chapter, the analytically predicted response of the specimens are compared with the experimental test results. Specifically, the analytical derived force-displacement behavior under monotonic loading is compared with the experimentally determined cyclic peak load values for successively increased displacement levels. The development of strain and stress in reinforcements and concrete are also analyzed, based on the finite element analysis results and tested results.

The challenge here was to find the correct matching model for the reinforced concrete.

The following variants of load and geometry are calculated and summarized. At the end of the calculation of the model house it is pursuant to Annex A for the x-direction (+ and -) performed.

5.2 Specimen #1 and #2

The advantage of the analytic test is being able, after the calibration of the concrete and the steel-models, to calculate different types of double walls:

The change in the core concrete, the height and also the length.

There were some parametric tests for the sample # 1 / # 2.
Since the original calculations are very time-consuming with the 3-layer wall construction, here we calculated relative comparisons with a wall thickness of 25 cm. First, this was tried in a 0-calculation with a normal force of 600 kN, which corresponds to the calculation of a lateral load of 0.8 MN / m².
The second variant was calculated with half of the vertical load and the third variant with twice the normal force that had been used during the test.
The results are shown in the XY images and summarized in the table XY.

In its geometric variant, the test specimen was extended from 3 m to 6 m.
It was then found that the deformation behavior is higher to a 3m body.

Table 8 Specimen #1 and Specimen #2 with double wall elements.

Specimen		**Type**	**Hight**	**H-load [MN]**	**V-load [MN]**	**Deflection**	**Drift ratio**	σ_c **Concrete**	**% Def.**
Comparison of Double-wall-cote-concrete									
#1	T	3,00 m	2,50 m	450	602	3,25 mm	0,13%		elastic
#1	T	3,00 m	2,50 m	1.057	602	24,50 mm	0,98%	break	max. plast
#1	A	3,00 m	2,50 m	-	602	45,40 mm	1,82%	123,40 [MPa]	
#2	T	3,00 m	2,50 m	495	610	2,50 mm	0,10%		elastic
#2	T	3,00 m	2,50 m	1.052	610	24,50 mm	0,98%	break	max. plast
#2	A	3,00 m	2,50 m	-	610	53,90 mm	2,16%	123,30 [MPa]	

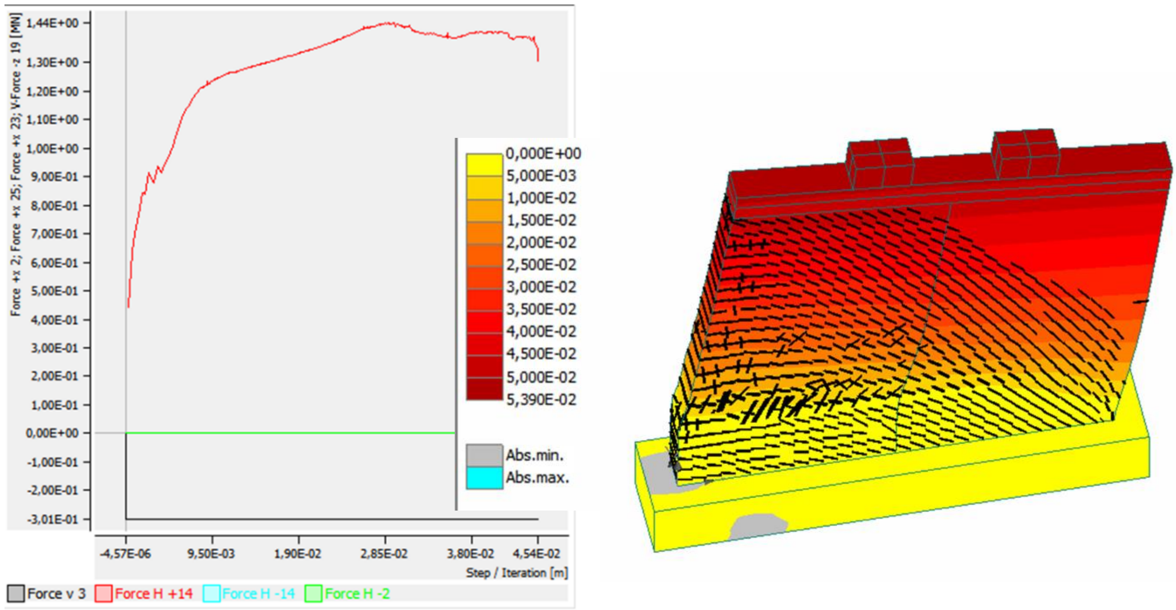

Figure 177 Specimen #1,no vertical .load Deformation-force relation and max deformation superelevation 8x.

For the specimen # 1 without vertical forces arise in the calculation a slightly higher fracture loads of about 10%, as shown in ***Table 9.***

Table 9 Specimen #1 vertical loads.

Specimen		Type	Hight	H-load [MN]	V-load [MN]	Deflection	Drift ratio	σ_c Concrete	% Def.
#1	A	3,00 m	2,50 m	-	602	42,71 mm	1,71%	113,40 [MPa]	100%
#1	A	3,00 m	2,50 m	-	-	45,40 mm	1,82%	123,40 [MPa]	109%

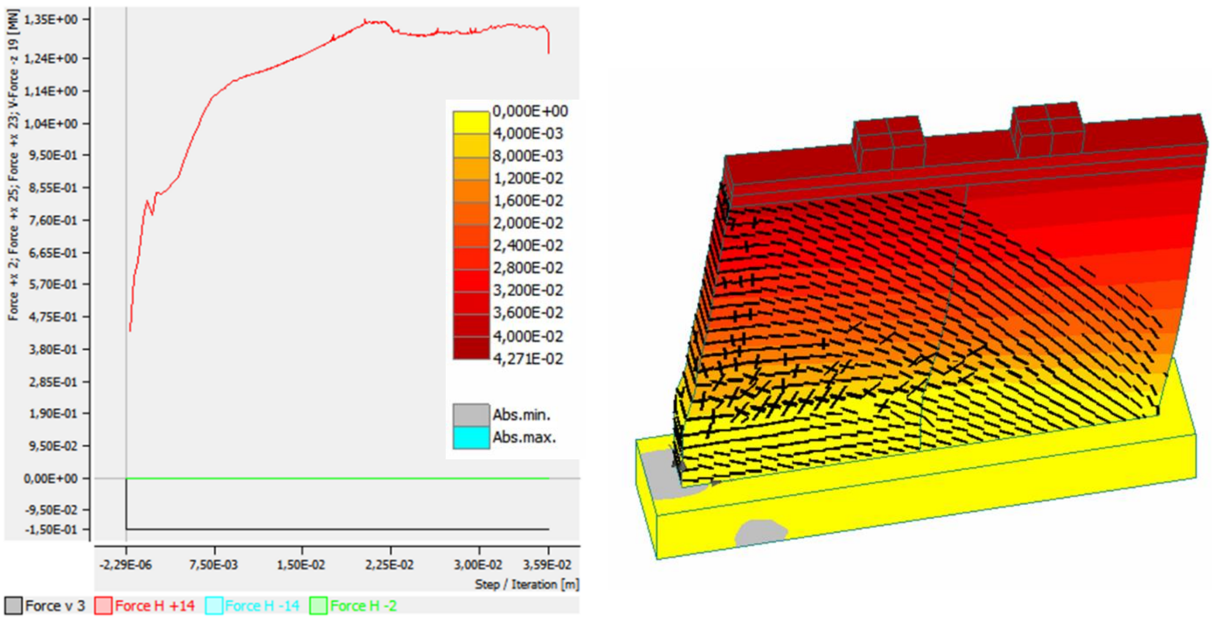

Figure 178 Specimen #1with 600 kN vertical load superelevation 8x.

A further comparative analysis was performed with a 6m wall element, the total load was also doubled. It has been shown that the total deformation to fracture is only 58.66 mm. The maximum concrete stress is 125.9 MPa.

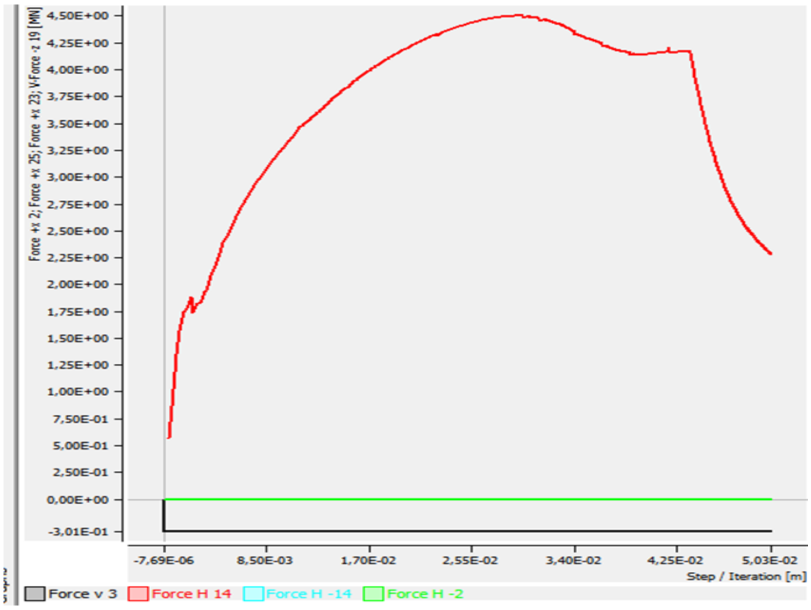

Figure 179 Specimen #1 in 6m length Deformation-force-diagram for +x1

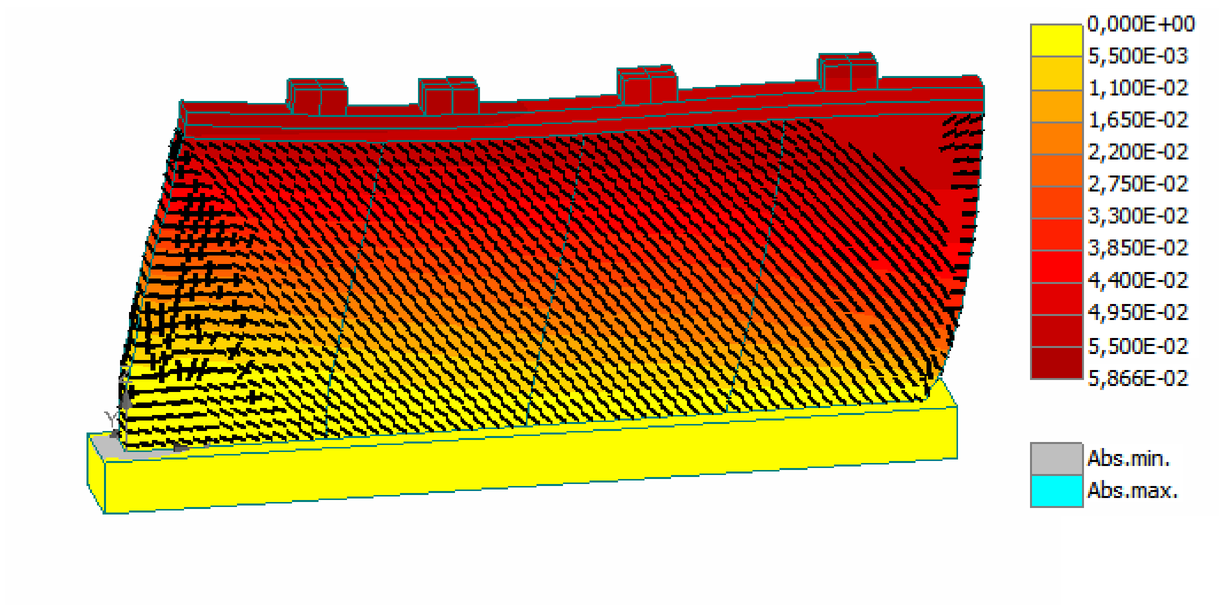

Figure 180 Specimen #1 in 6m length. Max. deformation 58.66 mm superelevation 8x.

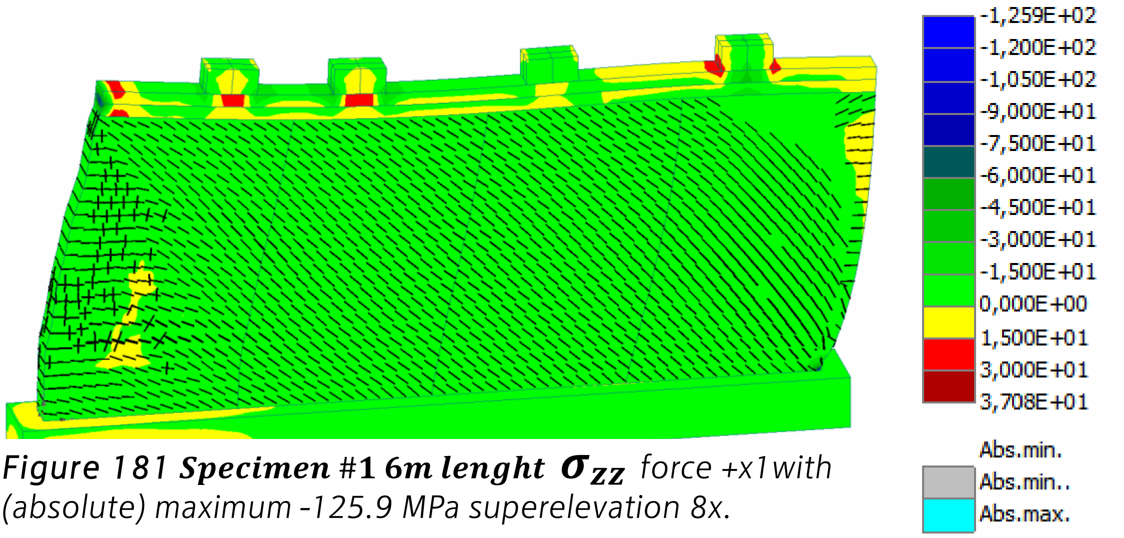

Figure 181 ***Specimen #1 6m lenght σ_{ZZ}*** *force +x1 with (absolute) maximum -125.9 MPa superelevation 8x.*

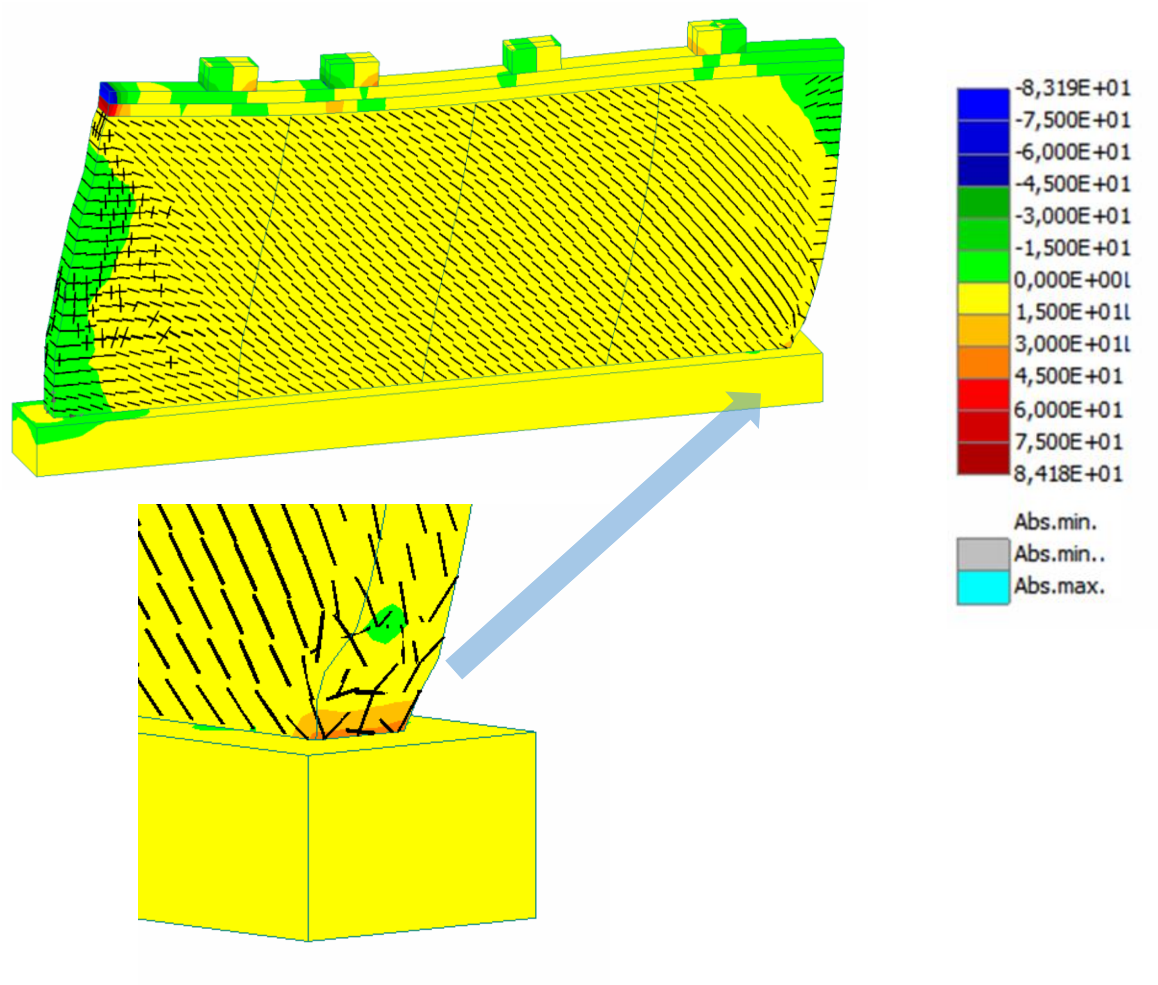

Figure 182 ***Specimen #1 6m length τ_{xz}*** *+x1 with (absolute) maximum -84.18 MPa superelevation 8x.*

5.3 Specimen #3

It was shown that the defection-crack stress and strain behavior of the analytic calculation are close to the practical tests. The calculation with the extension of 1,5m showed that the tested corner connection has even a better and more ductile behavior as the short version in the test. For further intensification different normal forces should be applied.

There were some parametric calculations for the sample # 3.
Since the original calculations are very time-consuming with the 3-layer wall construction, here we calculated *relative comparisons* with a wall thickness of 20 cm.

First, a 0-calculation (called #3.10) as carried out in the experiment without the normal force,
The second variant was with a vertical load of 0.4 MN / m² (called 3.12), calculated as a third variant with 1.6 MN/m² as normal force. The results are shown in the following images and summarized in the table **Table 10** .

These calculations are performed only for loads in the direction of the negative X-axis, as this stress, the connection of the two wall elements stressed maximal

To get the maximum force-displacement values, geometric variants were still expected to:
Length of the U-pieces to each extended one meter.

Table 10 *Specimen #3 Test versus Analytic.*

Specimen		Type	Hight	H-load [MN]	V-load [MN]	Deflection	Drift ratio	σ_c Concrete
#3	T	3,00 m	2,60 m	233	-	1,23 mm	0,05%	
#3	T	3,00 m	2,60 m	731	-	24,50 mm	0,94%	break
#3	A	3,00 m	2,60 m	-	-	46,62 mm	1,79%	-37,88 [MPa]

The tests with specimen #3 was performed with no vertical load. This was also the basic for the calculation. To analyze the influence of vertical load 4 analyzes different loads were applied.

Table 11 *Specimen #3 Mono-concrete with different loads.*

Specimen		Type	Hight	H-load [MN]	V-load [MN]	Deflection	Drift ratio	σ_c Concrete	% Def.	% Concrete
Comparison of Mono-concrete										
#3	A	3,00 m	2,60 m	(3.10)	-	61,33 mm	2,36%	-31,97 [MPa]	100,0%	100,0%
#3	A	3,00 m	2,60 m	(3.11)	0,8 MPa	79,23 mm	3,05%	-41,68 [MPa]	100,0%	100,0%
#3	A	3,00 m	2,60 m	(3.12)	0,4 MPa	92,36 mm	3,55%	-37,88 [MPa]	150,6%	118,5%
#3	A	3,00 m	2,60 m	(3.13)	1,6 Mpa	105,70 mm	4,07%	-46,71 [MPa]	172,3%	146,1%

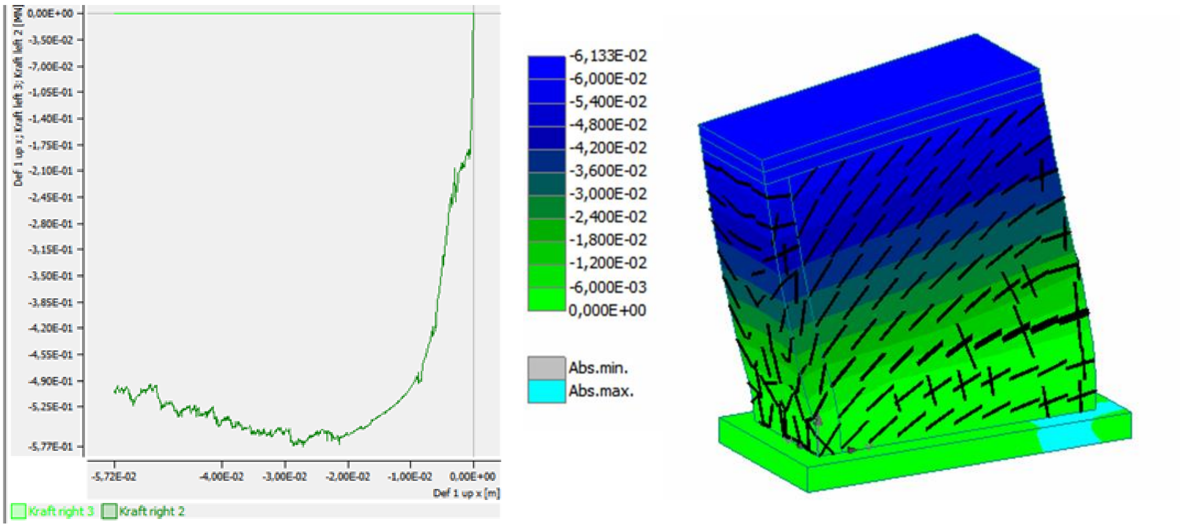

Figure 183 Deformation-force-diagram and deflection for specimen #3.10. superelevation 8x.

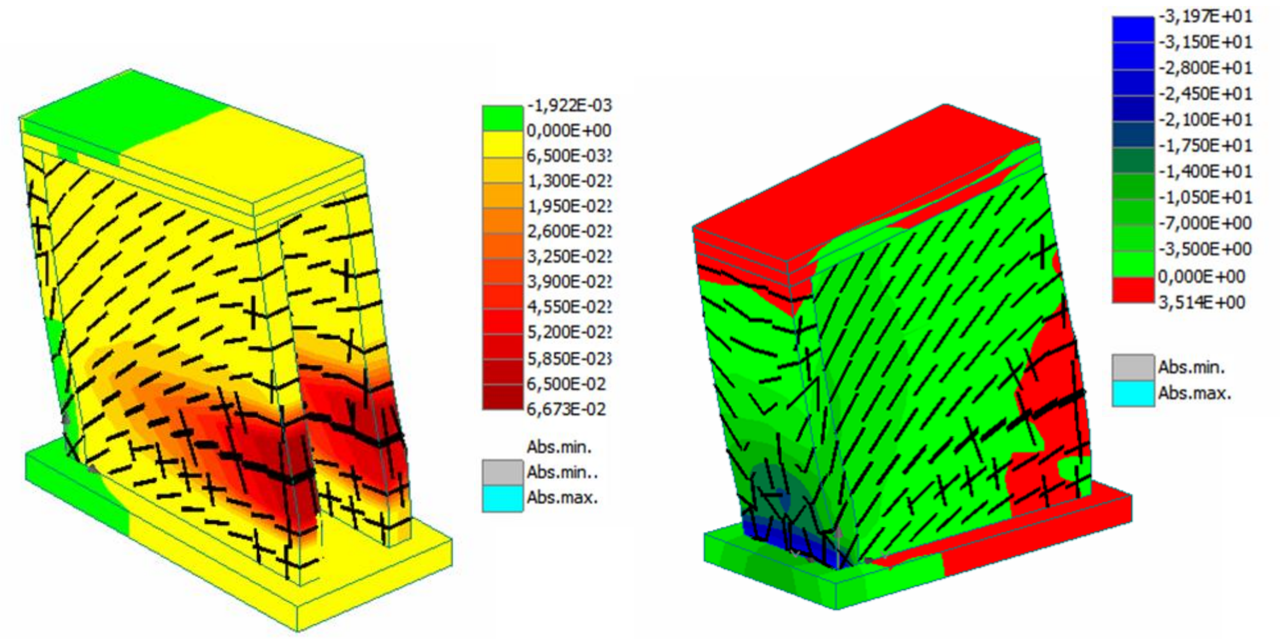

Figure 184 Strain ε_{zz} and stress σ_{zz} for specimen #3.10. superelevation 8x.

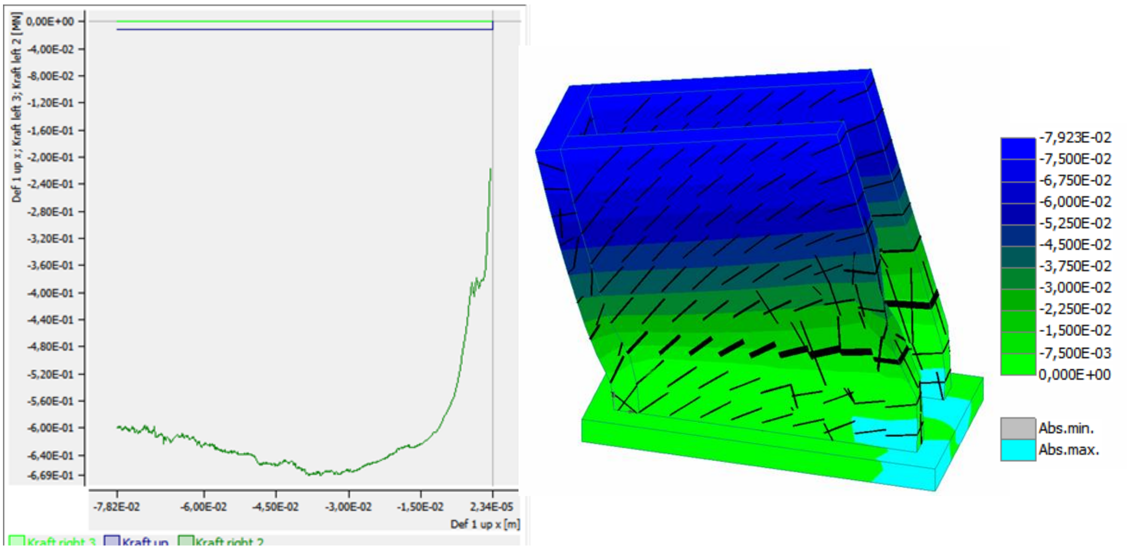

Figure 185 Deformation-force-diagram and deflection for specimen #3.11. superelevation 8x.

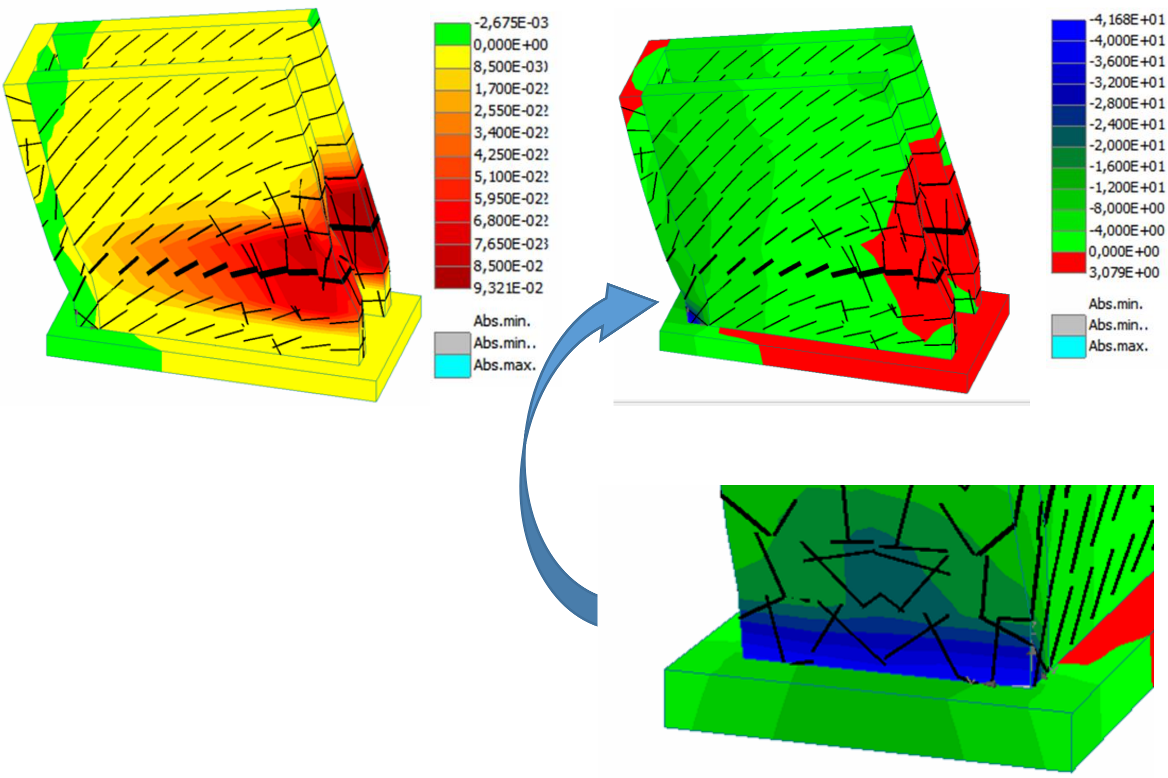

Figure 186 Strain $\boldsymbol{\varepsilon_{zz}}$ and stress $\boldsymbol{\sigma_{zz}}$ for specimen #3.11. superelevation 8x.

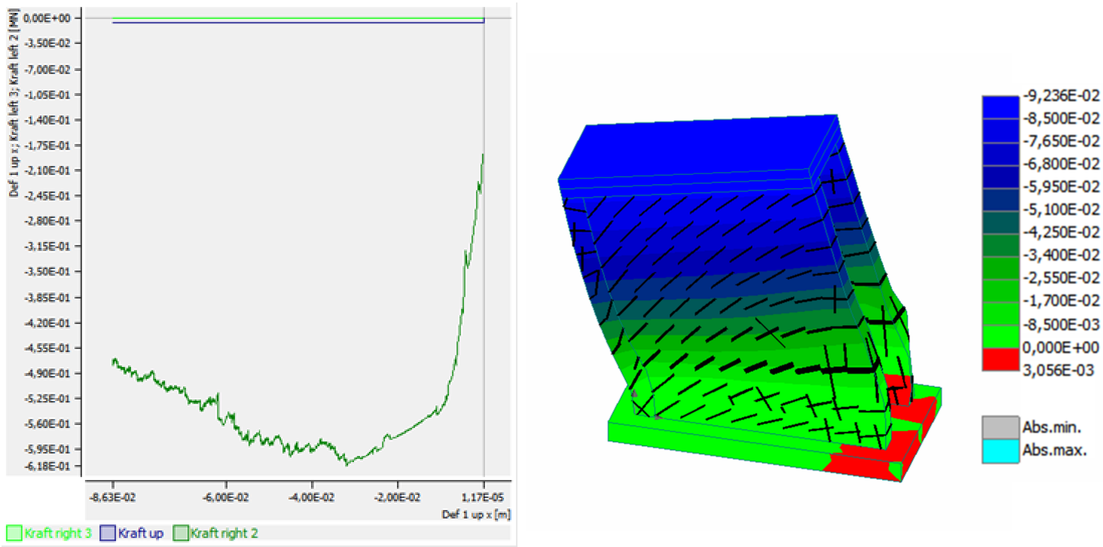

Figure 187 *Deformation-force-diagram and deflection for specimen #3.12. superelevation 8x.*

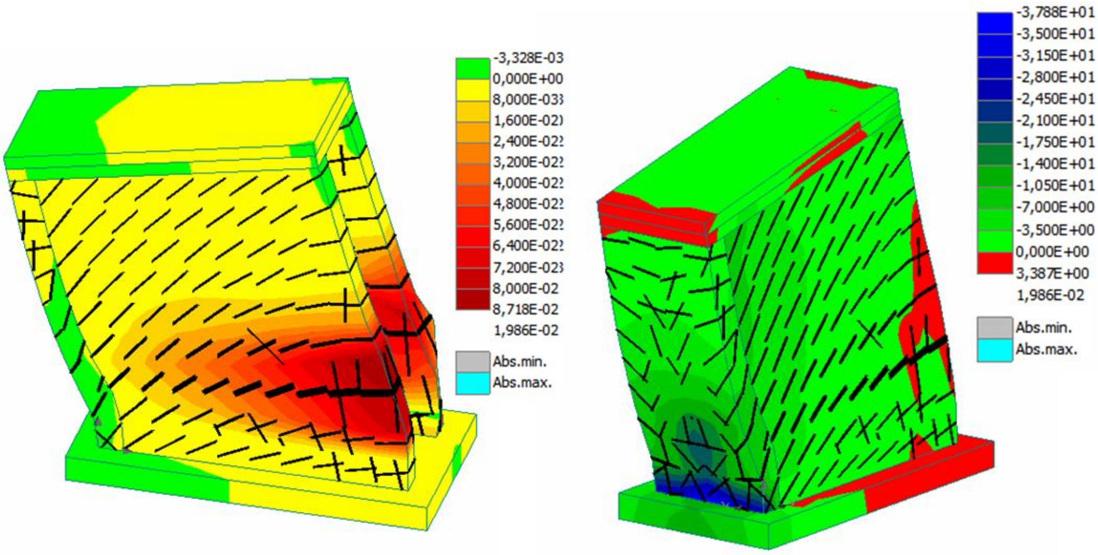

Figure 188 *Strain ε_{zz} and stress σ_{zz} for specimen #3.12. superelevation 8x.*

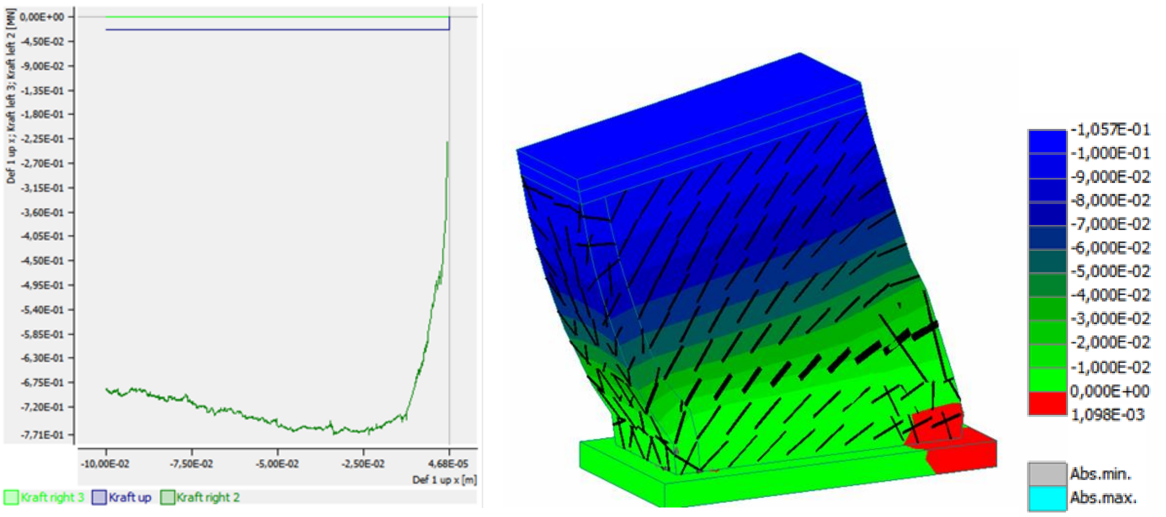

Figure 189 *Deformation-force-diagram and deflection for specimen #3.13. superelevation 8x.*

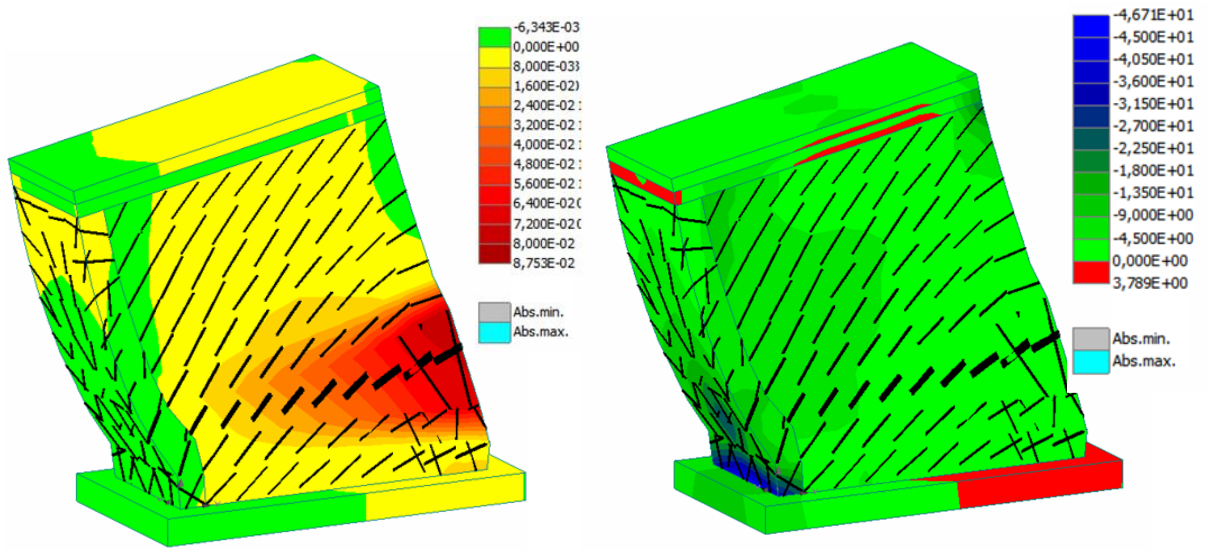

Figure 190 *Strain* ε_{zz} *and stress* σ_{zz} *for specimen #3.13. superelevation 8x.*

Since the restriction to 1000 kN for the horizontal force during the experiments on the strong wall, the calculation variant of the U-test specimen with a wider base was interesting to examine.

After some strong fluctuations, the iteration normalized and it showed a remarkable improvement of 35.8% for the ductility but with only a small increase of the concrete stress of 4.3%.

Table 12 *Specimen #3.11 versus #3.21with 3.0m base-length.*

Specimen		Type	Hight	H-load [MN]	V-load [MN]	Deflection	Drift ratio	σ_c Concrete	% Def.	% Concrete
Comparison of Mono-concrete										
#3	A	3,00 m	2,60 m	(3.11)	0,8 MPa	79,23 mm	3,05%	-41,68 [MPa]	100,0%	100,0%
#3 base 3m	A	3,00 m	2,60 m	(3.21)	-	107,60 mm	4,14%	-43,47 [MPa]	135,8%	104,3%

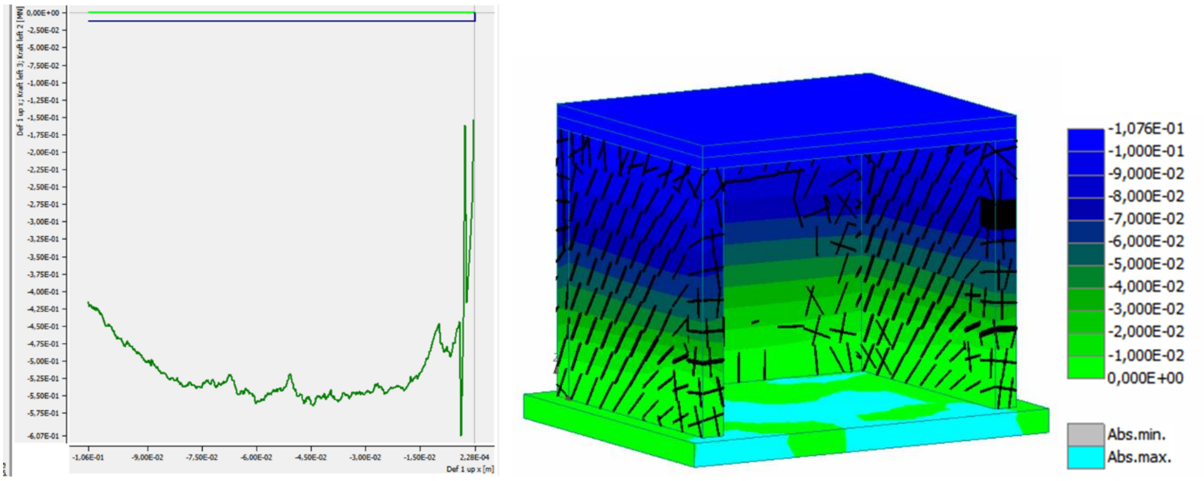

Figure 191 Deformation-force-diagram and deflection for specimen #3.21. superelevation 2x.

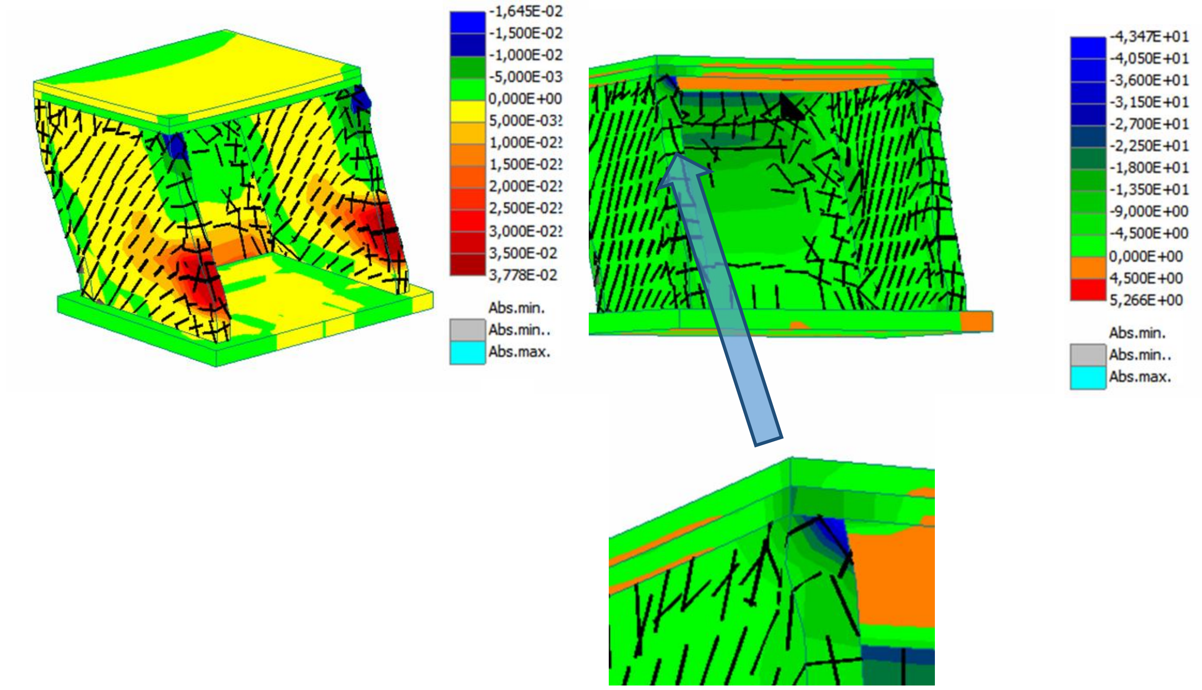

Figure 192 Strain ε_{zz} and stress σ_{zz} for specimen #3.21. superelevation 8x.

5.4 Specimen #4

As typical connection-part, or central part of a flanged shear wall, both test and analytic results showed that the force redirection even works with a small or short flange. Further investigation could optimize the length of flange in relation to the high and length of the wall. As we saw in the test, the focus of further investigation should be put on the contact between the slab or diaphragms and the wall.

As example, the results of the tested specimen #4 with a additional vertical load of 0.4MPa on the top.

Table 13 Specimen #4.10 versus specimen #12.

Specimen		Type	Hight	H-load [MN]	V-load [MN]	Deflection	Drift ratio	σ_c Concrete	% Def.	% Concrete
Comparison of Mono-concrete										
#4	A	3,00 m	2,60 m	-	-	79,23 mm	3,05%	-44,14 [MPa]	100,00%	100,00%
#4	A	3,00 m	2,60 m	-	0,4 Mpa	99,90 mm	3,84%	-42,39 [MPa]	126,09%	96,04%

The ductility rises up 26% with a lower concrete stress of 4%,

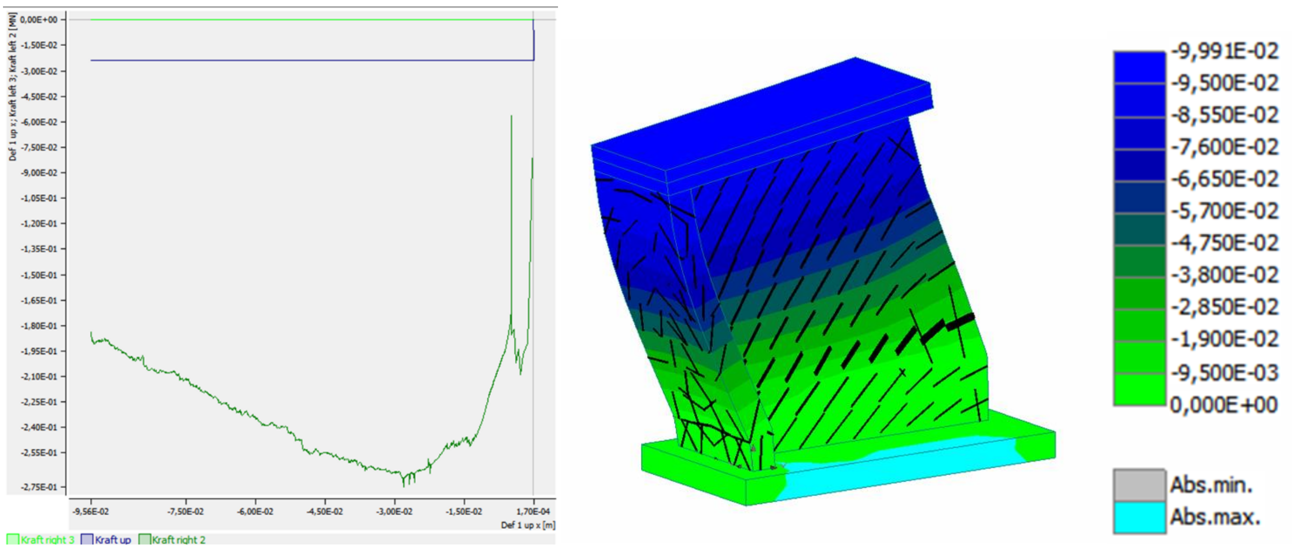

Figure 193 Deformation-force-diagram and deflection for specimen #4.12. superelevation 8x.

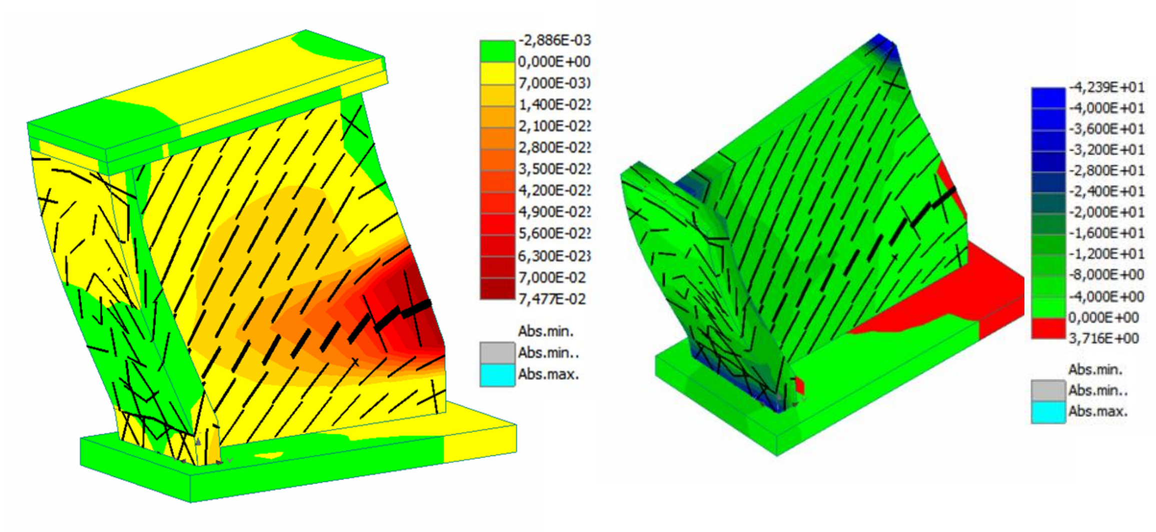

Figure 194 Strain $\boldsymbol{\varepsilon_{zz}}$ and stress $\boldsymbol{\sigma_{zz}}$ for specimen #4.12. superelevation 8x.

As for specimen #3 also for specimen #4 was calculated a sample with a base of 3.0m.

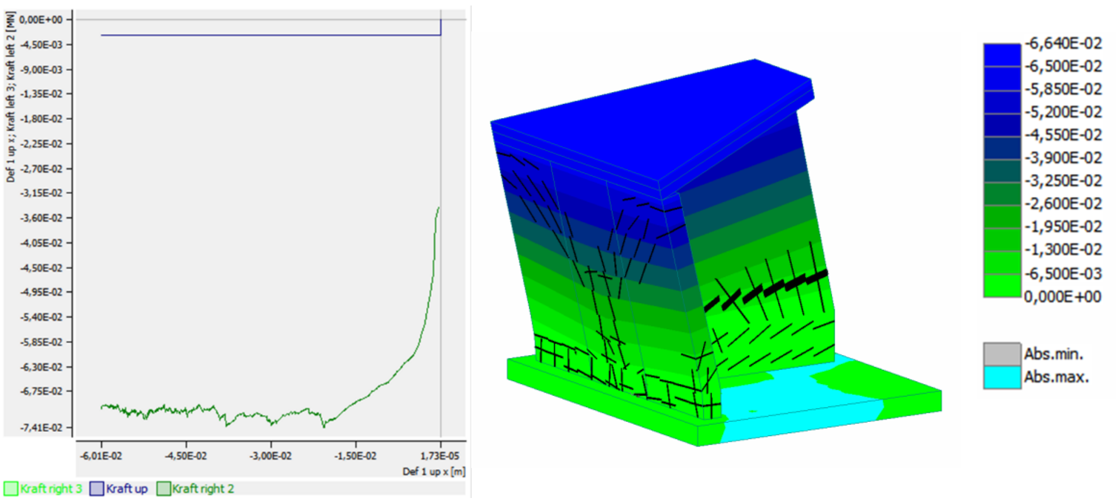

Figure 195 Deformation-force-diagram and deflection for specimen #4.23. superelevation 8x.

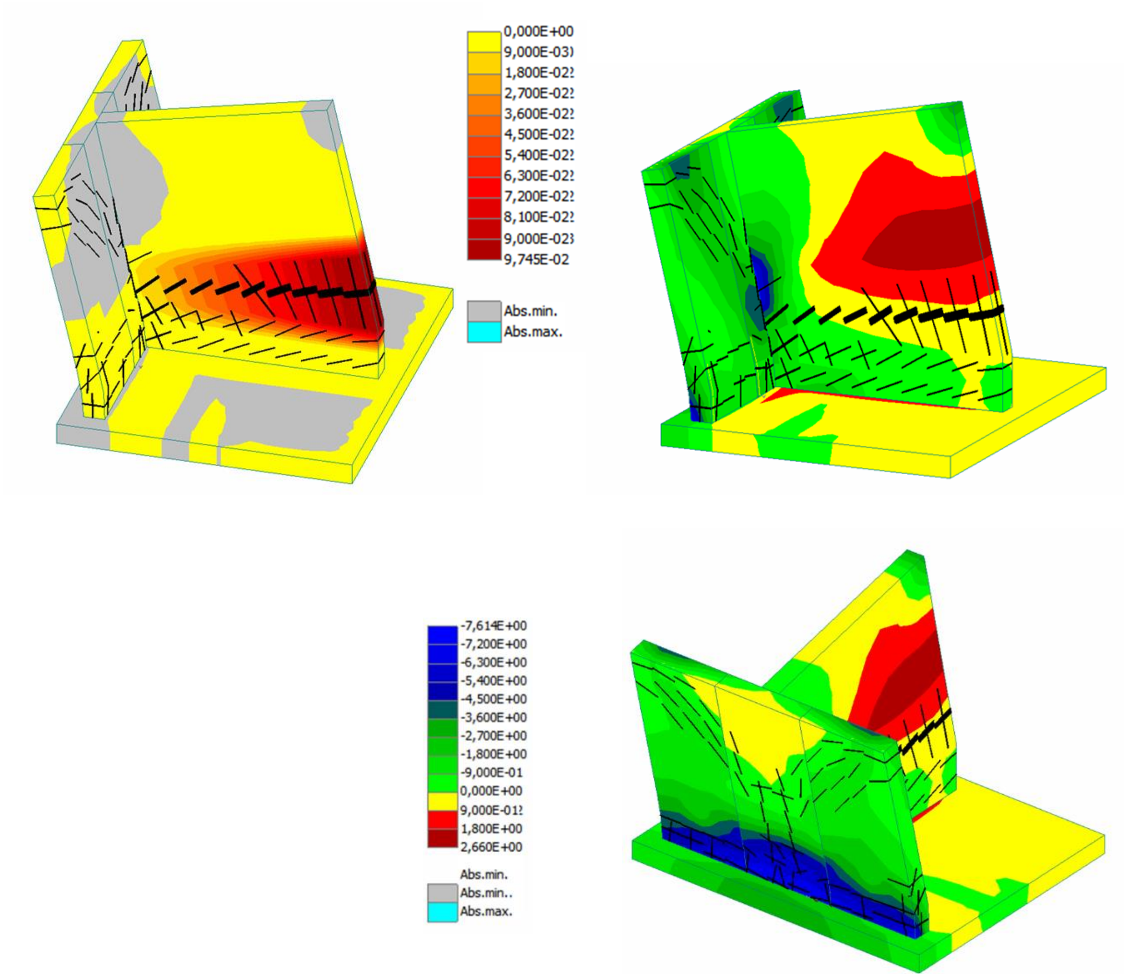

Figure 196 Strain $\boldsymbol{\varepsilon_{zz}}$ and 2 views of stress $\boldsymbol{\sigma_{zz}}$ for specimen #4.23. superelevation 8x.

5.5 Specimen #5

The column displayed remarkable behavior not only during the test but also during the analytic calculation. It was not possible to simulate the perforated sheet used in the manner of "what happens with the cracks", but the ductile behavior is identical. Further studies about variation of length, width, height and vertical load should be carried out, especially for the column-type of earthquake.

5.6 Specimen #6

The connection slab-wall with a slab-wall within the analytic view shows the same behavior as the practical test. In the analytic view we could not simulate the behavior at the end of the upper connecting reinforcement of the slab, therefore this large crack was not to be seen in the analytic test.

5.7 Floor of the House as calculated in Annex A

The calculation of the double wall system model house from ()in Annex A is reproduced here with ATENA.

The elastic calculations with Cubus task a floor-shift of about 10mm.

It can be seen that with ATENA the drift is also about 10mm, but the brake comes later at 15mm.

In the case of the (elastic) calculation with Cubus, a geometrically related torsion was also considered in the seismic action, and ATENA was calculated only in one direction, which was the x-direction in + and - direction.

Nevertheless, the deformation and stress very clearly display the points at which the reinforcement is actually being used and where a closer and more detailed examination could be helpful.

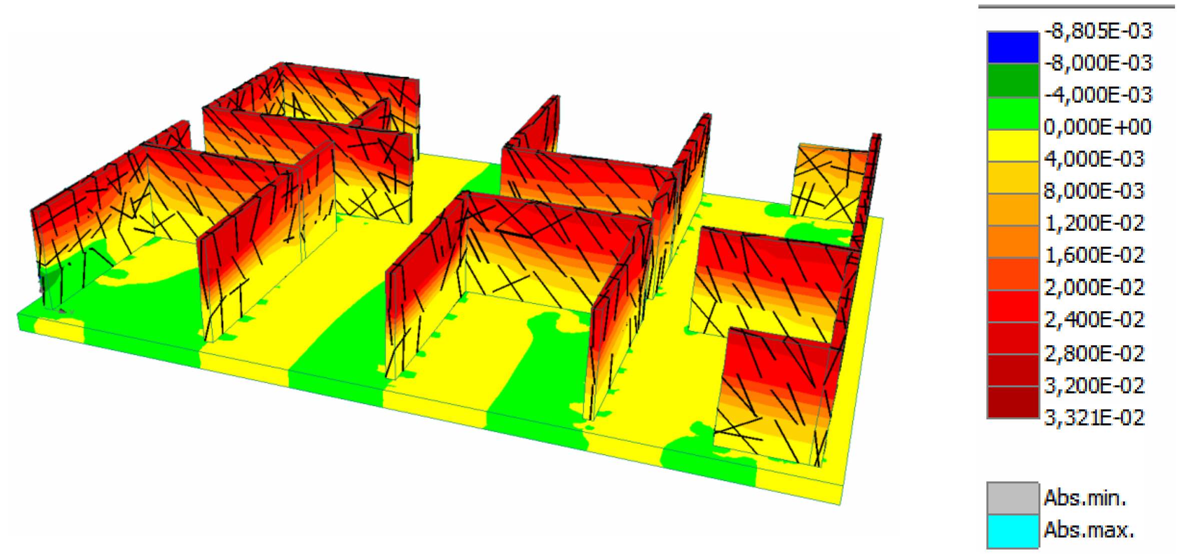

Figure 197 *Deformation +x1 direction scale [m] superelevation 2x.*

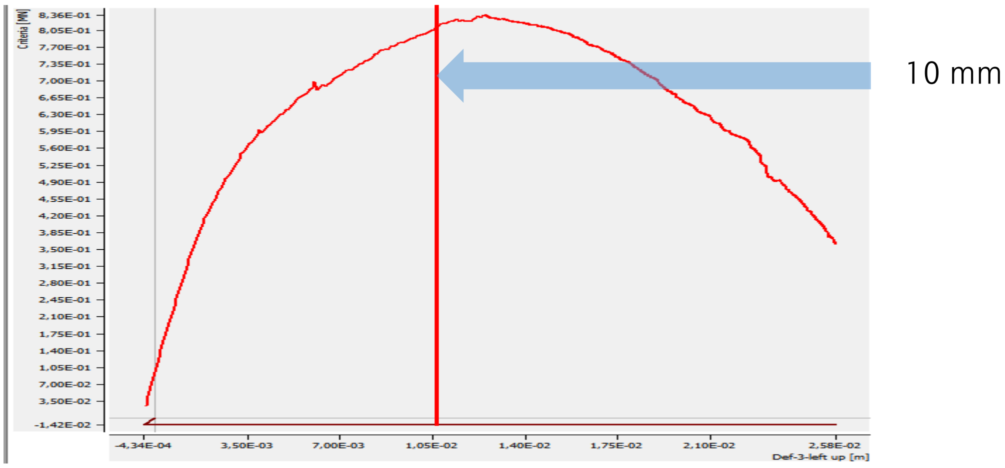

Figure 198 *House Deformation-force-diagram for +x1.*

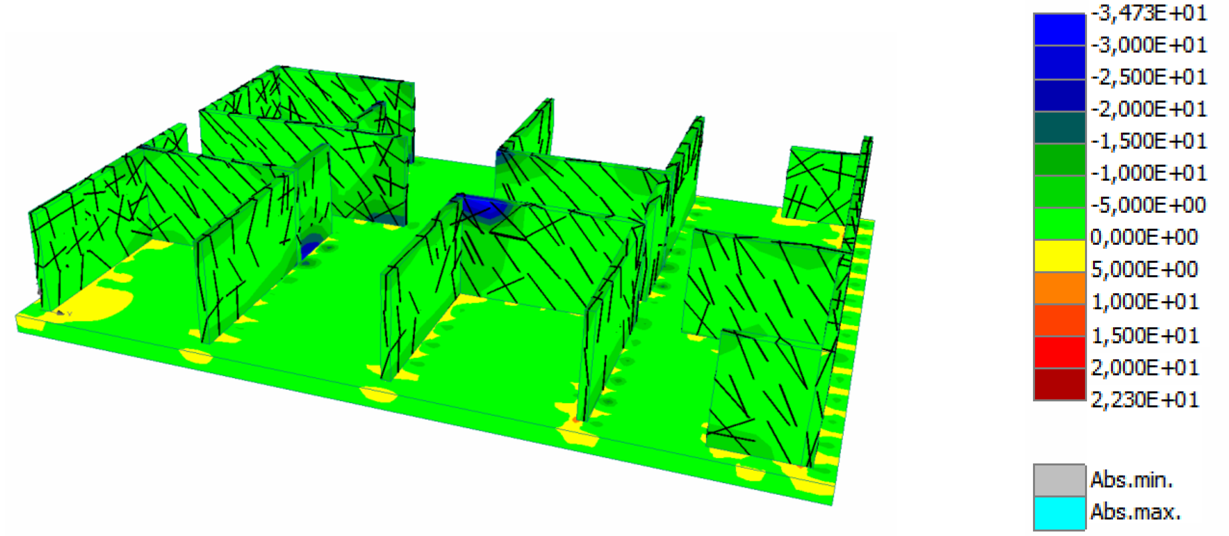

Figure 199 *House σ_{xx} force +x1with (absolutely) maximum -34.73 MPa superelevation 2x.*

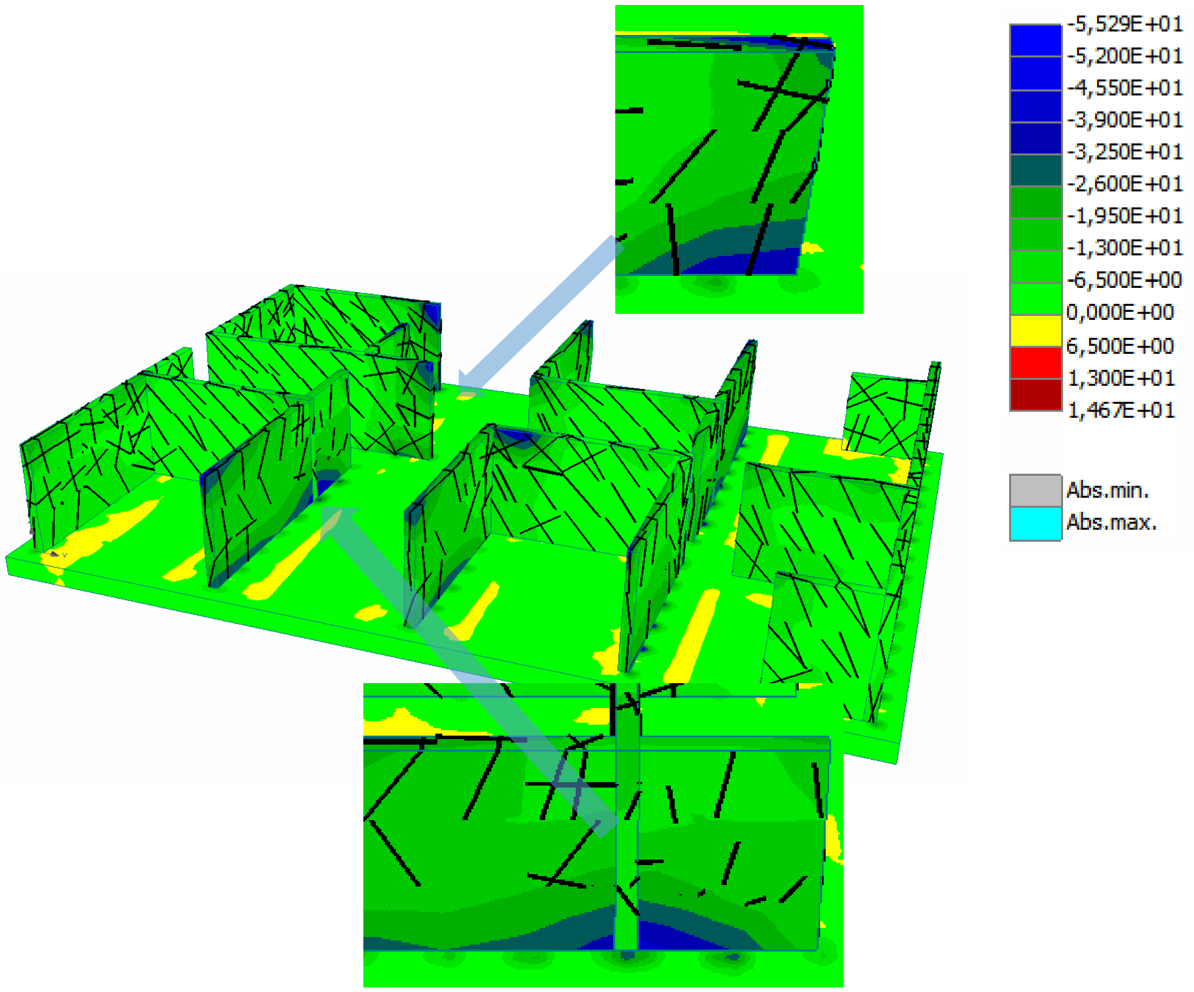

Figure 200 House σ_{zz} force +x1with (absolute) maximum -55.29 MPa superelevation 2x.

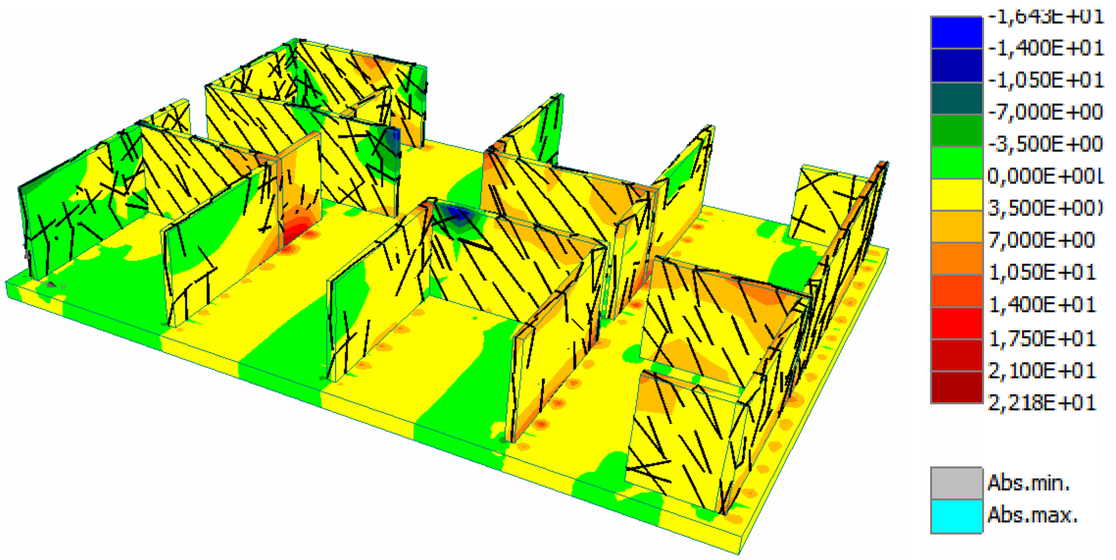

Figure 201 House τ_{xz} force +x1with maximum 22.18 MPa superelevation 2x.

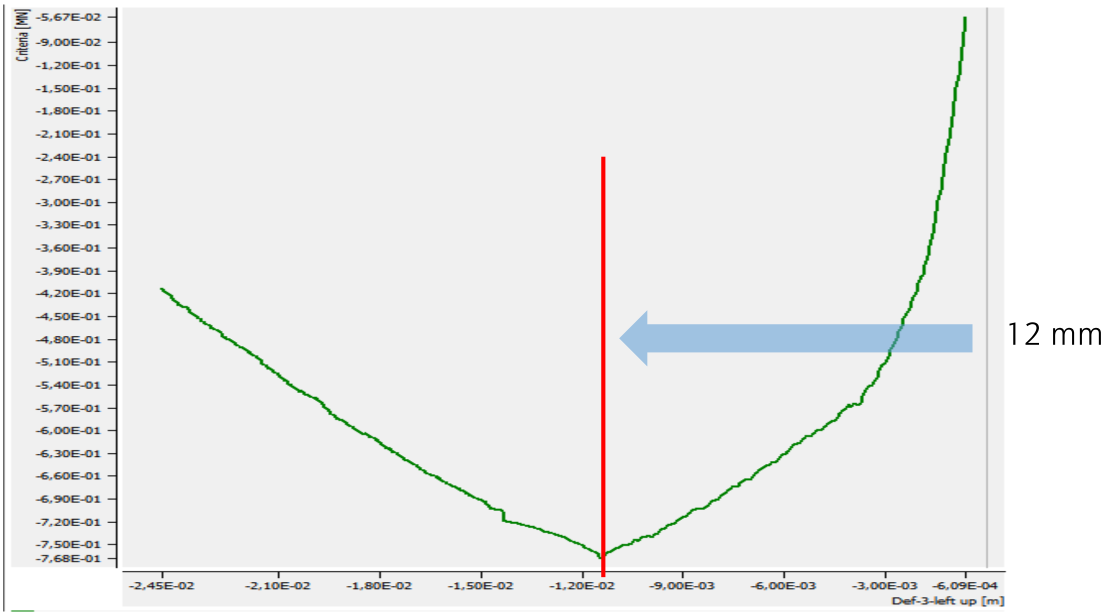

Figure 202 House Deformation-force-diagram for -x1.

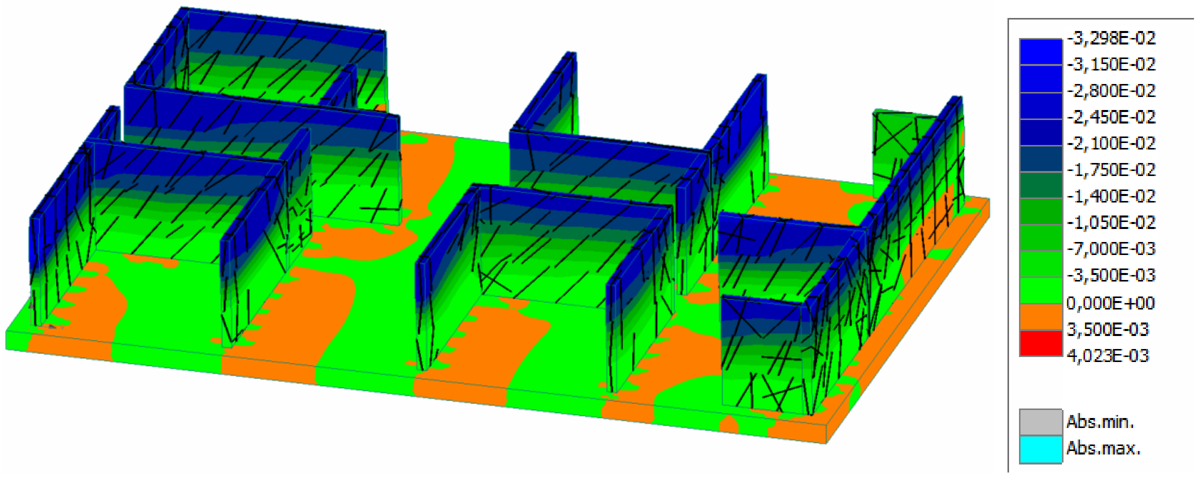

Figure 203 House Deformation -x1 direction scale [m] superelevation 2x.

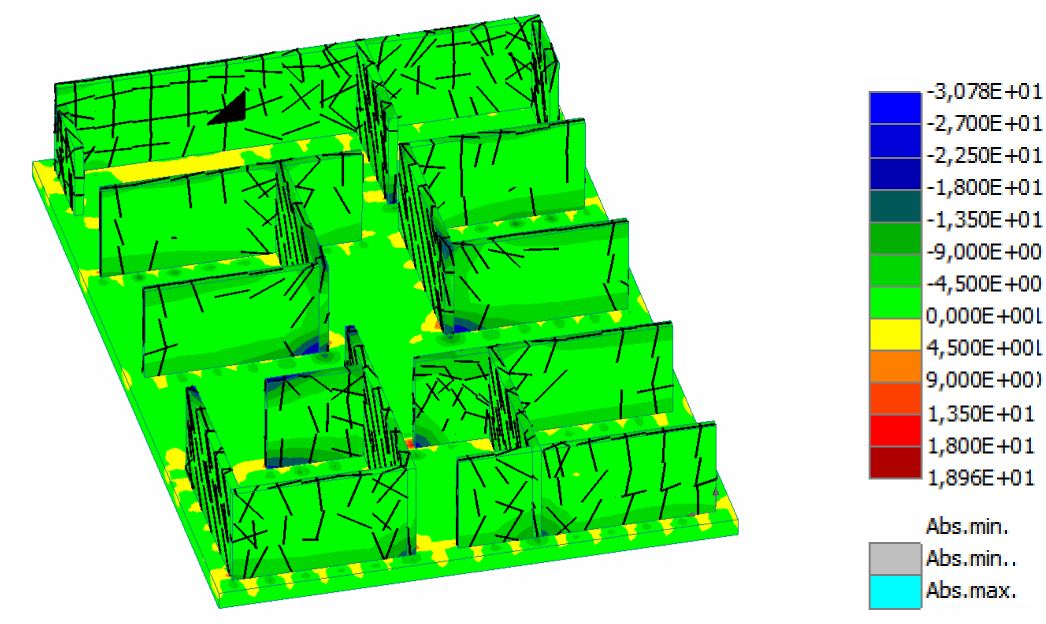

Figure 204 *House* $\boldsymbol{\sigma_{xx}}$ *force -x1with (absolutely) maximum -27.00 MPa superelevation 2x.*

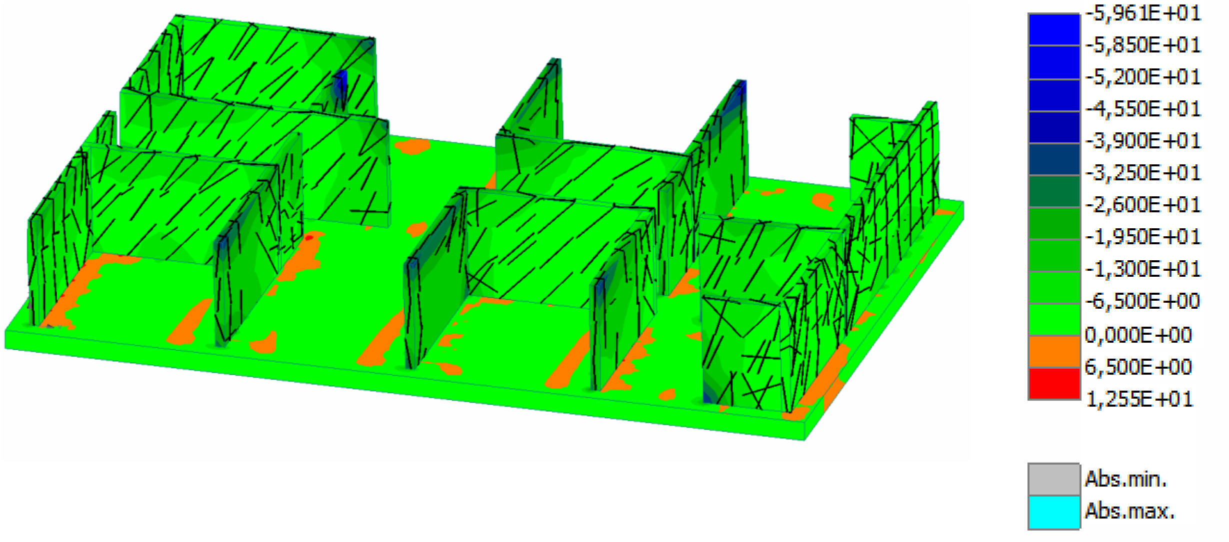

Figure 205 *House* $\boldsymbol{\sigma_{zz}}$ *force -x1with (absolutely) maximum -59.61 MPa superelevation 2x.*

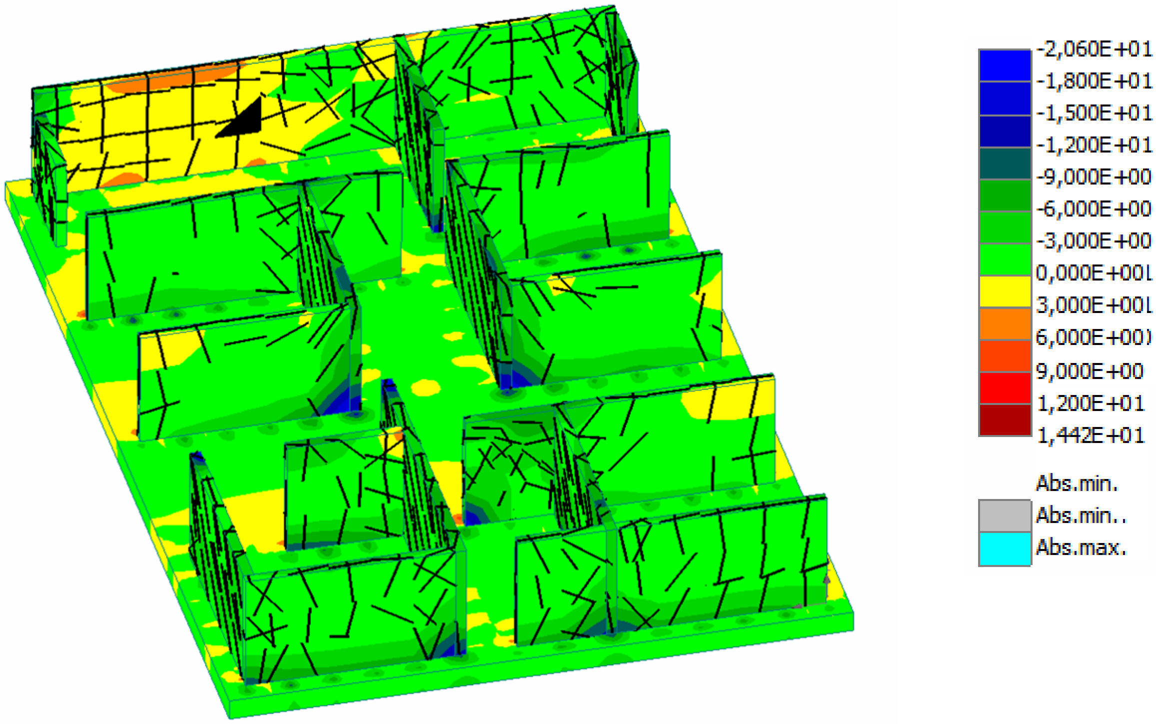

Figure 206 House $\boldsymbol{\tau_{xz}}$ force +x1with (absolutely) maximum 20.60 MPa superelevation 2x.

6 Summary and Conclusion

6.1 Further fine tuning

These tests and the analytic calculations are only the theoretical part of the storey, applied the product "double walls for earthquake-proof buildings". In addition, other technical adjustments, such as the procedure of moving the rebar cages, are necessary.

For the test we moved the reinforcement cages into position by hand, with a hook.

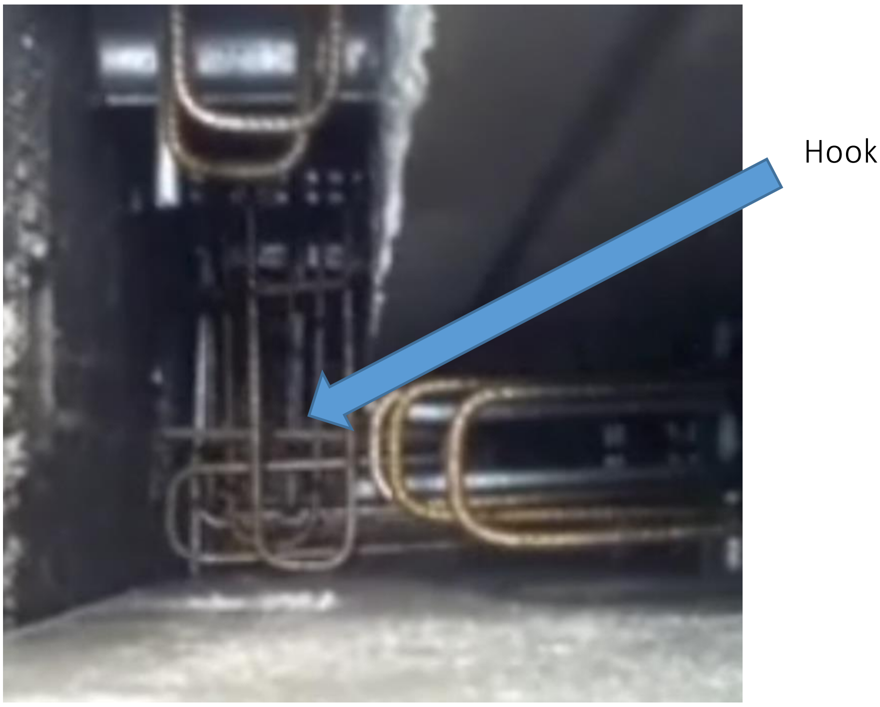

Figure 207 Moving reinforcement cage by hand (with hook).

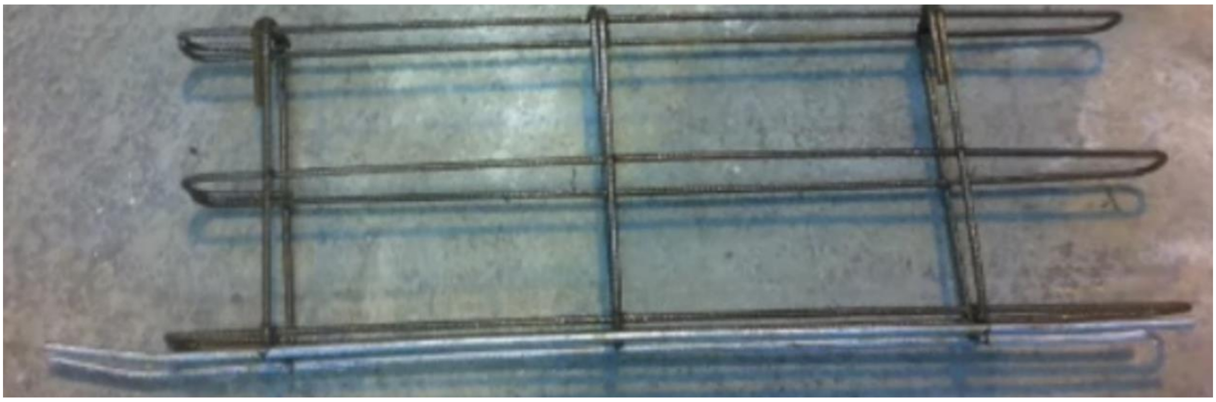

Figure 208 Reinforcement cage with sliding-steel-bars.

Thus, the best way to shift the reinforcement cage is still by means of a compressed air bolt.

6.2 Conclusion

Five tests were conducted on vertical load bearing systems built using the double wall system in the course of this project. In addition, one filigree slab-wall connection was conducted. Tests were performed under simulated earthquake loading with a reversed cyclic testing scheme. Both global and local deformations were measured during the experiments. Lateral load-lateral displacement profiles, moment curvature responses and damage patterns were reported for each test. Based on the test results and observations during tests, the following main conclusions can be drawn:

- Specimen #1 (monolithic double wall with insolation) and specimen #2 (built from two double walls, side by side with insulation) behaved in practically in the same manner. In other words, the lateral load carrying capacity, deformation capacity and ductility of the two specimens were similar for these two specimens. This result proves that walls built from adjacent double walls connected to each other with cages can be assumed to behave as monolithic walls.
- The behavior of specimen #3 with the U section was very ductile and did not experience any strength drop up to 1.25% drift ratio. The ductility of this specimen was as high as 7.5. This result shows that U section double walls can exhibit good seismic performance when detailed according to the seismic design principles.
- The behavior of specimen #4 with the T section was ductile and was able to sustain its lateral load carrying capacity up to 0.8% drift ratio. The ductility of this specimen was about 4. This result shows that T section double walls can exhibit acceptable ductility levels when detailed according to the seismic design principles.
- The response of specimen #3 was better compared to specimen #4, due to the presence of two web sections. This fact was reflected both in the load carrying capacity and ductility.
- The precast double wall column behaved in a very ductile manner. The significant damage zone was limited with the bottom 50 mm, which was left as a gap under the concrete shells (cast-in-place concrete filled this gap). This specimen was able to reach up to 3% drift ratio without losing its lateral strength.
- Comparisons with previous test results revealed that the behavior of the precast column was as good as a similar column prepared with cast-in-place concrete.
- Moment curvature results for the test specimens show that the strength and section response of the double walls can be conducted with standard section analysis procedures of reinforced concrete. This fact enables the use of existing analysis tools for structural design when double wall systems are employed.

- The test results show that double wall precast vertical load bearing members can be designed as ductile elements. These can be used safely in earthquake resistant design of buildings upon correct design and detailing. As the double walls can be designed with any desired reinforcement detailing, one can easily follow the requirements of earthquake codes during their production.
    - The displacement ductility levels of all the tested walls ranged between about 4 and 7.5.
- It should be recognized that tested walls were squatter than those that would be constructed in multi-storey buildings. One can easily realize that the seismic behavior of building walls will even be more ductile than those observed in the tests. It is known that the overstrength factor assumed by the Turkish Earthquake Code is 1.5.
- It was showed that the KAPPEMA-rebar-stick, as the connecting part of the KAPPEMA-waves, can substitute the obligatory S-hook.

- To summarize the results in two short sentences:
  The double wall with the wave-connection can be designed like a conventional in-situ concrete wall and also be reinforced like a construction sites produced wall.
  In addition, a single stick of the KAPPEMA wave is constructively and statically equivalent to an S-hook.

7. Bibliography

[1] E. Kastner, „freepatentonline," [Online]. Available: http://www.freepatentsonline.com/EP2669445.pdf. [Zugriff am 12 2014].

[2] DEPATISnet, „Deutsches Patent- und Markenamt," [Online]. Available: https://depatisnet.dpma.de/DepatisNet/depatisnet?window=1&space=menu&content=treffer&action=pdf&docid=WO002009112409A3&Cl=&Bi=1&Ab=1&De=&Dr=&Pts=&Pa=&We=&Sr=3&Eam=&Cor=&Aa=&so=asc&sf=vn&firstdoc=1&NrFaxPages=8&pdfpage=1&xxxfull=1. [Zugriff am 12 2014].

[3] „TU Wien Institut für Hochbau und Technologie," [Online]. Available: http://iht.tuwien.ac.at/home/. [Zugriff am 18 12 2014].

[4] MIDDLE EAST TECHNICAL UNIVERSITY-Ankara, „MIDDLE EAST TECHNICAL UNIVERSITY-Ankara," 2014. [Online]. Available: http://eerc.metu.edu.tr/executive-board. [Zugriff am 18 12 2014].

[5] Franz Oberndorfer GmbH & Co, „Franz Oberndorfer GmbH & Co KG," [Online]. Available: http://iht.tuwien.ac.at/home/. [Zugriff am 12 2014].

[6] Wikipedia, „Dreifachwand," [Online]. Available: http://de.wikipedia.org/wiki/Dreifachwand. [Zugriff am 12 2014].

[7] KAPPEMA, „KAPPEMA," [Online]. Available: http://www.kappema.com. [Zugriff am 12 2014].

[8] Cervenka Consulting, „ATENA 5," [Online]. Available: http://www.cervenka.cz/products/atena/. [Zugriff am 12 2014].

[9] Doppelwand Qualitätsgemeinschaft, „Qualitätsgemeinschaft Doppelwand," Qualitätsgemeinschaft Doppelwand Bayern, 2014. [Online]. Available: http://www.doppelwand.com/. [Zugriff am 14. Dezember 2014].

[10] H. Sucuoglu und S. Akkar, Introduction to Earthquake Engineering for structural Engineers, M. S. 2013, Hrsg., Ankara: UME Graduate School, 2013.

[11] M. Fischinger, P. Fajfar und F. Capuder, „Earthquake Resistabce of the "SCT" Large Panel Buildingf System," New Zealand National Society for Earthquake Engineering , Wellington, 1987.

[12] Oberndorfer, „Franz Oberndorfer GmbH & Co KG," 2015. [Online]. Available: http://www.oberndorfer.at. [Zugriff am 5 Jänner 2015].

[13] IADC, „IADC Drilling Lexicon," 2015. [Online]. Available: http://www.iadclexicon.org/ductility-ratio/. [Zugriff am 15 01 2015].

[14] A. Bekö und P. Rosko, „Testing of Stiff Shear Walls," IRIS-Integrated European Industrial Risk Reduction System CP-IP213968-2, Vienna, 2012.

[15] C. A. Whyte, Hybrid Simulation of the Seismic Response of Squat Reinforced Concrete Shear Walls, D. T. i. E. a. E. Engineering, Hrsg., Berkeley: Univerity of California, Berkeley, 2012.

[16] C. K. Gulec und A. S. Whittaker, „Performance-Based Assessement and Design of Squat Reinforced Concrete Shear Walls," Earthquake Engineering Research Centers Program, 2009.

[17] A. C. Heidebrecht und B. Stafford Smith, „Approximate analysis of tall wall-frame structures," *J Struct Div 98*, pp. 1233 - 1237, 1972.

[18] P. Linde und T. Wenk, „Numerical Modelling and Damage Evaluation of Earthquake-Resistant Reinforced Concrete Walls," in *10th European Conference on Earthquake Engineering (ECEE)*, Vienna, 19994.

[19] F. J. Vecchio, „Lessons from the Analysis of a 3-D Concrete Wall," *Struct. Enrg. and Mechanics Vol. 6*, pp. 439 - 455, 1998.

[20] D. Palermo und F. J. Vecchio, „Behavior and Analysis of Reinfrced Concrete Walls Subjected to Reversed Cyclic Loading," Toronto, 2002.

[21] D. Palermo und F. J. Vecchio, „Compression Field Modeling of Reinforced Concrete Subject to Reversed Loading: Formulation," *ACI Structural Journal*, pp. 616 - 625, 10 2003.

[22] E. Anderheggen, Starr-plastische Traglastberechnungen mittels der Methode der Finiten Elemente, I. f. B. E. T. Hochschule, Hrsg., Zürich, 1971.

[23] E. Anderheggen, „FLOWERS: Ein neues Finite-Element-Programm für Lehre, Forschung und Praxis," *Schweizer Ingenieur und Architekt*, Bd. 101 (1983), Nr. Heft 6, pp. 99 - 103, 1983.

[24] J. Lee und G. Fenves, „Plastic-Damage Model for Cyclic Loading of Concrete Structures," *J. Eng. Mech.*, Bd. 124(8), pp. 892 - 900, 1998.

[25] N. J. Stevens, M. P. Collins und S. M. Uzumeri, „Analytical Modeling of Reinforced Concrete Subjected to Monotonic and Reversed Loading," Toronto, 1987.

[26] X. Xu und A. Needleman, „Void nucleation by inclusing debonding in a crystal matrix," *Materials Science and Engineering*, pp. 111 - 132, 1993.

[27] J. Izumo, H. Shima und H. Okamura, „Analytical models for RC panel elements subjected to in-plane forces," JSCE, 1989.

[28] J. Cervenka und Z. Prochazkova, ATENA Program Documentation ATENA 3D Tutorial & Manual, Prague: Cervenka Consulting s.r.o., 2013.

[29] V. Cervenka, L. Jendele und J. Cervenka, ATENA Program Documentation, ATENA Theory, Prague: Cervenca Consilting s.r.o., 2014.

[30] R. T. Duarte und A. C. Costa, „Earthquake Design of Reinforced Concrete Structures based on Local Ductility Coefficients," in *Ninth World Conference on Eartquake Engineering*, Tokyo-Koyoto, 1988.

[31] J. D. Osteraas und H. Krawinkler, „Strenght and Ductility Considerations in Seismic Design," Stanford University, Stanford, 1990.

[32] J. B. Mander, F. D. Panthaki und A. Kasalanati, „Low-Cycle Fatigue Behavior of Reinfrcing Steel," *Civ. Eng. ASCE,6,* pp. 453-468, 1994.

[33] H. Sucuoglu und A. M. Erberik, „Energy Based Performance Evaluation of Deterioprating Structures," in *13th World Conference on Earthquake Engineering*, Vancouver, 2004.

[34] A. Ilki und Z. Celep, „Earthquake, Existing Buildings and Seismic Design Codes in Turkey," *Arabian Journal for Science and Engineering,* pp. 365 - 380, 2012.

[35] S. Pirringer und J. Kollegger, „Bond behavior between concrete and perforated metal shes for use in composite slabs," Brecia, 2012.

[36] Jaera GmbH & Co. KG, „JAERA," 2015. [Online]. Available: http://www.jaera.de/produkte/index.php?uid=1&pro=1. [Zugriff am 06 01 2015].

[37] „Deutsche Edelstahlwerke GmbH," 2015. [Online]. Available: http://www.dew-stahl.com/fileadmin/files/dew-stahl.com/documents/Publikationen/Werkstoffdatenblaetter/RSH/1.4301_de.pdf. [Zugriff am 06 01 2015].

[38] B. Acun, „Energy Based Seismic Performance Assessment of Reinforcef Concrete Volumns," Ankara, 2010.

[39] E. C. Bentz, Sectional Analysis of Reinforced Concrete Members, Bd. PhD Thesis, Toronto: Department of Civil Engineering, University of Toronto, 2000.

[40] M. P. Collins und D. . Mitchell, Prestressed Concrete Structures, Prentice Hall, 1991.

[41] F. J. Vecchio und M. P. Collins, „he Modified Compression Field Theory for Reinforced Concrete Elements Subjected to Shear," *ACI Journal,* Bde. %1 von %283-2, pp. 219 - 231, 1986.

[42] P. Menétrey und K. Willam, „Triaxial Failure Criterion for Concrete and its Generalization," *Structural Journal ACI,* pp. 311-318, 01 05 1995.

[43] CEB Euro-International Committee for Concrete , CEB/FIP Model Code for Concrete Structures 1990, 1990 Hrsg., f. -. F. i. d. béton, Hrsg., Lausanne: fib - Fédération internationale du béton, 1990.

[44] V. Cervenka, „Constitutive Model for Cracked Reinforced Concrete," *ACI Journal*, pp. 877 - 882, 11 1 1985.

[45] D. Darwin und D. A. W. Percknold, „Inelastic Model for Cyclic Biaxial Loading of Reinforced Concrete," 1974.

[46] F. J. Vecchio und M. P. Collins, „The Modfied Compression-Field Theory for Reinforced Concrete Elements Subjected to Shear," *ACI Journal,* Nr. p 219 -231, 1986.

[47] M. A. Crisfield und J. Wills, „Analysis of R/C panels using different concrete models," *Journal Engineering Mechanics,* Bd. 115, pp. 578 - 597, 1989.

[48] J. Kollegger, „Ein Materialmodell für die Berechnung von Stahlbetonflächentragwerken," *Sissertation Uni Kassel,* 1988.

[49] Z. P. Bazant und B. H. Oh, „Crack band Theory for fracture of concrte," *Material and Structures,* Bd. 16, pp. 155 - 177, 1983.

[50] P. H. Feenestra und R. de Borst, „Constitutive Model for Reinforced Concrete," *Journal of Engineerimg Mechanics*, pp. 587 - 595, May 1996.

[51] V. Cervenka, „Computer Simulation of failure of Concrete Structures for Practice," 2002.

[52] F. J. Vecchio, „Reinfirced Concrete Membrane Element Formulation," *Journal of Structural Engineering,* Bd. Val. 116 No. 3, Nr. p 730 - 750, 1990.

[53] M. Menegotto und P. E. Pinto, „Method of analysis for cyclicylly loaded reinforced concrete plane frames including changes in geometry and non-elastic behaviour of elements under combiend normal force and bending," in *IABSE Symp. of Resistnace and Ultimate Deformability of Structures Acted on by Well-Defined Repeated Loads*, Lisbon, Portugal, 1973.

[54] T. Albanesi und C. Nuti, „Reinforcing Steel Bar Model," 2007.

[55] Austrian Standard, ÖNORM 1992-1-1 Eurocode 2 - 1, Wien: Austrian Standard, 2011.

[56] H. Bachmann, A. Dazio, P. Bruchez, X. Mittaz, R. Peruzzi und P. Tissière, „SIA D 0171 Erdbebengerechter Entwurf und Kapazitätsbemessung eines Gebäudes mit Stahlbetontragwänden," Zürich, 2002.

[57] L. N. Lowes, „Finite Element Modeling of Reinforced Concrete Beam-," University of California, Berkeley, Berkeley, 1999.

[58] G. G. Deierlein, A. M. Reinhold and M. R. Willford, "Nonlinear Structural Analysis For Seismic Design," U.S.Department of Commerce NIST GCR 10-917-5, Gaithersburg, 2010.

[59] S. Sunley und K. Kusunoki, „Experimental Study of Flexural Behavior of Reinforced Concrete Walls," IISEE Publications Synopsis Database, Tsukuba, Ibaraki 305-0802, Japan., 2008.

[60] W. Potucek und M. Kofler, Eurocodes für die Planung und Berechnung von Betonbauten, Wien: Austrian Standards plus Publishing, 2014.

[61] H. Friedl, S. Lu und M. Ralbovsky, Erdbebenlasten Eurocode 8, Wien: Austrian Standards plus Publishing, 2014.

[62] S. Guner und J. F. Vecchio, „Simplified Method for Nonlinear Dynamic Analysis od Shear-Critical-Frames," *ACI Structural J. Vol. 109*, pp. 727-737, 2012.

[63] S. Gunar und F. Vecchio, „Analysis of Shear-Critical Reinforced Concrete Plane Frame Elements under Cyclic Loading,“ *ASCE J. of Structural Engrg. Vol. 137,* pp. 834 - 843, 2011.

[64] T. Branci und S. Bourada, „Accounting for ductility and overstrenght in seismic design of reinforced concrete structures,“ EURODYN 2014 9th International Conference on Structural Dynamics,, Porto, Portugal, 2014.

[65] J. W. Wallace, „Behavior, Design, and Modeling of Structural Walls and Coupling Beams,“ *International Journal of Concrete Structures and Materials*, pp. 3 -18, 2012.

[66] D. Moroder, A. H. Buchanan und S. Pampanin, „Preventing seismic damage to floors in post-tensioned timber frame buildings,“ in *2013 NZSEE Conference*, Wellington, 2013.

[67] P. E. Mergos und K. Beyer, „Modelling shear-flexure interaction in eqivalent frame models of slender RC walls,“ in *15 WCEE World Conferences on Earthquake Engineering (*, Lisboa, 2012.

[68] R. Constantin und K. Beyer, „Modelling of Reinforced Concrete Core Walls Under Bi-directional Loading,“ Lisboa, 2012.

[69] S. H. Lee, S. J. Hwang, K. B. Lee, C. B. Kang, S. H. Lee und S. H. Oh, „Earthquake Simulation Tests on a 1:5 Scale 10-Storey RC Residential Building Model,“ Lisbao, 2012.

[70] Z. Tuna, S. Gavridouz, J. W. Wallace, T. Nagae und T. Matsumori, „1010 E-Defense Four-Storey Reinforced Concrete and Post-Tensiond Buildings - Preliminary Comparitive Study of Experimantal ans Analytical Results,“ Lisbao, 2012.

[71] K. Beyer, A. Dazio, M. J. N. Pristley, D. Chem und K. Ge, „ShearDeformations of Slender Reinforced Concrete Walls under Seismic Loading,“ *ACI Structural Journal,* p. 167 p.p., 2011.

[72] H. Krawinkler, Y. Bozorgnia, C. B. Crouse, R. O. Hamburger, R. Klemencic, J. O. Malley, J. P. Moehle, F. Naeim und J. P. Stewart, „Tall Buiolding Initiative Respons Evaluatiopn,“ Berkeley, 2010.

[73] A. Mortezaei und A. Kheyroddin, „Size Effects in Reinforced Concrete Flanged Shear Walls,“ *Internationmal Journal of Cicil Engineering,* Bd. 7, 2009.

[74] C. Bora , M. Oliva, S. Dow Nakaki und R. Becker, „Development of a Precast Concret Shear-Wall System Requiring Special Code Acceptance,“ *PCI Journal,* Nr. January-February, 2007.

[75] P. Lestuzzi und H. Bachmann, „Displacement ductility and energy assessment from shaking table tests on RCstructural walls,“ *Engineering Structures Elsevier,* Bd. 29, Nr. 1708 - 1721, 2006.

[76] I. Merta und A. Kolbitsch, „Shear Area of Reinforced Concrete Circular Cross-Section Members,“ Signapore, 2006.

[77] A. Carbonari , M. De Grassi, C. Di Perna und P. Principi, „Numerical ans experimental analyses of PCM containing sanwich panels for prefabricated walls," *Energy and Buildings*, Bd. 38, Nr. p 472 - 483, 2006.

[78] S. J. Kuang und Y. B. Ho, „Inherent Ductility of Reinforced Concrete Shear Walls with Non-Seismic Detailing," Signapre, 2006.

[79] A. Dazio, „Tragfähigkeit von Betonbauten," Zürich, 2005.

[80] K. Pitilakis, C. Gazepis und A. Anastasiadis, „Design Response Spectra ans Soil Classification foe Seismic Code Provisions," Vancouver, 2004.

[81] H. Krawinkler, F. Zareian, R. A. Medina und L. Ibarra, „Contrasting Performance-based Design with Performance Assessement," Bled, 2004.

[82] D. Palermo und F. J. Vecchio, „Compression Filed Modeling of Reinforced Concrete Subjected to Reversed Loading: Verification," *ACI Structural Journal*, Bde. %1 von %2March - April , Nr. p 155 - 164, 2004.

[83] T. Wenk, „Nichtlineare dynamische Berechnung von Stahlbetonrahmen unter Erdbebenwirkung," Institut für Baustatik und Konstruktion ETH Zürich, Zürich, 2000.

[84] P. A. Hidalgo, C. A. Ledezma und R. M. Jordan, „Seismic Behavior of Squat Reinforced Concrete Shear Walls," *Earthquake Spectra*, Bde. %1 von %218-2, Nr. p 287 - 308, 2002.

[85] K. William, E. Hansen und H. D. Kang, „Performance Evaluation of Damage and Plasticity Formulations for Concrete," in *Modeling of inelastic Behavior of RC Structures under Seismic Loaf*, Reston, VA 20191, ASCE American Society of Cicil Engineers, 2001.

[86] B. Borzi und A. S. Elnashai, „Refined force reduction factors for seismic design," *Engineering Structures*, Bd. 22, Nr. p 1244 - 1260, 2000.

[87] P. Faifar, „Capacity Spectrum Method based on Inelastc Demand Spectra," *Earthquake Engineering and Structural Dynamics*, Bd. 28, Nr. p 979 - 993, 1999.

[88] U. Ersoy und G. Özcebe, „Moment-Curvature Relationship of Confined Concrete Sections," in *Digest 98*, Ankara , Turkish Chamber of Civil Engineers, 1989.

[89] H. Krawinkler und G. P. Seneviratna, „Pros and cons of a pushover analysis of seismic performance evaluation," *Engineering Structures*, Bd. 20, Nr. 99 452 464, 1998.

[90] M. S. Medhekar und S. K. Jain, „Seismic bhaviour, design and detailing of RC Shear walls, Part I: Behaviour and strenght," *The Indian Concrete Journal*, Bd. July 1993, 1993.

[91] B. J. Davidson, R. C. Fenwick und B. T. Chung, „P-delta effects in mult-storey structural design," Rotterdam, 1992.

[92] J. Kollegger, „Algorithmus zur Bemessung von Flächentagwerkelementen unter Normalkraft- und Momeneten-beans," *Beton- und Stahlbetonbau*, Bd. Heft 6, Nr. pp 114 - 119, 1991.

[93] D. Escolano-Margarit, A. Klenke, S. Pujol und A. Benavent-Climent, „Failure Mechanism of Reinforced Concrete Structural Walls with and without Confinement," Lisboa, 2012.

[94] J. P. Moehle, T. Ghodsi, J. D. Hooper, D. C. Fields und R. Gedhada, „NEHRP Seismic Design Technical Brief no. 6," Gaithersburg, 2012.

[95] C. Greifenhagen, „Seismic Behavior of Light Reinforced Concrete Squat Shear Walls," Lausanne, 2006.

[96] M. N. Shirali, „Seismic Resistance of a Hybrid Shearwall System," Darmstadt, 2002.

[97] B. Rusnov, „Analyse von erdbebengefährdeten Bauwerken mit dem Schwerpunkt auf alten und historischen Gebäuden," Wien, 2006.

[98] D. Palermo und F. J. Vecchio, „Behavior of Cyclically Loaded Shear Walls," 2003. [Online]. Available: http://www.civ.utoronto.ca/vector/journal_publications/jp39.pdf. [Zugriff am 12 2014].

[99] K. Beyer und T. Wenk, „Das Verhalten von Gebäuden mit Stahlbetontragwänden während des Erdbebens Centro-Sur in Chile am 27.2.2010," Bde. %1 von %2D-A-CH Mitteilungsblatt , Nr. Band 85, September 2010, pp. 10 - 20, 2010.

[100] H. Cho, „Virtual Earthquake Engineering Laboratory Capturing Nonlinear Shear, Locolized Damage and Progressive Buckling of Bar," *Earthquake Spectra*, pp. 103 - 126, 02 2013.

[101] D. Palermo und F. J. Vecchio, „Behavior of Tree-Dimensional Reinforced Concrete Shear Walls," *ACI Structural Journal*, pp. 81 - 89, 02 2002.

[102] D. Palermo und F. J. Vecchio, „Compression Field Modeling of Reinforced Concrete Subjected to ReveLoading: Verification," *ACI Structural Journal*, pp. 155 - 164, 04 2004.

[103] F. J. Vecchio, O. A. Haro de la Pena, F. Bucci und D. Palermo, „Behavior of Repoired Cycilcally Loadet Shearwalls," *ACI Structural Journal*, pp. 327 - 334, 05 2002.

[104] J. L. Humar und M. A. Rahgozar, „Concet of Overstrength in Seismic Design," in *Eleventh World Converence on Earthquake Engineering*, Acapulco, Mecico, 1996.

[105] R. Pukl, J. Cervenca und V. Cervenca, „Simulating a respoponse of connections," in *RELEM Symp. on Connections between Steel ans Concrete*, Stuttgart, Germany, 2001.

[106] International Code Council Inc., IBC International Building Code, U.S.A.: International Code Council Inc., 2011.

[107] M. o. H. a. U.-R. C. o. t. P. R. o. China, „Code for Seismic Design of Buildings GB 50011-2010," Ministery of Housing and Urban-Rural Construction of the People's Republic of China, Beijing, 2010.

[108] Normeninstitut, „ÖNORM EN 1998-1," Austrian Standard, Vienna, 2008.

[109] ÖNORM B1998-1Bauwesen, Normenkomitee 176 Belastungsannahme, „ÖNORM B1998-1," Austrian Standards Institute, Wien, 2011.

[110] W. Raongjant, „Seismic Behaviour of Lightweight Reinforced Concrete Shear Walls," Gottfried Wilhelm Leibnitz Universität, Hannover, 2007.

[111] fib Task Group 7.6, Critical comparison of major seismic codes for buildings, Bde. %1 von %2fib Bulletin No, 69, f. -. F. i. d. béton, Hrsg., Lausanne: fib - Fédération internationale du béton, 2013.

[112] G. Achs und C. Adam, „Risikobewertung von Wiener Gründerzeithäusern unter Erdbebeneinwirkung," in *SEISMID*, Vienna, 2011.

[113] C. Doneux, Etude du méchanisme de transfet des Flexions à la jonction poter poteau dans les structures en portique mixtes soumises à une action sismique, Liège: Université de Liége, 2002.

[114] D. Yuzugullu, Finite Element Approach for the Prediction of Inelastic Behaviour of Shear Wall-Frame Systems, U. o. I. a. U. Department of Cicil Engineering, Hrsg., Urbana IL: PhD, Dissertation, 1972.

[115] P. Lestuzzi und H. Bachmann, „Displacement ductility and energy assessment from shaking table tests on RC structural walls," *Engineering Structures*, pp. 1708 -1721, 2006.

[116] C. Doneux, ètude du mécanisme de ftransfert des flexions à la jontion poutre poteau dans les structures en portiquees mixtes soumises à une action sismique, T. d. Doctorat, Hrsg., Liège: Université de Liège, 2002.

[117] P. A. Hidalgo, C. A. Ledezma und R. M. Jordan, „Seismic Behavior of SAquat Reinforced Concrete Shear Walls," *Earthquake Spectra*, 2002.

[118] G. Watanabe und K. Kawashima, „An Evaluation of the Force Reduction Factor in the Force-Based Seismic Design," O-Okayama, Meguro Tokio, JKapan 152-8552, 2002.

[119] X. Lu und J. Jiang, „Analysis for Concrete Structure under Complex Stress Condition with Solid 65 FEA Element of Ansys," *Building structures*, Bd. 33(6), pp. 22 - 24, 2003.

[120] CubusAG, „Cubus-Software," 2015. [Online]. Available: http://www.cubus-software.com. [Zugriff am 12 01 2015].

[121] J. Maier und B. Thürlimann, „Bruchversuche an Stahlbetonscheiben," Birkhäuser, Stuttgart, Boston, 1085.

[122] E. C. Bentz und M. P. Collins, „Response 2000," 2015. [Online]. Available: http://www.ecf.utoronto.ca/~bentz/r2k.htm. [Zugriff am 14 01 2015].

[123] E. Bentz und M. Collins, „Response 2000," 2010. [Online]. Available: http://www.ecf.utoronto.ca/~bentz/r2k.htm. [Zugriff am 15 01 2015].

[124] M. o. P. W. a. Settlement, „Turkish Earthquake Code 2007," 2007.

[125] J. Matos, „Uncertainty evaluation of reinforced concrete and composite structures behavior," 2013.

[126] V. Cervenka, D. Novak, D. Lehky und R. Pukl, „Identification of Shear Wall Failure Mode," ICF International Congress on Fracture , Turin, 2005.

[127] H. Cifuentes, M. Alcalde und F. Medina, „Comparison of the Size-Independent Fracture Energy of Concrete Obtained by Two Test Methods," Toledo, 2013.

[128] Sievert, „Technical specification for superimposed slab concrete shear wall structure," 2008.

[129] KIPTAS, „KIPTAS Kardelen Blokları Ev Tipi," 2015. [Online]. Available: http://www.kiptas.com.tr/en/page/en-kardelen-bloklari-ev-tipi. [Zugriff am 05 Jänner 2015].

8. Abbreviations, Notation

Most of the Abbreviations are explained, when used within the text.

<u>Latin upper case symbols</u>

A	Cross-section area
A_a	Cross sectional areas of the structural steel
A_c	Gross cross-sectional area of concrete
A_e	Minimum cross sectional area in any horizontal plane of a Structural wall in the first storey of a structural wall
A_i	Effective cross sectional area in any horizontal plane in the first storey of a structural wall
A_s	Cross sectional areas of the reinforcement
A_{vf}	Shear-friction reinforcement across the shear plane
DR	Drift Ratio
E_o -	Initial elastic modulus
E_a	Modulus of elasticity of the structural steel
E_c	Modulus of elasticity of the concrete and (ATENA) Secant elastic modulus at the peak stress and initial elastic modulus
E_s	Modulus of elasticity of the reinforcement
F_b	Seismic base shear force
F_R	Experimental reference force value
F_i^f	Rankine criterion for concrete cracking
G_c	Initial concrete shear modulus
G_f	Fracture energy
G_t	Tangent shear modulus
N	Axial force
R	Reduction factor due to ductility according Turkish Earthquake Code

Latin lower case symbols

$\boldsymbol{a_g}$	Maximum aggregate size
$\boldsymbol{c}$	Compressive strength in cracked concrete
$\boldsymbol{f_c}$	Compressive strength concrete
$\boldsymbol{f'_c}$	Cylinder strength (ATENA)
$\boldsymbol{f'_{cu}}$	Cube strength
$\boldsymbol{f_c^{\prime ef}}$	Concrete effective compressive strength
$\boldsymbol{f_y}$	Yield stress of steel
$\boldsymbol{f_c}$	Compressive strength concrete
$\boldsymbol{f'_t}$	Tensile strength
$\boldsymbol{f_c^{\prime ef}}$	Concrete effective compressive strength
k	Shape parameter,
p	Transformed reinforcing ratio
$\boldsymbol{r_{et}}$	Reduction factor of the compressive strengths
$\boldsymbol{w}$	Crack with
$\boldsymbol{w_d}$	Softening compression

Greek letters

$\boldsymbol{\varepsilon}$	Strain
ε_c	Strain at the peak stress $f_c^{\prime ef}$
$\boldsymbol{\varepsilon_u}$	Crack opening strain
$\boldsymbol{\nu}$	Poisson's ratio
$\boldsymbol{\sigma_c^{ef}}$	Concrete compressive stress
γ_{max}	Orientation factor for strain localization

Appendix

A Design of a-Seismic Double-Wall 5- Storey Building

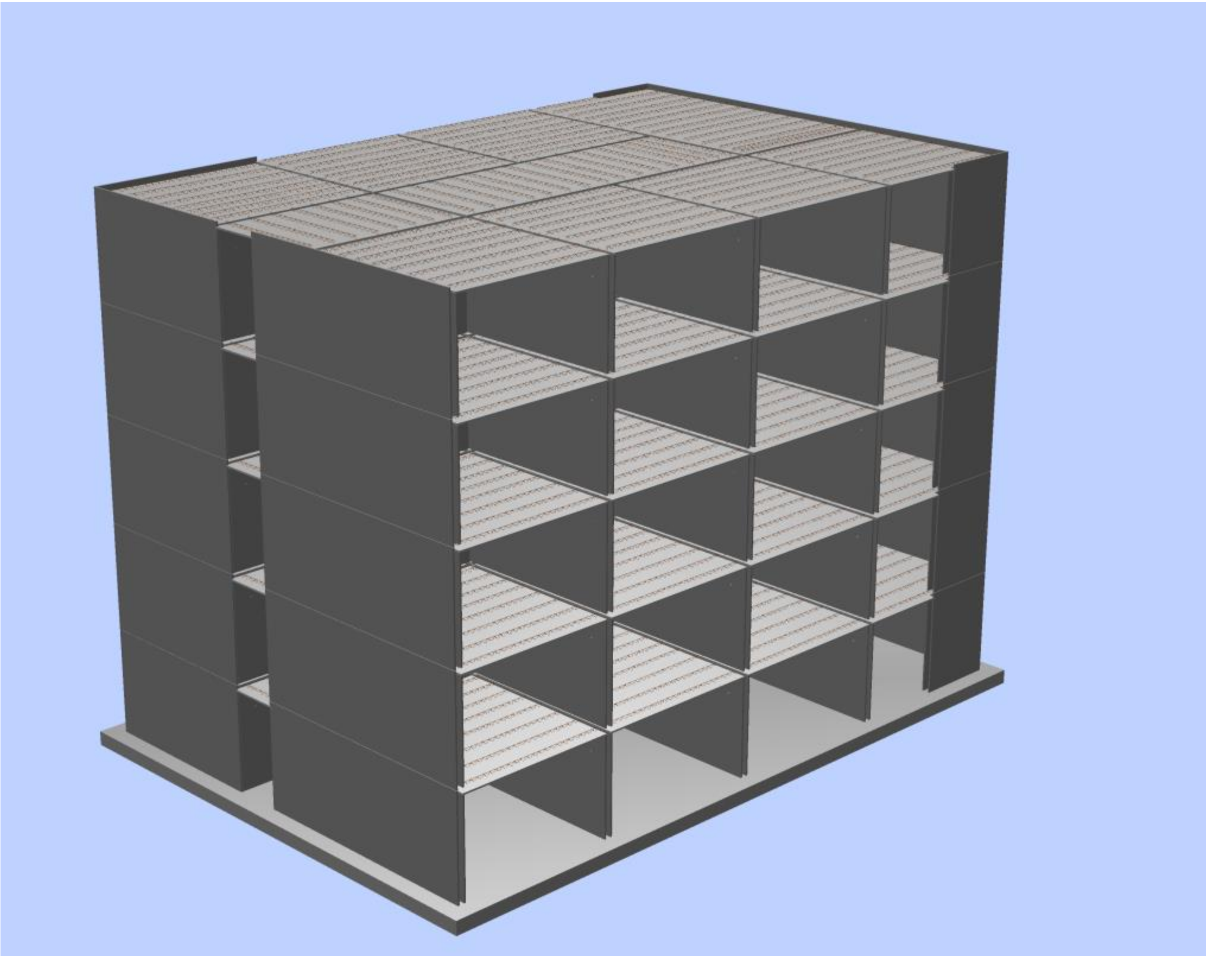

Figure 209 Double-wall and filigree slabs- building as sample for model-calculation

For the sample-calculation a type of 5-store house, as already showed by Sucuoglu *et al.* [10].

The 3D-view of the walls (without slabs) is shown in ***Figure 210.***
To show the way to use double-walls, there are calculated 2 of the typical situations:

1. Corner and
2. Intersection off wall

The calculation is done for earthquake in the **x**-direction, and the maximal achieved forces and bending moments are calculated.

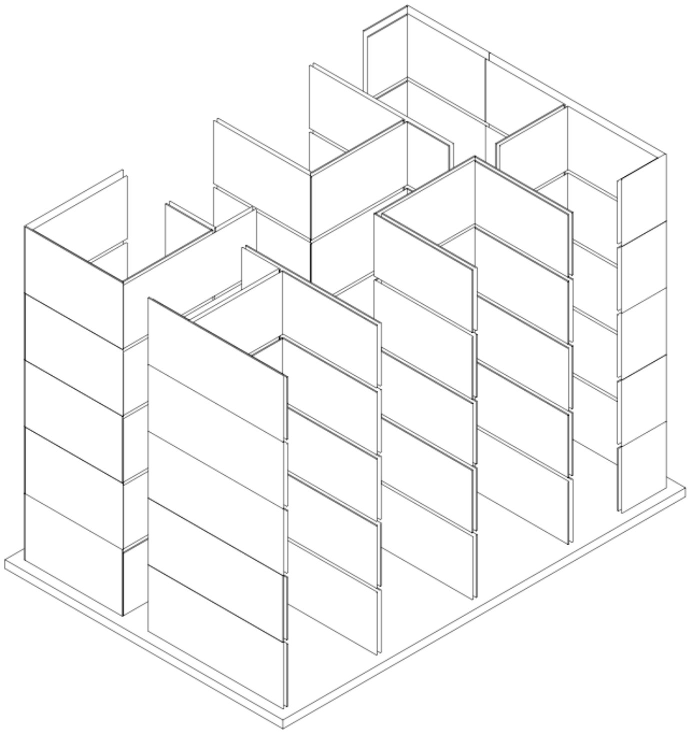

Figure 210 *3-D view of sample-construction.*

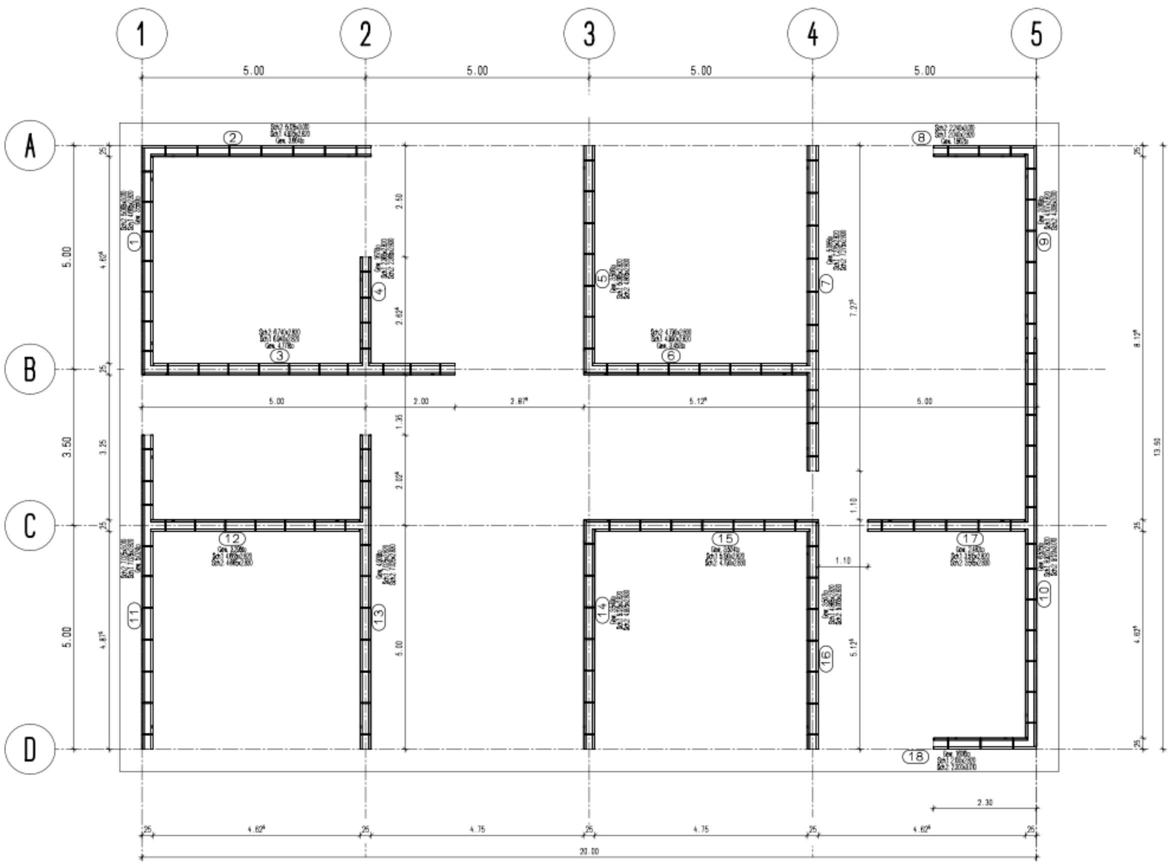

Figure 211 *Plan to transpose the wall-segments at the construction site.*

This calculation is made with the following conditions:

Basic for the calculation is the Turkish Seismic Code 2007 (TSK), overview at [34].

Typical floor plan of a 5-storey reinforced concrete double-wall all member dimensions are given in Plan, ***Figure 211 Plan to transpose the wall-segments at the construction site.*** Floor plan and member dimensions are the same in all stories. The building is located in Seismic Zone 1, and soil condition is Z3. Design Frame 3 according to the Turkish Seismic Code 2007. Concrete grade is C25 and steel grade is S420. Ductility level is,

as found in our tests R=6. The earthquake direction is “Y”.

The calculation was executed by the CUBUS Program **Cedrus-Gebäude-vers-6**: (www.cubus.ch)

Surface and Volume

Storey	Element	Material	Height	Surface		Volume			
				Slabs	Walls	Slabs	Walls	Columns	Sum
			[m]	[m²]	[m²]	[m³]	[m³]	[m³]	[m³]
L5				270,00	272,10	48,60	68,02	0	116,63
L4				270,00	272,10	48,60	68,02	0	116,63
L3				270,00	272,10	48,60	68,02	0	116,63
L2				270,00	272,10	48,60	68,02	0	116,63
L1				270,00	272,10	48,60	68,02	0	116,63
L0				0	0	0	0	0	0
				1350,00	1360,50	243,00	340,12	0	583,13

Storey	Element	Slabs	Wall segments		Columns		Sum
							[t]
L5		121,500	170,063	0	0	0	291,563
L4		121,500	170,063	0	0	0	291,563
L3		121,500	170,063	0	0	0	291,563
L2		121,500	170,063	0	0	0	291,563
L1		121,500	170,063	0	0	0	291,563
L0		0	0	0	0	0	0
		607,500	850,313	0	0	0	1457,813

Figure 212 Surfaces, volume and Masses.

NATURAL FREQUENCIES
"for analysis: Dyn; Mass distribution=M"

AC-nr.	ω^2 [(rad/s)²]	ω [rad/s]	Period [s]	Frequency [s⁻¹]
1	474,53	21,784	0,28843	3,47
2	747,24	27,336	0,22985	4,35
3	1079,68	32,859	0,19122	5,23
4	14344,15	119,767	0,05246	19,06
5	22039,47	148,457	0,04232	23,63
6	29103,12	170,596	0,03683	27,15
7	80289,82	283,355	0,02217	45,10
8	121124,72	348,030	0,01805	55,39
9	149992,98	387,289	0,01622	61,64
10	199184,84	446,301	0,01408	71,03

Figure 213 Natural frequencies.

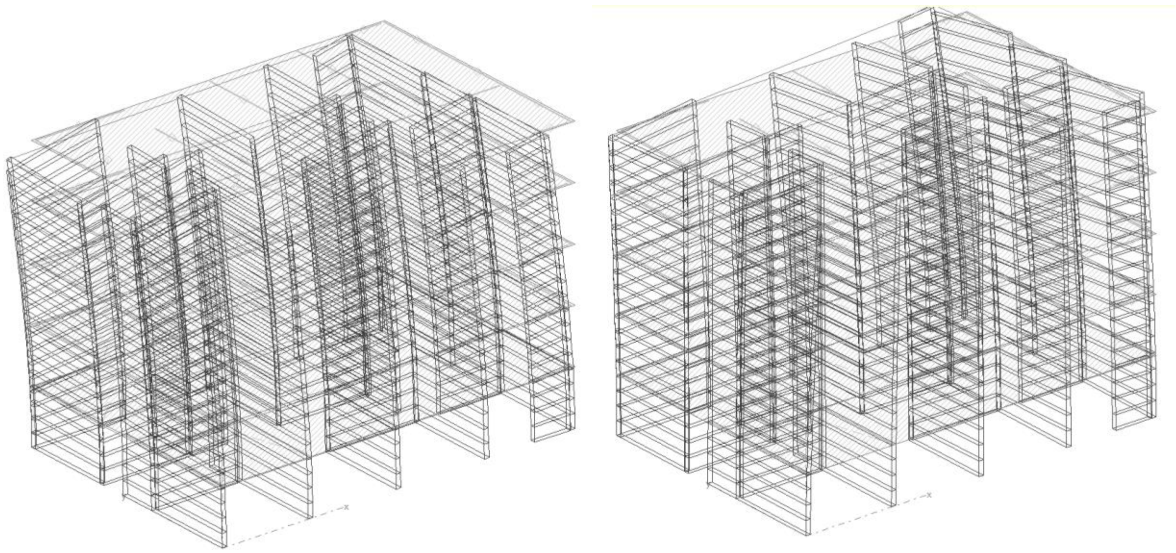

a) Nat freq. 3.5 [s^{-1}] b) Nat. freq. 4.35 [s^{-1}]

Figure 214 Displacement with Eigenmode 1 and 2.

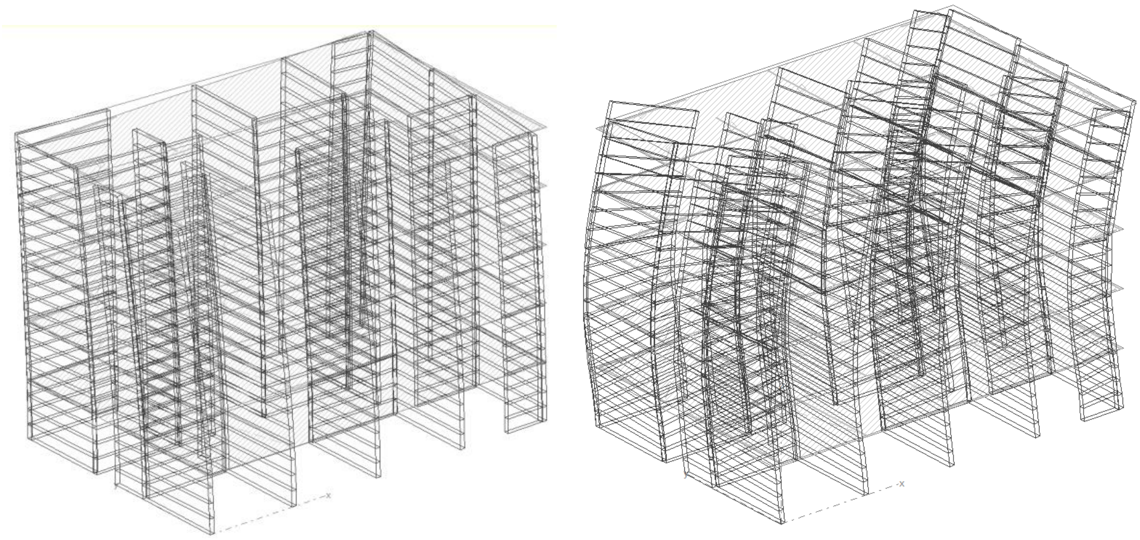

a) Nat. freq, 5,2 [s^{-1}] b) Nat freq. 19,1 [s^{-1}]

Figure 215 Displacement with Eigenmode 3 and 4.

MODAL MASS (per direction sorted by part. factor)
"for analysis: Dyn; Mass distribution=M"

EV-pos.	X-Direction			Y-Direction			Z-Direction		
	AC-nr.	me_X [t]	Σme_X [%]	AC-nr.	me_Y [t]	Σme_Y [%]	AC-nr.	me_Z [t]	Σme_Z [%]
1	1	1005,32	60,7%	2	524,38	31,7%	9	0,00	0,0%
2	4	335,80	81,0%	3	493,68	61,5%	10	0,00	0,0%
3	7	103,45	87,2%	5	179,78	72,3%	8	0,00	0,0%
4	3	97,41	93,1%	6	159,70	82,0%	7	0,00	0,0%
5	10	35,83	95,3%	1	117,04	89,0%	5	0,00	0,0%
6	2	31,38	97,2%	8	60,08	92,7%	4	0,00	0,0%
7	6	22,04	98,5%	9	40,90	95,1%	6	0,00	0,0%
8	5	9,51	99,1%	4	28,47	96,8%	2	0,00	0,0%
9	9	3,45	99,3%	7	7,27	97,3%	3	0,00	0,0%
10	8	2,81	99,4%	10	2,59	97,4%	1	0,00	0,0%

Figure 216 Modal mass.

Eigenvalues considered for analysis 'AX' (Calculation: 'Aws')

EV	Eigenvalue results		Damp.	Substitutional mass							
	frequency $[s^{-1}]$	Period [s]	ξ	$me_{\phi=0}$ [t]	%	me_X [t]	%	me_Y [t]	%	me_Z [t]	%
Dyn_1	3,47	0,28843	0.050	1005,32	61	1005,32	61	117,04	7	0,00	0
Dyn_4	19,06	0,05246	0.050	335,80	20	335,80	20	28,47	2	0,00	0
Dyn_7	45,10	0,02217	0.050	103,45	6	103,45	6	7,27	0	0,00	0
Dyn_3	5,23	0,19122	0.050	97,41	6	97,41	6	493,68	30	0,00	0
Sum me				1541,99	93	1541,99	93	646,47	39	0,00	0

Figure 217 Eigenvalues considered for analysis “Ax”.

Modal results for analysis 'AX', (Calculation 'Aws')

EV	Eigenvalues		Spectral value			Modal values		Base Shear
	Frequency $[s^{-1}]$	Period [s]	S_d/g	S_d $[m/s^2]$	S_d/ω^2 [m]	Part.fact.	Amplitude	[kN]
Dyn_1	3,47	0,28843	0,192	1,92	0,004	-3171E-2	-1281E-4	1926,87
Dyn_4	19,06	0,05246	0,277	2,77	0,000	-1832E-2	-3532E-6	928,50
Dyn_7	45,10	0,02217	0,294	2,94	0,000	-1017E-2	-3723E-7	304,06
Dyn_3	5,23	0,19122	0,197	1,97	0,002	-9870E-3	-1798E-5	191,62

Figure 218 Modal results for analysis "AX".

Eigenvalues considered for analysis 'AY' (Calculation: 'Aws')

EV	Eigenvalue results		Damp.	Substitutional mass							
	frequency $[s^{-1}]$	Period [s]	ξ	$me_{\phi=90}$ [t]	%	me_X [t]	%	me_Y [t]	%	me_Z [t]	%
Dyn_2	4,35	0,22985	0.050	524,38	32	31,38	2	524,38	32	0,00	0
Dyn_3	5,23	0,19122	0.050	493,68	30	97,41	6	493,68	30	0,00	0
Dyn_5	23,63	0,04232	0.050	179,78	11	9,51	1	179,78	11	0,00	0
Dyn_6	27,15	0,03683	0.050	159,70	10	22,04	1	159,70	10	0,00	0
Dyn_1	3,47	0,28843	0.050	117,04	7	1005,32	61	117,04	7	0,00	0
Dyn_8	55,39	0,01805	0.050	60,08	4	2,81	0	60,08	4	0,00	0
Sum me				1534,67	93	1168,47	71	1534,67	93	0,00	0

Figure 219 Eigenvalues considered for analysis “Ay”.

Modal results for analysis 'AY', (Calculation 'Aws')

EV	Eigenvalues Frequency [s^{-1}]	Period [s]	Spectral value S_d/g	S_d [m/s^2]	S_d/ω^2 [m]	Modal values Part.fact.	Amplitude	Base Shear [kN]
Dyn_2	4,35	0,22985	0,192	1,92	0,003	2290E-2	5874E-5	1005,07
Dyn_3	5,23	0,19122	0,197	1,97	0,002	2222E-2	4048E-5	971,15
Dyn_5	23,63	0,04232	0,282	2,82	0,000	-1341E-2	-1718E-6	507,58
Dyn_6	27,15	0,03683	0,285	2,85	0,000	1264E-2	1240E-6	455,93
Dyn_1	3,47	0,28843	0,192	1,92	0,004	-1082E-2	-4370E-5	224,33
Dyn_8	55,39	0,01805	0,296	2,96	0,000	-7751E-3	-1896E-7	178,00

Figure 220 Modal results for analysis "Ay"

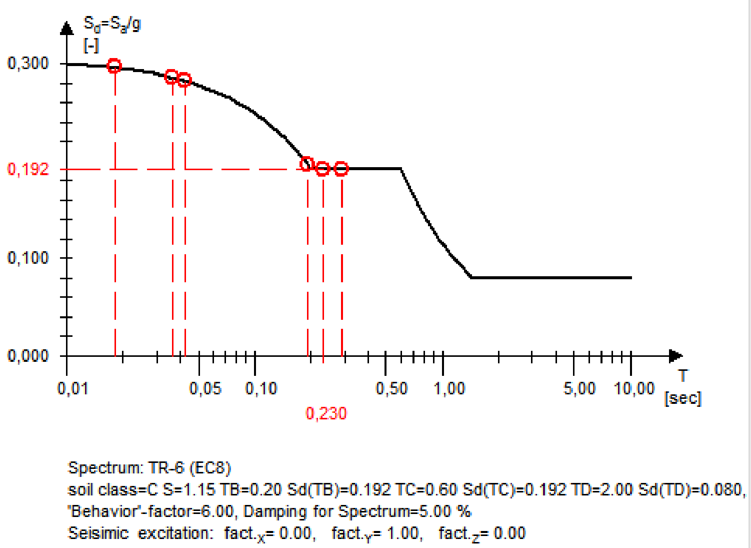

Figure 221 The used response spectrum.

Shear wall reinforcement (remaining wall sections)

Member	Elem	Distance [m]	Node N3 [mm^2]	N4 [mm^2]	N5 [mm^2]	N6 [mm^2]	Shear walls distributed W2 [mm^2]	W3 [mm^2]	W4 [mm^2]	W5 [mm^2]	Stirrup A_{sw} W2 [mm^2/m]	W3 [mm^2/m]	W4 [mm^2/m]	W5 [mm^2/m]
L1-P4	1	0,00	3056	3056	3056		1021	2592			0	0		
L1-P24	1	0,00	3704	3704			2576				3218			
L2-P24	1	0,00	2505	2505			2576				3449			

Figure 222 Shear wall reinforcement.

In floor L1, the following double wall members are “most-loaded”:

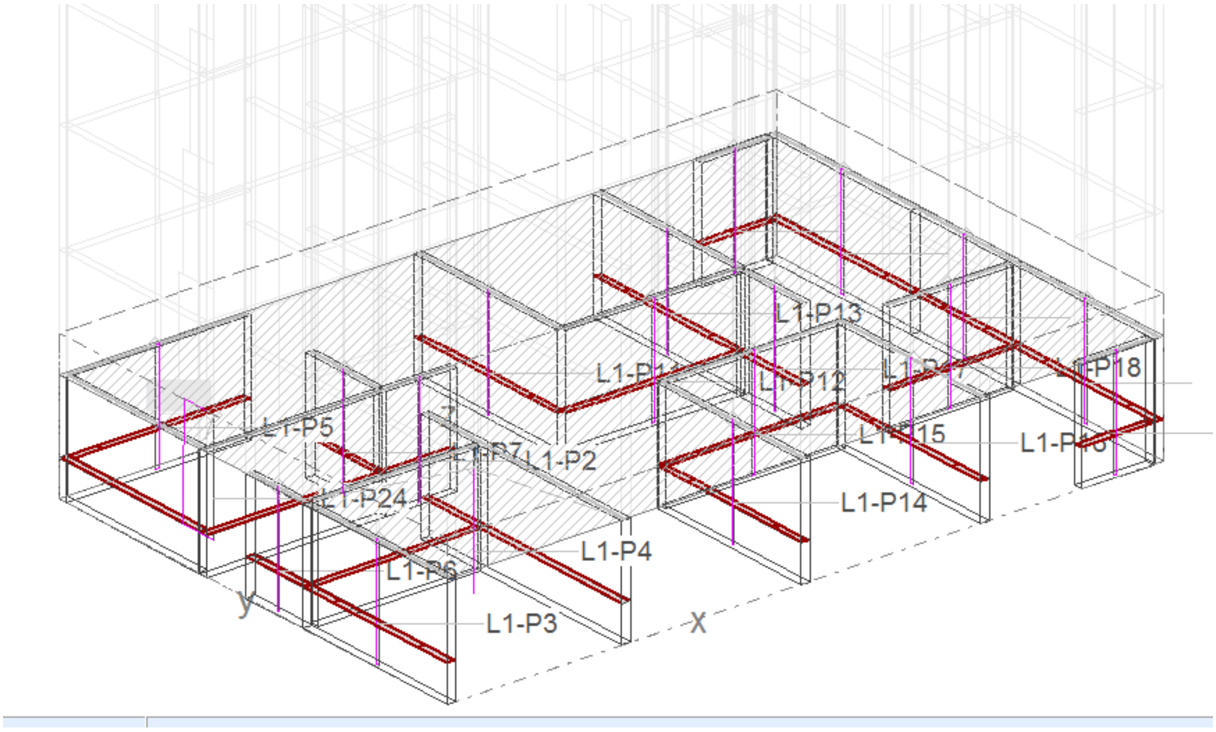

Figure 224 *Overview level L1 with member numbers.*

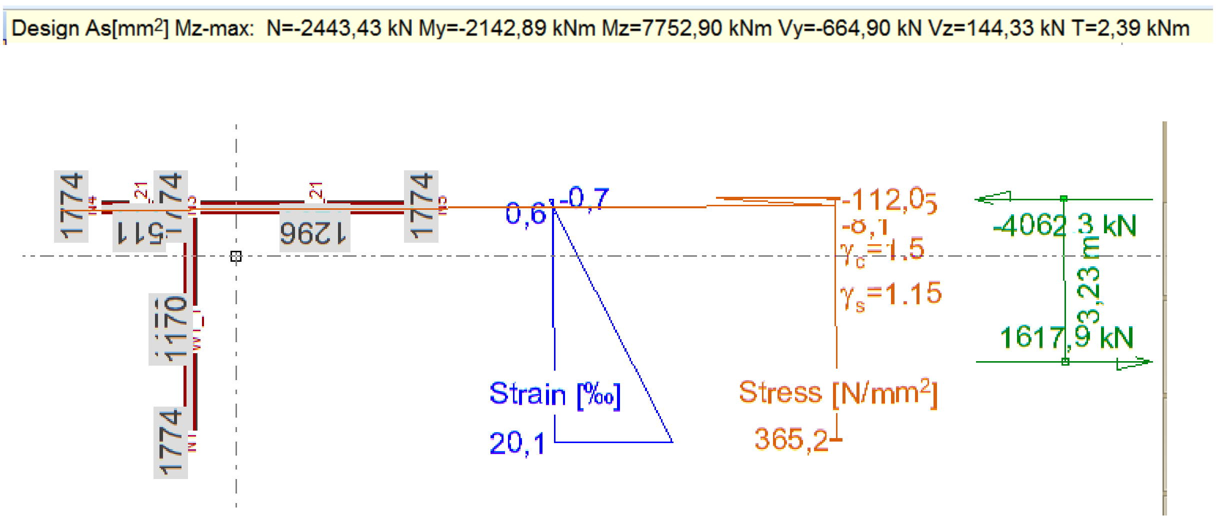

Figure 225 *Member L1-P4.*

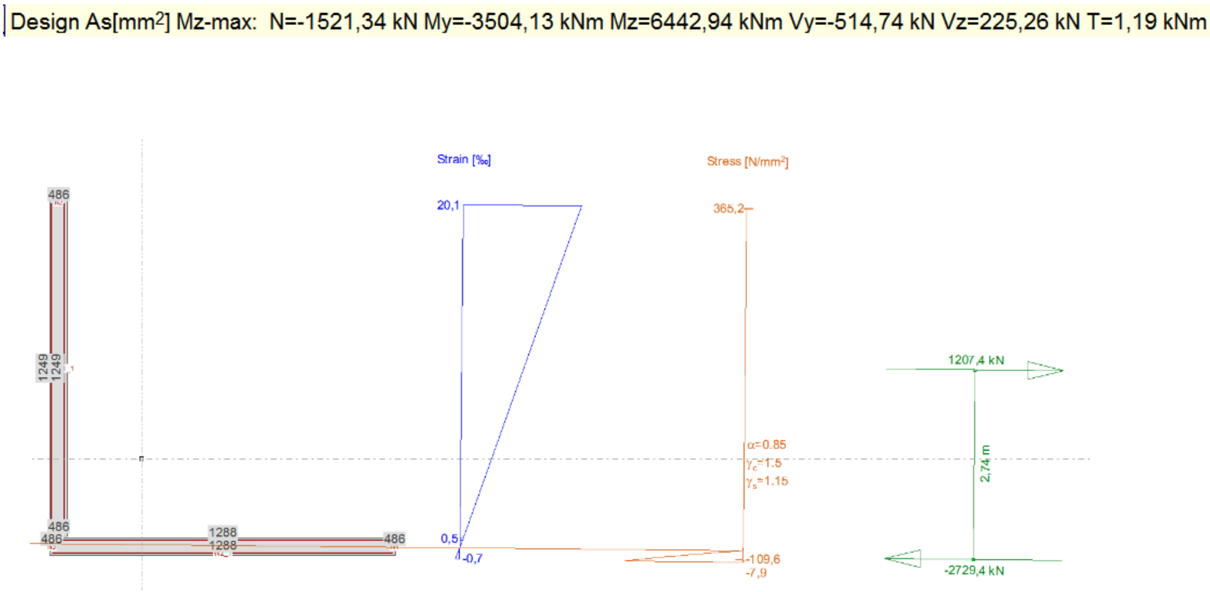

Figure 226 *Member L1-P24.*

B Initial Design of the U-shaped Shear Wall

<u>According to Turkish Earthquake Code</u>

Walls length 5 m

width 25 cm,

Building height 15 m

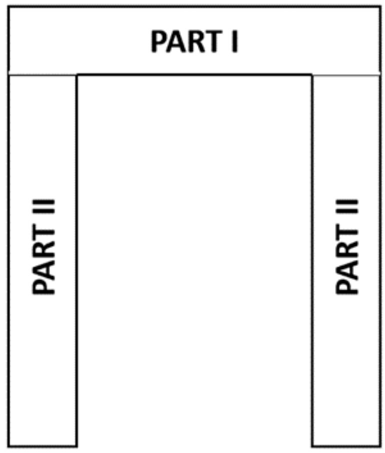

PART I

Critical Wall Height

<u>Code.</u> *Critical wall height measured from the foundation*

$$max\left(l_w, \frac{H_w}{6}\right) \leq H_{cr} \leq 2l_w$$

$$\rightarrow \max\left(5\text{ m}, \frac{15}{6}\right) = 2.5\text{ m} \leq \mathrm{H_{cr}} \leq 2 \times 5 = 10\text{ m} \rightarrow \mathrm{H_{cr}} = 10\text{ m}$$

The whole height of the wall will be considered as critical height.

Cross-section Requirements

a) Wall End Zones Cross-Section Requirements:

<u>Code.</u> *Wall Thickness:* $b_w \geq max(\frac{1}{15}H_{storey}, 200mm)$

$\mathrm{b_w} \geq \max\left(\frac{1}{15} \times 3.0, 200\text{mm}\right) = 200\text{ mm} \rightarrow \mathrm{b_w} = 200\text{ mm}$, real dimension = 25 cm

<u>Code.</u> *Length of each end zone:*

Along the critical height $\rightarrow l_u \geq max(0.2l_w, 2b_w)$

Above the critical height $\rightarrow l_u \geq max(0.1l_w, b_w)$

$$\text{Along the critical height} \rightarrow \mathrm{l_u} \geq \max(0.2 \times 5 \times 0.2) = 1.0\text{ m}$$

$$\text{Above the critical height} \rightarrow \mathrm{l_u} \geq \max(0.1 \times 5\text{ X }0.2) = 0{,}5\text{m}$$

Since the whole height of wall as critical height has been considered as critical height, the length of the end zone will be taken as 100 cm.

b) Web Cross-Section Requirements:

<u>Code.</u> *Wall thickness:* $b_w \geq max(\frac{1}{20}H_{storey}, 200mm)$

$$\mathrm{b_w} \geq \max\left(\frac{1}{20} \times 3., 0.2\text{ m}\right) = 200\text{ mm} \rightarrow \mathrm{b_w} = 200\text{ mm}$$

Reinforcement Requirements

a) Wall End Zones Reinforcement Requirements:

<u>Code.</u> *Vertical reinforcement*

Along critical height $\rightarrow \sum A_{ver.} \geq \max(0.002A_w, 4\Phi 14)$

Above critical height $\rightarrow \sum A_{ver.} \geq \max(0.001A_w, 4\Phi 14)$

Along critical height:

$$\sum A_{ver.} \geq \max(0.002 \times 0.2 \times 5 \times 154 \times 10^{-6}) = \max(0.002\ m^2, 0.000616\ m^2) = 2000\ mm^2$$

As calculated before, the length of each wall end zone is taken as 40cm. For mesh in precast layer Φ6 and for the confinement part Φ8 as vertical reinforcement with 10 cm spacing are considered. Therefore, there are 10 bars in 4 layers Φ 8;

$$10 \times 4 \times 50 = 2000 = 2000\ \mathrm{mm}^2$$

<u>Code.</u> *In wall end zones, vertical spacing of hoops must be as follows:*

$$Along\ critical\ height \rightarrow 50\ mm \leq s \leq \min\left(\frac{b_w}{2}, 100mm\right)$$

$$Above\ critical\ height \rightarrow s \leq \min(b_w, 200mm)$$

$$\text{Along critical height} \rightarrow 50\ \text{mm} \leq \text{s} \leq \min(100\text{mm}, 100\text{mm}) = 100\text{mm} \rightarrow \text{s} = 10\text{cm}$$

For confinement part, hoops of Φ8 with 10cm spacing is considered.

b) Web Reinforcement Requirements:

<u>Code.</u>

$$Vertical\ Reinforcement \quad \sum A_{ver.} \geq 0.0025\ l_{web} b_w$$

$$Horizontal\ Reinforcement \quad \sum A_{hor.} \geq 0.0025\ l_{web} b_w$$

$$\sum \mathrm{A}_{\text{ver.\& hor.}} \geq 0.0025 \times 0.2 \times 0.2 = 0.0001\ \mathrm{m}^2$$

<u>Code.</u> *The spacing of longitudinal and transverse reinforcement in wall web shall not be more than 250 mm.*

Considering 20 cm as the length of wall web and Φ6 for mesh bar a there are 6 bar in web zone;

$$6 \times 50 = 300\ \mathrm{mm}^2 \geq 100\ \mathrm{mm}^2$$

For horizontal reinforcement Φ8 with 25cm spacing will be considered, we have 13 bars in 2 layers:

$$2 \times 13 \times 50 = 1300 mm^2 > 100\ \mathrm{mm}^2$$

Since "Part I" is considered as the end zone of "PART II", there must confinement along the whole length.

PART II

Critical Wall Height

<u>Code.</u> *Critical wall height measured from the foundation* $max\left(l_w, \frac{H_w}{6}\right) \leq H_{cr} \leq 2l_w$

$$\rightarrow \max\left(5\text{m}, \frac{15}{6}\right) = 2{,}5\ \text{m} \leq \text{H}_{\text{cr}} \leq 2 \times 5 = 10\ \text{m} \rightarrow \text{H}_{\text{cr}} = 10\ \text{m}$$

Cross-section Requirements

a) Wall End Zones Cross-Section Requirements:

<u>Code.</u> *Wall Thickness:* $b_w \geq max(\frac{1}{15} H_{storey}, 200mm)$

$$\mathrm{b_w} \geq \max\left(\frac{1}{15} \times 3, 200\mathrm{mm}\right) = 200\ \mathrm{mm} \ \rightarrow\ \mathrm{b_w} = 200\ \mathrm{mm}$$

<u>*Code.*</u> *Length of each end zone:*

Along the critical height $\rightarrow\ l_u \geq max(0.2l_w, 2b_w)$

Above the critical height $\rightarrow\ l_u \geq max(0.1l_w, b_w)$

$$\text{Along the critical height} \ \rightarrow\ \mathrm{l_u} \geq \max(0.2 \times 5, 2 \times 0.2) = 1.0\ \mathrm{m}$$

$$\text{Above the critical height} \ \rightarrow\ \mathrm{l_u} \geq \max(0.1 \times 5, 0.2) = 0{,}5\ \mathrm{m}$$

<u>*Code.*</u> *In the case where wall end zones are arranged within an adjoining walls or at enlarged sections at the edges of the wall, cross section area of each of the wall end zones shall*

be equal at least to the area defined for rectangular section walls (A ≥ $b_w l_u$).

As we have considered the whole height of wall as critical height, the length of the end zone will be taken as 200 cm. The other end zone, since it is arranged within another wall, the adjoining wall itself will be considered as the end zone of the other wall.

b) Web Cross-Section Requirements:

<u>*Code.*</u> *Wall thickness:* $b_w \geq max(\frac{1}{20} H_{storey}, 200mm)$

$$\mathrm{b_w} \geq \max\left(\frac{1}{20} \times 3., 0.2\ \mathrm{m}\right) = 200\ \mathrm{mm} \ \rightarrow\ \mathrm{b_w} = 200\ \mathrm{mm}$$

Reinforcement Requirements

a) Wall End Zones Reinforcement Requirements:

<u>*Code.*</u> *Vertical reinforcement*

Along critical height $\rightarrow\ \sum A_{ver.} \geq \max(0.002A_w, 4\Phi 14)$

Above critical height $\rightarrow\ \sum A_{ver.} \geq \max(0.001A_w, 4\Phi 14)$

Along critical height:

$$\sum A_{ver.} \geq \max(0.002 \times 0.2 \times 5, 4 \times 154 \times 10^{-6}) = \max(0.002\ m^2, 0.000616\ m^2) = 2000\ mm^2$$

Like 'Part I', for mesh in precast layer Φ6 and for the confinement part Φ8 (vertical reinforcement) with 10 cm spacing are considered. Therefore, there are 4 bars in 4 layers;

$$10 \times 4 \times 50 = 2000\ \mathrm{mm^2} = 2000\ \mathrm{mm^2}$$

<u>*Code.*</u> *In wall end zones, vertical spacing of hoops must be as follows:*

$$\textit{Along critical height} \ \rightarrow\ 50\ mm \leq s \leq \min\left(\frac{b_w}{2}, 100mm\right)$$

$$\textit{Above critical height} \ \rightarrow\ s \leq \min(b_w, 200mm)$$

$$\text{Along critical height} \ \rightarrow\ 50\ \mathrm{mm} \leq \mathrm{s} \leq \min(100\mathrm{mm}, 100\mathrm{mm}) = 100\mathrm{mm} \ \rightarrow\ \mathrm{s} = 10\mathrm{cm}$$

b) Web Reinforcement Requirements:

<u>Code.</u>
$$Vertical\ Reinforcement \quad \sum A_{ver.} \geq 0.0025\ l_{web} b_w$$
$$Horizontal\ Reinforcement \quad \sum A_{hor.} \geq 0.0025\ l_{web} b_w$$

$$\sum A_{ver.\&\,hor.} \geq 0.0025 \times 1.00 \times 0.2 = 0.0005\ m^2$$

<u>Code.</u> *The spacing of longitudinal and transverse reinforcement in wall web shall not be more than 250 mm.*

Considering 100 cm as the length of wall web and Φ8 as vertical reinforcement with 20 cm spacing, we have 6 bars in 2 layers;

$$6 \times 2 \times 50 = 600\ mm^2 > 500\ mm^2$$

For horizontal reinforcement Φ8 with 25cm spacing will be considered, we have 13 bars in 2 layers:

$$2 \times 13 \times 50 = 1300\ mm^2 \quad > \quad 500\ \mathrm{mm}^2$$

<u>Code.</u>

$$Along\ critical\ height \quad \rightarrow \quad Min.\,10\ special\ seismic\ crossties\ per\ unit\ square\ meter$$
$$Above\ critical\ height \quad \rightarrow \quad Min.\,4\ special\ seismic\ crossties\ per\ unit\ square\ meter$$

$$\text{Along critical height} \quad \rightarrow \quad 5 \times 3 = 15\ \mathrm{m}^2 \quad \rightarrow \quad 150\ \text{units}$$

Here, the equivalent of **xx** crossties (Φ8) will be used. It consists of a hoop (Φ8 with 10cm spacing) and **xx** waves.

Shear strength

<u>Code.</u> *Shear strength of wall cross section shall be calculated as follows:*

$$V_r = A_{ch}\left(0.65 f_{ctd} + \rho_{sh} f_{yd}\right)$$

Ach = Gross section area of a solid wall, wall segment of a coupled wall, a floor or a floor segment of a perforated floor

fctd = Design tensile strength of concrete

fyd = Design yield strength of longitudinal reinforcement

sh = Volumetric ratio of horizontal web reinforcement of wall

$$\mathrm{A_{ch}} = 0.4 \times 1.4 = 0.56\ \mathrm{m}^2 \quad , \quad \mathrm{f_{ctd}} = 3\ \mathrm{MPa} \ , \ \mathrm{f_{yd}} = 425\ \mathrm{MPa} \ ,$$

$$\rho_{\mathrm{sh}} = \frac{\mathrm{A_{v,horiz}}}{\mathrm{ts_2}} = \frac{4 \times 28}{400 \times 250} = 0.002$$

$$\mathrm{V_r} = 0.56(0.65 \times 3 + 0.002 \times 425) = 2800\mathrm{KN}$$

C Initial Design of the T-shaped Shear Wall

<u>According to Turkish Earthquake Code</u>

Walls length 5 m
width 25 cm,
Building height 15 m

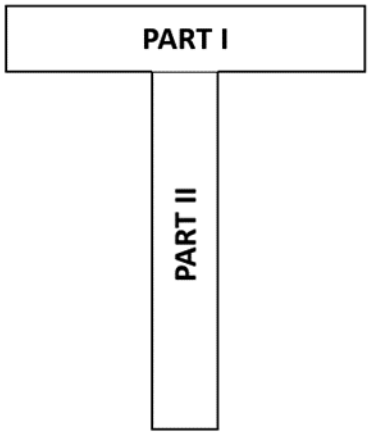

PART I

Critical Wall Height

<u>*Code.*</u> *Critical wall height measured from the foundation* $max\left(l_w, \frac{H_w}{6}\right) \leq H_{cr} \leq 2l_w$

$$\rightarrow \max\left(5\text{m}\,, \frac{15}{6}\right) = 5 \text{ m} \;\leq\; \text{H}_{\text{cr}} \;\leq 2 \times 5 = 10 \text{ m} \;\rightarrow\; \text{H}_{\text{cr}} = 10\text{m}$$

All walls will be considered as within the critical height.

Cross-section Requirements

a) Wall End Zones Cross-Section Requirements:

<u>*Code.*</u> *Wall Thickness:* $b_w \geq max(\frac{1}{15}H_{storey}, 200mm)$

$$\text{b}_\text{w} \geq \max\left(\frac{1}{15} \times 3.0, 200\text{mm}\right) = 200 \text{ mm} \;\rightarrow\; \text{b}_\text{w} = 200 \text{ mm}$$

<u>*Code.*</u> *Length of each end zone:*

$Along\ the\ critical\ height \rightarrow l_u \geq max(0.2l_w, 2b_w)$

$Above\ the\ critical\ height \rightarrow l_u \geq max(0.1l_w, b_w)$

$$\text{Along the critical height} \rightarrow \text{l}_\text{u} \geq \max(0.2 \times 5\,, \quad 2\text{x}0.2) = 1.0\text{m}$$

$$\text{Above the critical height} \rightarrow \text{l}_\text{u} \geq \max(0.1 \times 5, \; 0.2) = 0.5 \text{ m}$$

Since the whole height of wall as critical height has been considered as critical height, the length of the end zone will be taken as 100 cm.

b) Web Cross-Section Requirements:

<u>*Code.*</u> *Wall thickness:* $b_w \geq max(\frac{1}{20}H_{storey}, 200mm)$

$$\text{b}_\text{w} \geq \max\left(\frac{1}{20} \times 3.0, 0.2 \text{ m}\right) = 150 \text{ mm} \;\rightarrow\; \text{b}_\text{w} = 200 \text{ mm}$$

Reinforcement Requirements

a) Wall End Zones Reinforcement Requirements:

<u>Code.</u> *Vertical reinforcement*

$Along\ critical\ height \quad \rightarrow \quad \sum A_{ver.} \geq \max(0.002A_w, 4\Phi 14)$

$Above\ critical\ height \quad \rightarrow \quad \sum A_{ver.} \geq \max(0.001A_w, 4\Phi 14)$

Along critical height:

$$\sum A_{ver.} \geq \max(0.002 \times 0.2 \times 5\ , 4 \times 154 \times 10^{-6}) = \max(0.002\ m^2, 0.000616\ m^2) = 2000\ mm^2$$

As calculated before, the length of each wall end zone is taken as 40cm. For mesh in precast layer and for the confinement part Φ8 as vertical reinforcement with 10 cm spacing are considered. Therefore, there are 10 bars in 4 layersΦ 8;

$$10 \times 4 \times 50 = 2000\ \mathrm{mm}^2 = 2000\ \mathrm{mm}^2$$

<u>Code.</u> *In wall end zones, vertical spacing of hoops must be as follows:*

$$Along\ critical\ height \quad \rightarrow \quad 50\ mm\ \leq s \leq \min\left(\frac{b_w}{2}, 100mm\right)$$

$$Above\ critical\ height \quad \rightarrow \quad s \leq \min(b_w, 200mm)$$

$$\text{Along critical height} \quad \rightarrow \quad 50\ \mathrm{mm}\ \leq \mathrm{s} \leq \min(100\mathrm{mm}, 100\mathrm{mm}) = 100\mathrm{mm} \quad \rightarrow \quad \mathrm{s} = 10\mathrm{cm}$$

For confinement part, hoops of Φ8 with 10cm spacing is considered.

b) Web Reinforcement Requirements:

<u>Code.</u> $Vertical\ Reinforcement \quad \sum A_{ver.} \ \geq 0.0025\ l_{web} b_w$

$Horizontal\ Reinforcement \quad \sum A_{hor.} \ \geq 0.0025\ l_{web} b_w$

$$\sum \mathrm{A}_{\mathrm{ver.}\&\ hor.} \ \geq 0.0025 \times 0.2 \times 0.2 = 0.0001\ \mathrm{m}^2$$

<u>Code.</u> *The spacing of longitudinal and transverse reinforcement in wall web shall not be more than 250 mm.*

Considering 20 cm as the length of wall web and Φ8 as vertical reinforcement, there are 6 bars in web zone;

$$6 \times 50 = 300\ \mathrm{mm}^2 \geq 100\ \mathrm{mm}^2$$

For horizontal reinforcement Φ8 with 25cm spacing will be considered, we have 13 bars in 2 layers:

$$2 \times 13 \times 50 = 1300\ mm^2 \ \ > \ \ 100\ \mathrm{mm}^2$$

<u>Since "Part I" is considered as the end zone of "PART II", there must confinement along the whole length.</u>

PART II

Critical Wall Height

<u>Code.</u> *Critical wall height measured from the foundation* $max\left(l_w, \frac{H_w}{6}\right) \leq H_{cr} \leq 2l_w$

$$\rightarrow \max\left(5\text{m}, \frac{15}{6}\right) = 2.5\text{ m} \leq \text{H}_{\text{cr}} \leq 2 \times 5 = 10\text{ m} \quad \rightarrow \quad \text{H}_{\text{cr}} = 10\text{ m}$$

<u>Cross-section Requirements</u>

a) Wall End Zones Cross-Section Requirements:

<u>Code.</u> *Wall Thickness:* $b_w \geq max(\frac{1}{15}H_{storey}, 200mm)$

$$\text{b}_\text{w} \geq \max\left(\frac{1}{15} \times 3, 200\text{mm}\right) = 200\text{ mm} \rightarrow \text{b}_\text{w} = 200\text{ mm}$$

<u>Code.</u> *Length of each end zone:*

Along the critical height $\rightarrow$ $l_u \geq max(0.2l_w, 2b_w)$

Above the critical height $\rightarrow$ $l_u \geq max(0.1l_w, b_w)$

$$\text{Along the critical height} \rightarrow \text{l}_\text{u} \geq \max(0.2 \times 5, 2 \times 0.2) = 1.0\text{ m}$$

$$\text{Above the critical height} \rightarrow \text{l}_\text{u} \geq \max(0.1 \times 5, 0.2) = 0.5\text{ m}$$

<u>Code.</u> *In the case where wall end zones are arranged within an adjoining walls or at enlarged sections at the edges of the wall, cross section area of each of the wall end zones shall*

Be equal at least to the area defined for rectangular section walls ($A \geq b_w l_u$).

As we have considered the whole height of wall as critical height, the length of the end zone will be taken as 100 cm. The other end zone, since it is arranged within another wall, the adjoining wall itself will be considered as the end zone of the other wall.

b) Web Cross-Section Requirements:

<u>Code.</u> *Wall thickness:* $b_w \geq max(\frac{1}{20}H_{storey}, 200mm)$

$$\text{b}_\text{w} \geq \max\left(\frac{1}{20} \times 3, 0.2\text{ m}\right) = 200\text{ mm} \rightarrow \text{b}_\text{w} = 200\text{ mm}$$

Reinforcement Requirements

a) Wall End Zones Reinforcement Requirements:

<u>Code.</u> *Vertical reinforcement*

Along critical height $\rightarrow$ $\sum A_{ver.} \geq \max(0.002A_w, 4\Phi14)$

Above critical height $\rightarrow$ $\sum A_{ver.} \geq \max(0.001A_w, 4\Phi14)$

Along critical height:

$$\sum A_{ver.} \geq \max(0.002 \times 0.2 \times 5, 4 \times 154 \times 10^{-6}) = \max(0.002\ m^2, 0.000616\ m^2) = 2000\ mm^2$$

Considering 100 cm as the length of each wall end zone, Φ8 as vertical reinforcement with 10 cm spacing, we have 10 bars in 4 layers;

$$10 \times 4 \times 50 = 2000 \text{ mm}^2 = 2000 \text{ mm}^2$$

<u>*Code.*</u> *In wall end zones, vertical spacing of hoops must be as follows:*

$$Along\ critical\ height \quad \rightarrow \quad 50\ mm\ \le s \le \min\left(\frac{b_w}{2}, 100mm\right)$$

$$Above\ critical\ height \quad \rightarrow \quad s \le \min(b_w, 200mm)$$

$$\text{Along critical height} \quad \rightarrow \quad 50 \text{ mm } \le \text{s} \le \min(100\text{mm}, 100\text{mm}) = 100\text{mm} \quad \rightarrow \quad \text{s} = 10\text{cm}$$

b) Web Reinforcement Requirements:

<u>*Code.*</u>

$$Vertical\ Reinforcement \quad \sum A_{ver.} \ \ge 0.0025\ l_{web} b_w$$

$$Horizontal\ Reinforcement \quad \sum A_{hor.} \ \ge 0.0025\ l_{web} b_w$$

$$\sum A_{ver.\&\ hor.} \ \ge 0.0025 \times 1. \times 0.2 = 0.0005 m^2$$

<u>*Code.*</u> *The spacing of longitudinal and transverse reinforcement in wall web shall not be more than 250 mm.*

Considering 100 cm as the length of wall web and Φ8 as vertical reinforcement with 20 cm spacing, we have 6 bars in 2 layers;

$$6 \times 2 \times 50 = 600\ mm^2 > 500\ mm^2$$

For horizontal reinforcement Φ8 with 25cm spacing will be considered, we have 13 bars in 2 layers:

$$2 \times 13 \times 50 = 1300\ mm^2 \ > \ 500 \text{ mm}^2$$

<u>*Code.*</u>

$$Along\ critical\ height \quad \rightarrow \quad Min.10\ special\ seismic\ crossties\ per\ unit\ square\ meter$$

$$Above\ critical\ height \quad \rightarrow \quad Min.4\ special\ seismic\ crossties\ per\ unit\ square\ meter$$

$$\text{Along critical height} \quad \rightarrow \quad 5 \times 3 = 15 \text{ m}^2 \quad \rightarrow \quad 150 \text{ units}$$

Here, the equivalent of 150 crossties (Φ8) will be used. It consists of a hoop (Φ8 with 10cm spacing) and subtracted 3 sticks for one KAPPEMA-wave.

Shear strength

<u>*Code.*</u> *Shear strength of wall cross section shall be calculated as follows:*

$$V_r = A_{ch}\left(0.65 f_{ctd} + \rho_{sh} f_{yd}\right)$$

Ach = Gross section area of a solid wall, wall segment of a coupled wall, a floor or a floor segment of a perforated floor

fctd = Design tensile strength of concrete

fyd = Design yield strength of longitudinal reinforcement

ρsh = Volumetric ratio of horizontal web reinforcement of wall

$$\text{A}_{\text{ch}} = 0.2 \times 5 = 1.0\text{m}^2 \ , \ \text{f}_{\text{ctd}} = 3 \text{ MPa} \ , \ \text{f}_{\text{yd}} = 425 \text{ MPa} \ , \qquad \rho_{\text{sh}} = 0.002$$

$$\text{V}_\text{r} = 1(0.65 \times 3 + 0.002 \times 425) = 2800 \text{ KN}$$

D Lebenslauf /CV

Personal Data

Name	Dipl.-Ing. Falko Ducia
Date of birth	26. November 1944
Place of birth	Seefeld / Tirol
Country	Austria
Citizenship	Austrian
Marital Status	Married
Universities	Eidgenössische Technische Hochschule Zürich-Schweiz
Professional Experience	Zivilingenieur für Bauwesen Baumeister Bauträger Prof. an HTL-Bau Innsbruck
Wien	January 2015